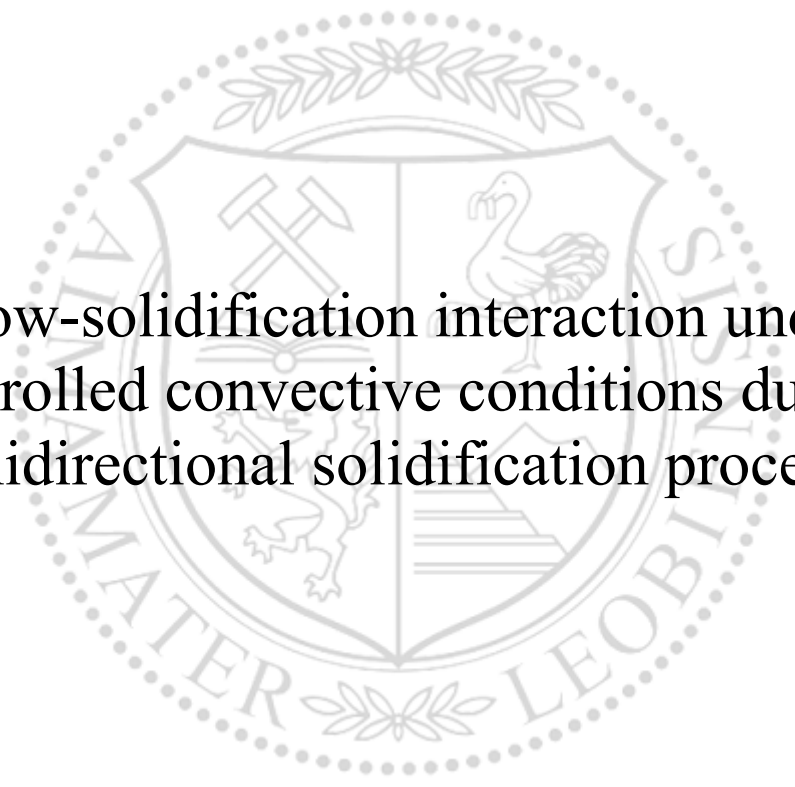




Chair of Simulation and Modelling of Metallurgical Processes

Doctoral Thesis



Flow-solidification interaction under
controlled convective conditions during
unidirectional solidification process

Haijie Zhang

May 2021



AFFIDAVIT

I declare on oath that I wrote this thesis independently, did not use other than the specified sources and aids, and did not otherwise use any unauthorized aids.

I declare that I have read, understood, and complied with the guidelines of the senate of the Montanuniversität Leoben for "Good Scientific Practice".

Furthermore, I declare that the electronic and printed version of the submitted thesis are identical, both, formally and with regard to content.

Date 12.05.2021

Haijie Zhang

Signature Author
Haijie Zhang

Acknowledgements

First and foremost, I would like to acknowledge my Ph.D advisor, Prof. Menghuai Wu for his support, guidance, encouragement, patience, and great insight. Scientific discussions let me learn a great deal from him, including how to conduct research scientifically, and how to analyze data properly. I am very grateful to have gotten the opportunity to study with Prof. Wu and enjoyed so much to work with him.

I want to express sincere thanks to Prof. Andreas Ludwig for giving me the opportunity to work in his group. It is such an honor to work at the chair of Simulation and Modelling of Metallurgical Processes (SMMP), one of the best groups on numerical modeling. I also want to thank Prof. Abdellah Kharicha for his generous help and excellent assistance in numerical problems.

I am grateful to my mentor Prof. Peter Schumacher for his generous help in the lecture about solidification fundamentals. It is really a fruitful and pleasant experience to discuss with him.

The research leading to these results has received the financial support from Austrian Research Promotion Agency (FFG) -Austrian Space Application Program (ASAP) through the project FLOWSICONS (No. 859777), as well as the support from European Space Agency (ESA) through the project MICAST. Support from NASA grant NNX14AM18G is gratefully acknowledged.

Great thanks to Prof. Lifeng Zhang in Yanshan University for his guidance and encouragement. Without his recommendation, it would not have been possible for me to come to Montanuniversität Leoben.

I would like to thank my great colleagues in SMMP: Alexander Vakhrushev, Ebrahim Karimi Sibaki, Jan Bohacek, Tobias Holzmann, Christian Rodrigues, Hadi Barati, Johann Mogeritsch, Michaela Stefan-Kharicha, Zhao. Zhang, Mohamad Al Nasser, Rui Guan, Mehran Abdi, Otto Klaus-Jürgen, Sabine Strassegger, Claudia Heinzl, for their help in my daily life and academic field.

I would express many thanks to my parents and my sisters for their love, support, and encouragement. Finally, I would like to thank my wife, Jingting Shao, and my son, Jinkai Zhang. Without their support and unfailing understanding, I could not concentrate on this thesis. This work is dedicated to them.

Kurzfassung

Die Wechselwirkung zwischen der Strömung von flüssigen Schmelze und der Mushy Zone während der Erstarrung ist immer noch ein Thema, das noch nicht vollständig verstanden ist, obwohl es eine wichtige Rolle bei der Bildung von Mikrostrukturen und vielen anderen damit verbundenen Gussfehlern wie Makroseigerung, Schrumpfungsporosität, Heißriss usw. spielt. Diese Wechselwirkung kann äußerst kompliziert sein. Die Strömung kann die Dendritenmorphologie (Armabstände) durch Beeinflussung des Vergrößerungsgesetzes modifizieren, die Wachstumskinetik der Dendritenspitzen verändern, die Dicke der Mushy Zone variieren, sowie Makroseigerung, Fragmentation (Verzweigungen, Ablösung und Fragmentierung) verursachen, Phasen transportieren und führt zum Umschmelzen und Kornzerstörung. Die Einflüsse der Mushy Zone auf den Strömung wiederum umfassen: (1) die Veränderung des Strömungsmusters (laminares oder turbulentes Verhalten) und (2) die Verringerung oder Verstärkung der Turbulenz.

In dieser Arbeit wird das volumengemittelte Mehrphasen-Erstarrungsmodell, wie es von Wu und Ludwig entwickelt wurde, verwendet und erweitert, um die Strömungs-Erstarrungs-Wechselwirkung zu untersuchen. Folgende wesentliche Erweiterungen werden vorgenommen. 1) Ein neuartiges volumengemittelte Drei-Phasen-Erstarrungsmodell wird eingeführt, um die Bildung der intermetallischen Phase (β -Al₅FeSi) während der unidirektionalen Erstarrung einer AlSi₇Fe₁-Legierung unter rotierende Magnetfeld (RMF) zu simulieren. Der Blockierungseffekt des β -Al₅FeSi wird durch eine modifizierte anisotrope Permeabilitätsgleichung berücksichtigt. Die Dendritenvergrößerung wird berücksichtigt und ihre Auswirkung auf die endgültige Makroseigerung und das Mikrogefüge wurde untersucht. 2) Ein neues Modell zur Behandlung des Schmelzens und der Kornzerstörung während der Erstarrung globularer äquiaxialen Kristalle wird vorgeschlagen. Sowohl die Keimbildung als auch die Zerstörung von äquiaxialen Kristalle werden berücksichtigt. Dabei dienen nichtschmelzende Partikel als heterogene Keimbildungsstellen für die endogenen Kristalle. Ein umgeschmolzener und aufgelöster endogener Kristalle setzt seinen Keimbildungspartikel frei und wird zu einem Impfmittel und somit zu einer zukünftigen potentiellen Keimbildungsstelle für weitere Erstarrungsvorgänge.

Um die Strömungs-Erstarrungs-Interaktion zu untersuchen, werden sowohl das ursprünglich entwickelte als auch das neu erweiterte Modell auf die unidirektionalen Erstarrungssimulationen von AlSi7- und AlSi7Fe1-Legierungen unter Naturkonvektions- und/oder Zwangskonvektionsbedingungen angewendet. Es ist nicht möglich, alle Aspekte der oben genannten Wechselwirkungen in einer Arbeit zu behandeln. Sie befasst sich lediglich um mehrere Unterthemen: (1) die Rolle der Permeabilität in der erstarrenden Mushy Zone; (2) der geometrische Effekt auf die Makroseigerung und die Gefügebildung; (3) der Effekt der intermetallischen Phasenausscheidung und der Dendritenvergrößerung auf die Makroseigerung; (4) Umschmelz- und Kornzerstörungsphänomene während der Erstarrung. Alle diese Simulationen werden durch Experimente qualitativ oder quantitativ verifiziert.

Die modellgestützte Visualisierung der Strömung-Erstarrungs-Interaktionsphänomene ist für Metallurgen von größter Bedeutung, um ein tiefes Verständnis der Erstarrungsgrundlagen zu erlangen und dadurch die Gussfehler zu kontrollieren und die Produktqualität zu verbessern. Darüber hinaus können die erweiterten numerischen Modelle in verschiedenen Gießtechniken, wie Strangguss, Kokillenguss, unidirektionale Erstarrung, Schweißen und additive Fertigung, eingesetzt werden.

Abstract

The interaction between the melt flow and the developing mushy zone during solidification is still an issue that is not yet completely understood, although it plays an important role in the formation of microstructures and many other associated casting defects like macrosegregation, shrinkage porosity, hot tearing, etc. This interaction can be extremely complicated. The flow can modify the dendrite morphology and arm spacings by affecting the coarsening law, alter the growth kinetics of the dendrite tips, change the thickness of the mushy zone, induce the macrosegregation, cause fragmentation (branches, detachment and fragmentation), transport phases, and lead to remelting and grain-destruction. In turn, the influences of the mushy zone on the melt flow include: (1) modify the flow pattern (laminar or turbulence behaviour), (2) reduce or enhance the turbulence.

In this thesis, the volume-average multiphase solidification model, as developed by Wu and Ludwig, is used and extended to study the flow-solidification interaction. Following major extensions are made. 1) A novel three-phase volume-average-based solidification model is introduced to simulate the formation of the intermetallic phase (β -Al₅FeSi) during the unidirectional solidification of an AlSi₇Fe₁ alloy under rotating magnetic field (RMF). The blocking effect of the β -Al₅FeSi is considered through a modified anisotropic permeability formulation. Dendrite coarsening is coupled and its effect on the final macrosegregation and microstructure was studied. 2) A new model to treat the melting and grain destruction during globular equiaxed grains solidification is proposed. Both nucleation and destruction of equiaxed grains are considered. The inoculants serve as heterogeneous nucleation sites for the equiaxed grains. One re-melted/disappeared equiaxed grain will turn into one inoculant, which is reserved for a future potential nucleation site.

In order to investigate the flow-solidification interactions, both the originally developed and newly-extended models are implemented on the unidirectional solidification simulations of AlSi₇ and AlSi₇Fe₁ alloys under nature convection and/or forced convection conditions. It is not possible to cover all aspects of the aforementioned interactions in one thesis. Only several sub-topics are involved: (1) the role of mush permeability in the solidifying mushy zone; (2) geometrical effect on macrosegregation and microstructure formation; (3) effect of intermetallic phase precipitation and dendrite coarsening on

macrosegregation; (4) remelting and grain destruction phenomena during solidification. All these simulations are verified by experiments qualitatively or quantitatively.

Model-aided visualization of the flow-solidification interaction phenomena is of ultimate importance for metallurgists to get deep understanding of solidification fundamentals, and thus to control the casting defects and improve the product quality. Furthermore, the extended numerical models can be implemented in different casting techniques, such as continuous casting, mould casting, unidirectional solidification, welding, and additive manufacture.

Thesis structure

This thesis consists of two parts. Part I includes the motivation and targets of this work, a literature review, an executive summary of the Ph.D work, and the main conclusions. Part II presents the main results of the thesis in the form of paper collection. Five published journal papers are included.

Contents

Acknowledgements	iii
Kurzfassung.....	v
Abstract	vii
Thesis structure	ix
Nomenclature	xiii
Part I:.....	xvii
1. Introduction	1
1.1 Background.....	1
1.2 Objectives	2
2. Literature review	3
2.1 Flow driven by different mechanisms during solidification	3
2.2 Effect of flow on solidifying mushy zone.....	5
2.2.1 Macrosegregation	6
2.2.2 Mushy zone morphology	11
2.2.3 Dendrite arm spacing.....	14
2.2.4 Columnar to equiaxed transition.....	19
2.3 Permeability laws.....	23
2.3.1 Permeability laws for columnar structure.....	24
2.3.2 Permeability laws for equiaxed structure	28
3. Executive summary	31
3.1 Numerical study of the role of mush permeability in the solidifying mushy zone under forced convection.....	31
3.2 Directional solidification of AlSi7Fe1 alloy under forced flow conditions: effect of intermetallic phase precipitation and dendrite coarsening.....	35
3.3 Geometrical effect on macrosegregation during unidirectional solidification.....	37
3.3.1 Macrosegregation caused by shrinkage-induced feeding flow	39
3.3.2 Macrosegregation caused by shrinkage-induced feeding flow and natural convection	40
3.3.3 Analysis of possible formation of spurious crystals	43

3.4 Modelling melting and grain destruction phenomena during globular equiaxed solidification	45
3.4.1 Cooling from the right side.....	47
3.4.2 Heating from the left side	48
3.4.3 Transport of a bulk crystal network.....	49
4. Main conclusions.....	51
5 References	53
Part II:.....	61

Nomenclature

B	Magnetic induction	T
c_0	Initial concentration of the alloy	-
$c_\ell, c_e, c_c, c_{\ell, Si}, c_{\ell, Fe}$	Species concentration	-
c_{mix}	Mixture concentration	-
$\nabla c_\ell, \nabla c_s$	Concentration gradient	-
$c^{index}, c_{mix, Fe}^{index}, c_{mix, Si}^{index}$	Macrosegregation index	-
d_e	Volume-averaged grain diameter	m
D_ℓ, D_s	Diffusion coefficient	$m^2 s^{-1}$
\bar{e}	Unit vector	-
$f_\ell, f_e, f_c, f_s, f_\beta$	Phase fraction	-
f_s^c	Phase fraction of solid skeleton of columnar	-
f_d^c	Phase fraction of interdendritic melt of columnar	-
\bar{F}_θ	Azimuthal component of the electromagnetic force	N
\bar{g}	Gravitational acceleration	$m s^{-2}$
G	Temperature gradient	$K m^{-1}$
k	Solute partition coefficient	-
k_ℓ, k_s, k_m	Thermal conductivity	$W m^{-1} K^{-1}$
K, K_p, K_N	Permeability and its components	m^2
$K_{p, int}, K_{N, int}$	Permeability components with intermetallics	m^2
m	Liquidus slope	-
$M_{\ell e}$	Mass transfer rate between liquid and equiaxed	$kg \cdot m^{-3} \cdot s^{-1}$
$M_{\ell \beta}$	Mass transfer rate between liquid and intermetallics	$kg \cdot m^{-3} \cdot s^{-1}$
M_{ce}	Mass transfer rate between columnar and equiaxed	$kg \cdot m^{-3} \cdot s^{-1}$
$n_{in, 0}, n_{in}$	Number density of inoculant	m^{-3}

$n_{\text{eq},0}, n_{\text{eq}}$	Number density of equiaxed grains	m^{-3}
\dot{n}	Grain number density changing rate	$\text{m}^{-3} \text{s}^{-1}$
∇p	Pressure gradient	Pa m^{-1}
r	Radial position	m
R	Sample radius	m
S_v	Interfacial area density	m^{-1}
t	Time	s
t_f	Local solidification time	s
T_0	Initial temperature	K
T_{eut}	Eutectic temperature	K
∇T	Temperature gradient	K m^{-1}
$\bar{u}_\ell, \bar{u}_e, \bar{u}_c, \bar{u}_s$	Velocity for different phase	m s^{-1}
$\bar{u}_{\ell,\text{max}}$	Maximum liquid velocity	m s^{-1}
\bar{v}_T	Moving speed of isotherm	m s^{-1}
V	Rate of interface movement	m s^{-1}
β	Solidification shrinkage	-
β_P, β_N	Constants	-
ρ_ℓ, ρ_s	Density	$\text{kg} \cdot \text{m}^{-3}$
$\bar{\rho}$	Volume-averaged density	$\text{kg} \cdot \text{m}^{-3}$
σ	Electrical conductivity	$\Omega^{-1} \text{m}^{-1}$
δ	Mushy zone thickness	m
λ_1, λ_2	Primary and secondary dendrite arm spacings	m
μ	Viscosity	$\text{kg} \cdot \text{m}^{-1} \cdot \text{s}^{-1}$
ω	Angular velocity	Rad/s

Subscripts ℓ , e, c, β , s, and mix indicate liquid, equiaxed, columnar, intermetallic (β -Al5FeSi), solid and mixture phases. Subscript 0 denotes the initial value of variables. Subscript P and N indicate the flow parallel and normal to the primary dendrite direction, respectively.

Auxiliary equations:

$$c^{\text{index}} = \frac{c_{\text{mix}} - c_0}{c_0} \times 100\%$$

$$c_{\text{mix,Fe}}^{\text{index}} = \frac{c_{\text{mix,Fe}} - c_{0,\text{Fe}}}{c_{0,\text{Fe}}} \times 100\%, \quad c_{\text{mix,Fe}} = \frac{(c_{\ell,\text{Fe}} \cdot \rho_{\ell} \cdot f_{\ell} + c_{\text{c,Fe}} \cdot \rho_{\text{c}} \cdot f_{\text{c}} + c_{\beta,\text{Fe}} \cdot \rho_{\beta} \cdot f_{\beta})}{(\rho_{\ell} \cdot f_{\ell} + \rho_{\text{c}} \cdot f_{\text{c}} + \rho_{\beta} \cdot f_{\beta})} \cdot 100\%$$

$$c_{\text{mix,Si}}^{\text{index}} = \frac{c_{\text{mix,Si}} - c_{0,\text{Si}}}{c_{0,\text{Si}}} \times 100\%, \quad c_{\text{mix,Si}} = \frac{(c_{\ell,\text{Si}} \cdot \rho_{\ell} \cdot f_{\ell} + c_{\text{c,Si}} \cdot \rho_{\text{c}} \cdot f_{\text{c}} + c_{\beta,\text{Si}} \cdot \rho_{\beta} \cdot f_{\beta})}{(\rho_{\ell} \cdot f_{\ell} + \rho_{\text{c}} \cdot f_{\text{c}} + \rho_{\beta} \cdot f_{\beta})} \cdot 100\%$$

Part I:

1. Introduction

1.1 Background

The solidification, i.e. the state transformation from liquid to solid, is a phenomenon central to a wide range of manufacturing and processes. The presence of the phase transformation can drive convection in the melt through the liberation of latent heat, the rejection of solute, and the change of material properties [1]. In turn, the solidification can be strongly altered by the induced convection through the modification of the thermal and solutal environment of the solid-liquid interface, which governs the solidification characteristics at the interface.

Understanding to this flow-solidification interaction belongs to a comprehensive research field. Flow can change the dendrite morphology, influence the mush morphology thickness, alter the growth kinetics of dendrite tips, induce macrosegregation, cause fragmentation and detachments, transport the phases (as-formed solid crystals and solute-enriched melt), lead to remelting/grain destruction of as-formed structure, and affect the precipitation and distribution of the intermetallics. In turn, the mushy zone will modify the flow by dampening the flow and even change the flow pattern. Such coupled processes are significant on a large range of scales. Numerous attempts and investigations have already been done, and a lot of studies remain ongoing. However, the understanding of the interaction between the fluid flow and the developed mushy zone is still an open issue. One main challenge on this topic is that all above-mentioned phenomena are coupled and interacted with each other during the solidification.

Generally, solidification in metallic systems is investigated through post-mortem analysis, and thus the flow-solidification interaction can only be analyzed and deduced based on the as-solidified structure and composition distribution. Recently, the synchrotron tomography approach provided a way for visualizing the in-situ observations of the three-dimensional interior structure of real objects non-destructively and with a high spatial resolution. However, the sample size for the synchrotron X-ray tomography solidification experiment is only limited to the thickness of $\sim 100 \mu\text{m}$, and therefore only very local phenomena can be seen. Moreover, these experimental investigations are time-consuming and expensive.

Mathematical models, which are of great advantage for their high flexibility, accuracy, and low cost, have been successfully used to simulate the solidification of the various casting processes. Different numerical models (molecular dynamics (MD) model [2], phase-field model [3], Lattice Boltzmann method [4], dendritic needle network (DNN) model [5], CAFE model [6], volume-average model [7,8], etc.) have been tried to try to involve these phenomena and make the simulation results closer and closer to the reality. The most promising model should be the volume-average model, which could almost cover all above-mentioned phenomena. Although great progress has been made in past decades, a lot of important solidification phenomena, like the precipitation of the intermetallic phase and its blocking effect on the fluid flow, dendrite coarsening, remelting and grain-destruction, fragmentation, can not be quantified yet. Furthermore, how they are interacting with each other is not clear. Modification and extension of the previously published models are needed for further understanding of the flow-solidification interaction.

1.2 Objectives

In this thesis, the unidirectional solidification of a cylindrical Al-based sample under nature convection and/or forced convection conditions was simulated. The forced convection is applied with a rotating magnetic field (RMF).

1. The first objective of this thesis is to extend the previous developed multiphase volume-average solidification model: (1) to consider dynamic precipitation of intermetallic phase and its blocking effect on fluid flow; (2) to include dendrite coarsening phenomenon and study its effect on the macrosegregation and microstructure; (3) to calculate remelting and grain destruction during globular equiaxed solidification.
2. The second target of this thesis is to verify the current multiphase model by comparison of its results with as-published experimental results.
3. The ultimate goal is to use the as-developed and newly extended models to perform simulations under controlled convective conditions, so as to get a deep understanding of the aforementioned flow-solidification interactions.

2. Literature review

2.1 Flow driven by different mechanisms during solidification

During solidification, convection arises because of body forces acting on the fluid. These body forces can be originated naturally or induced by external forces. According to different mechanisms of the driving force, the fluid flow can be termed as different types of convection.

(1) Buoyancy-induced convection (the so-called nature convection) owing to thermal and/or solutal gradients in the liquid. The thermal and solutal buoyancy forces can either aid or oppose each other, depending on the direction of the thermal gradient and whether the rejected solutes cause an increase or a decrease in the density of the liquid [9,10]. Because the essential driving force for buoyancy is gravity acceleration, buoyancy-induced convection is almost unavoidable under terrestrial conditions. Under some special conditions, for example, the solidification in space and the solidification in the free fall cartridge [11,12], where the gravity acceleration is extremely weak, the buoyancy-induced convection can be negligible.

(2) Solidification-shrinkage-induced feeding flow. Thermal contractions between the liquid and solid due to cooling, and solidification shrinkage lead to the feeding flow, which is toward to the solid-liquid interface [13–15]. Normally the shrinkage-induced feeding flow is several orders of magnitude smaller than the thermo-solutal convection. For some castings with cross-section change, the feeding flow will be magnified to be comparable to the thermo-solutal convection at the contracted regions. In this case, it significantly affects the onset of freckles [16,17]. Investigations also show that shrinkage-induced feeding flow causes the ‘inverse segregation’ [18] and is related to the formation of shrinkage porosity [19].

(3) Forced flow. The forced flow is induced by external forces on the melt. The most widely used external force is the electromagnetic field, which can be mainly sorted as rotating magnetic field (RMF) and traveling magnetic field (TMF) [20]. RMF is produced by the three-phase current of the stator in the actual three-phase induction motor. It can be replaced by permanent magnets in a permanent magnet synchronous motor [21]. The RMF

has been widely employed to stir the liquid melt in the continuous casting process [22], the unidirectional solidification process [23], and also the laboratory investigations [11]. A traveling magnetic field (TMF) is created by means of applying out-of-phase currents to a number of coils. When TMF is applied to a conducting melt inside a cylindrical container, it induces a Lorentz force that acts in the meridional directions (radial and axial). This is different from the rotating magnetic field (RMF), which creates a force in the azimuthal direction [24,25]. One can adjust the magnitude of the force by adjusting the strength of the magnetic field not only to counteract the effects of the buoyancy, but also to create conditions similar to varying levels of gravity [24]. Except for the electromagnetic field, external forces can also be induced by blowing bubbles [26], rotating impeller (mechanical stirring) [27], falling material jet [28], rotating casting mold [29,30], and the application of the ultrasonic technique [31–33].

(4) Liquid flow driven by grain motion. The floating and sinking of equiaxed grains and fragments will drag the liquid to flow with them [34].

(5) Marangoni motion (thermo-capillary force-induced convection). The Marangoni effect is the convection of fluid along an interface between dissimilar substances (liquid–liquid immiscible alloys) because of variations in surface tension [35]. Surface tension can vary because of composition and temperature. Due to the temperature gradient during solidification, the thermo-capillary force-induced convection leads to the droplet moving from cold towards hot regions [36].

(6) Deformation of the solid network. Because of thermal stresses, shrinkage stresses, metallostatic pressure, and other external mechanical forces (e.g. soft reduction [37]), the as-solid structure will be deformed. Deformation of the as-solid phase squeezes the liquid to flow. This mechanism is significant during the continuous casting process. Due to the high metallostatic pressure of the liquid melt inside the strand, the thin shell bulges between adjacent guiding rolls. The bulging-induced flow makes an important effect on final segregation profiles [37,38].

During the engineering casting process, the flow in a solidification system may be governed by one or several of the above-mentioned flow mechanisms. Different flow mechanisms interact with each other, which makes the flow extremely complex. A comprehensive understanding of different flow mechanisms is the basis for studying flow-solidification interactions.

2.2 Effect of flow on solidifying mushy zone

The morphological stability of the solid-liquid interface during solidification has been extensively studied [39,40]. Most works have considered the melt to be quiescent so that heat and mass transportation within it occur by diffusive processes only. However, it is well recognized that flow plays a significant role in solidification. Typically, the interface between the fully molten and fully solid state is an extended region in space and just an open, sponge-like network of primary, secondary and tertiary dendrite arms, simply called “mush or mushy zone”. The flow interacts with the mush just like a storm does with a forest, but the former is more complicated. The flow accelerates both the heat and mass transfer near the solidification tip front [41–44], and thereby influence the mushy zone significantly. As schematically shown in **Figure 2.1**, the influences of the flow on the mushy zone include: (1) induce macrosegregation [45]; (2) change the mushy zone thickness [46,47]; (3) affect the grain morphology (λ_1, λ_2)[48,49]; (4) update the microstructure (CET, ECT); (5) modify the growth kinetics of the dendrite tip [50,51]; (6) influence the sedimentation and fragmentation (detachment of sidearms and branches) [52,53]; (7) transport fragments and equiaxed grains into/out of mushy zone [42,54]; (8) accelerate or decelerate the melting of grains and dendrites [55,56]. In turn, the solidifying mushy zone could damp the flow and change the flow pattern. Investigation of the effect of flow on solidifying mushy zone belongs to a comprehensive and complex research field, which includes many ongoing sub-topics. In this part, a literature review is made only on some sub-topics related to this thesis.

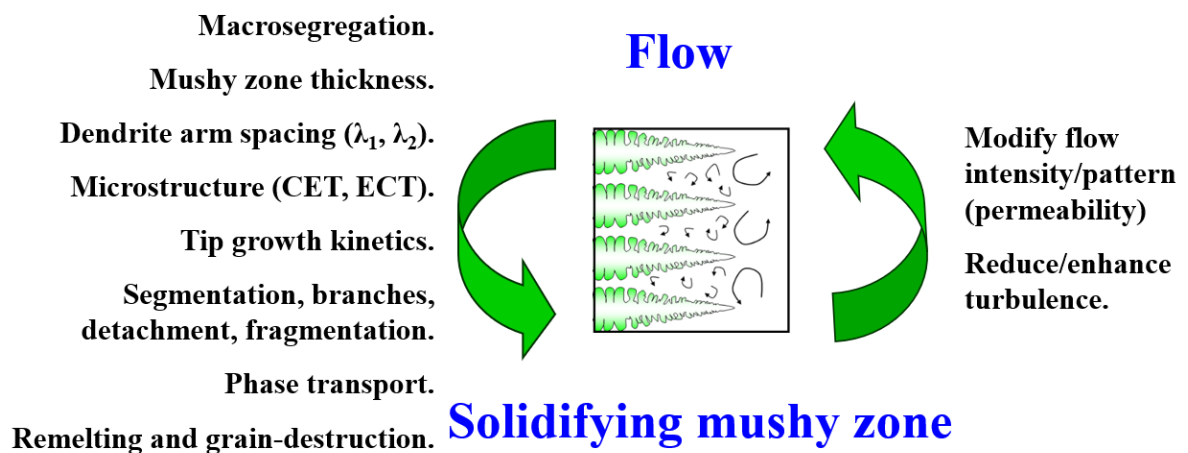


Figure 2.1 Schematic of flow-solidification interactions.

2.2.1 Macrosegregation

During the solidification of alloys, due to the solute partitioning at the solid-liquid interface, the solid usually has a different concentration compared to the parent melt where it crystallizes, and the rejected solute accumulates in the liquid. A solute concentration gradient develops both in the solid and the liquid. The resulting inhomogeneity of the solute is termed as microsegregation, which occurs on the scale of the growing crystal. Different theoretical models have been proposed to handle the microsegregation: (1) the lever rule assuming the infinite diffusion both in liquid and solid; (2) the Gulliver-Scheil rule, a more practical model, assuming no diffusion in solid but infinite diffusion in liquid [40]; (3) the real diffusion model considering the real diffusion in solid and liquid [57,58]. Because of the melt convection, species are transported, which leads to the solute variation on the scale of the whole casting. This macroscopic inhomogeneity of solute elements is termed as macrosegregation. The difference between microsegregation and macrosegregation is that macrosegregation cannot be removed by heat treatment as diffusion in solids is slow even for elevated temperatures and long holding time for homogenization [13,45,59].

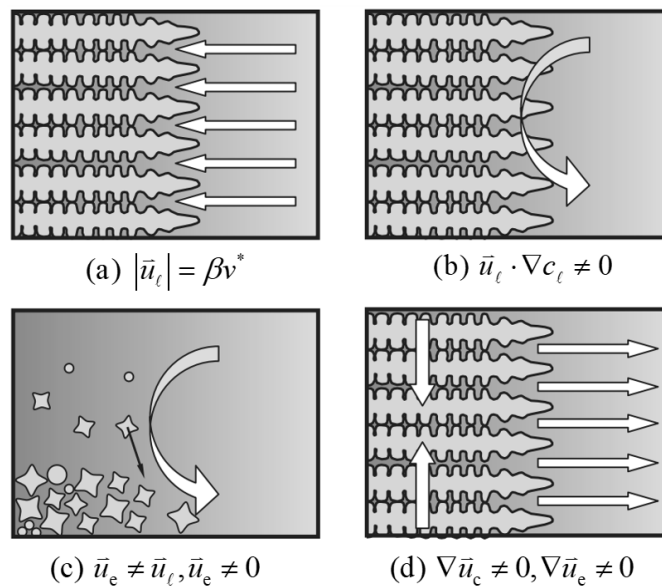


Figure 2.2 Various types of macrosegregation induced by (a) solidification shrinkage, (b) melt convection, (c) grain movement, and (d) deformation of the solid network [39].

In the past decades, numerous investigations on macrosegregation have been reviewed [45,59,60]. Generally, macrosegregation is caused by the relative movement of the liquid

and the solid due to their different solute concentrations. As shown in **Figure 2.2**, four mechanisms were summarized for the origin of macrosegregation. In this thesis, only the alloy with a solute partition coefficient lower than 1 ($k < 1$) was considered and analyzed.

(a) Macrosegregation associated with solidification shrinkage, **Figure 2.2 (a)**. The shrinkage-induced feeding flow, which compensates the volume shrinkage of the casting, is opposite to the solidification direction, leading to what is known as ‘inverse macrosegregation’ [61]. The pioneering work on shrinkage-induced feeding flow was done by Flemings et al. [14,62]. It was assumed that the solid phase is fixed ($\bar{u}_s = 0$), and the densities of the liquid and the solid are constant but not equal ($\rho_s \neq \rho_\ell$). Microsegregation was presumed to occur according to Gulliver-Scheil model ($D_s = 0, D_\ell = \infty$). Based on these assumptions, the classical local solute redistribution equation (LSRE) was proposed, which is shown as **Eq. (2.1)**. With this equation, a typical concentration profile along the 1D benchmark revealed a positive segregation region (i.e. inverse segregation) in the vicinity of the chilling wall, a ‘steady state’ region in the mid-section of the sample, and a negative segregation region in the solidifying mushy zone. The final transient of the sample exhibits a negative macrosegregation. In the engineering ingots with cross-section change, the solidification shrinkage-induced feeding flow will be magnified in the contraction region, which significantly affects the onset of the freckles [17,63].

$$\frac{\partial f_\ell}{\partial t} = \frac{(1-\beta)}{(1-k)} \cdot \left(1 - \frac{\bar{u}_\ell}{\bar{v}_T}\right) \cdot \frac{f_\ell}{c_\ell} = 0 \quad (2.1)$$

(b) Macrosegregation associated with melt convection, **Figure 2.2 (b)**. The solid phase is also fixed ($\bar{u}_s = 0$), and global species transfer by diffusion is ignored ($D_s = D_\ell = 0$). If the solidification shrinkage-induced feeding flow is ignorable, i.e. $\rho_s = \rho_\ell$. **Eq. (2.2)** can be easily derived [60,64]. If the liquid flow is parallel to the concentration isopleths, i.e. $\bar{u}_\ell \cdot \nabla c_\ell = 0$, no macrosegregation occurs. If \bar{u}_ℓ and ∇c_ℓ point in the similar direction ($\bar{u}_\ell \cdot \nabla c_\ell > 0$), the flow depletes the local c_{mix} . Specifically, the melt with a lower c_ℓ entering a region to replace the melt of a higher c_ℓ leads to depletion of c_{mix} . If \bar{u}_ℓ is opposite to ∇c_ℓ ($\bar{u}_\ell \cdot \nabla c_\ell < 0$), the melt with a higher c_ℓ entering a region to replace the melt of a lower c_ℓ leads to an increase in c_{mix} .

In some special cases, e.g. the sample with cross-section change, the solidification shrinkage-induced feeding flow is comparable to the natural convection, and thereby it has

to be considered. For this case ($\rho_s \neq \rho_\ell$), a new equation, **Eq. (2.3)**, was derived to analyze the formation of the macrosegregation. Corresponding to the two right-hand side (RHS) terms in **Eq. (2.3)** [65], the local variation rate of c_{mix} is the outcome of two contributions. The first RHS term is related to the solidification shrinkage, and the second term is due to the melt flow, which can be caused by the solidification shrinkage, thermo-solutal convection, or forced convection.

$$\frac{\partial c_{\text{mix}}}{\partial t} = -f_\ell \bar{u}_\ell \cdot \nabla c_\ell \quad (2.2)$$

$$\frac{\partial c_{\text{mix}}}{\partial t} = (\rho_s - \rho_\ell) \left(\frac{c_\ell - c_{\text{mix}}}{\bar{\rho}} \right) \cdot \frac{\partial f_s}{\partial t} - \frac{\rho_\ell}{\bar{\rho}} f_\ell \bar{u}_\ell \cdot \nabla c_\ell \quad (2.3)$$

(c) Macrosegregation associated with the motion of solid phase, **Figure 2.2 (c)**. For the alloy with $k < 1$, the solid phase has a lower solute concentration than the liquid phase. The movement of the solid phase, i.e. the sedimentation or floatation of equiaxed grains, gives rise to the macrosegregation. For instance, the sedimentation of the equiaxed grains is believed to be responsible for the cone negative macrosegregation of the ingot [66,67]. To analyze the formation of the macrosegregation induced by solid motion, **Eq. (2.4)** was proposed [60]. It was assumed that there was no solidification shrinkage, $D_s = D_\ell = 0$. The volume-averaged concentration gradients in the melt and solid phase are ignored, $\nabla c_\ell = 0$ and $\nabla c_s = 0$. According to **Eq. (2.4)**, if more solid phase leaving than entering the volume element, $\nabla \cdot (f_s \bar{u}_s)$ gets positive, and thus the increase of the mixture concentration c_{mix} .

$$\frac{\partial c_{\text{mix}}}{\partial t} = (c_\ell - c_s) \cdot \nabla \cdot (f_s \bar{u}_s) \quad (2.4)$$

However, for most of the engineering castings, the solute concentration gradient in the melt and the solid can not be ignored i.e. $\nabla c_\ell \neq 0$ and $\nabla c_s \neq 0$. A more general equation, **Eq. (2.5)**, was derived [68]. Similar to the derivation of **Eq. (2.4)**, solidification shrinkage and global species transport by diffusion was ignored. The variation of the local mixture concentration, c_{mix} , is caused by three RHS terms of **Eq. (2.5)**. The first RHS term ' $(c_\ell - c_s) \cdot \nabla (f_s \bar{u}_s)$ ' represents the effect of equiaxed crystal motion, which is totally the same with **Eq. (2.4)**. The second RHS term, which is the same with **Eq. (2.2)**, indicate the effect of the melt convection. The third RHS term, $-f_s \bar{u}_s \cdot \nabla c_s$, can be understood in terms of the effect of ' $-f_\ell \bar{u}_\ell \cdot \nabla c_\ell$ '. If a solid moves in the direction of ∇c_s , c_{mix} decreases. On the

of the ingot (hot-top segregation), arises from buoyancy-driven and shrinkage-driven interdendritic flow during the final stages of solidification [72]. (2) ‘A’ segregates in the middle radius region of the ingot, (also called freckles [17]), appear as long and narrow trails of equiaxed grains. The solute-enriched liquid from the solidifying mushy prefers to take the path of the still open channels, where the flow resistance is low, into the bulk liquid. Accumulation of solute-enriched liquid in these channels lowers the liquidus, thereby slowing down local solidification. This kind of flow-solidification interaction promotes the development of the ‘A’ segregates [66]. The shape of these segregation channels are sensitive to the flow patterns and flow intensity [47]. (3) The ‘V’ segregates along the centerline of the ingot are believed to arise from equiaxed grains settling in the core and forming a loosely connected network that can easily rupture owing to metallostatic head and liquid being drawn down to feed solidification shrinkage and hot tears. Fissures then open up along shear planes oriented in a V-pattern, and are filled with enriched liquid [47,73]. (4) The cone-shape negative segregation results from the sedimentation of equiaxed grains. The replacement of solute-enriched melt by the solute-depleted equiaxed grains leads to negative segregation.

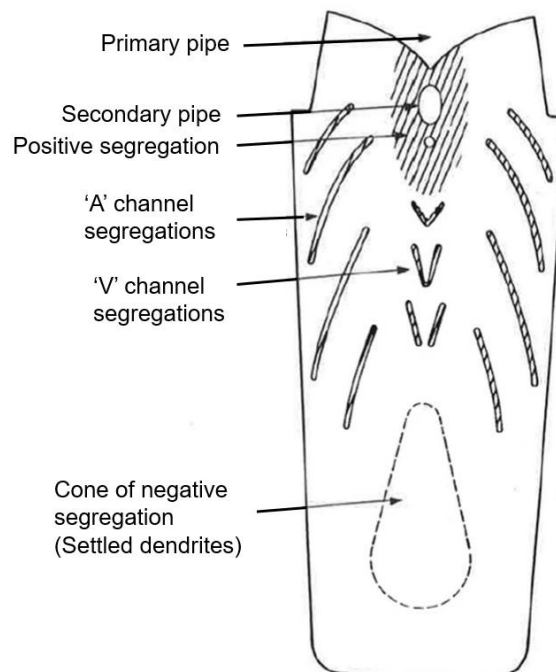


Figure 2.4 Schematic of the macrosegregation pattern in steel ingot [67].

In some directional solidification experiments [17,63,74–76], the center of the sample solidifies earlier than the surface of the sample, and a segregation channel is found near the surface. In this case, except for the effect of the melt convection, the shrinkage of the solid skeleton, which squeezes the solute-enriched liquid from the center to the periphery of the sample, can also promote the formation of surface channels.

2.2.2 Mushy zone morphology

Most industry alloys solidify in a temperature interval. As schematically shown in **Figure 2.5**, the alloy subjects a phase transition from the pure liquid to a completely solid-state through a liquid-solid two-phase co-existing region, which is also called mushy zone, in which microstructure forms and evolves. The liquid flow in the mushy zone transports heat and species to update the local thermodynamic equilibrium. For the alloy with a negative liquidus slope ($m < 0$), the solute accumulation decreases the liquidus, and the solute depletion increases the liquidus. As a consequence, the fluid flow plays a significant role in determining the shape of the mushy zone.

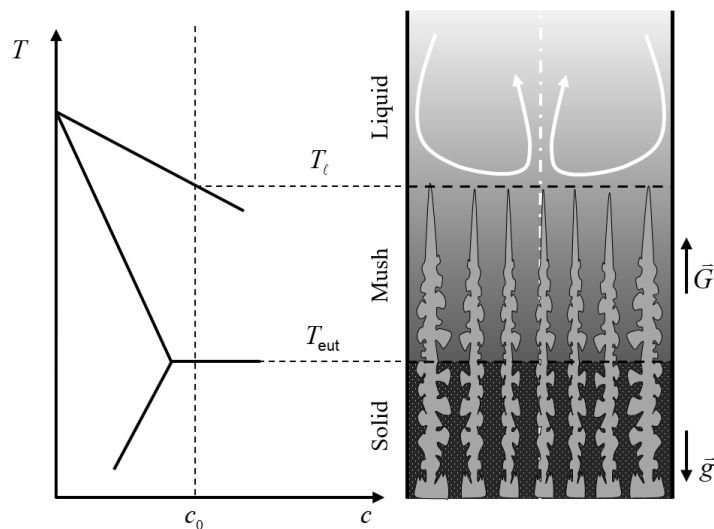


Figure 2.5 Schematic of the two-phase nature of a solidifying mushy zone.

The effect of the flow on the mushy zone morphology under natural or forced flow conditions has been investigated comprehensively [46,47,77–82]. For the solidification of a binary alloy, the flow enhances the heat dispersion in the melt region, and thereby enhance the local temperature gradient in/near the mushy region. Furthermore, the rejected solute-enriched liquid was transported by the flow, which modifies the local solute concentration. The local solidification kinetics, as influenced by the local temperature and solute

concentration, directly determines the morphology of the mushy zone. The effect of the forced convection on the mushy zone morphology was investigated by Zimmermann and Sturz [83]. The AISi7Mg0.3 alloy was unidirectionally solidified in a Bridgman furnace with or without RMF. To obtain information about the structure of the as-grown solid-liquid interface (the top surface of the mushy zone), the directional solidification process was terminated by decanting the samples. The experimental observations of two sample are displayed in **Figure 2.6**. It can be seen that the mushy zone morphology is drastically influenced by convection. In the case without RMF, **Figure 2.6 (a)**, an almost flat top surface of the mushy zone is observed. In the case with RMF, **Figure 2.6 (b)**, a central void region can be seen [84]. The main reason for these differences is the convection induced macrosegregation. The RMF induced meridional flow transports the solute-enriched liquid from the periphery of the sample to the central part. The accumulation of solute at the center lowers the liquidus, and thereby delays the solidification. After decanting the samples, a central hole was observed.

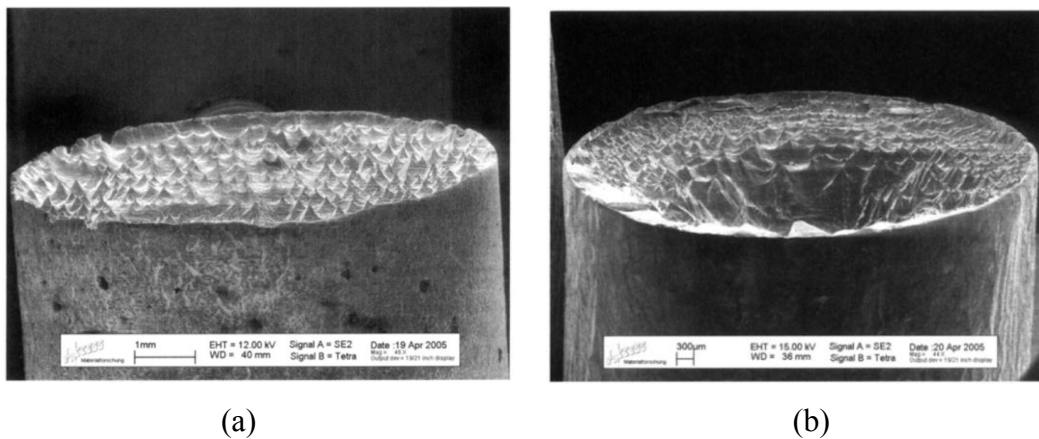


Figure 2.6 SEM-micrograph of mushy zone of AISi7Mg0.3 alloy: (a) without RMF, (b) with RMF [83].

Recently, the synchrotron tomography approach provides a way for visualizing the in situ and real-time observation of the three-dimensional interior structure of real objects non-destructively and with a high spatial resolution [85]. By Combining with the simulation, it is possible to understand the effect of flow on the evolution of the mushy zone. As displayed in **Figure 2.7**, the Al–3.5 wt.% Ni alloy solidified unidirectionally in a Bridgman furnace [81]. A comparison between in situ X-ray radiography and CAFE simulation of the grain structure was made. Under thermo-solutal buoyancy, a so-called steeping convection develops near the solidification front, which sweeps the solute-enriched liquid to the

periphery of the sample. The enrichment of solute lowers the liquidus of the melt near the sample surface, which inhibits the dendrite growth there. As shown in **Figure 2.7 (a)**, a mushy zone with a bulged top surface was observed. Simulations with and without consideration of flow were carried out to study the effect of convection on the morphology of the mushy zone. As demonstrated in **Figure 2.7 (b)** and **(c)**, different from the case with the liquid flow, a flat solidification front can be seen for the case without considering the flow. The bulged solidification front and deformed mushy zone were also observed on other different alloys [86,87].

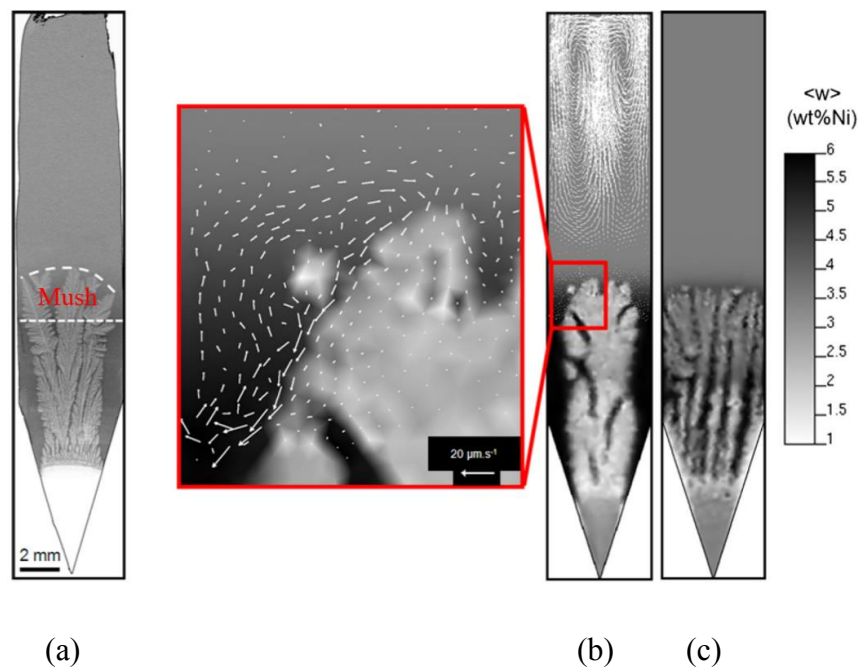


Figure 2.7 (a) Radiograph of the solidification front at $t = 5140$ s. (b) and (c) Corresponding simulation of the average composition distribution with convection and without convection respectively [81].

In another publication [79], the effect of convection on mushy zone morphology was investigated based on the solidification of $\text{NH}_4\text{Cl}-70$ wt.% H_2O solution in a water-cooled mold using a volume-average dendritic solidification model. Two hydrodynamic phases were considered: the primary melt and columnar phase. The ‘dendritic envelop’ model was employed to separately considered the solid skeleton (f_s^c) and enclosed interdendritic melt (f_d^c) of a columnar dendrite. Simulations with (Case Ia) and without (Case Ib) convection were performed. As shown in **Figure 2.8 (a)**, the mushy zone of Case Ia (with flow) is significant thinner but denser than that of Case Ib (without flow). In Case Ib, contours of

f_s^c are more uniformly distributed, while in Case Ia, f_s^c contours are irregular. The evolution of $\oint f_s^c dV$ is shown in **Figure 2.8 (b)**. The results revealed that the flow tended to hinder the growth of the columnar primary dendrite tips and reduce the mushy zone thickness, but the flow speeds up the solidification inside the mushy zone and leads to the formation of more massive columnar dendrite trunks.

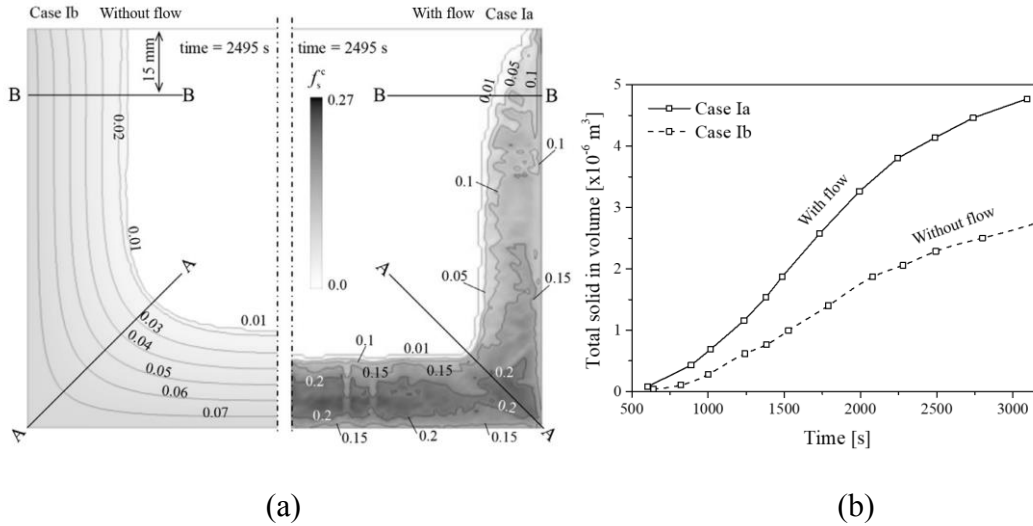


Figure 2.8 Effect of the flow on the mushy zone. (a) Solid contours (f_s^c) on the symmetry plane in grey scale and isolines ($t = 2495$ s): Case Ia (right half, with flow) vs. Case Ib (left half, without flow). (b) Evolution of total solid in the entire mould volume ($\oint f_s^c dV$) [79].

The above-mentioned mushy zone is typical for the rigid solid structure, i.e. the columnar dendrites and/or packed equiaxed grains. It should be distinguished with the definition of the mushy zone in the literature [88], where the mushy zone involves the rigid solid structure as well as the movable equiaxed grains. It is known that the melt convection and solid transport reduce the temperature of the bulk liquid, so that nucleation can occur far away from the solid-liquid interface [89]. If the movable equiaxed grains are regarded as part of the mushy zone, the flow may expand the mushy zone.

2.2.3 Dendrite arm spacing

Generally, the dendrite morphology is characterized by the primary dendrite arm spacing (λ_1) and the secondary dendrite arm spacing (λ_2). Three parameters control the dendrite arm spacings, namely the initial solute concentration, temperature gradient at the

solid-liquid interface, and the solidification rate [40]. For the case where the solidification rate is constant, fluid flow in the mushy zone alters the local thermal and solutal profiles and hence it influences the dendrite morphology.

The effect of natural and forced melt convection on dendritic solidification in Ga–In alloys was investigated by Shevchenko et al. [48,90]. The directional solidification of Ga–25wt%In alloys within a Hele-Shaw cell was visualized by means of X-ray radiography. Melt flow-induced various effects on the grain morphology primarily caused by the convective transport of solute. The snapshots of the dendrites during the solidification without and with forced convection are shown in **Figure 2.9 (a)** and **(b)**, respectively. The forced flow eliminated the solutal plumes and damped the local fluctuations of solute concentration. It provoked a preferential growth of the secondary arms at the upstream side of the primary dendrite arms, whereas the high solute concentration at the downstream side of the dendrites can inhibit the formation of secondary branches completely. Moreover, under the condition of forced convection, the dendrites are thinner and more inclined than the case under natural convection. Another interesting effect is the angle between the primary trunks and the secondary arms. In the case of natural convection, the secondary arms are almost perpendicular to the primary trunk. The secondary arms developing under forced convection are slightly tilted towards the flow direction represented by an angle of about 80° .

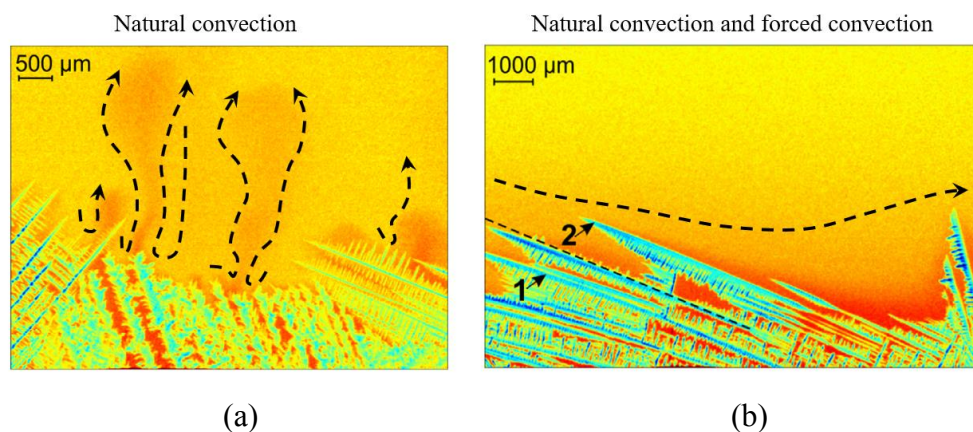


Figure 2.9 Snapshots of the dendrite (a) with and (b) without forced convection. The contour denotes the solute concentration, and the dash lines indicate the flow direction [48].

Fundamentals of the selection of λ_1 and λ_2 during solidification are well understood in the absence of convection [40,91]. Under diffusive conditions, λ_1 is estimated as a function

of the local temperature gradient and solidification velocity. As shown in **Eq. 2.6**, G is the temperature gradient, and V is the growth speed, and A is a coefficient depending on material properties. Different formulations were proposed to evaluate the value of A [92–96]. However, the effect of convection on λ_1 was not included in all those models. Based on the published experimental observations [97,98] and phase-field simulations [80,99,100], the convection influences λ_1 considerably.

$$\lambda_1 = AG^{-0.5}V^{-0.25} \quad (2.6)$$

A series of unidirectional solidification experiments of A357 alloy was conducted by Steinbach and Ratke with and without RMF [101–103]. λ_1 was measured based on the as-solidified microstructure. The measured values were fitted to a dimensionalized model of Hunt and Lu [104]. As shown in **Figure 2.10**, the results indicate a significant decrease of λ_1 under convection. It was explained that the convection altered the solute concentration in the interdendritic region, and thereby modify the local constitutional undercooling. If the maximum of undercooling is located between two dendrites but not at the tips of the dendrites, the developed ternary sidearms can be developed into a new primary dendrite [105]. From **Figure 2.10**, it seems that λ_1 can be increased continuously by increasing the convection in a certain range.

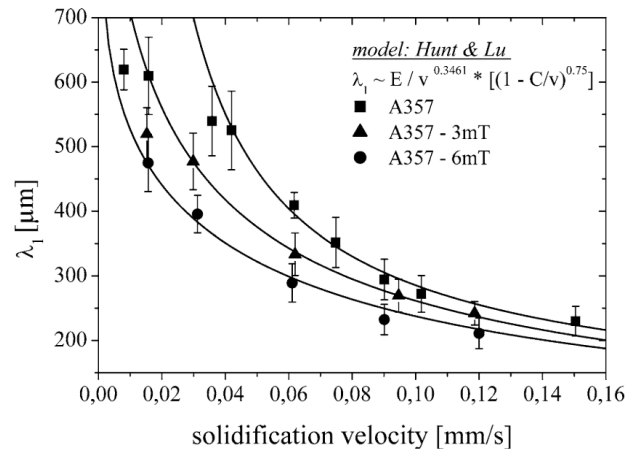


Figure 2.10 λ_1 varying with solidification velocity of A357 samples solidified without and with RMF (3 and 6 mT at 50 Hz) [102].

After the development of the primary dendrites, the occurrence of the random sinusoidal disturbances makes the solid-liquid boundary surface unstable. The resulting perturbations will be grown into cells, and they will further develop into the secondary dendrites [40]. In the subsequent solidification, coarsening (also known as Ostwald ripening)

plays an important role in the shape of secondary dendrites (also the further ternary dendrites), which may lead to remelting (retraction), pinch-off, and coalescence of the side arms [106]. It is well known that coarsening occurs near thermodynamic equilibrium through a reduction in the surface free energy, during which the higher-order dendrite arms adjust their spacing in a solidifying mush. Under pure diffusive conditions (or when the flow is negligible), the coarsening law is described by **Eq. 2.7** [107–109], in which B is the geometric magnification factor, and M is the alloy-dependent magnification factor.

$$\lambda_2 = B(M \cdot t_f)^{1/3} \quad (2.7)$$

To verify the classical coarsening law, considerable investigations including 4D in-situ observations or numerical simulations have been done [53,106,110,111]. Because most of these works were done under diffusive conditions or with ignorable convection, the effect of convection on secondary dendrites and how the convection adjusts the coarsening law was not studied.

Study on the effect of convection on dendrite coarsening can be traced to 1990s. A coarsening theory, as developed by Ratke and Thieringer [112], pronounced the significant role of convection on coarsening. They announced that the relative motion between the liquid and the solid particles accelerated the coarsening process. This theory was supported by a later phase-field modelling study performed by Diepers et al. [113]. According to their modelling results, the coarsening exponent changes from the classical value of 1/3 for diffusion-controlled coarsening to 1/2 under convection conditions. After that, Steinbach [105] worked up a theoretical model to express λ_2 under forced convection conditions. As shown in **Eq. 2.8**, in which K_{conv} is a coefficient depending on the material properties.

$$\lambda_2 = K_{conv} \cdot t_f^{1/2} \quad (2.8)$$

Please note that under forced convection conditions, the coarsening exponent changes from 1/3 to 1/2. Steinbach's model was verified by her following experiments [103,114–116]. As shown in **Figure. 2.11**, directional solidification experiments were performed with Al-Si and Al-Si-Fe alloys, using a microgravity environment for diffusive solidification and adding an RMF to generate flow. All measured data exhibited that λ_2 increased with solidification time. The classical coarsening law (**Eq. 2.7**) was verified by the solidification of AlSi7 alloy under diffusive conditions. When the RMF was applied, the coarsening exponent increased from 1/3 to 1/2, which verified the modified coarsening law, **Eq. 2.8**.

Interestingly, the same experiments were repeated with another alloy (AlSi7Fe1) in which intermetallic precipitates (β -Al₅FeSi) formed during solidification. The results showed that the applied RMF seemed to have no influence on the coarsening/ripening law, i.e., the coarsening exponent was maintained at 1/3. A tentative explanation for the undisturbed $\lambda_2 - t_f$ relationship in the solidification of AlSi7Fe1 under RMF is that the formation of β -Al₅FeSi suppresses the interdendritic flow, so that the conditions of solidification and the corresponding coarsening/ripening phenomenon approaches the pure diffusive case. Although it has been confirmed that the convection will modify the coarsening and thus the modification of λ_2 , further proof supported by in-site observations and small-scale numerical modelling is urged to reveal the underlying mechanism.

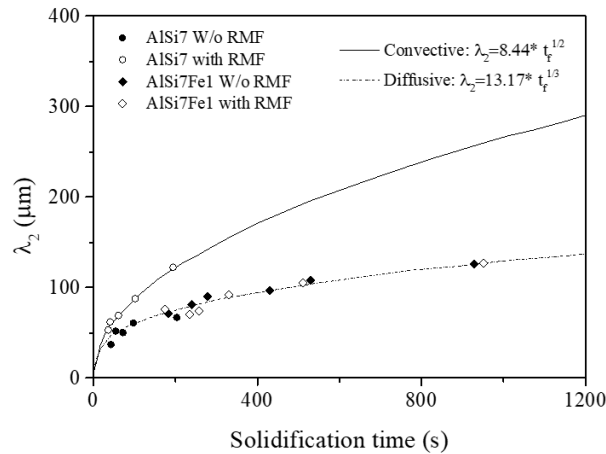


Figure 2.11 The evolution of λ_2 with time in microgravity environment. The black circles and squares are the experimentally measured λ_2 of the as-solidified state with/without RMF. The black lines are the fitting curves. [103].

Except for the effect on the dendrite morphology and dendrite orientation, convection also influences the dendrite morphology by affecting the side branching, dendrite remelting and fragmentation. These would not be introduced in this thesis. The convection occurring in the mushy zone can also influence the uniformity of the dendrites across the cross-section of the casting. It was reported that the convection may lead to ‘dendrite clustering’ and the formation of dendrite-free regions [74,86]. During the unidirectional solidification of turbine blades, this convection induced uniformity of the dendrites gives risk to the onset of freckles.

2.2.4 Columnar to equiaxed transition

There are two types of grains in as-solidified casting: columnar dendrites (which are preferentially oriented perpendicular to the heat flux) and equiaxed grains (which are growing in all space directions). The phase transition from one to another, i.e. from the columnar to equiaxed transition (CET) and from equiaxed to columnar (ECT), has been of high technological relevance both from the metallurgical point of view and for the understanding of scientific fundamentals related to physical phenomena [37,117,118], e.g. the formation of spurious/stray grains and the development of macrosegregation. The relative amount of columnar phase and equiaxed phase, as determined by the position of CET, also directly affect the mechanical properties of the alloy. A theoretical understanding and accurate prediction of CET become particularly important.

There is a consensus that the CET occurs when the moving front of columnar dendrites is blocked by equiaxed grains growing in the undercooled liquid ahead of this front [118–120]. There is still controversy, however, about the details of how the equiaxed grains stop the columnar front. The early theoretical studies relate the CET phenomenon to the thermal field (G and V) [121,122] and the nucleation parameters (e.g. with or without grain refiner) [123,124]. The first mechanism to predict the CET was proposed by Hunt [121], which is known as the ‘hard blocking’ or ‘mechanical blocking’. The CET was assumed to occur when the volume fraction of equiaxed grains at the columnar front reached 0.49. This mechanism was later modified by Martorano et al. [125] to consider the impingement of the solute concentration field. A new mechanism for CET, ‘soft blocking’ or ‘solute blocking’, was proposed. It suggests that the growth driving force (constitutional undercooling) is exhausted because of the enrichment with the solute element rejected by the growing equiaxed grains, which stops the growth of columnar primary dendrite tips [125]. However, the CET is still an open topic today, since the classical CET theories are derived under purely diffusive conditions. They are not sufficient to predict structure transitions (CET and ECT) in the engineering castings, where the flow is intensive and solid transfer is occurring. For example, it was found that during continuous casting, RMF promoted the formation of equiaxed crystals, thereby affecting the position of CET [126].

Laboratory experiments were conducted to study the effect of forced convection on CET [23,127–129]. As shown in **Figure 2.12**, the AlSi7Fe1 alloy was unidirectionally in the Bridgman furnace under controlled convection conditions. Based on the observation of

the as-solidified structure: without RMF, the sample was solidified as pure columnar dendrites; with the increase of the magnetic induction, some equiaxed crystals were observed in the center of the sample; when the magnetic induction is further elevated, a total columnar to equiaxed transition was seen [23,102,128,129]. The influence of RMF on microstructure can be attributed to: (1) promote the formation of equiaxed grains; (2) transport the nucleated equiaxed grains. The effect of RMF on grain transport is understandable and seems to be clear, but there is controversy on how RMF promotes the formation of equiaxed grains. Fan and Liu [130] believes the forced flow uniform the temperature and concentration fields, all the nuclei could survive in the melt, and heterogeneous nucleation occurs continuously throughout the entire volume of the solidifying melt. Zimmermann et al. [127] suggest that intensifying the fluid flow leads to a higher fragmentation rate. Those broken dendrite arms transported by the melt flow serve as the nuclei of new grains or directly grow into equiaxed grains. Their study also shows that the flow-induced grain-refinement effect only occurs when the flow intensity exceeds a certain minimum value, likely associated with the transition from a laminar to a turbulent flow structure at the solidification front. According to the work done by Griffiths and McCartney [131], fragmentation of dendrites is the most probable mechanism for the promotion of CET with high velocity flows, while with low velocity flows, CET was probably significantly influenced by heterogeneous nucleation effects. To distinguish the origin of the equiaxed grains either from fragmentation or heterogeneous nucleation, and to quantify their separate contributions are still open issues up to date.

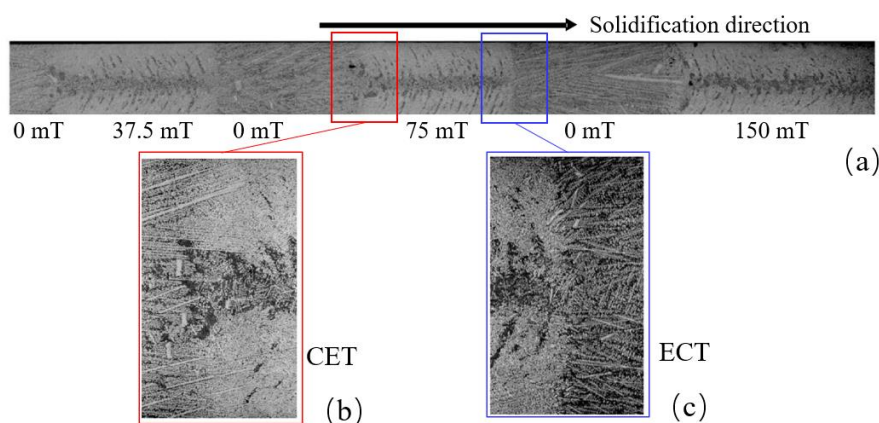


Figure 2.12 Solid structure of AlSi7Fe1 alloy under different magnetic inductions. (a) The whole sample, (b) and (c) zoom-in views of the microstructure to show CET and ECT, respectively [128].

Alternatively, numerical modelling is an efficient and powerful approach to investigate the effect of flow on CET. The popular CET models can be classified as stochastic or deterministic [118,125]. Stochastic models, which aim to follow the nucleation and growth of each individual grain, are usually implemented in cellular-automaton (CA) models [81,132]. Deterministic models, which rely on averaged quantities and equations that are solved on a macroscopic scale, are mostly employed in volume-average models [7,133,134]. The main difference between the stochastic model and the deterministic model lies in the treatment of the nucleation event. As shown in **Figure 2.13**, for the stochastic approach, no assumptions are made regarding the grain morphology, and thus the shape evolution of each grain is computed as a function of the local thermal and/or solute environment. The CET may then be determined based on the geometry (aspect ratio) of the generated grains. Deterministic models, on the other hand, by tracking the movement of the columnar front and calculating the growth of equiaxed grains in the undercooled liquid in front of it, the CET can still be predicted without directly resolving the nucleation and growth of each grain.

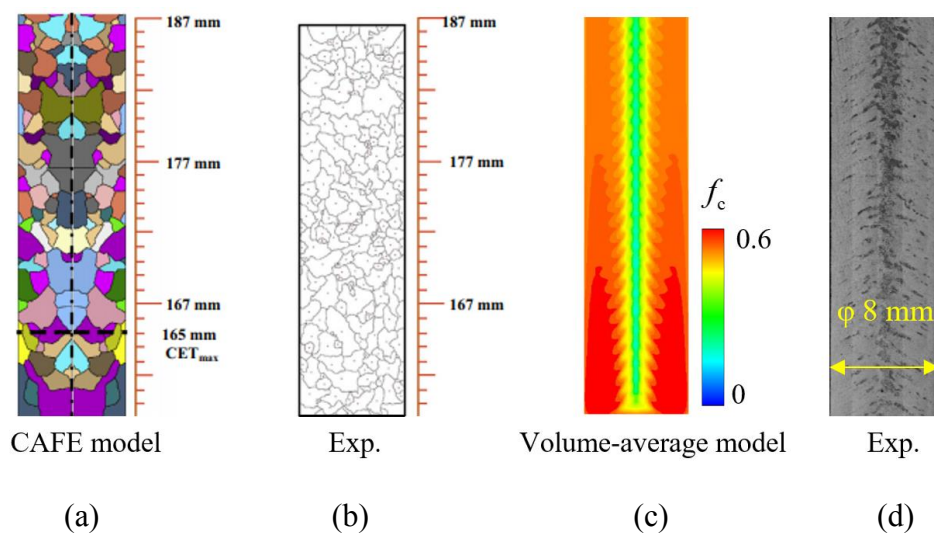


Figure 2.13 Comparison of grain structures calculated using different numerical models. (a) Grain structure calculated with CAFE model, and (b) the corresponding experimental measurement [135]. (c) Distribution of the columnar phase calculated with volume-average model, and (d) the corresponding experiment observation.

The volume-average model, which takes the deterministic model, has been successfully applied to calculate the solidification of different engineering castings. The solidification of a 10.5 tons ingot was simulated by Wu et al. [72]. The development of the columnar

dendrites, melt convection, and grain transport were calculated. In this way, the interaction between the melt flow and grain transport, and grain-sedimentation-induced macrosegregation can be investigated. As shown in **Figure 2.14**, the liquid melt and equiaxed crystals flow with different velocities. More solute-depleted equiaxed grains sediment to the bottom of the ingot, leading to the formation of the CET and the so-called cone of negative macrosegregation.

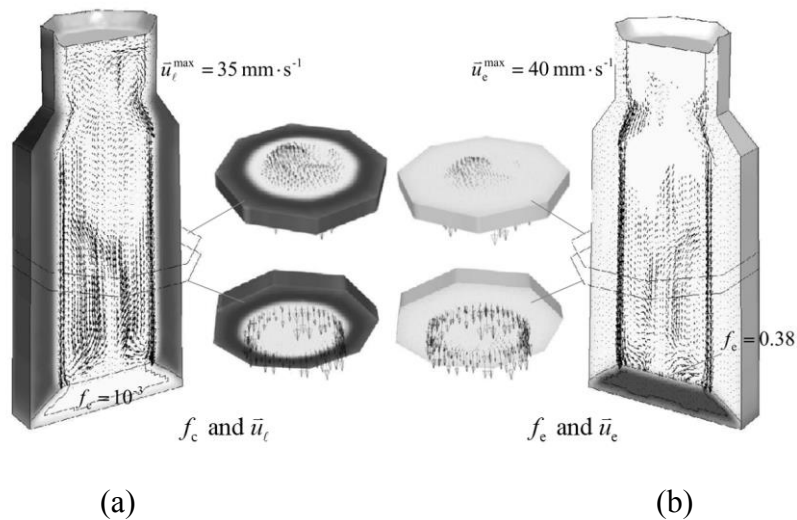


Figure 2.14 Solidification sequence at 1880 s. Both f_c and f_e are shown in grey scale. The velocity of the melt (\bar{u}_l) is shown together with f_c in (a), while the velocity of the equiaxed crystals (\bar{u}_e) is shown with f_e in (b) [72].

Compared with CET, ECT pays relatively little attention in engineering. ECT will be triggered when the origin of equiaxed grains is cut off (i.e. the completely consumption of existing grain refinement particles) [136,137], the updating of the cooling condition [138], or the change of the flow intensity [128,139]), the remaining melt in the casting can only solidify as columnar structure, which leads to ECT [140,141]. In continuous casting, a typical ECT between chill zone and columnar zone can be seen near the billet surface.

As reviewed by Kurz et al. [91,142], the effect of flow on the microstructure is far beyond on CET, for instance, the influence of flow on dendrite tip growth kinetics, the influence of flow on formation rate of equiaxed grains by nucleation and/or fragmentation, the influence of flow on the morphology of the grains, the influence of flow on remelting, interaction between the flow and solid transport, *etc.* Further in-situ experiments and numerical models are needed to have a deep understanding on this topic.

2.3 Permeability laws

Typically, as shown in **Figure 2.15 (a)**, the mushy zone is an open, sponge-like network of primary, secondary and tertiary dendrite arms. As demonstrated in **Figure 2.15 (b)**, the flow could pass the mushy zone only between the dendrites. When the liquid flows through the dendrites, it will be dampened, and its pattern will be modified. Because of the directional nature of the columnar dendrites, the resistance on the liquid to flow parallel and normal to the primary dendrites are different. Depending on the flow in the relevant with the microstructure, the fluid flow in the mushy zone can be classified as three patterns: (1) flow through the isotropic equiaxed grains; (2) flow through the columnar dendrites with flow normal to the primary dendritic arms; (3) flow through the columnar dendrites with flow parallel to the primary dendritic arms [143].

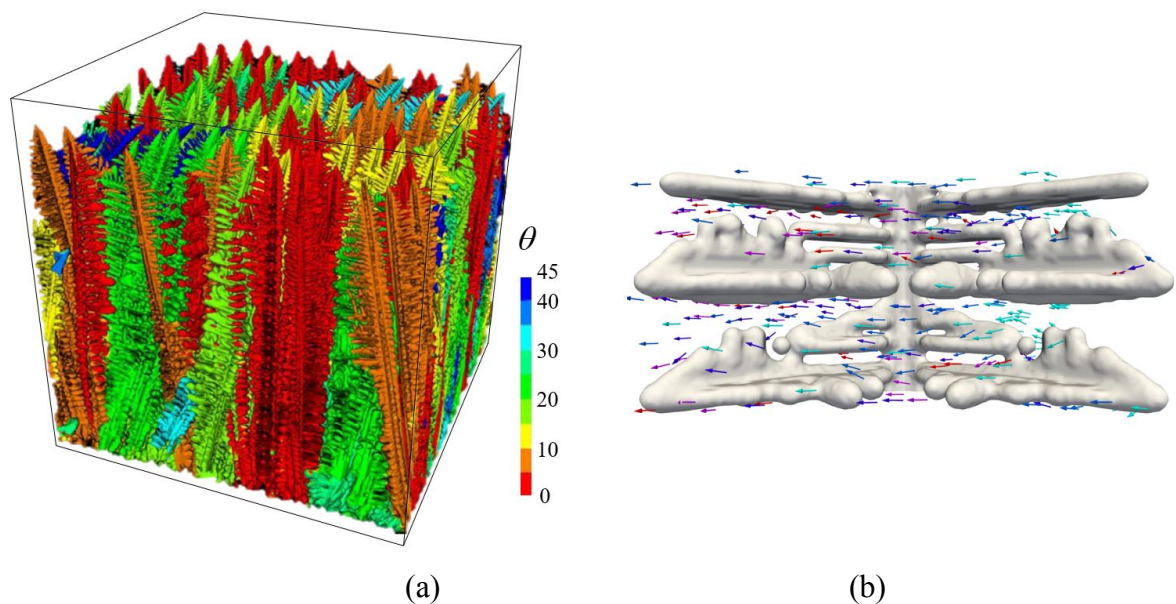


Figure 2.15 (a) Dendrite morphology calculated by a phase-field approach [144]. (b) Flow through a dendritic structure [145].

When modeled at macroscopic length scales, e.g. the currently used volume-average approach, the complex dendritic network of a solidifying mushy zone is usually approximated as a continuum based on the theory of porous media, through which the Darcy's equation is solved. Darcy's equation is written as **Eq. (2.9)** [146].

$$\bar{u}_\ell f_\ell = -(K / \mu)(\nabla P - \rho \bar{g}) \quad (2.9)$$

Knowledge of the permeability, which is usually as a function of the local liquid volume fraction and the characterized length of the dendrites (e.g. λ_1 and/or λ_2 , or S_v), is thus essential to successfully calculate the interdendritic flow during solidification. In this section, a literature review was made on permeability laws for different microstructures.

2.3.1 Permeability laws for columnar structure

In early studies, the Carman-Kozeny equation, as shown in **Eq. 2.10**, is widely used to approximate the permeability of the mushy zone [20,147,148]. However, for columnar dendritic structures, the permeability is anisotropic due to the directional nature of the dendrite arms, and thus the Carman–Kozeny equation is not appropriate.

$$K = \frac{f_\ell^3}{CS_v^2(1-f_\ell)^2} \quad (2.10)$$

The anisotropic permeability of alloys with columnar structure has been measured by Streat and Weinberg [149], Murakami et al. [150,151], Nasser-Rafi et al. [152], and Poirier [153]. A pressure gradient was applied to a partially solidified sample while measuring the discharge velocity of a working fluid. The permeability of specimens was then calculated from the experimental data on the basis of Darcy's law. The measured permeability from different alloys was integrated by Poirier [153], and two permeability formulas for flow normal (K_N) and parallel to (K_p) the primary dendrites were proposed by the regression method. As shown in **Eqs. 2.11** and **2.12**, K_p only depended upon λ_1 , while K_N depended upon both λ_1 and λ_2 . In a different work proposed by Santos and Melo [154], a tortuosity factor was considered to estimate the anisotropic permeability. However, they are only valued for low-liquid-fraction alloy, $f_\ell < 0.7$.

$$K_p = 4.53 \times 10^{-4} + 4.02 \times 10^{-6} \times (f_\ell + 0.1)^{-5} \frac{\lambda_1^2 f_\ell^3}{(1-f_\ell)} \quad (0.17 \leq f_\ell \leq 0.61) \quad (2.11)$$

$$K_N = 1.73 \times 10^{-3} (\lambda_1 / \lambda_2)^{1.09} \lambda_2^2 f_\ell^3 (1-f_\ell)^{-0.749} \quad (0.19 \leq f_\ell \leq 0.66) \quad (2.12)$$

In recent years, numerical models have been developed to assess permeability [143,155,156]. The dendrite size and morphology of the designed microstructure are quite

flexible. Numerical models solve the Stokes equations for a domain representing the interdendritic liquid, and thus the derivation of the permeability. By merging the calculated results at high liquid volume fractions with the available experimental data at lower liquid volume fractions, permeability formulas, which cover the whole range of the liquid volume fraction, can be obtained. As shown in **Eqs. 2.13** and **2.14** [157], different formulas were given for $f_\ell < 0.7$ and $f_\ell \geq 0.7$. The permeability-jump (by nearly a factor of 100) at $f_\ell = 0.7$ reveals a strong correlation between the dendritic geometry and the resulting permeability. When the interdendritic liquid is surrounded by solid phase during the solidification, some isolated liquid pockets are formed, and the liquid could no longer flow through these zones. This is the possible reason for the permeability jump. The permeability-jump is not desired for modeling the interdendritic flow because it will cause serious convergence problems. Heinrich and Poirier [158] proposed permeability formulas using a simple interpolation in the medium region to eliminate the sudden jump of the permeability, as shown in **Eqs. 2.15** and **2.16**. For the columnar dendrites, λ_2 also has significant effect on permeability, especially on K_N . However, the effect of λ_2 on K_N was not included in Heinrich's model.

$$K_p = \begin{cases} \left[4.53 \times 10^{-4} + 4.02 \times 10^{-6} (f_\ell + 0.1)^{-5} \right] \frac{\lambda_1^2 f_\ell^3}{(1-f_\ell)} & (f_\ell < 0.7) \\ 0.07425 \lambda_1^2 \left[-\ln(1-f_\ell) - 1.487 + 2(1-f_\ell) - 0.5(1-f_\ell)^2 \right] & (f_\ell \geq 0.7) \end{cases} \quad (2.13)$$

$$K_N = \begin{cases} \left[1.73 \times 10^{-3} \left(\frac{\lambda_1}{\lambda_2} \right)^{1.09} \right] \frac{\lambda_2^2 f_\ell^3}{(1-f_\ell)^{0.749}} & (f_\ell < 0.7) \\ 0.03979 \lambda_1^2 \left[\begin{array}{l} -\ln(1-f_\ell) - 1.476 + 2(1-f_\ell) - 1.774(1-f_\ell)^2 \\ + 4.076(1-f_\ell)^3 \end{array} \right] & (f_\ell \geq 0.7) \end{cases} \quad (2.14)$$

$$K_p = \begin{cases} 3.75 \times 10^{-4} f_\ell^2 \lambda_1^2 & (f_\ell \leq 0.65) \\ 2.05 \times 10^{-7} \left(\frac{f_\ell}{1-f_\ell} \right)^{10.739} \lambda_1^2 & (0.65 < f_\ell \leq 0.75) \\ 0.074 \left[\log(1-f_\ell)^{-1} - 1.49 + 2(1-f_\ell) - 0.5(1-f_\ell)^2 \right] \lambda_1^2 & (0.75 < f_\ell \leq 1.0) \end{cases} \quad (2.15)$$

$$K_N = \begin{cases} 1.09 \times 10^{-3} f_\ell^{3.32} \lambda_1^2 & (f_\ell \leq 0.65) \\ 4.04 \times 10^{-6} \left(\frac{f_\ell}{1-f_\ell} \right)^{6.7336} \lambda_1^2 & (0.65 < f_\ell \leq 0.75) \\ \left[-6.49 \times 10^{-2} + 5.43 \times 10^{-2} \left(\frac{f_\ell}{1-f_\ell} \right)^{0.25} \right] \lambda_1^2 & (0.75 < f_\ell \leq 1.0) \end{cases} \quad (2.16)$$

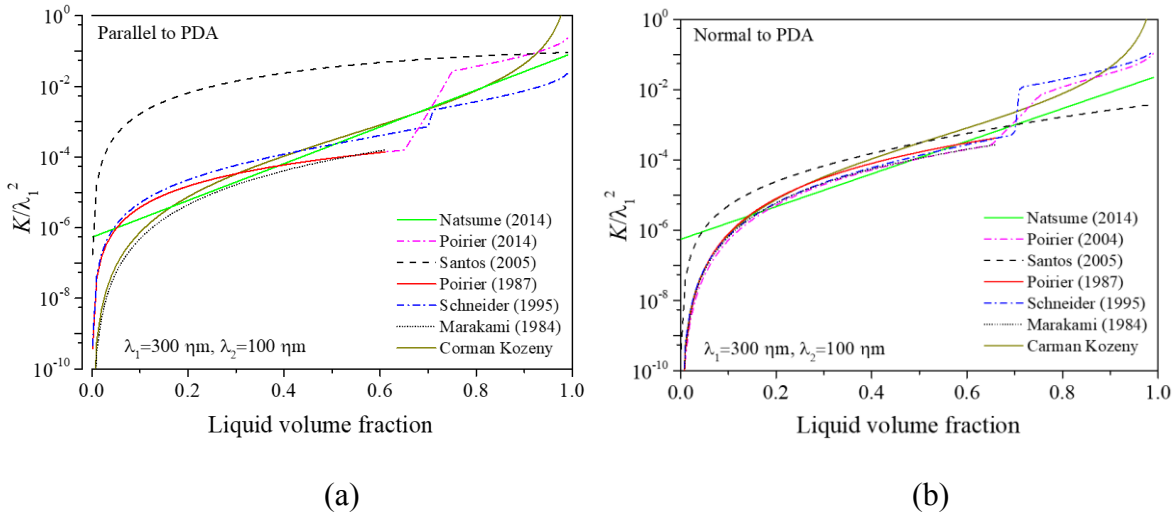


Figure 2.16 Variation of permeability with liquid fraction for flow (a) parallel and (b) normal to the primary dendrite arms with $\lambda_1 = 300 \mu\text{m}$ and $\lambda_2 = 100 \mu\text{m}$.

A comparison of the different permeability laws was made by taking the same character lengths, $\lambda_1 = 300 \mu\text{m}$ and $\lambda_2 = 100 \mu\text{m}$. As shown in **Figure 2.16**, the permeability calculated by different formulas differs by several orders of magnitude. Ludwig et al. [146] performed a series of simulations using Lattice Boltzmann technique to study the effect of the input microstructure on the calculated permeability. They found that different predefined artificial microstructures gave good data for low solid volume fraction. However, for microstructures which was mainly governed by the presence of any type of side arms, permeability data varied even for similar solid volume fractions. From **Figure 2.16**, it can also be seen that K_p is always larger than K_N , which indicates the higher resistance for the flow normal to the primary dendrites. The main difference between isotropic permeability and anisotropic permeability is shown as the liquid fraction approaches unit. According to the previous numerical investigations [47,79,159], small differences in the permeabilities

can have a significant effect on the prediction of flow structures and macrosegregation. The selection of the permeability during the numerical simulation should be very careful considered.

In some technical alloys, the existence of alloy or impurity elements leads to the formation of intermetallic precipitates [155,160–162]. For instance, Iron is a common impurity element in Al-based alloys. The morphology of intermetallic phases is very complex depending on cooling rate and alloy composition. It can be curved, bent, branched, hole-shaped, and with imprints [160,163]. One typical intermetallic precipitate is β -Al₅FeSi. It has a needle-shaped feature in 2D observation, and a plate-shaped feature in 3D observation. The influence of β -Al₅FeSi on permeability in the interdendritic mushy region was analyzed by Puncreobutr et al. [155] for an aluminum-based alloy. A 4D in situ synchrotron X-ray tomography technique was used to reconstruct the microstructure, which was further used to perform CFD calculations to estimate the permeability. Simulations with and without β -Al₅FeSi were performed. The permeability values extracted from the CFD calculations for flow parallel and normal to primary dendrites are shown in **Figure 2.17**. The permeability is significantly lower for the case with intermetallics as compared to without, although the trends are similar. The results qualitatively and quantitatively demonstrate the blocking effect of intermetallics on fluid flow and the ensuing loss in permeability, particularly in the direction parallel to the primary dendrites. Based on the numerical simulation results, the original permeability formulas (**Eqs. 2.11** and **2.12**) were modified by considering the blocking effect of the intermetallics. As shown in **Eqs. 2.17** and **2.18**, an additional term was added to quantify the blocking effect of β -Al₅FeSi with $\beta_p = 15$ and $\beta_N = 10$, respectively. The modified permeability significantly affects the calculated interdendritic flow [155,164], and thus the prediction of the casting defects like the formation of porosity [165–167] and the development of the macrosegregation [115,168]. It is necessary to consider the blocking effect of intermetallics through modified permeability to improve the accuracy of the simulation.

$$K_{P,int} = (1 - \beta_p f_\beta) K_P \quad (2.17)$$

$$K_{N,int} = (1 - \beta_N f_\beta) K_N \quad (2.18)$$

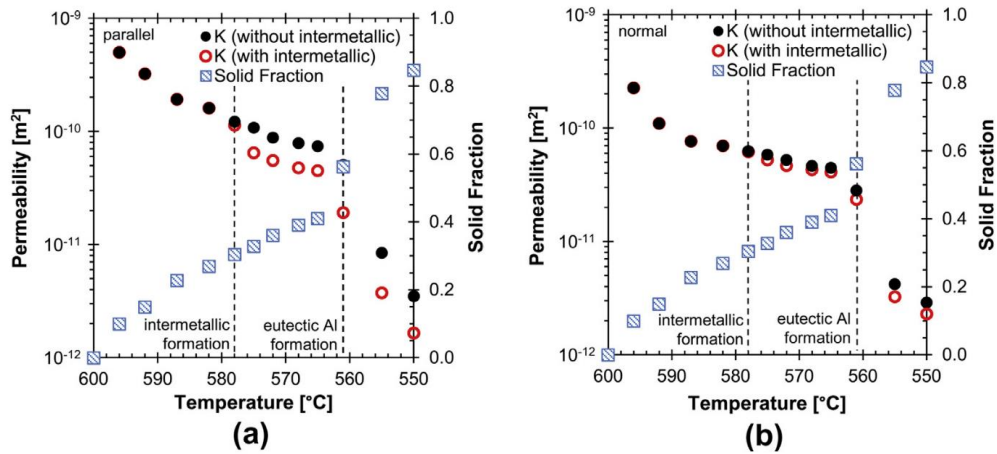


Figure 2.17 The evolution in permeability for liquid flow (a) parallel and (b) normal to the primary columnar dendrites both without and with intermetallics (β -Al₅FeSi) [155].

2.3.2 Permeability laws for equiaxed structure

Relative motion between equiaxed grains and liquid melt is one of the most critical transport phenomena associated with macrosegregation and microstructure development in the solidification of metal alloys. Due to the interfacial drag force between the equiaxed grains and liquid melt, the liquid flow can be obviously influenced by grain motion. Two regimes can be distinguished in the casting domain according to the status of the solid grains: (1) the free particle regime, where the equiaxed grains can move and interact with the melt; (2) the packed regime in the high solid fraction region, where the grains are stationary and the melt penetrates through the voids [34]. Showering of multiple equiaxed dendrites under an environment with gravity is simulated by Sakane et al. [169] using the phase-field lattice Boltzmann model. Growth of multiple dendrites with solid motion (translation and rotation), liquid flow, collision and coalescence of multiple grains, and subsequent grain growth were simulated. As shown in **Figure 2.18**, nuclei generated at the top of the sample, grew into the equiaxed dendrites while settling in the undercooled melt, and these dendrites deposited on the bottom of the computational domain. A liquid flow was driven in the free particle regime by the grain motion. The flow intensity was significantly damped in the packed regime.

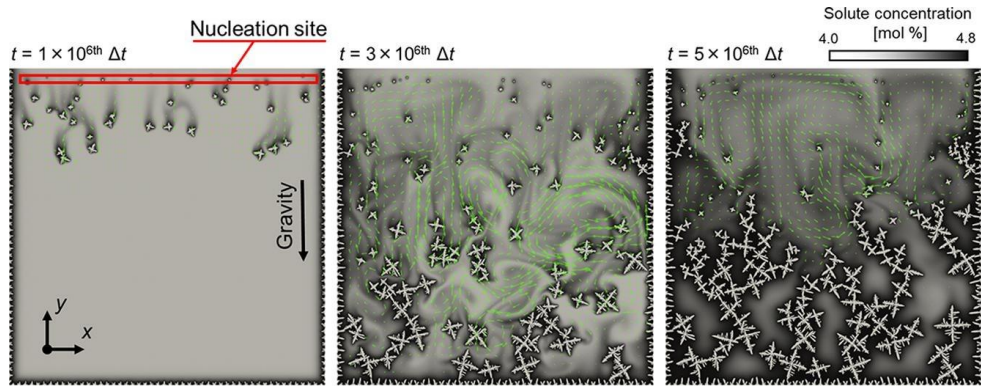


Figure 2.18 Time evolutions of distributions of solute concentration and flow velocity (green vectors) during showering of multiple equiaxed dendrites nucleated on the top of the domain [169].

Similar to the flow through the columnar dendrites, permeability for equiaxed structure is indispensable when modeled at macroscopic length scales. For the equiaxed structure, the isotropic Carman–Kozeny equation [148] (**Eq. 2.11**) is widely adopted to approximate the permeability in the semisolid region. It assumes that there is a uniform distribution of liquid in the solid, and all liquid channels have the same cross-section. Wang et al. [34] proposed a physical model for the solid/liquid interfacial drag in both globular and dendritic equiaxed solidification. The permeability correlation reflects the effects of numerous structural parameters, including the internal porosity of dendritic grains, the interdendritic arm spacings, the sphericity of the dendrite envelope or of globular grains, and the equiaxed grain density.

In order to verify the proposed permeability formulas, numerous measurements for flow passing the equiaxed structure have been carried out. Murakami et al. [170] measured the permeability of organic borneol-paraffin alloy with granular structure at various liquid fractions. The permeability estimated based on Carman-Kozeny equation was in fairly good agreement with the measured one. Poirier and Ganesan [171] measured permeability of Al–15.6 wt.% Cu with equiaxial structure using the eutectic Al–Cu as fluid to analyze the influence of the coarsening of the dendrites. They found that permeabilities for globular structures (non-dendritic) are approximately one order of magnitude greater than permeabilities for dendritic structures at the same volume fraction of solid. Permeability measurements for high solid fractions on a series of Al-Cu alloys with equiaxed microstructure were performed by Nielsen et al. [172]. Their measurements constitute experimental validation of Wang’s model. Since microstructure changes continuously

during a permeameter test (due to solidification or dendrite coarsening), and tests can only be performed if there is a rigid solid structure, the accuracy of experimentation is sometimes questionable. Furthermore, those liquid pockets, that are surrounded by solid, cannot be distinguished and quantified by experiments.

In recent years, with the development of simulation technology and the additive manufacture technique, the permeability can be obtained through numerical modeling and physical modeling. The 4D *in situ* synchrotron X-ray tomography technique can be used to reconstruct the microstructure, which can be used as the input of the numerical simulation or the model for the 3D printing [155,173–175]. **Figure 2.19 (a)** and **(b)** present an example of the surface-based (triangulated interface) microstructure along with the corresponding scaled replica. The permeability values were determined numerically by solving the full incompressible Navier–Stokes equation. In the meantime, the permeability can also be measured physically by passing a working fluid through the physical model and measuring the resulting discharge flow rate and pressure drop. The permeability can then be calculated according to the Darcy’s law. As shown in **Figure 2.19 (c)**, the permeabilities, as calculated by numerical method and physical approach, were compared with various reported results and Carman-Kozeny model. With the flexibility of numerical and/or physical modelling, precious measurements of permeability can be achieved in the future. The effect of dendrite coarsening on the permeability can thus be investigated quantitatively [106,111].

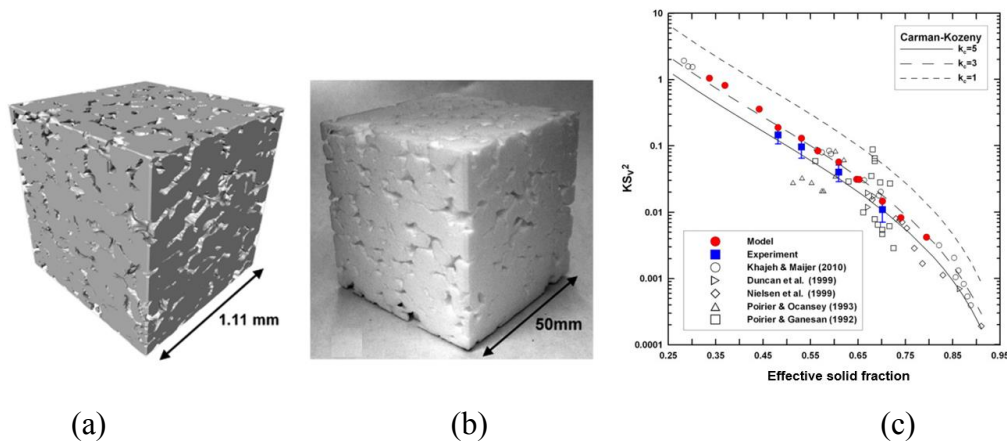


Figure 2.19 Permeability evolution during equiaxed dendritic solidification of Al–4.5 wt.% Cu alloy. (a) Surface-based (triangulated interface) representation of the microstructure of a sample cast with a mould diameter of 29 mm and quenched at 898 K. (b) selective laser sintering replica of (a). (c) Comparison of dimensionless permeabilities with reported results and Carman-Kozeny model [173].

3. Executive summary

3.1 Numerical study of the role of mush permeability in the solidifying mushy zone under forced convection

The choice of approximate permeability law plays an important role in the modelling of meso-segregation and macrosegregation [79,159]. However, the influence of mush permeability on the mushy zone itself (e.g. mushy zone thickness), especially under forced convection conditions, is not yet sufficiently understood. This study presents a two-phase volume-average based solidification model, developed by Wu et al. [8,176], to simulate the unidirectional solidification of the binary AlSi7 alloy under the conditions of RMF and nature convection.

For the purpose of a numerical parameter study, five simulation cases are defined in **Table 3.1**. We take the permeability as reported by Ramirez as a reference case (K), three further cases are considered, for which the permeability is increased/decreased arbitrarily by a factor, i.e. $10 K$, $0.1 K$ and $0.01 K$.

Table 3.1 Cases definition for parameter study by varying permeability.

Cases	Expression	Relationship	Referred to	Parameters
A	-	$0.01 K$	-	
B	-	$0.1 K$	-	
C	$K = \frac{\lambda_1^2 f_\ell^3}{1667(1-f_\ell)^2}$	K	Ramirez [147]	$\lambda_1 = 300 \mu m$ and $\lambda_2 = 50 \mu m$, which are taken from experiments [101].
D	$K = \frac{\lambda_2^2 f_\ell^3}{4\pi^2 K_c (1-f_\ell)^2}$	$4K$	Noepfel [20]	
E	-	$10K$	-	

The configuration of the sample is shown in **Figure 3.1 (a)**. The alloy (AlSi7) solidifies in an Al_2O_3 crucible directionally [177]. On the top and bottom of the sample, a decreasing temperature is imposed T_{Top} and T_{Bottom} , as demonstrated in **Figure 3.1 (b)**. The lateral wall of the sample is considered to be adiabatic. The mushy zone thickness (δ) is calculated as the distance from the solidification front to the point of eutectic temperature isotherm. An RMF inductor ($B=20$ mT, $f=50$ Hz) is installed outside the sample, which is

controlled by a switch (on/off). An analytical approximation of the azimuthal component of the electromagnetic force (\vec{F}_θ) is valid (**Eq. 3.1**) [20,21].

$$\vec{F}_\theta = \frac{1}{2} \sigma \omega B^2 r \left(1 - \frac{u_\theta}{\omega R} \right) \vec{e} \quad (3.1)$$

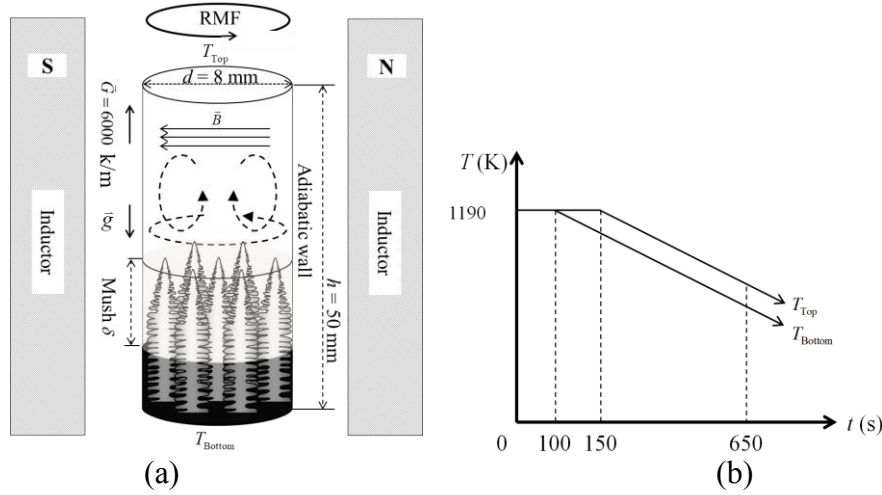


Figure 3.1 Geometric and boundary conditions of the experimental setup. (a) Schematic for the flow pattern and formation of different phases and (b) cooling conditions at the top and bottom of the sample.

Figure 3.2 (a)-(b) shows the melt flow pattern in the bulk liquid. Under RMF (20 mT, 50 Hz), an intensive azimuthal flow up to the velocity magnitude of 0.15 m/s is generated in the region at the center of the radius. As demonstrated by the streamline in **Figure 3.2 (a)**, the fluid rotates downwards at the periphery of the sample, then it rotates and flows upwards in the sample's center. The Ekman effect [178] leads to a meridional circulation with the velocity of 0.04 m/s. The meridional velocity is characterized by a random occurrence of Taylor-Görtler (T-G) vortices along the lateral wall of the sample [178]. Some T-G vortices move up and down to the top/bottom surface, and then disappear; while some of the vortices aggregate with the neighboring ones to form a large vortex. As shown in **Figure 3.2 (c)-(d)**, the flow pattern in the mushy zone is similar to that in the bulk liquid, but the flow is suppressed by the dendrites to a magnitude of $10^{-3} \sim 10^{-6}$ m/s. A tube-like channel, filled with solute-enriched liquid, forms in the sample center. It penetrates the entire mushy zone. The central tube-like channel acts as a pump, sucking solute-enriched melt out of the mush and transporting it back into the bulk region of the sample.

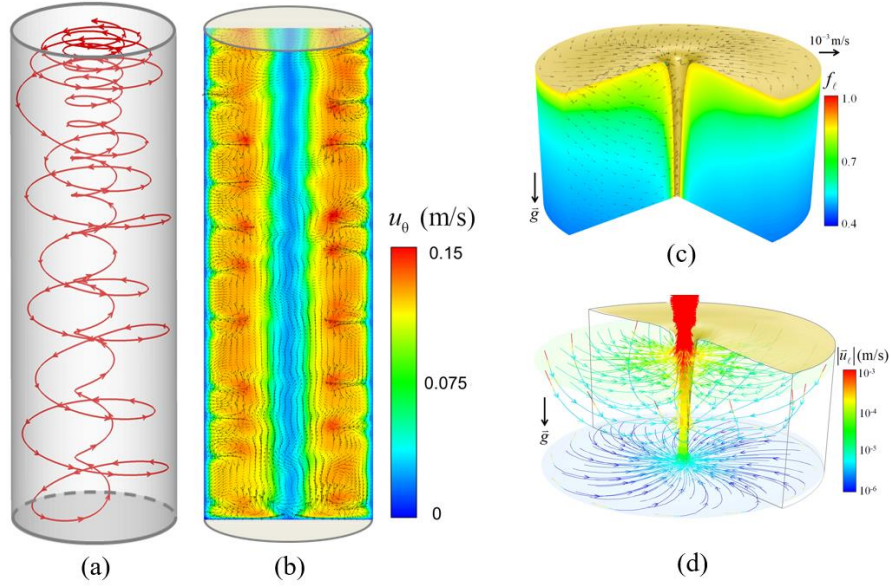


Figure 3.2 Flow pattern in the bulk liquid and in the mushy zone. (a) One streamline to show the mass transfer; (b) contour of the azimuthal velocity (color scaled) in the central section, overlaid with the vectors of the meridional velocity; (c) contour of the liquid phase fraction (color scaled) in the mushy zone in two vertical sections and one iso-surface of the liquid phase fraction ($f_\ell = 0.85$) at the top and center of the mush, overlaid with the vectors of the liquid velocity; (d) streamlines of the flow in the mushy zone colored by liquid velocity magnitude ($|\bar{u}_\ell|$).

The calculation results of the solidification (620 s) by varying permeability (listed in **Table 3.1**) are shown in **Figure 3.3**. In all cases, a central segregation channel with a diameter of 1 mm, strongly enriched with Si forms, where c_{mix} is close to the eutectic concentration. At the periphery of the sample, c_{mix} decreases with the permeability. The intensity of macrosegregation increases with the permeability. Except for the cases (a) and (e), all simulations present a “Christmas tree” segregation pattern.

Near the solidification front, the liquid velocity is close to that in the bulk liquid. In the deep mushy zone, the liquid velocity is decelerated by the resistance of the columnar dendrites. As indicated by the pink dash lines, as soon as side-arms of the segregation channel forms, the flow takes the path of the least resistance through the side-arms of the channel, hence the flow directions are strongly influenced by the forming side-arms. It is difficult to determine the maximum or average liquid velocity in the mushy zone, but it is

still evident that the meridional liquid velocity increases with the rate of permeability. Clearly, the mushy zone thickness δ decreases with the permeability. As a conclusion, the thickness of the mushy zone decreased and the global macrosegregation intensity increased with the mush permeability.

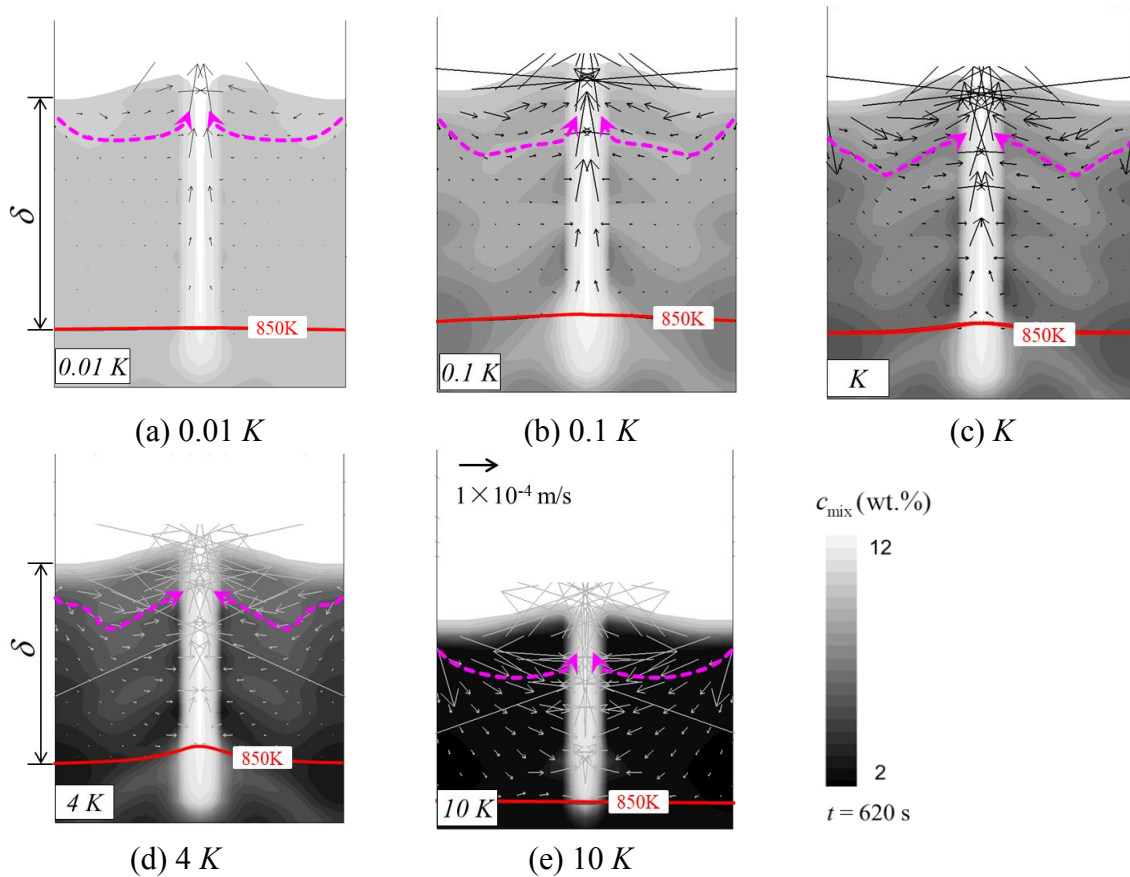


Figure 3.3 Parameter study by varying permeability. Cases (a)-(e), corresponding to those in **Table 3.1**, show the solidification in the mushy zone at 620 s. The grayscale shows c_{mix} that is lighter for higher concentrations. Vector shows the meridional component of liquid velocity. The red solid lines are isotherms of the eutectic temperature, pink dash lines indicate the flow direction, and the top profile is the solidification front.

3.2 Directional solidification of AlSi7Fe1 alloy under forced flow conditions: effect of intermetallic phase precipitation and dendrite coarsening

The main goal of this study is to quantify the effect of the intermetallic phase and dendrite coarsening on the solidification of AlSi7Fe alloy under RMF, and hence to explain the experimental results of Steinbach et al. [103], i.e. the experimental observation of coarsening law exponent is equal to 1/3 in the presence of RMF when sufficient β -Al₅FeSi are present.

In this study, a previously developed multiphase solidification model [8,179] is modified to simulate the solidification of an AlSi7Fe1 alloy. The three phases are the melt, the primary solid phase of columnar dendrites, and the second solid phase of intermetallic precipitates. The dynamic precipitation of the intermetallic phase is modelled, and its blocking effect on the flow is considered by a modified permeability [155,157]. Dendrite coarsening, which influences the permeability, is also considered [106]. The configuration of the simulation domain can be seen in **Figure 3.1**. An AlSi7Fe1 alloy is solidified unidirectionally under controlled temperature gradient ($G=3000$ K/m) and cooling rate ($R=0.12$ K/s) [168]. RMF is applied with $f=50$ Hz and $B=6$ mT [168].

The simulation results at $t=600$ s are shown in **Figure 3.4**. Since the interdendritic liquid prefers to take the path with a higher liquid volume fraction, streamlines near the sidearms of the central channel are twisted/distorted, **Figure 3.4 (a)**. This kind of flow transports solute-enriched liquid from the periphery of the sample to the central part, forming the central segregation channel, as shown by $c_{\text{mix, Fe}}^{\text{index}}$ and $c_{\text{mix, Si}}^{\text{index}}$ in **Figure 3.4 (b)** and **(c)**. In contrast to Si, Fe is less segregated along the centreline of the sample. As shown in **Figure 3.4 (d)**, $c_{\ell, \text{Fe}}$ starts with an increase near the solidification front due to solute rejection during the formation of the primary aluminium dendrites, until it reaches a maximum value ($c_{\ell, \text{Fe}} = 1.29\%$). Since the formation of β -Al₅FeSi by the binary eutectic reaction consumes a large amount of Fe, $c_{\ell, \text{Fe}}$ gradually decreases until the ternary eutectic reaction occurs. $c_{\ell, \text{Si}}$ is displayed in **Figure 3.4 (e)**. Although the formation of β -Al₅FeSi also consumes a considerable amount of Si, due to the massive rejection of Si during the

solidification of α -Al, $c_{\ell, \text{Si}}$ increases consistently until the ternary eutectic point. $M_{\ell\beta}$ and $M_{\ell c}$ are presented in **Figure 3.4 (f), (g)**. In the upper part of the mushy zone (A in **Figure 3.4 (f) and (g)**), only α -Al develops. As the solidification path reaches the binary eutectic valley, β -Al₅FeSi starts to precipitate. In the periphery region (B in **Figure 3.4 (f)**), $M_{\ell\beta}$ is small ($\sim 0.15 \text{ Kg/m}^3/\text{s}$). Near the central channel (C in **Figure 3.4 (f)**), where $c_{\ell, \text{Fe}}$ is large and the liquid volume fraction is high, $M_{\ell\beta}$ is quite large ($\sim 0.4 \text{ Kg/m}^3/\text{s}$). In contrast to $M_{\ell\beta}$, the value of $M_{\ell c}$ reaches a maximum near the solidification front at a value of $38.6 \text{ Kg/m}^3/\text{s}$, and then sharply drops to a value of $5.0 \text{ Kg/m}^3/\text{s}$. As shown in **Figure 3.4 (f)**, most of β -Al₅FeSi forms near the sidearms of the central channel.

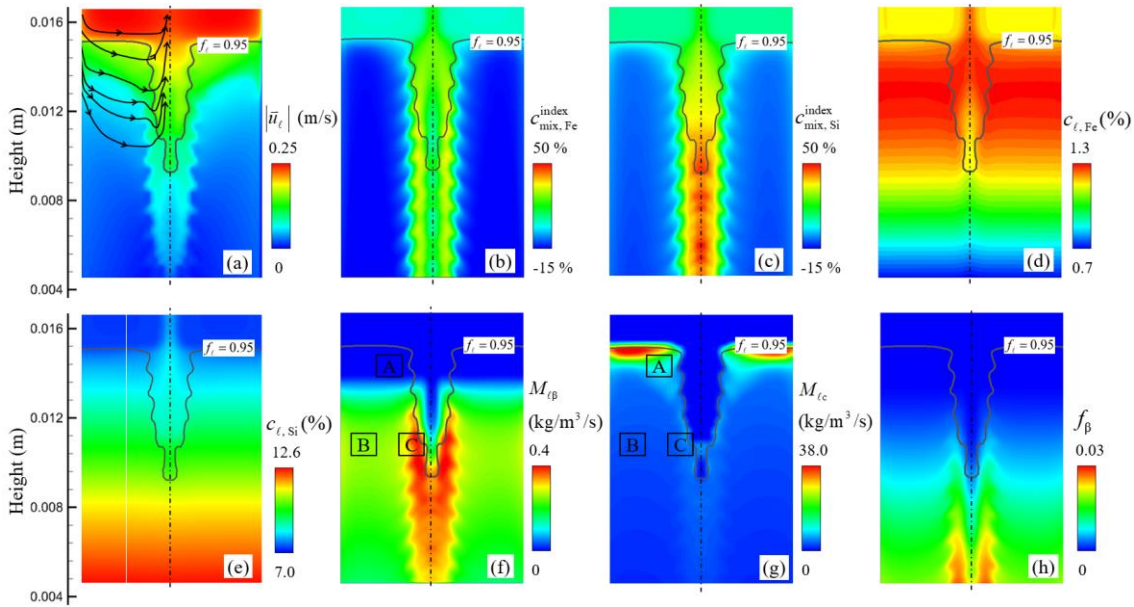


Figure 3.4 Analysis of the solidification sequence and the formation of β -Al₅FeSi at $t = 600 \text{ s}$. The black solid isopleth denotes the solidification front ($f_{\ell} = 0.95$), and the bottom of these figures coincides with the position of the ternary eutectic isotherm (850 K). (a) $|\bar{u}_{\ell}|$ overlaid by streamlines of the meridional flow; (b) $c_{\text{mix, Fe}}^{\text{index}}$ and (c) $c_{\text{mix, Si}}^{\text{index}}$; (d) $c_{\ell, \text{Fe}}$ and (e) $c_{\ell, \text{Si}}$; (f) $M_{\ell\beta}$ and (g) $M_{\ell c}$; (h) f_{β} .

The simulation results were validated by the experimental data measured by Mikolajczak and Ratke [163,168]. As displayed in **Figure 3.5**, very good agreement between the experimental and the calculated results is obtained. The macrosegregation profiles of Si and Fe across the RMF-stirred sample section are very different. Si is mostly

concentrated at the sample centre, while Fe shows two segregation peaks at approximately 1 mm from the centre. The formed β -Al₅FeSi is captured by the columnar dendrites where Fe is ‘frozen’. Migration of β -Al₅FeSi in the mushy zone is likely negligible.

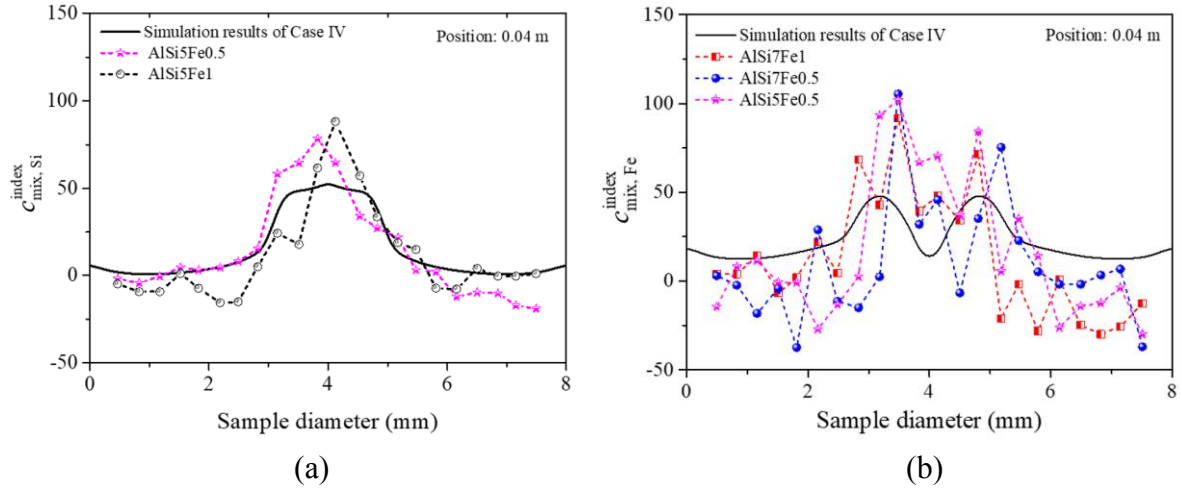


Figure 3.5 Experiment–simulation comparison (the experimental data is referred to [168]). Radial distribution of the segregation indexes of (a) $c_{mix, Si}^{index}$ and (b) $c_{mix, Fe}^{index}$.

Based on the current simulation results, the formed β -Al₅FeSi significantly blocks the interdendritic flow under the influence of an RMF. Hence, dendrites appear to follow the coarsening law ($\lambda_2 \propto t_f^{1/3}$) of solidification under pure diffusive conditions. This conclusion supports the work of Steinbach et al. [103,115]. When the dendrite coarsening law of Neumann-Heyme et al. [106] is incorporated in the model to consider the dynamic evolution of λ_2 and its effect on the interdendritic flow, the current model can improve the simulation accuracy by 8%, demonstrated by the results for $c_{mix, Si}^{index}$.

3.3 Geometrical effect on macrosegregation during unidirectional solidification

The casting geometry is an important factor influencing the melt flow pattern during solidification, and an inappropriate geometry design may intensify macrosegregation or cause the formation of other defects. Turbine blades, which are key components in aircraft engines, are produced as single crystals by a unidirectional solidification technique. However, several geometrical features of the turbine blade casting, e.g. abrupt change in the casting section, can lead to the onset of freckles or formation of spurious/stray crystals,

which severely deteriorate the creep-rupture life of single-crystal blades. A recent investigation by Ma et al. [17,76] confirmed that the casting geometry significantly affected the onset of freckles during the unidirectional solidification. It was found that with increasing cross-section, the freckle chains were not formed immediately at the bottom edge of the steps, but after an incubation distance. In contrast, contracting the dimension reveals a promoting effect on the freckle onset. In order to study the geometrical effect on the macrosegregation, the solidification of an Al-Si casting sample with cross-section change was simulated.

The previously developed two-phase volume-average-based solidification model was considered here [8,133,176]. The feeding flow is due to the density difference between the liquid ($\rho_l = 2408 \text{ kg/m}^3$) and solid ($\rho_s = 2545 \text{ kg/m}^3$). The Boussinesq approximation is employed to calculate the thermo-solutal convection. The casting sample, AlSi7, and the cooling conditions are taken from the published experiment in [74]. As displayed in **Figure 3.6 (a)**, 105 mm of the crucible is simulated, including the two large section zones ($\phi 9.5$) and one small section zone ($\phi 3.2$). The calculation is initialized with a constant temperature (T_0) in the alloy and the crucible, and a homogeneous solute distribution (c_0) in the alloy. On the top and bottom of the crucible, a Dirichlet boundary condition (decreasing temperature: T_{Top} and T_{Bottom}) is applied, **Figure 3.6 (b)**. The temperature boundary condition on the outer wall of the crucible is a spatial linear interpolation of T_{Top} and T_{Bottom} . A pressure inlet is applied on the top surface of the sample, and a hot melt is allowed to feed the solidification shrinkage.

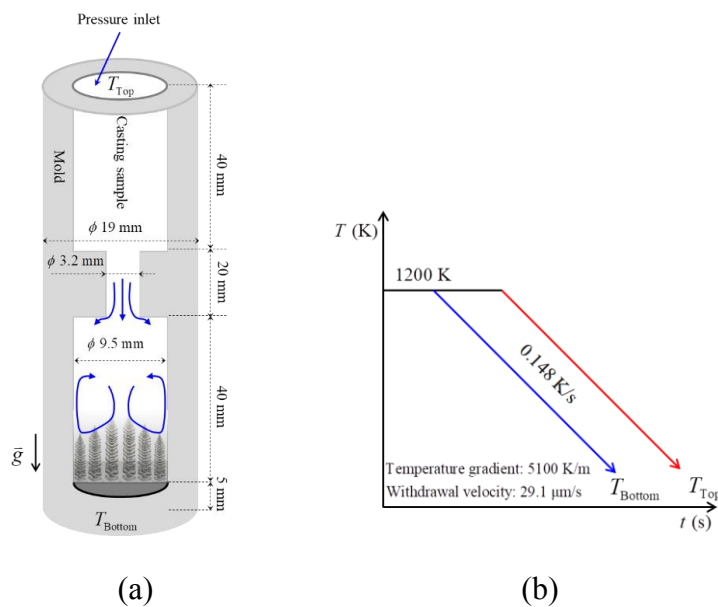


Figure 3.6 (a) Geometry configuration, and (b) boundary conditions.

3.3.1 Macrosegregation caused by shrinkage-induced feeding flow

This work is to ‘reproduce’ Flemings’ analytical solution [14,62]. As shown in **Figure 3.7 (a)**, a so-called reverse segregation develops in the casting surface bottom. The maximum c_{mix} reaches to 0.0703, in comparison to the initial value of 0.07 (c_0). The magnitude of feeding flow is small with an average velocity of $1.3 \mu\text{m/s}$. When the solidification proceeds to steady state, e.g. at 900 s, the change of c_{mix} in the mushy zone, from initial a value of c_0 to the minimum (0.06985) and then recover to c_0 , **Figure 3.7 (b)**, follows the typical evolution profile of c_{mix} in the mushy zone of constant thickness [14,62].

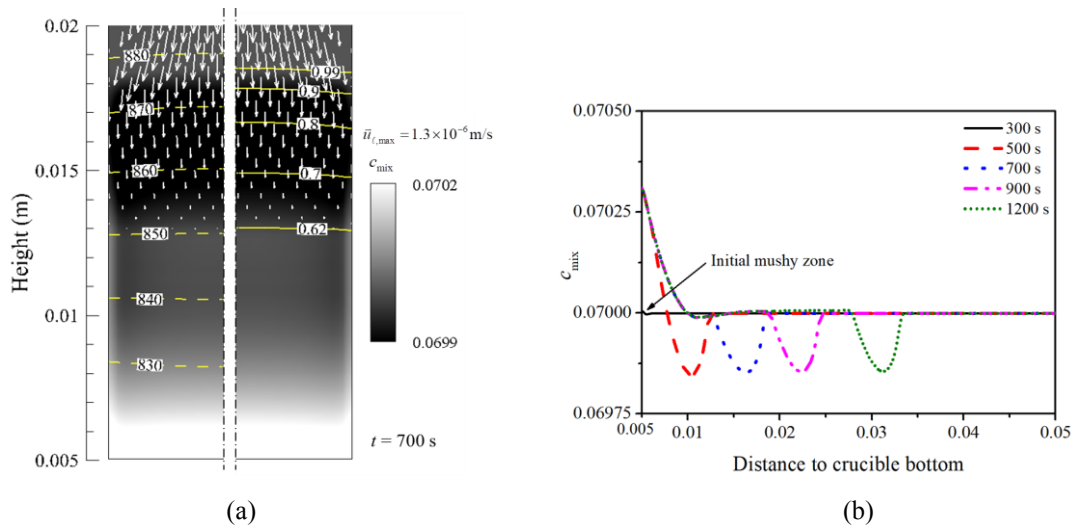


Figure 3.7 Analysis of the inverse segregation in the bottom of the sample. (a) c_{mix} in grey scale at 700 s, overlaid with \bar{u}_ℓ in vectors, isotherms (left) and isolines of f_ℓ (right); (b) evolution of c_{mix} along the axis.

As the solidification front proceeds into the region of cross-section change (reduction) at 1800 s, as shown in **Figure 3.8**, the magnitude of feeding flow reaches to $11 \mu\text{m/s}$. A typical divergent flow pattern develops in the region below the cross-section reduction, leading to the formation of a strong negative ($c_{\text{mix}} < c_0$) segregation in Zones I and II. The negative segregation extreme is about $c_{\text{mix}} = 0.0675$. Just below the shadow of the cross-section reduction (Zone III), a positive segregation forms, because the solidification shrinkage there needs to be fed by the solute-enriched melt.

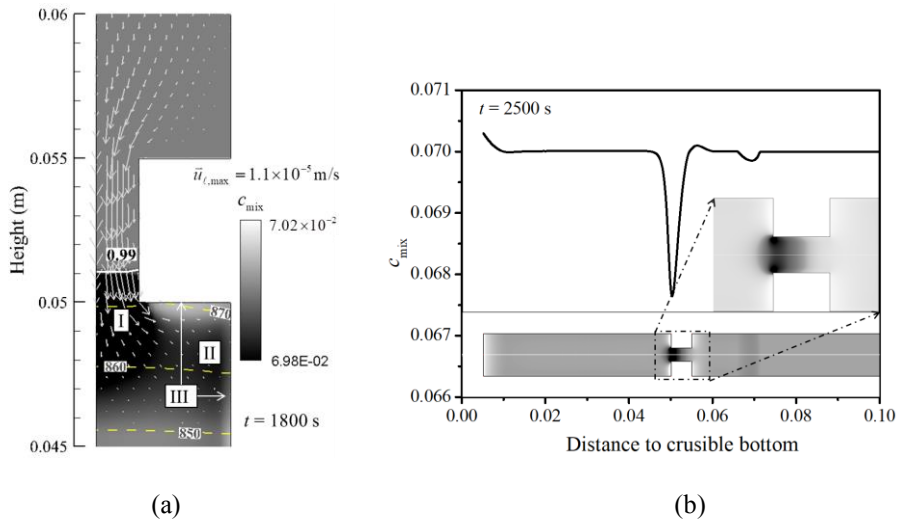


Figure 3.8 Analysis of macrosegregation formation in the region of cross-section change region. (a) c_{mix} in grey scale at 1800 s, overlaid with \bar{u}_ℓ in vectors and isotherms (the solidification front is indicated by a white solid line, $f_\ell = 0.99$); (b) c_{mix} profile along the axis at $t = 2500$ s.

3.3.2 Macrosegregation caused by shrinkage-induced feeding flow and natural convection

The solidification sequence when the columnar tip front approaches and passes the position of the cross-section contraction is displayed in **Figure 3.9**. The mushy zone is represented and confined by two iso-surfaces: top one for $f_\ell = 0.95$, and bottom one for T_{eut} . The thermal conductivity of the solid phase is higher than those of the liquid phase and the graphite mould ($k_s \approx 2.5k_\ell$ or $2.8k_m$), and this causes a radial heat transfer from the mould to the casting sample towards the solidification front. At $t = 1330$ s (**Figure 3.9 (a)**), the solidification front is bulged in the sample centre, i.e. a so-called ‘steeping convection’ is developed. The interdendritic melt, enriched with solute, is gradually transported from the sample centre to the periphery. This type of solute transport leads to a negative segregation in the casting centre and a positive segregation in the outer periphery. The liquid velocity reaches as high as $406 \mu\text{m/s}$, which is mainly driven by the thermo-solutal buoyancy. At 1450 s, **Figure 3.9 (b)**, the space for the bulk flow is largely limited to the volume between the columnar tip front and the ‘shoulder’ of the sample, and thus the maximum liquid velocity reduces to $93 \mu\text{m/s}$. **Figure 3.9 (c)** depicts the simulation result when the solidification tip front passes the position of the cross-section contraction. Above the

solidification front, the steepening convection also develops in a small section, but the flow ($\sim 17 \mu\text{m/s}$) is weaker than that presented in **Figure 3.9 (a)**. In the mushy zone, the interdendritic melt flows downward to compensate the volume shrinkage. In the large cross-section zone, the steepening convection can still be observed in the mushy zone near the sample shoulder surface, but with a low intensity ($\sim 5 \mu\text{m/s}$). This interdendritic flow, despite its low intensity, strengthens the positive macrosegregation below the sample shoulders significantly. A solute-depleted region covering the whole cross-section of the sample is observed exactly above the cross-section contraction.

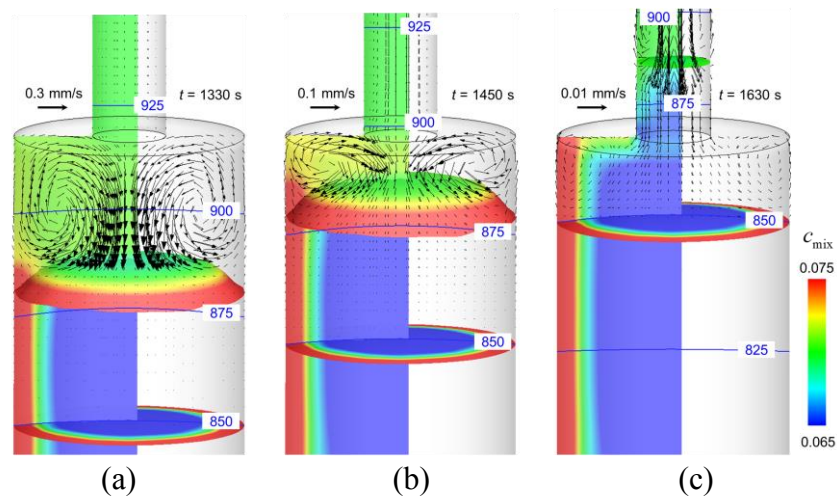


Figure 3.9 Solidification sequence of the sample when the columnar tip front approaches and passes the position of the cross-section contraction: (a) $t = 1330$ s; (b) $t = 1450$ s; (c) $t = 1630$ s. Vectors indicate \bar{u}_ℓ , overlaid by isotherms (solid lines). Two iso-surfaces depict the mushy zone: top one for $f_\ell = 0.95$, bottom one for $T_{\text{eut}} = 850$ K. The colour in all the section/iso-surfaces denotes c_{mix} .

Figure 3.10 displays the solidification sequence near the cross-section expansion. As the solidification front reaches the position of the cross-section expansion (**Figure 3.10 (a)**), the bulk flow is still quite weak ($50 \mu\text{m/s}$); only a weak negative macrosegregation forms at the sample centre. After the solidification front passes the cross-section expansion (**Figure 3.10 (b)**), a flow pattern similar to that in **Figure 3.9 (a)** develops. The iso-surface of $f_\ell = 0.7$ appears like a growing mushroom: a small cap develops from the contraction zone, which subsequently grows and extends sideways along the platform of the expansion region. At 2700 s (**Figure 3.10 (c)**) the bulk flow becomes stronger ($243 \mu\text{m/s}$). The solute-enriched melt accumulates in the periphery of the sample and inhibits the solidification

there. The solidification front becomes further bulged, and the aforementioned steepening convection continues again.

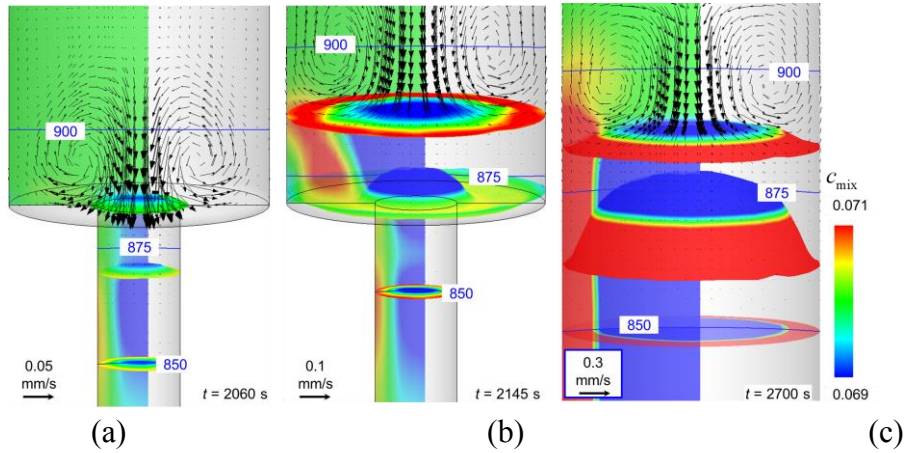


Figure 3.10 Solidification sequence of the sample when the columnar tip reaches and passes the position of the cross-section expansion: (a) $t = 2060$ s; (b) $t = 2145$ s; (c) $t = 2700$ s. Vectors indicate \bar{u}_ℓ , overlaid by the isotherms (solid lines). The two iso-surfaces display the mushy zone: top one for $f_\ell = 0.95$, bottom one for $T_{\text{cut}} = 850$ K. An additional iso-surface ($f_\ell = 0.7$) is drawn in the mushy zone. The colour in all the section/iso-surfaces denotes C_{mix} .

The experiment–simulation comparison of macrosegregation is presented in **Figure 3.11**. The macrosegregation is characterized by c^{index} . **Figure 3.11 (b)–(d)** display the radial macrosegregation distributions on different transverse sections, whose positions are marked in **Figure 3.11 (a)**. Excellent agreement between the simulation and the experiment results is obtained. **Figure 3.11 (e)** illustrates the axial macrosegregation (c^{index}) distribution. Both the experimental and calculated results exhibit a significant positive macrosegregation before the cross-section contraction, followed by a strong negative macrosegregation after the cross-section contraction. Finally, the negative segregation gradually recovers to a neutral composition along the axial direction. A weak negative macrosegregation, with the local minimum c^{index} of 3%, is numerically predicted at the position of the cross-section expansion; this minor negative segregation appears difficult to detect experimentally.

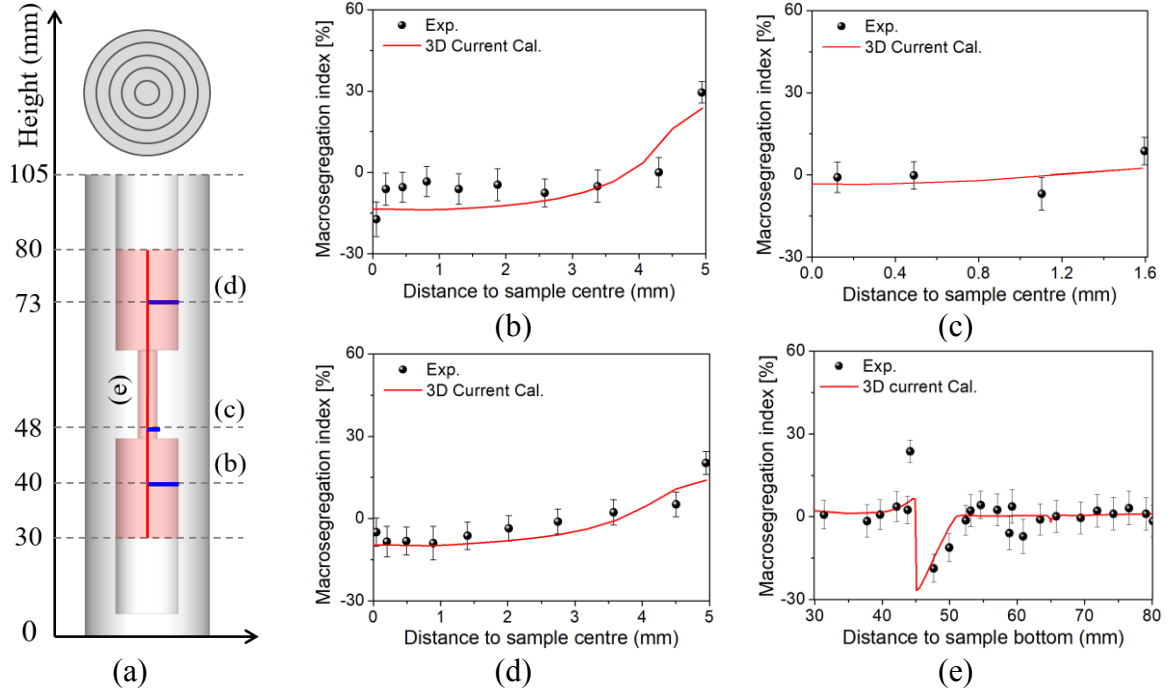


Figure 3.11 Experiment–simulation comparison of the macrosegregation. (a) Schematic of the sample geometry and the positions for the macrosegregation measurement; (b)–(d) radial distribution of c^{index} on different cross-sections, whose positions are marked in (a); (e) section-averaged c^{index} distribution along the axial direction. Black dots denote the experimental measurement [86], and the red lines denote the simulation results.

3.3.3 Analysis of possible formation of spurious crystals

The solute-driven re-melting of the secondary or high-order dendrites, as enhanced by the interdendritic melt flow, is the key formation mechanism for the dendrite fragmentation, which serves as the origin of spurious/stray crystals [54]. A simple formulation have been proposed for the crystal fragmentation [179]: $M_{ce} \propto \bar{u}_\ell \cdot \nabla c_\ell$. Therefore, $\bar{u}_\ell \cdot \nabla c_\ell$ is used here to analyse the possible formation of spurious crystals. **Figure 3.12 (a)–(e)** display the evolution sequence of $\bar{u}_\ell \cdot \nabla c_\ell$. A zoom-in view of Zoom B, as marked by the red rectangle in **Figure 3.12 (b)**, is presented in **Figure 3.12 (f)**. In the ‘blue’ region with a negative value of $\bar{u}_\ell \cdot \nabla c_\ell$, spurious crystals are prone to form. This blue region is mostly located close to the casting surface and near the front of mushy zone, where flow is strong. With time evolution (from 1960 to 2560 s), when the solidification front advances from the small cross-section to the large cross-section regions, the magnitude of $\bar{u}_\ell \cdot \nabla c_\ell$ increases, i.e. the

probability to form spurious crystals increases. To assist in understanding the mechanism, the solidification and the melt flow are schematically depicted in **Figure 3.12 (g)**. The spurious crystals, attributed to the solute-driven re-melting of the secondary or high-order dendrites, possibly form near the sample surface. Few of them may be transported by the flow into the bulk liquid region and re-melted completely; however, most of them might be captured by the columnar dendrites and develop into freckle chains there.

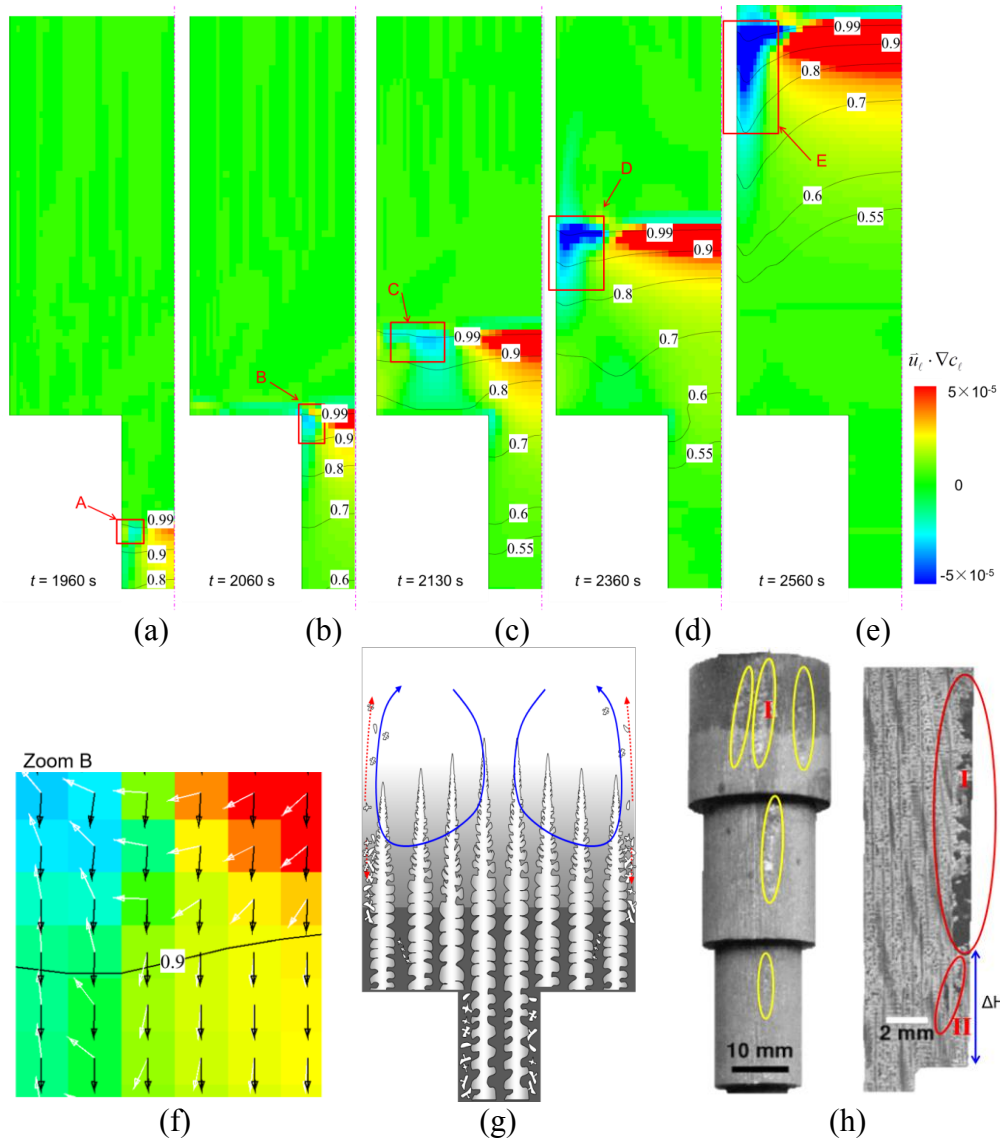


Figure 3.12 Analysis of the possible formation of spurious/stray crystals. (a)–(e) Evolution sequence $\bar{u}_t \cdot \nabla c_t$ contours; (f) zoom-in view of Zoom B in (b); (g) schematics of the solidification and the melt flow; (h) Example of the stray crystals coupled with freckles in the laboratory castings [76].

Solidification experiments with similar casting geometry (cross-section changes) on superalloys was conducted by Ma et al. [76], and more evidences were found. Specifically, the formation of spurious/stray crystals and freckle chain was correlated to the abrupt cross-section expansion, as displayed in **Figure 3. 12 (h)**. At the position of the abrupt section expansion, the freckle chain in the small cross-section zone cannot extend immediately along the bottom edge of the large cross-section zone, but it continues to appear at an incubation height of approximately $\Delta H = 10$ mm above the bottom edge of the sections [76]. From the longitudinal section of the casting sample, it can be seen that below the position of the surface freckle chain (freckle I), a short but clear under-surface freckle (freckle II) forms. Immediately after the solidification front passes the position of the cross-section expansion (**Figure 3. 12 (b)**), the flow is so weak that spurious crystals may not form. In the next moment, **Figure 3. 12 (c)**, the flow becomes stronger but is still not sufficiently strong to form freckle and spurious crystals at the sample surface; some under-surface freckle (freckle II) may form. Only when the flow is sufficiently strong (**Figure 3. 12 (e)**), surface freckles (freckle I) can generate.

3.4 Modelling melting and grain destruction phenomena during globular equiaxed solidification

Melting or re-melting accompanies solidification in many technical castings. For example, during ingot casting, some crystal fragments or equiaxed grains can enter the superheated region and be remelted, while solidification continues in other regions. This simultaneous solidification/melting process acts as an important species/energy transport mechanism, which impacts the structural/compositional homogeneity of the castings. The re-melting is typically understood as a reduction in the equiaxed grain size, but it can also lead to the destruction (disappearance) of equiaxed grains. Existing process-based models cannot treat the solidification/melting by considering both crystal nucleation and destruction properly.

Nucleation/grain-growth and remelting/grain-destruction processes are schematically shown in **Figure 3.13**. Inoculants exist in the parent melt (**Figure 3.13 (a-1)**). With sufficient undercooling, they are activated to become equiaxed grains (**Figure 3.13 (a-2)**). Consequently, the number of inoculants in the melt gradually decreases. The final solidification structure of the sample may consist of a eutectic phase, primary equiaxed

grains with various sizes, and inactivated inoculants embedded in the eutectic phase (**Figure 3.13 (a-3)**). The melting/grain-destruction process is schematically shown in **Figure 3.13 (b)**. The primary material includes the as-cast structure, i.e. eutectic phase, equiaxed grains and some inactivated inoculants (**Figure 3.13 (b-1)**). As the temperature increases, the eutectic phase begins melting first. This process releases the embedded equiaxed grains and inactivated inoculants, and they are free to move again. With further re-melting of the equiaxed grains, their size decreases, which is followed by grain destruction (**Figure 3.13 (b-2)**). The two smallest equiaxed grains (numbered 9–10) are completely melted/destroyed; thus, they are turned into inoculants. At a later stage, **Figure 3.13 (b-3)**, most grains are melted/destroyed, and there are only three equiaxed grains (1–3) that remain.

In this work, a new model is proposed based on a two-phase (liquid and equiaxed crystals) volume-average approach [8,141,180]. A test casting (AlSi7, 60 width \times 80 height mm²) is calculated to illustrate the modelling features. A no-slip boundary condition was assumed to be valid on the domain surface. Before the start of the simulation, the domain was set to be uniform in concentration ($c_0 = 0.07$) and temperature ($T_0 = 900$ K). As the initial condition, the minimum value was assigned for $n_{eq,0}$ (10^7 m⁻³), while a very large value was assigned for $n_{in,0}$ (2.0×10^{10} m⁻³). The sample was firstly solidified by cooling the right-side wall. After the solidification process, the sample is heated on the left side wall.

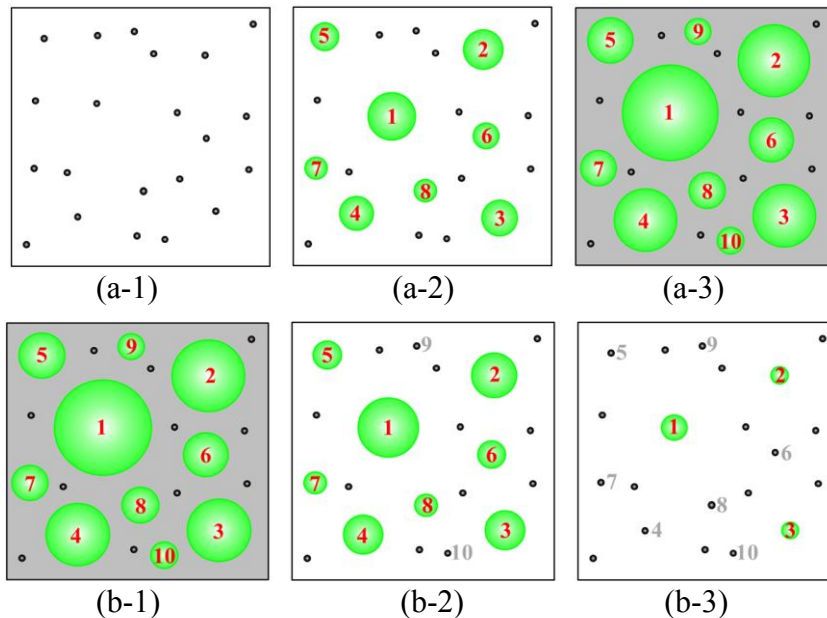


Figure 3.13 Schematic of (a) the nucleation and grain growth and (b) the re-melting and grain destruction processes. The black dots denote the inoculants, the green

spheres indicate the equiaxed grains, and the grey background indicates the eutectic phase. All grains are numbered from 1 to 10.

3.4.1 Cooling from the right side

Solidification was triggered by cooling from the right wall. The solidification sequence at 110 s is shown in **Figure 3.14**. A clockwise thermo-solutal convection formed (**Figure 3.14 (g)**). The flow transported both the liquid and solid phases and modified the temperature field. T and ΔT are shown in **Figure 3.14 (a)**, which shows that the melt was strongly undercooled near the right surface and slightly superheated in the left part. As shown in **Figure 3.14 (b)**, in the upper-right corner where the melt was most undercooled ($\Delta T \approx -11\text{K}$), the fastest nucleation rate was observed ($\dot{n} \approx 2.0 \times 10^{10} \text{ m}^{-3} \cdot \text{s}^{-1}$). Because the grains were denser than the liquid, the formed grains sedimented and dragged the liquid melt to flow with them. Some of these newly formed equiaxed grains (with small size) were transported to the superheated region. As displayed in **Figure 3.14 (c)**, the grains further solidified in the undercooled melt (as indicated by the positive M_{ℓ_e}), and those grains that were transported to the hot region melted ($M_{\ell_e} < 0$). Re-melting accompanying solidification during casting process was numerically verified by the current model. As shown in **Figure 3.14 (b)**, melting in the superheated region caused the grains to be destroyed, which reduced n_{eq} locally (as shown in **Figure 3.14 (f)**). Owing to solute partitioning ($m = 0.13$), solute-enriched liquid was rejected during the solidification process. High c_{ℓ} can be seen in **Figure 3.14 (d)** near the right surface. The rejected c_{ℓ} modified ΔT ($\Delta T = T_f + m \cdot c_{\ell} - T$) and thereby affected M_{ℓ_e} . n_{in} and n_{eq} are shown in **Figure 3.14 (e)–(f)**, respectively. Nucleation consumed a large number of inoculants near the right surface (**Figure 3.14 (b)**), leading to a lower value of n_{in} in this region. After nucleation, the grains were transported along the vertical wall and piled up in the bottom ($n_{\text{eq}} \approx 10^{11} \text{ m}^{-3} \cdot \text{s}^{-1}$). The calculated f_e and d_e are shown in **Figure 3.14 (g)–(h)**, respectively. The grains that nucleated on the surface adhered to the wall owing to the applied no-slip boundary condition. These grains grew quickly under strong undercooling, leading to a high f_e and large d_e on the right surface. In the lower-left corner, numerous small grains piled up. These small grains grew slowly because of the relatively high local temperature. From

Figure 3.14 (g), it can be seen f_e was below f_e^c in the lower-left corner, which means that these small grains could be advected by liquid flow.

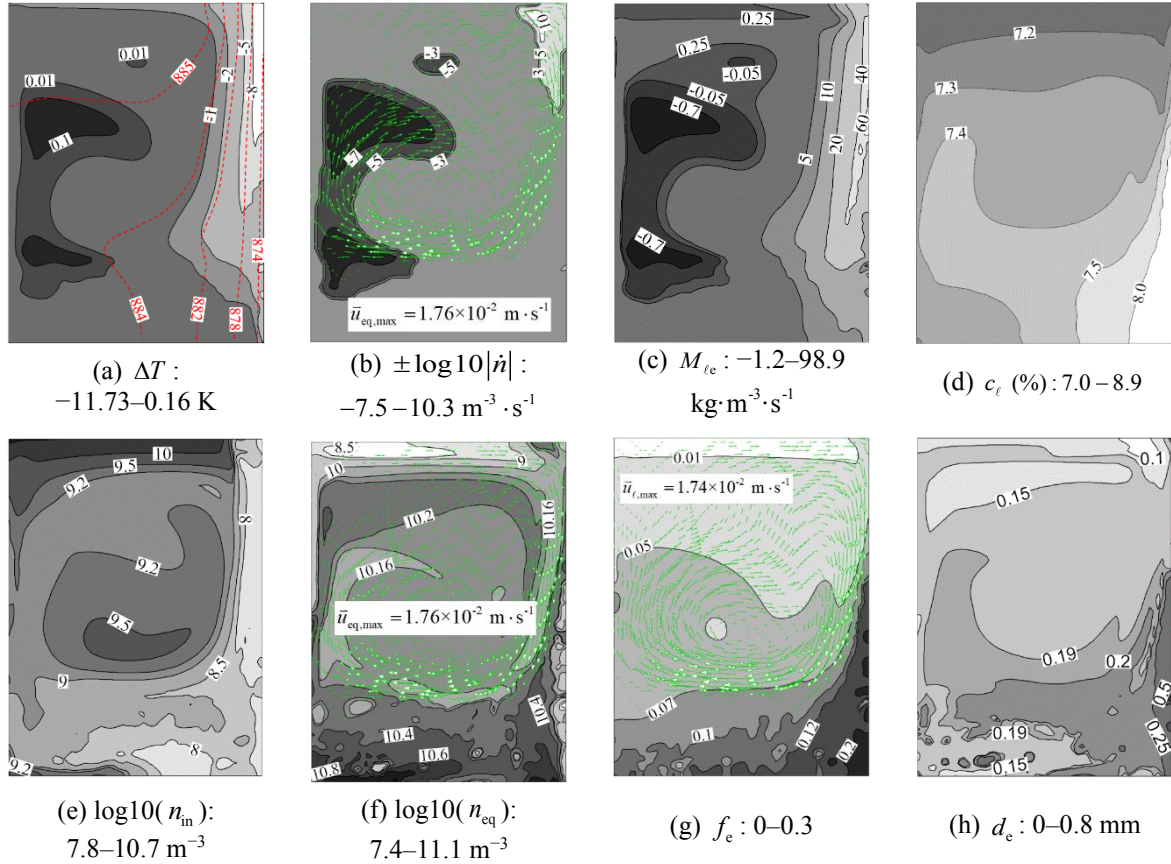


Figure 3.14 Solidification sequence of case II (stage A) at 110 s. Contours and corresponding isolines of (a) ΔT overlaid by isotherms (red dashed lines); (b) $\pm \log_{10}|\dot{n}|$ overlaid by the vectors of \bar{u}_{eq} ; (c) $M_{\ell e}$; (d) c_{ℓ} ; (e) $\log_{10}(n_{\text{in}})$; (f) $\log_{10}(n_{\text{eq}})$ overlaid by the vectors of \bar{u}_{eq} ; (g) f_e overlaid by the vectors of \bar{u}_{ℓ} ; and (h) d_e .

3.4.2 Heating from the left side

The melting sequence is presented in **Figure 3.15**. The eutectic phase melted first at the eutectic isotherm, followed by gradual melting of the equiaxed grains. As shown in **Figure 3.15 (a)**, after the remelting of eutectic phase, some liquid pockets were created, and a clockwise flow develops. The embedded grains (or grain clusters) were released and began to move again (**Figure 3.15 (e)**). c_{ℓ} (**Figure 3.15 (b)**) is large in region A, but it is relatively small in regions B and C. ΔT ($=T_f + m \cdot c_{\ell} - T$) is as a function of c_{ℓ} and T . As

shown in **Figure 3.15 (c)**, the alloy was overheated in region A and undercooled in regions B and C, which led to melting in region A and re-solidification in regions B and C (**Figure 3.15 (d)**). As shown in **Figure 3.15 (e)**, from 320 to 380 s, d_e increased from 3.1 to 3.8 mm in region C and decreased from 0.48 to 0.37 mm in region A. The large grains sedimented quickly, but the small grains could easily be advected by the liquid flow. As shown in **Figure 3.15 (f)**, nucleation occurred in regions B and C, but the nucleation rate was very small ($\sim 10^5 \text{ m}^{-3} \cdot \text{s}^{-1}$). In region A, the destruction rate was $-7.1 \times 10^7 \text{ m}^{-3} \cdot \text{s}^{-1}$. n_{eq} and n_{in} are presented **Figure 3.15 (g)–(h)**, respectively.

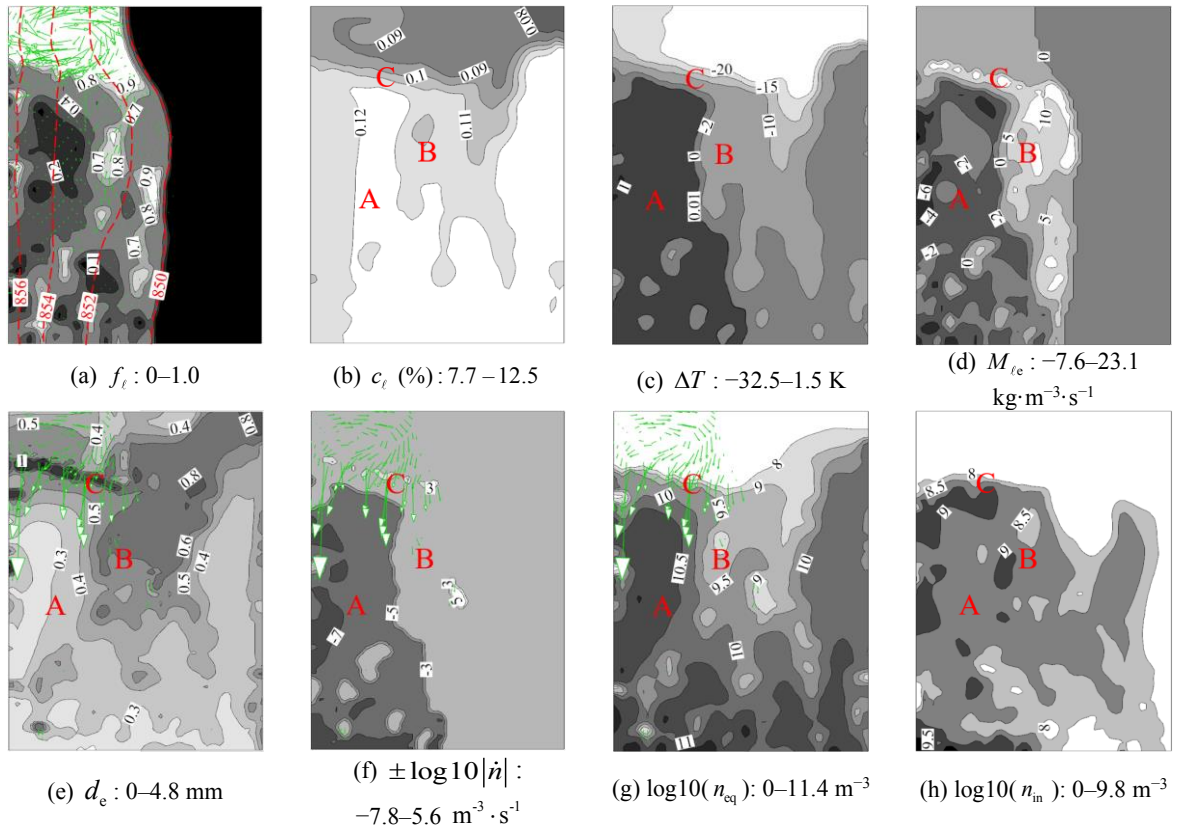


Figure 3.15 Melting sequence at 380 s. Contours and corresponding isolines of (a) f_ℓ overlaid by the isotherms (red dashed lines) and vectors of \bar{u}_ℓ ; (b) c_ℓ ; (c) ΔT ; (d) $M_{\ell e}$; (e) d_e overlaid by the vectors of \bar{u}_{eq} ; (f) $\pm \log_{10} |\dot{n}|$ overlaid by the vectors of \bar{u}_ℓ ; (g) $\log_{10}(n_{\text{eq}})$ overlaid by the vectors of \bar{u}_{eq} ; and (h) $\log_{10}(n_{\text{in}})$.

3.4.3 Transport of a bulk crystal network

An interesting phenomenon was observed: transport of a bulk crystal network during melting, as shown in **Figure 3.16**. Two isolines are drawn: $f_e = 0.01$ (indicating the melt

front), and $f_e = 0.15$ (indicating the packing front). At 600 s (**Figure 3.16 (a)**), more than half of the domain had melted. The packed region is marked as A, B, and C. Region A is connected to the main solid part (region C) through a thin bridge (region B). Two flow vortices developed, which were separated by the rigid solid structure. Only the liquid could flow through this rigid porous medium. At 610 s (**Figure 3.16 (b)**), region B had re-melted. Region A detached from region C, but it was still partially connected to the left wall. At 615 s (**Figure 3.16 (c)**), region A detached from the left wall and turned into the bulk melt region. The red vectors in **Figure 3.16** indicate the direction of rotation. In the subsequent melting process, this bulk crystal network became increasingly smaller until it was completely melted.

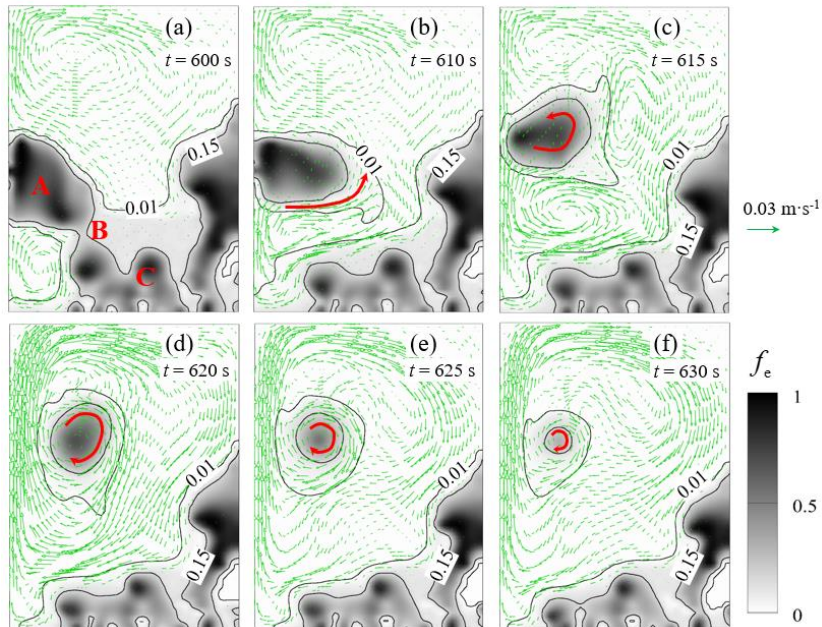


Figure 3.16 Transport of a bulk crystal network during the melting process shown by the contours of f_e overlaid by the vectors of \vec{u}_l . The red vectors indicate the rotation direction of the bulk crystal network.

Based on the current numerical study, it was found that melting cannot be simply considered to be inverse solidification. The simultaneous solidification/melting phenomenon presents an important species/energy transport mechanism, influencing the structural and compositional heterogeneity of the final as-cast product.

4. Main conclusions

The previously developed multiphase volume-average solidification model was used and extended to study the flow-solidification interaction during unidirectional solidification process. Understanding to the flow-solidification interaction phenomena was improved. The main conclusions are drawn as follow.

1. A two-phase columnar-solidification model is used to study the role of permeability in the solidifying mushy zone under forced convection (RMF) conditions.
 - Under RMF, an azimuthal flow superimposed with the meridional circulation was generated. A special macrosegregation profile resembling a “Christmas tree”, as typically observed experimentally, can be numerically predicted only when the permeability falls in a certain range.
 - Numerical parameter study shows that the thickness of the mushy zone decreases, and the global macrosegregation intensity increases monotonically with the mush permeability.
2. A novel/different model for the solidification of AlSi7Fe1 is developed. This improved three-phase solidification model is employed to simulate the unidirectional solidification of an AlSi7Fe1 alloy under RMF.
 - The difference in macrosegregation pattern between elements Si and Fe is understood through this study. Formation mechanism of β -Al₅FeSi is mainly caused by solute macrosegregation, and migration of β -Al₅FeSi in the mushy zone is likely negligible.
 - The formed β -Al₅FeSi significantly blocks the interdendritic flow under the influence of an RMF. Hence, dendrites appear to follow the coarsening law ($\lambda_2 \propto t_f^{1/3}$) of solidification under pure diffusive conditions. The role of dendrite coarsening phenomenon in the interdendritic flow is investigated.
3. A unidirectional solidification experiment with both cross-section contraction and expansion between $\phi 9.5$ and $\phi 3.2$ mm in one cylindrical casting sample (AlSi7) is simulated. Geometrical effect on macrosegregation formation during unidirectional solidification is investigated.

- When only shrinkage-induced feeding flow is considered, the current could reproduce the Flemings' LSRE model, i.e. a 'inverse macrosegregation' in the sample bottom, a 'steady state' region in the mid-section of the sample, and a negative segregation region in the solidifying mushy zone.
- Under thermo-solutal convection, a so-called 'steeping convection' is induced, leading to a relatively strong positive macrosegregation on the periphery of the sample. With cross-sectional change: (1) a positive macrosegregation under the 'shoulder' of the cross-section contraction is induced; (2) in the small cross-section part, where the shrinkage-induced feeding flow is magnified, a severe negative segregation is formed; (3) cross-section expansion in the geometry leads to a high risk for the formation of spurious/stray crystals.
- A mathematical equation (Eq. (4.1)) is derived to analyse the macrosegregation. Freckles and spurious crystals are formed at the locations where the negative value of $\bar{u}_\ell \cdot \nabla c_\ell$ is distributed.

$$\frac{\partial c_{\text{mix}}}{\partial t} = (\rho_s - \rho_\ell) \left(\frac{c_\ell - c_{\text{mix}}}{\bar{\rho}} \right) \cdot \frac{\partial f_s}{\partial t} - \frac{\rho_\ell}{\bar{\rho}} f_\ell \bar{u}_\ell \cdot \nabla c_\ell \quad (4.1)$$

4. A new melting/grain-destruction model is developed using the volume-average approach. melting and grain destruction phenomena during globular equiaxed solidification is studied numerically.

- The numerical model helps to visualize the remelting phenomenon during solidification process.
- During cooling, some as-nucleated equiaxed grains were transported to superheated regions where re-melting and grain destruction occurred. During heating, there were some locally undercooled regions where nucleation and solidification could occur. Solidification and remelting occurring simultaneously at different locations present an important species/energy transport mechanism.

5 References

- [1] S.H. Davis, H.E. Huppert, U. Müller, M.G. Worster, *Interactive Dynamics of Convection and Solidification*, Springer Netherlands, 1992.
- [2] A. Mahata, M. Asle Zaeem, M.I. Baskes, Understanding homogeneous nucleation in solidification of aluminum by molecular dynamics simulations, *Model. Simul. Mater. Sci. Eng.* 26 (2018) 025007.
- [3] I. Steinbach, Phase-field models in materials science, *Model. Simul. Mater. Sci. Eng.* 17 (2009) 1–31.
- [4] L. Liu, S. Pian, Z. Zhang, Y. Bao, R. Li, H. Chen, A cellular automaton-lattice Boltzmann method for modeling growth and settlement of the dendrites for Al-4.7%Cu solidification, *Comput. Mater. Sci.* 146 (2018) 9–17.
- [5] D. Tourret, A. Karma, Multiscale dendritic needle network model of alloy solidification, *Acta Mater.* 61 (2013) 6474–6491.
- [6] C.A. Gandin, M. Rappaz, A coupled finite element-cellular automaton model for the prediction of dendritic grain structures in solidification processes, *Acta Metall. Mater.* 42 (1994) 2233–2246.
- [7] C.Y. Wang, C. Beckermann, Equiaxed dendritic solidification with convection: Part I. Multiscale/multiphase modeling, *Metall. Mater. Trans. A Phys. Metall. Mater. Sci.* 27 (1996) 2754–2764.
- [8] M. Wu, A. Ludwig, A. Kharicha, Volume-averaged modeling of multiphase flow phenomena during alloy solidification, *Metals (Basel)*. 9 (2019) 229.
- [9] D.R. Poirier, Density, viscosity, and diffusion coefficients in hypoeutectic Al-Si liquid alloys: An assessment of available data, *Metall. Mater. Trans. B Process Metall. Mater. Process. Sci.* 45 (2014) 1345–1354.
- [10] T. Magnusson, L. Arnberg, Density and solidification shrinkage of hypoeutectic aluminum-silicon alloys, *Metall. Mater. Trans. A Phys. Metall. Mater. Sci.* 32 (2001) 2605–2613.
- [11] G. Zimmermann, L. Sturz, B. Billia, N. Mangelinck-Noël, D.R. Liu, H. Nguyen Thi, N. Bergeon, C.A. Gandin, D.J. Browne, C. Beckermann, D. Tourret, A. Karma, Columnar-to-equiaxed transition in solidification processing of AlSi7 alloys in microgravity-the CETSOL project, *Mater. Sci. Forum.* 790–791 (2014) 12–21.
- [12] G. Zimmermann, L. Sturz, B. Billia, N. Mangelinck-Noël, H.N. Thi, C.A. Gandin, D.J. Browne, W.U. Mirihanage, Investigation of columnar-to-equiaxed transition in solidification processing of AlSi alloys in microgravity - The CETSOL project, *J. Phys. Conf. Ser.* 327 (2011) 012003.
- [13] C. Beckermann, Macrosegregation, in: *Encycl. Mater. Sci. Technol.*, (2001) 4733–4738.
- [14] M.C. Flemings, R. Mehrabian, G.E. Nereo, Macrosegregation: part II, *Trans. Metall. Soc. AIME.* 241 (1968) 41–49.
- [15] K.C. Chiang, H.L. Tsai, Shrinkage-induced fluid flow and domain change in two-dimensional alloy solidification, *Int. J. Heat Mass Transf.* 35 (1992) 1763–1770.
- [16] D. Ma, J. Ziehm, W. Wang, A. Bührig-Polaczek, Freckle formation in directionally solidified superalloy components with expanding cross-section, *IOP Conf. Ser. Mater. Sci. Eng.*, (27) 2011 012034.
- [17] D. Ma, A. Bührig-Polaczek, The geometrical effect on freckle formation in the directionally solidified superalloy CMSX-4, *Metall. Mater. Trans. A Phys. Metall. Mater. Sci.* 45 (2014) 1435–1444.
- [18] V.R. Voller, S. Sundarraj, A model of inverse segregation: the role of microporosity, *Int. J. Heat Mass Transf.* 38 (1995) 1009–1018.
- [19] A.S. Sabau, S. Viswanathan, Microporosity prediction in aluminum alloy castings, *Metall. Mater. Trans. B Process Metall. Mater. Process. Sci.* 33 (2002) 243–255.
- [20] A. Noepfel, A. Ciobanas, X.D. Wang, K. Zaidat, N. Mangelinck, O. Budenkova, A. Weiss, G. Zimmermann, Y. Fautrelle, Influence of forced/natural convection on segregation during the directional solidification of Al-based binary alloys, *Metall. Mater. Trans. B Process Metall. Mater. Process. Sci.* 41 (2010) 193–208.
- [21] J.K. Roplekar, J.A. Dantzig, A study of solidification with a rotating magnetic field, *Int. J. Cast Met. Res.* 14 (2001) 79–95.
- [22] J. Zeng, W. Chen, S. Zhang, L.I. Yi, Q. Wang, Development and application of final permanent magnet stirring during continuous casting of high carbon rectangular billet, *ISIJ Int.* 55 (2015) 2142–2149.
- [23] A. Roósz, J. Kovács, A. Rónaföldi, Á. Kovács, Effect of high rotating magnetic field on the solidified structure of Al-7wt.%Si-1wt.%Fe alloy, *Mater. Sci. Forum.* 752 (2013) 57–65.

- [24] S. Yesilyurt, S. Motakef, R. Grugel, K. Mazuruk, The effect of the traveling magnetic field (TMF) on the buoyancy-induced convection in the vertical Bridgman growth of semiconductors, *J. Cryst. Growth.* 263 (2004) 80–89.
- [25] I. Grants, G. Gerbeth, Stability of melt flow due to a traveling magnetic field in a closed ampoule, *J. Cryst. Growth.* 269 (2004) 630–638.
- [26] H. Duan, L. Zhang, B.G. Thomas, Effect of Melt Superheat and Alloy Size on the Mixing Phenomena in Argon-Stirred Steel Ladles, *Steel Res. Int.* 90 (2019) 1–8.
- [27] Y. Nakai, I. Sumi, N. Kikuchi, Y. Kishimoto, Y. Miki, Aggregation behavior of desulfurization flux in hot metal desulfurization with mechanical stirring, *ISIJ Int.* 53 (2013) 1411–1419.
- [28] M. Ahmadein, M. Wu, J.H. Li, P. Schumacher, A. Ludwig, Prediction of the as-cast structure of Al-4.0 Wt Pct Cu ingots, *Metall. Mater. Trans. A Phys. Metall. Mater. Sci.* 44 (2013) 2895–2903.
- [29] G. Chirita, D. Soares, F.S. Silva, Advantages of the centrifugal casting technique for the production of structural components with Al-Si alloys, *Mater. Des.* 29 (2008) 20–27.
- [30] J.W. Gao, C.Y. Wang, Modeling the solidification of functionally graded materials by centrifugal casting, *Mater. Sci. Eng. A.* 292 (2000) 207–215.
- [31] J. wen LI, T. Momono, Y. FU, Z. JIA, Y. Tayu, Effect of ultrasonic stirring on temperature distribution and grain refinement in Al-1.65%Si alloy melt, *Trans. Nonferrous Met. Soc. China (English Ed.)* 17 (2007) 691–697.
- [32] S.E. Shim, S. Ghose, A.I. Isayev, Formation of bubbles during ultrasonic treatment of cured poly(dimethyl siloxane), *Polymer (Guildf.)* 43 (2002) 5535–5543.
- [33] T. V. Atamanenko, D.G. Eskin, L. Zhang, L. Katgerman, Criteria of grain refinement induced by ultrasonic melt treatment of aluminum alloys containing ZR and Ti, *Metall. Mater. Trans. A Phys. Metall. Mater. Sci.* 41 (2010) 2056–2066.
- [34] C.Y. Wang, S. Ahuja, C. Beckermann, H.C. de Groh, Multiparticle interfacial drag in equiaxed solidification, *Metall. Mater. Trans. B.* 26 (1995) 111–119.
- [35] F. Nota, R. Savino, S. Fico, The interaction between drops and solidification front in presence of Marangoni effect, *Acta Astronaut.* 59 (2006) 20–31.
- [36] M. Wu, A. Ludwig, L. Ratke, Modeling of marangoni-induced droplet motion and melt convection during solidification of hypermonotectic alloys, *Metall. Mater. Trans. A Phys. Metall. Mater. Sci.* 34 (2003) 3009–3019.
- [37] R. Thome, K. Harste, Principles of billet soft-reduction and consequences for continuous casting, *ISIJ Int.* 46 (2006) 1839–1844.
- [38] J. Domitner, M. Wu, A. Kharicha, A. Ludwig, B. Kaufmann, J. Reiter, T. Schaden, Modeling the effects of strand surface bulging and mechanical softreduction on the macrosegregation formation in steel continuous casting, *Metall. Mater. Trans. A Phys. Metall. Mater. Sci.* 45 (2014) 1415–1434.
- [39] J. Dantzig, M. Rappaz, *Solidification*, EPFL, London, 2009.
- [40] W. Kurz, D.J. Fisher, *Fundamentals of Solidification*, in: *Metallogr. Microstruct.*, second, Trans Tech Publications Ltd, Zuerich, 2018.
- [41] M. Akif Ezan, A. Ereğ, I. Dincer, A study on the importance of natural convection during solidification in rectangular geometry, *J. Heat Transfer.* 133 (2011) 1–9.
- [42] C.J. Paradies, R.N. Smith, M.E. Glicksman, The influence of convection during solidification on fragmentation of the mushy zone of a model alloy, *Metall. Mater. Trans. A Phys. Metall. Mater. Sci.* 28 (1997) 875–883.
- [43] P.J. Prescott, F.P. Incropera, Convection Heat and Mass Transfer in Alloy Solidification, *Adv. Heat Transf.* 28 (1996) 231–338.
- [44] D.T.J. Hurle, E. Jakeman, A.A. Wheeler, Effect of solutal convection on the morphological stability of a binary alloy, *J. Cryst. Growth.* 58 (1982) 163–179.
- [45] A. Ludwig, M. Wu, A. Kharicha, On Macrosegregation, *Metall. Mater. Trans. A Phys. Metall. Mater. Sci.* 46 (2015) 4854–4867.
- [46] M. Wu, A. Vakhruşev, G. Nummer, C. Pfeiler, A. Kharicha, A. Ludwig, Importance of melt flow in solidifying mushy zone, *Open Transp. Phenom. J.* 2 (2010) 16–23.
- [47] H. Zhang, M. Wu, Y. Zheng, A. Ludwig, A. Kharicha, Numerical study of the role of mush permeability in the solidifying mushy zone under forced convection, *Mater. Today Commun.* 22 (2020) 100842.
- [48] N. Shevchenko, O. Roshchupkina, O. Sokolova, S. Eckert, The effect of natural and forced melt convection on dendritic solidification in Ga-In alloys, *J. Cryst. Growth.* 417 (2015) 1–8.

- [49] A. Zhang, J. Du, Z. Guo, Q. Wang, S. Xiong, A Phase-Field Lattice-Boltzmann Study on Dendritic Growth of Al-Cu Alloy Under Convection, *Metall. Mater. Trans. B Process Metall. Mater. Process. Sci.* 49 (2018) 3603–3615.
- [50] Q. Li, C. Beckermann, Modeling of free dendritic growth of succinonitrile-acetone alloys with thermosolutal melt convection, *J. Cryst. Growth.* 236 (2002) 482–498.
- [51] Y.-W. Lee, R.N. Smith, M.E. Glicksman, M.B. Koss, Effects of Buoyancy on the Growth of Dendritic Crystals, *Annu. Rev. Heat Transf.* 7 (1996) 59–139.
- [52] T. Cool, P.W. Voorhees, The evolution of dendrites during coarsening: Fragmentation and morphology, *Acta Mater.* 127 (2017) 359–367.
- [53] H. Neumann-Heyme, K. Eckert, C. Beckermann, Dendrite fragmentation in alloy solidification due to sidearm pinch-off, *Phys. Rev. E - Stat. Nonlinear, Soft Matter Phys.* 92 (2015) 060401.
- [54] A. Hellowell, S. Liu, S.Z. Lu, Dendrite fragmentation and the effects of fluid flow in castings, *Jom.* 49 (1997) 18–20.
- [55] M. Rettenmayr, Melting and remelting phenomena, *Int. Mater. Rev.* 54 (2009) 1–17.
- [56] M. Rettenmayr, Benefits of modeling of melting for the understanding of solidification processes, *Mater. Sci. Forum.* 649 (2010) 53–59.
- [57] J.A. Burton, R.C. Prim, W.P. Slichter, The distribution of solute in crystals grown from the melt. Part I. Theoretical, *J. Chem. Phys.* 21 (1953) 1987–1991.
- [58] W.A. Tiller, K.A. Jackson, J.W. Rutter, B. Chalmers, The redistribution of solute atoms during the solidification of metals, *Acta Metall.* 1 (1953) 428–437.
- [59] M.C. Flemings, Our understanding of macrosegregation: Past and present, *ISIJ Int.* 40 (2000) 833–841.
- [60] M. Wu, L. Könözy, A. Ludwig, W. Schützenhöfer, R. Tanzer, On the Formation of Macrosegregations in Steel Ingot Castings, *Steel Res. Int.* 79 (2008) 637–644.
- [61] I.L. Ferreira, C.A. Siqueira, C.A. Santos, A. Garcia, Theoretical and experimental analysis of inverse segregation during unidirectional solidification of an Al-6.2 wt.% Cu alloy, *Scr. Mater.* 49 (2003) 339–344.
- [62] M.C.Flemings, G.E.Nereo, Macrosegregation: Part I, *Trans. Metall. Soc. AIME.* 239 (1967) 1449–1461.
- [63] D.X. Ma, Z.H. Dong, F. Wang, H.B. Dong, A Phenomenological Analysis of Freckling in Directional Solidification of Ni-Base Superalloy: The Role of Edge and Curvature in Casting Components, *Metall. Mater. Trans. A Phys. Metall. Mater. Sci.* 51 (2020) 88–92.
- [64] J. Li, M. Wu, J. Hao, A. Kharicha, A. Ludwig, Simulation of channel segregation using a two-phase columnar solidification model - Part II: Mechanism and parameter study, *Comput. Mater. Sci.* 55 (2012) 419–429.
- [65] H. Zhang, M. Wu, S.N. Tewari, A. Ludwig, A. Kharicha, Geometrical effect on macrosegregation formation during unidirectional solidification of Al-Si alloy, *J. Mater. Process. Technol.* 288 (2020) 116913.
- [66] J. Li, M. Wu, A. Ludwig, A. Kharicha, Simulation of macrosegregation in a 2.45-ton steel ingot using a three-phase mixed columnar-equiaxed model, *Int. J. Heat Mass Transf.* 72 (2014) 668–679.
- [67] J. Campbell, *Casting*, 2nd ed., Butterworth, Amsterdam, 1991.
- [68] Y. Zheng, Multiphase modeling of as-solidified structure and macrosegregation in semi-continuously cast steel strand, University of Leoben, Ph. D. thesis, 2018.
- [69] C.M.G. Rodrigues, A. Ludwig, M. Wu, A. Kharicha, A. Vakhrushev, Two-phase viscoplastic model for the simulation of twin roll casting, *J. Mater. Process. Technol.* 286 (2020) 116814.
- [70] M. Wu, J. Domitner, A. Ludwig, Using a two-phase columnar solidification model to study the principle of mechanical soft reduction in slab casting, *Metall. Mater. Trans. A Phys. Metall. Mater. Sci.* 43 (2012) 945–964.
- [71] F. Mayer, M. Wu, A. Ludwig, On the formation of centreline segregation in continuous slab casting of steel due to bulging and/or feeding, *Steel Res. Int.* 81 (2010) 660–667.
- [72] M. Wu, A. Ludwig, A. Kharicha, A four phase model for the macrosegregation and shrinkage cavity during solidification of steel ingot, *Appl. Math. Model.* 41 (2017) 102–120.
- [73] R. Pierer, C. Bernhard, C. Chimani, A contribution to hot tearing in the continuous casting process, *Rev. Métallurgie.* 104 (2007) 72–83.
- [74] M. Ghods, L. Johnson, M. Lauer, R.N. Grugel, S.N. Tewari, D.R. Poirier, Radial macrosegregation and dendrite clustering in directionally solidified Al-7Si and Al-19Cu alloys, *J. Cryst. Growth.* 441 (2016) 107–116.
- [75] M. Ghods, M. Lauer, R.N. Grugel, S.N. Tewari, D.R. Poirier, Convection and macrosegregation in Al-19Cu alloy directionally solidified through an abrupt contraction in cross-section: A comparison with Al-7Si, *J. Cryst.*

Growth. 459 (2017) 135–145.

- [76] D. Ma, Q. Wu, A. Bührig-Polaczek, Some new observations on freckle formation in directionally solidified superalloy components, *Metall. Mater. Trans. B Process Metall. Mater. Process. Sci.* 43 (2012) 344–353.
- [77] V.R. Voller, A.D. Brent, C. Prakash, Modelling the mushy region in a binary alloy, *Appl. Math. Model.* 14 (1990) 320–326.
- [78] P. Zhao, R. Dai, W. Li, Q. Wang, M. Zeng, Modeling the mushy zone during the melting process under Neumann boundary condition using the improved enthalpy-porosity method, *Numer. Heat Transf. Part A Appl.* 78 (2020) 1–20.
- [79] M. Wu, M. Stefan-Kharicha, A. Kharicha, A. Ludwig, Flow-solidification interaction: A numerical study on solidification of NH₄Cl – 70 wt.%H₂O solution in a water-cooled mould with a large sample thickness, *Int. J. Heat Mass Transf.* 164 (2021) 120566.
- [80] I. Steinbach, Pattern formation in constrained dendritic growth with solutal buoyancy, *Acta Mater.* 57 (2009) 2640–2645.
- [81] G. Reinhart, C.A. Gandin, N. Mangelinck-Noël, H. Nguyen-Thi, J.E. Spinelli, J. Baruchel, B. Billia, Influence of natural convection during upward directional solidification: A comparison between in situ X-ray radiography and direct simulation of the grain structure, *Acta Mater.* 61 (2013) 4765–4777.
- [82] T. Nelson, B. Cai, N. Warnken, P.D. Lee, E. Boller, O. V. Magdysyuk, N.R. Green, Gravity effect on thermal-solutal convection during solidification revealed by four-dimensional synchrotron imaging with compositional mapping, *Scr. Mater.* 180 (2020) 29–33.
- [83] G. Zimmermann, L. Sturz, Microstructure formation in AlSi7Mg alloys directionally solidified in a rotating magnetic field, *Steel Res. Int.* 78 (2007) 379–385.
- [84] L. Ratke, S. Steinbach, G. Müller, M. Hainke, J. Friedrich, A. Roos, K. Fautrelle, M.D. Dupuy, G. Zimmermann, A. Weiss, J. Lacaze, R. Valdes, G.U. Grün, H.P. Nicolai, H. Gerke-Cantow, MICAST - The effect of magnetically controlled fluid flow on microstructure evolution in cast technical Al-alloys, *Microgravity Sci. Technol.* 15 (2005) 99–103.
- [85] S. Akamatsu, H. Nguyen-Thi, In situ observation of solidification patterns in diffusive conditions, *Acta Mater.* 108 (2016) 325–346.
- [86] M. Ghods, L. Johnson, M. Lauer, R.N. Grugel, S.N. Tewari, D.R. Poirier, Macrosegregation in Al-7Si alloy caused by abrupt cross-section change during directional solidification, *J. Cryst. Growth.* 449 (2016) 134–147.
- [87] A. Bogno, H. Nguyen-Thi, A. Buffet, G. Reinhart, B. Billia, N. Mangelinck-Noël, N. Bergeon, J. Baruchel, T. Schenk, Analysis by synchrotron X-ray radiography of convection effects on the dynamic evolution of the solid-liquid interface and on solute distribution during the initial transient of solidification, *Acta Mater.* 59 (2011) 4356–4365.
- [88] A.K. Dahle, D.H. StJohn, Rheological behaviour of the mushy zone and its effect on the formation of casting defects during solidification, *Acta Mater.* 47 (1998) 31–41.
- [89] S. Kunstreich, Electromagnetic stirring for continuous casting - Part 2, *Rev. Metall. CIT.* 100 (2003) 1043–1061.
- [90] N. Shevchenko, S. Boden, G. Gerbeth, S. Eckert, Chimney formation in solidifying Ga-25wt pct in alloys under the influence of thermosolutal melt convection, *Metall. Mater. Trans. A Phys. Metall. Mater. Sci.* 44 (2013) 3797–3808.
- [91] W. Kurz, D.J. Fisher, R. Trivedi, Progress in modelling solidification microstructures in metals and alloys: dendrites and cells from 1700 to 2000, *Int. Mater. Rev.* 64 (2019) 311–354.
- [92] W. Kurz, D.J. Fisher, Dendrite growth at the limit of stability: tip radius and spacing, *Acta Metall.* 29 (1981) 11–20.
- [93] K. Somboonsuk, J.T. Mason, R. Trivedi, Interdendritic Spacing: Part I. Experimental Studies., *Metall. Trans. A, Phys. Metall. Mater. Sci.* 15 A (1984) 967–975.
- [94] D. Ma, P.R. Sahm, Primary spacing in directional solidification, *Metall. Mater. Trans. A Phys. Metall. Mater. Sci.* 29 (1998) 1113–1119.
- [95] J.D. Hunt, Pattern formation in solidification, *Sci. Technol. Adv. Mater.* 2 (2001) 147–155.
- [96] J. Strickland, B. Nenchev, H. Dong, On directional dendritic growth and primary spacing—a review, *Crystals.* 10 (2020) 1–30.
- [97] C.C. Battalle, R.N. Grugel, A.B. Hmelo, T.G. Wang, The effect of enhanced gravity levels on microstructural development in Pb-50 wt pct Sn alloys during controlled directional solidification, *Metall. Mater. Trans. A.* 25 (1994) 865–870.

- [98] H.N. Thi, Y. Dabo, B. Drevet, M.D. Dupouy, D. Camel, B. Billia, J.D. Hunt, A. Chilton, Directional solidification of Al-1.5 wt% Ni alloys under diffusion transport in space and fluid-flow localisation on earth, *J. Cryst. Growth*. 281 (2005) 654–668.
- [99] C. Yang, Q. Xu, B. Liu, Study of dendrite growth with natural convection in superalloy directional solidification via a multiphase-field-lattice Boltzmann model, *Comput. Mater. Sci.* 158 (2019) 130–139.
- [100] T. Takaki, S. Sakane, M. Ohno, Y. Shibuta, T. Aoki, Large-scale phase-field lattice Boltzmann study on the effects of natural convection on dendrite morphology formed during directional solidification of a binary alloy, *Comput. Mater. Sci.* 171 (2020) 109209.
- [101] S. Steinbach, L. Ratke, The effect of rotating magnetic fields on the microstructure of directionally solidified Al-Si-Mg alloys, *Mater. Sci. Eng. A*. 413-414 (2005) 200-204.
- [102] S. Steinbach, L. Ratke, The influence of fluid flow on the microstructure of directionally solidified AlSi-base alloys, *Metall. Mater. Trans. A Phys. Metall. Mater. Sci.* 38 A (2007) 1388–1394.
- [103] S. Steinbach, L. Ratke, G. Zimmermann, L. Sturz, A. Roósz, J. Kovács, Y. Fautrelle, O. Budenkova, L. J., S. Dost, G. G.-U, N. Warnken, M. Wu, W.H. Sillekens, Investigation of the effect of fluid flow on microstructure evolution in Al-Si-Fe alloys: The MICAST project, *Proc. 5th Decenn. Int. Conf. Solidif. Process., Old Windsor*, (2017) 267–271.
- [104] J.D. Hunt, S.Z. Lu, Numerical modelling of cellular and dendritic array growth: spacing and structure predictions, *Metall. Mater. Trans. A*. 27A (1996) 611–623.
- [105] S. Steinbach, Einfluss von Strömungen auf die Entwicklung des Mikrogefüges bei der gerichteten Erstarrung von Al-Si und Al-Si-Mg Legierungen, Ph.D. thesis, 2005.
- [106] H. Neumann-Heyme, K. Eckert, C. Beckermann, General evolution equation for the specific interface area of dendrites during alloy solidification, *Acta Mater.* 140 (2017) 87–96.
- [107] D.H. Kirkwood, A simple model for dendrite arm coarsening during solidification, *Mater. Sci. Eng.* 73 (1985) L1.
- [108] D. Kammer, P.W. Voorhees, R. MENDOZA, J. ALKEMPER, P.W. Voorhees, D. Kammer, P.W. Voorhees, The morphological evolution of dendritic microstructures during coarsening, *Acta Mater.* 54 (2006) 1549–1558.
- [109] M.C. Flemings, Coarsening in solidification processing, *Mater. Trans.* 46 (2005) 895–900.
- [110] N. Limodin, L. Salvo, E. Boller, M. Suéry, M. Felberbaum, S. Gailliégue, K. Madi, In situ and real-time 3-D microtomography investigation of dendritic solidification in an Al-10 wt.% Cu alloy, *Acta Mater.* 57 (2009) 2300–2310.
- [111] T. Cool, P.W. Voorhees, The evolution of dendrites during coarsening: Fragmentation and morphology, *Acta Mater.* 127 (2017) 359–367.
- [112] L. Ratke, W.K. Thieringer, The influence of particle motion on ostwald ripening in liquids, *Acta Metall.* 33 (1985) 1793–1802.
- [113] H.J. Diepers, C. Beckermann, I. Steinbach, Simulation of convection and ripening in a binary alloy mush using the phase-field method, *Acta Mater.* 47 (1999) 3663–3678.
- [114] S. Steinbach, N. Euskirchen, V. Witusiewicz, L. Sturz, L. Ratke, The influence of fluid flow on intermetallic phases in al-cast alloys, *Mater. Sci. Forum*. 519–521 (2006) 1795–1800.
- [115] S. Steinbach, L. Ratke, Melt flow in a mushy zone - Barrier effect of intermetallic phases, *Int. J. Cast Met. Res.*, 22 (2009) 290–293.
- [116] S. Steinbach, L. Ratke, The effect of rotating magnetic fields on the microstructure of directionally solidified Al-Si-Mg alloys, *Mater. Sci. Eng. A*. 413–414 (2005) 200–204.
- [117] W.U. Mirihanage, H. Dai, H. Dong, D.J. Browne, Computational modeling of columnar to equiaxed transition in alloy solidification, *Adv. Eng. Mater.* 15 (2013) 216–229.
- [118] J.A. Spittle, Columnar to equiaxed grain transition in as solidified alloys, *Int. Mater. Rev.* 51 (2006) 247–269.
- [119] H. Nguyen-Thi, G. Reinhart, N. Mangelinck-Noël, H. Jung, B. Billia, T. Schenk, J. Gastaldi, J. Härtwig, J. Baruchel, In-Situ and real-time investigation of columnar-to-equiaxed transition in metallic alloy, *Metall. Mater. Trans. A Phys. Metall. Mater. Sci.* 38 A (2007) 1458–1464.
- [120] D.A. Pineda, M.A. Martorano, Columnar to equiaxed transition in directional solidification of inoculated melts, *Acta Mater.* 61 (2013) 1785–1797.
- [121] J.D. Hunt, Steady state columnar and equiaxed growth of dendrites and eutectic, *Mater. Sci. Eng.* 65 (1984) 75–83.
- [122] A. Mitchell, S.L. Cockcroft, T. Wang, Some observations on the columnar-to-equiaxed transition in nickel- base

superalloys, *High Temp. Mater. Process.* 24 (2005) 131–138.

- [123] I. Ziv, F. Weinberg, The columnar-to-equiaxed transition in Al 3 Pct Cu, *Metall. Trans. B.* 20 (1989) 731–734.
- [124] M. Gäumann, R. Trivedi, W. Kurz, Nucleation ahead of the advancing interface in directional solidification, *Mater. Sci. Eng. A.* 226–228 (1997) 763–769.
- [125] M.A. Martorano, C. Beckermann, C.A. Gandin, A solutal interaction mechanism for the columnar-to-equiaxed transition in alloy solidification, *Metall. Mater. Trans. A Phys. Metall. Mater. Sci.* 34 A (2003) 1657–1674.
- [126] J. Szajnar, M. Stawarz, T. Wróbel, W. Sebzda, Influence of electromagnetic field on pure metals and alloys structure, *Worldw. Congr. COMMENT.* 34 (2009) 95-102.
- [127] G. Zimmermann, C. Pickmann, E. Schaberger-Zimmermann, V. Galindo, K. Eckert, S. Eckert, Do rotating magnetic fields unconditionally lead to grain refinement? A case study for directionally solidified Al-10wt%Cu alloys, *Materialia.* 3 (2018) 326–337.
- [128] A. Rónaföldi, J. Kovács, A. Roósz, A suggested effective method for unidirectional solidification under rotating magnetic field in the space experiments, *Trans. Indian Inst. Met.* 62 (2009) 475–477.
- [129] G. Zimmermann, A. Weiss, Z. Mbaya, Effect of forced melt flow on microstructure evolution in AlSi7Mg0.6 alloy during directional solidification, *Mater. Sci. Eng. A.* 413–414 (2005) 236–242.
- [130] Z. Fan, G. Liu, Solidification behaviour of AZ91D alloy under intensive forced convection in the RDC process, *Acta Mater.* 53 (2005) 4345–4357.
- [131] W.D. Griffiths, D.G. McCartney, The effect of electromagnetic stirring during solidification on the structure of Al-Si alloys, *Mater. Sci. Eng. A.* 216 (1996) 47–60.
- [132] D.R. Liu, G. Reinhart, N. Mangelinck-Noel, C.A. Gandin, H. Nguyen-Thi, B. Billia, Coupled Cellular Automaton (CA) - Finite Element (FE) Modeling of Directional Solidification of Al-3.5 wt% Ni Alloy: A Comparison with X-ray Synchrotron Observations, *ISIJ Int.* 54 (2014) 392–400.
- [133] M. Wu, A. Ludwig, Using a three-phase deterministic model for the columnar-to-equiaxed transition, *Metall. Mater. Trans. A Phys. Metall. Mater. Sci.* 38 A (2007) 1465–1475.
- [134] M. Bedel, K.O. Tveito, M. Založnik, H. Combeau, M. M'Hamdi, A model study of the impact of the transport of inoculant particles on microstructure formation during solidification, *Comput. Mater. Sci.* 102 (2015) 95–109.
- [135] D.R. Liu, ScienceDirect Simulation of directional solidification of refined Al – 7 wt. % Si alloys – Comparison with benchmark microgravity experiments, 93 (2015) 24–37.
- [136] G. Zimmermann, L. Sturz, H. Nguyen-Thi, N. Mangelinck-Noel, Y.Z. Li, C.A. Gandin, R. Fleurisson, G. Guillemot, S. McFadden, R.P. Mooney, P. Voorhees, A. Roosz, A. Ronaföldi, C. Beckermann, A. Karma, C.H. Chen, N. Warnken, A. Saad, G.U. Grün, M. Grohn, I. Poitraul, T. Pehl, I. Nagy, D. Todt, O. Minster, W. Sillekens, Columnar and Equiaxed Solidification of Al-7 wt.% Si Alloys in Reduced Gravity in the Framework of the CETSOL Project, *Jom.* 69 (2017) 1269–1279.
- [137] D.R. Liu, N. Mangelinck-Noël, C.A. Gandin, G. Zimmermann, L. Sturz, H. Nguyen Thi, B. Billia, Structures in directionally solidified Al-7 wt.% Si alloys: Benchmark experiments under microgravity, *Acta Mater.* 64 (2014) 253–265.
- [138] R.S. Rerko, H.C. de Groh, C. Beckermann, Effect of melt convection and solid transport on macrosegregation and grain structure in equiaxed Al-Cu alloys, *Mater. Sci. Eng. A.* 347 (2003) 186–197.
- [139] Y.Z. Li, N. Mangelinck-Noël, G. Zimmermann, L. Sturz, H. Nguyen-Thi, Modification of the microstructure by rotating magnetic field during the solidification of Al-7 wt.% Si alloy under microgravity, *J. Alloys Compd.* 836 (2020) 155458.
- [140] J.W. Gao, C.Y. Wang, An experimental investigation into the effects of grain transport on columnar to equiaxed transition during dendritic alloy solidification, *J. Heat Transfer.* 121 (1999) 430–437.
- [141] Y. Zheng, M. Wu, A. Kharicha, A. Ludwig, Numerical analysis of macrosegregation in vertically solidified Pb-Sn test castings – Part II: Equiaxed solidification, *Comput. Mater. Sci.* 124 (2016) 456–470.
- [142] W. Kurz, M. Rappaz, R. Trivedi, Progress in modelling solidification microstructures in metals and alloys. Part II: dendrites from 2001 to 2018, *Int. Mater. Rev.* 0 (2020) 1–47.
- [143] M.S. Bhat, D.R. Poirier, J.C. Heinrich, Permeability for cross flow through columnar-dendritic alloys, *Metall. Mater. Trans. B.* 26 (1995) 1049–1056.
- [144] T. Takaki, T. Shimokawabe, M. Ohno, A. Yamanaka, T. Aoki, Unexpected selection of growing dendrites by very-large-scale phase-field simulation, *J. Cryst. Growth.* 382 (2013) 21–25.
- [145] <https://docs.micress.rwth-aachen.de/micress/examples/flow/>, (n.d.).

- [146] A. Ludwig, A. Kharicha, C. Hölzl, J. Domitner, M. Wu, T. Pusztai, 3D Lattice Boltzmann flow simulations through dendritic mushy zones, *Eng. Anal. Bound. Elem.* 45 (2014) 29–35.
- [147] J.C. Ramirez, C. Beckermann, Evaluation of a rayleigh-number-based freckle criterion for Pb-Sn alloys and Ni-base superalloys, *Metall. Mater. Trans. A Phys. Metall. Mater. Sci.* 34 A (2003) 1525–1536.
- [148] P.C. Carman, Fluid flow through granular beds, 75 (1937) S32-S48.
- [149] N. Streat, F. Weinberg, Interdendritic fluid flow in a lead-tin alloy, *Metall. Trans. B.* 7 (1976) 417–423.
- [150] K. Murakami, A. Shiraishi, T. Okamoto, Interdendritic fluid flow normal to primary dendrite-arms in cubic alloys, *Acta Metall.* 31 (1983) 1417–1424.
- [151] K. Murakami, A. Shiraishi, T. Okamoto, Fluid flow in interdendritic space in cubic alloys, *Acta Metall.* 32 (1984) 1423–1428.
- [152] R. Nasser-Rafi, R. Deshmukh, D.R. Poirier, Flow of interdendritic liquid and permeability in pb-20 Wt Pct Sn alloys, *Metall. Trans. A.* 16 (1985) 2263–2271.
- [153] D.R. Poirier, Permeability for flow of interdendritic liquid in columnar-dendritic alloys, *Metall. Trans. B.* 18 (1987) 245–255.
- [154] R.G. Santos, M.L.N.M. Melo, Permeability of interdendritic channels, *Mater. Sci. Eng. A.* 391 (2005) 151–158.
- [155] C. Puncreobutr, A.B. Phillion, J.L. Fife, P.D. Lee, Coupling in situ synchrotron X-ray tomographic microscopy and numerical simulation to quantify the influence of intermetallic formation on permeability in aluminium-silicon-copper alloys, *Acta Mater.* 64 (2014) 316–325.
- [156] X. Zhang, J. Kang, Z. Guo, Q. Han, Effect of the forced flow on the permeability of dendritic networks: A study using phase-field-lattice Boltzmann method, *Int. J. Heat Mass Transf.* 131 (2019) 196–205.
- [157] M.C. Schneider, C. Beckermann, A numerical study of the combined effects of microsegregation, mushy zone permeability and flow, caused by volume contraction and thermosolutal convection, on macrosegregation and eutectic formation in binary alloy solidification, *Int. J. Heat Mass Transf.* 38 (1995) 3455–3473.
- [158] J.C. Heinrich, D.R. Poirier, Convection modeling in directional solidification, *Comptes Rendus - Mec.* 332 (2004) 429–445.
- [159] A. Kumar, M. Založnik, H. Combeau, Study of the influence of mushy zone permeability laws on macro- and meso-segregations predictions, *Int. J. Therm. Sci.* 54 (2012) 33–47.
- [160] J.A. Taylor, Iron-Containing Intermetallic Phases in Al-Si Based Casting Alloys, *Procedia Mater. Sci.* 1 (2012) 19–33.
- [161] S. Terzi, J.A. Taylor, Y.H. Cho, L. Salvo, M. Suéry, E. Boller, A.K. Dahle, In situ study of nucleation and growth of the irregular α -Al/ β -Al₅FeSi eutectic by 3-D synchrotron X-ray microtomography, *Acta Mater.* 58 (2010) 5370–5380.
- [162] P. Mikołajczak, L. Ratke, Directional solidification of alsi alloys with Fe intermetallic phases, *Arch. Foundry Eng.* 14 (2014) 75–78.
- [163] P. Mikołajczak, L. Ratke, Interplay Between Melt Flow and the 3D Distribution and Morphology of Fe-Rich Phases in AlSi Alloys, *Metall. Mater. Trans. A Phys. Metall. Mater. Sci.* 46 (2015) 1312–1327.
- [164] S. Steinbach, L. Ratke, G. Zimmermann, O. Budenkova, Formation of intermetallic phases in AlSi₇Fe₁ alloy processed under microgravity and forced fluid flow conditions and their influence on the permeability, *IOP Conf. Ser. Mater. Sci. Eng.*, 117 (2016) 012019.
- [165] C.M. Dinnis, J.A. Taylor, A.K. Dahle, Iron-related porosity in Al-Si-(Cu) foundry alloys, *Mater. Sci. Eng. A.* 425 (2006) 286–296.
- [166] M. Dash, M. Makhlof, Effect of key alloying elements on the feeding characteristics of aluminum-silicon casting alloys, *J. Light Met.* 1 (2001) 251–265.
- [167] C. Puncreobutr, P.D. Lee, K.M. Kareh, T. Connolley, J.L. Fife, A.B. Phillion, Influence of Fe-rich intermetallics on solidification defects in Al-Si-Cu alloys, *Acta Mater.* 68 (2014) 42–51.
- [168] P. Mikołajczak, L. Ratke, Effect of stirring induced by rotating magnetic field on β -Al₅FeSi intermetallic phases during directional solidification in AlSi alloys, *Int. J. Cast Met. Res.* 26 (2013) 339–353.
- [169] S. Sakane, T. Takaki, M. Ohno, Y. Shibuta, T. Aoki, Two-dimensional large-scale phase-field lattice Boltzmann simulation of polycrystalline equiaxed solidification with motion of a massive number of dendrites, *Comput. Mater. Sci.* 178 (2020) 109639.
- [170] G. Britain, Fluid flow in the mushy zone composed of granular grains, 32 (1984) 1741–1744.
- [171] D.R. Poirier, S. Ganesan, Permeabilities for flow of interdendritic liquid in equiaxial structures, *Mater. Sci. Eng.*

A. 157 (1992) 113–123.

- [172] Nielsen, L. Arnberg, A. Mo, H. Thevik, Experimental determination of mushy zone permeability in aluminum-copper alloys with equiaxed microstructures, *Metall. Mater. Trans. A Phys. Metall. Mater. Sci.* 30 (1999) 2455–2462.
- [173] E. Khajeh, D.M. Maijer, Permeability evolution during equiaxed dendritic solidification of Al-4.5 wt%Cu, *Model. Simul. Mater. Sci. Eng.* 20 (2012).
- [174] E. Khajeh, D.M. Maijer, Permeability of dual structured hypoeutectic aluminum alloys, *Acta Mater.* 59 (2011) 4511–4524.
- [175] T. Takaki, S. Sakane, M. Ohno, Y. Shibuta, T. Aoki, Permeability prediction for flow normal to columnar solidification structures by large-scale simulations of phase-field and lattice Boltzmann methods, *Acta Mater.* 164 (2019) 237–249.
- [176] M. Wu, Y. Zheng, A. Kharicha, A. Ludwig, Numerical analysis of macrosegregation in vertically solidified Pb-Sn test castings – Part I: Columnar solidification, *Comput. Mater. Sci.* 124 (2016) 444–455.
- [177] J. Kovács, A. Rónaföldi, Á. Kovács, A. Roósz, Effect of the rotating magnetic field on the unidirectionally solidified macrostructure of Al6Si4Cu alloy, *Trans. Indian Inst. Met.* 62 (2009) 461–464.
- [178] S. Eckert, P.A. Nikrityuk, D. Rábiger, K. Eckert, G. Gerbeth, Efficient melt stirring using pulse sequences of a rotating magnetic field: Part I. flow field in a liquid metal column, *Metall. Mater. Trans. B Process Metall. Mater. Process. Sci.* 38 (2007) 977–988.
- [179] Y. Zheng, M. Wu, E. Karimi-Sibaki, A. Kharicha, A. Ludwig, Use of a mixed columnar-equiaxed solidification model to analyse the formation of as-cast structure and macrosegregation in a Sn-10 wt% Pb benchmark experiment, *Int. J. Heat Mass Transf.* 122 (2018) 939–953.
- [180] J. Ni, C. Beckermann, A volume-averaged two-phase model for transport phenomena during solidification, *Metall. Trans. B.* 22 (1991) 349–361.

Part II:

Papers included in this thesis ([hyperlinked to the pdf-file of each article](#)):

- [1] **H. Zhang**, M. Wu, Y. Zheng, A. Ludwig, A. Kharicha, [Macroseggregation Formation in an Al–Si Casting Sample with Cross-sectional Change During Directional Solidification](#), Trans. Indian Inst. Met. 71 (2018) 2639–2643.
- [2] **H. Zhang**, M. Wu, Y. Zheng, A. Ludwig, A. Kharicha, [Numerical study of the role of mush permeability in the solidifying mushy zone under forced convection](#), Mater. Today Commun. 22 (2020) 100842.
- [3] **H. Zhang**, M. Wu, S.N. Tewari, A. Ludwig, A. Kharicha, [Geometrical effect on macroseggregation formation during unidirectional solidification of Al–Si alloy](#), J. Mater. Process. Technol. 288 (2020) 116913.
- [4] **H. Zhang**, M. Wu, C. Rodrigues, A. Ludwig, A. Kharicha, [Directional solidification of AlSi7Fe1 alloy under forced flow conditions: effect of intermetallic phase precipitation and dendrite coarsening](#), Metall. Mater. Trans. A. 2021.
- [5] **H. Zhang**, M. Wu, P. Schumacher, C. Rodrigues, A. Ludwig, A. Kharicha, [Modelling melting and grain destruction phenomena during globular equiaxed solidification](#), Appl. Math. Model. 2021.

Author's contribution table

	Idea	Model & simulation	Result analysis	Paper writing
Publication I	90%	90%	80%	80%
Publication II	80%	90%	80%	80%
Publication III	90%	90%	90%	80%
Publication IV	90%	90%	80%	80%
Publication V	80%	90%	90%	80%

Papers not included in this thesis:

- [1] H. Zhang, M. Wu, Y. Zheng, A. Ludwig, A. Kharicha, [Numerical simulation of fluid flow in the mushy zone under rotation magnetic field: influence of permeability](#), 7th Int. Conf. Solidification and Gravity (SG 2018), Miskolc, Hungary, pp. 265-270.
- [2] H. Zhang, M. Wu, Z. Zhang, A. Ludwig, A. Kharicha, [Influence of crystal fragmentation on the formation of microstructure and macrosegregation during directional solidification under forced convection condition](#), IOP Conf. Ser. Mater. Sci. Eng. 861 (2020) 012048.
- [3] Z. Zhang, M. Wu, H. Zhang, E. Karimi-Sibaki, A. Ludwig, A. Kharicha, [Modeling mixed columnar-equiaxed solidification of Sn-10wt%Pb alloy under forced convection driven by travelling magnetic stirring](#), IOP Conf. Ser. Mater. Sci. Eng. 861 (2020) 012024.
- [4] C. Rodrigues, M. Wu, H. Zhang, A. Ludwig, A. Kharicha, Bridging capillary-driven fragmentation and grain transport with mixed columnar-equiaxed solidification, Metall. Mater. Trans. A. 2021. Under review.
- [5] Z. Zhang, M. Wu, H. Zhang, A. Ludwig, A. Kharicha, The role of mold electromagnetic stirring (M-EMS) in the dissipation of superheat in the mold region of billet continuous casting, STEELSIM (2021), Vienna, Austria. Submitted.

Macroseggregation Formation in an Al–Si Casting Sample with Cross-sectional Change During Directional Solidification

Haijie Zhang¹ · Menghuai Wu¹ · Yongjian Zheng¹ · Andreas Ludwig¹ · Abdellah Kharicha¹

Received: 11 July 2018 / Accepted: 6 September 2018
© The Author(s) 2018

Abstract A unidirectional solidification experiment of hypoeutectic Al-7.0 wt% Si alloy against gravity direction in a cylindrical mold with cross-sectional change was made, and the macroseggregation in different parts of the as-solidified sample was investigated (Ghods et al. in *J Cryst Growth* 441:107–116, 2016; *J Cryst Growth* 449:134–147, 2016). The current study is to use a two-phase columnar solidification model to analyze the segregation mechanisms as used in this experiment. Following flow phenomena and their contributions to the formation of macroseggregation are simulated and compared: (1) solidification shrinkage-induced feeding flow; (2) thermo-solutal convection; and (3) combined thermo-solutal convection and shrinkage-induced feeding flow. The shrinkage-induced feeding flow leads to an inverse (positive) segregation in the bottom part, and a severe negative segregation in the part below cross-sectional change. Thermo-solutal buoyancy leads to a so-called steeping convection in the main part of the sample (away from the bottom and cross-sectional change), and this kind of flow leads to a positive macroseggregation near the sample surface. The calculations have successfully explained the experimental result of macroseggregation.

Keywords Macroseggregation · Fluid flow · Shrinkage · Directional solidification

✉ Menghuai Wu
menghuai.wu@unileoben.ac.at

¹ Chair for Simulation and Modeling of Metallurgy Processes, Department of Metallurgy, University of Leoben, 8700 Leoben, Austria

1 Introduction

Macroseggregation is caused by different flow phenomena during solidification [1–3]. To improve understanding of the macroseggregation mechanisms, unidirectional solidification experiments, based on Al–Si and Al–Cu alloys, were recently performed by Ghods [4–6]. One special feature of these experiments is that the cylindrical casting sample is designed with a cross-sectional change. Therefore, following flows and their impact on the macroseggregation formation can be quantitatively investigated: the solidification shrinkage-induced feeding flow, the thermo-solutal convection, and the flow pattern as caused by the section-change. The as-solidified structure is dominantly columnar. The current paper is to use a two-phase solidification model to “reproduce” the above experiments, with a focus on the Al-7.0 wt%Si alloy.

2 Simulation Settings

A volume-average-based solidification model has been introduced previously [7–9]. Here only two phases are considered: liquid and columnar. Fluid flow in the mushy zone is approximated with the Darcy’s law, with its permeability being treated as a function of the primary dendrite arm space, $\lambda_1 = 500 \mu\text{m}$ [4]. The columnar phase develops from the bottom of the sample, growing in the direction of temperature gradient. The feeding flow is due to the density difference between the liquid ($\rho_\ell = 2408 \text{ kg/m}^3$) and solid ($\rho_s = 2545 \text{ kg/m}^3$). The Boussinesq approximation has been employed to calculate the thermo-solutal convection, with the solutal (β_c) and thermal (β_T) expansion coefficients, $1.31 \times 10^{-3} \text{ wt}\%^{-1}$ and $-1.8 \times 10^{-4} \text{ K}^{-1}$, respectively. Temperature fields in the casting sample and in the mold

(graphite) are calculated, and an ideal mold-alloy contact is assumed for the heat transfer boundary condition.

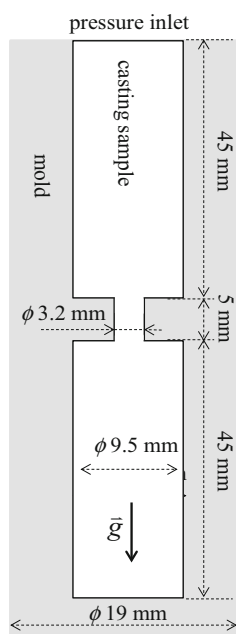
As shown in Fig. 1, a graphite mold with section change is considered. The casting domain is filled with liquid melt of initial composition (Al—7.0 wt% Si). Both the casting and mold are initialized with a uniform temperature (1490 K). The sample solidifies directionally with a fixed growth speed (29.1 $\mu\text{m/s}$) and temperature gradient ($G = 5100 \text{ K/m}$). Other simulation settings are consistent with Ghods' experiments [4, 6]. Material properties refer to Ref. [4]. Two cases have been simulated: Case 1—solidification with the shrinkage-induced feeding flow only; and Case 2—solidification with combination of thermo-solutal convection and shrinkage-induced feeding flow. All simulations are performed in 2D axisymmetric, and a very fine mesh ($\Delta x = 0.2 \text{ mm}$) and a small time step ($\Delta t = 0.002 \text{ s}$) have been used.

3 Results and Discussions

3.1 Case 1: Macroseggregation Caused by Shrinkage-Induced Feeding Flow Only

Figure 2 shows the evolution of macroseggregation in the bottom region of sample (far away from the region of section change). As an ideal unidirectional solidification casting condition is applied at this initial stage of solidification, a so-called reverse segregation develops in the casting surface region (bottom). This work is to “reproduce” the early analytical solution of Flemings' [10]. As the initially formed columnar structure at the sample

Fig. 1 Geometry of the simulation domain



bottom is stationary, the solute-enriched melt in the mushy zone feeds the solidification shrinkage, leading to an increase in the mixture concentration (c_{mix}) of the surface region. The maximum c_{mix} reaches to 0.0703, in comparison with the initial value of 0.07 (c_0). The magnitude of feeding flow is small (Fig. 2b). In the region of uniform cross section (far away from the cross-sectional change), average velocity is 1.3 $\mu\text{m/s}$, which reduces gradually to zero in the mushy zone. The maximum velocity (ca. 10 $\mu\text{m/s}$) occurs in the region of cross section change of the sample. When the solidification proceeds to a steady state, e.g., at 900 s, the change of c_{mix} in the mushy zone (from initial value of c_0 to the minimum (0.06985) and then recovering to c_0), follows the typical evolution profile of c_{mix} in the mushy zone of constant thickness [3, 10].

As the solidification front proceeds into the region of cross-sectional change (reduction) at 1800 s, the magnitude of feeding flow reaches to 11 $\mu\text{m/s}$, as shown in Fig. 3. A typical divergent flow pattern develops in the region below the cross-sectional reduction, leading to the formation of a strong negative ($c_{\text{mix}} < c_0$) segregation in Zones I and II. The negative segregation extreme is about $c_{\text{mix}} = 0.0675$ (Fig. 3b). Just below the shadow of the cross-sectional reduction (Zone III), a positive segregation forms, because the solidification shrinkage there needs to be fed by the solute-enriched melt.

3.2 Case 2: Macroseggregation Caused by a Combination of Thermo-Solutal Convection and Shrinkage-Induced Feeding Flow

As the thermo-solutal convection is considered, the magnitude of the liquid velocity is increased by 1–2 orders of magnitude, especially in the bulk region, i.e., the effect of flow on the macroseggregation formation is dominated by the thermo-solutal convection. At the initial stage ($t = 366 \text{ s}$) of solidification in the bottom region of sample, Fig. 4a, a clockwise vortex (right half of the sample) is developed just ahead of solidification front. Although the isotherms seem almost flat, the latent heat released by solidifying the first layer of solid from the bottom sample can only be extracted by the graphite mold, leading to the outward heat flux and inward flow pattern. The solute rejected from the columnar dendrite mushy zone is swept to the center of the sample, which enriches the c_{mix} in the center part of the sample and depletes the c_{mix} near the sample surface.

As solidification proceeds to a later stage ($t = 1666 \text{ s}$), Fig. 4b, the flow pattern changes. A quite portion of sample is solidified from the bottom sample. The thermal diffusivity (185 W/mK) of the solid phase is roughly two times bigger than that (76.7 W/mK) of the liquid. Now, the

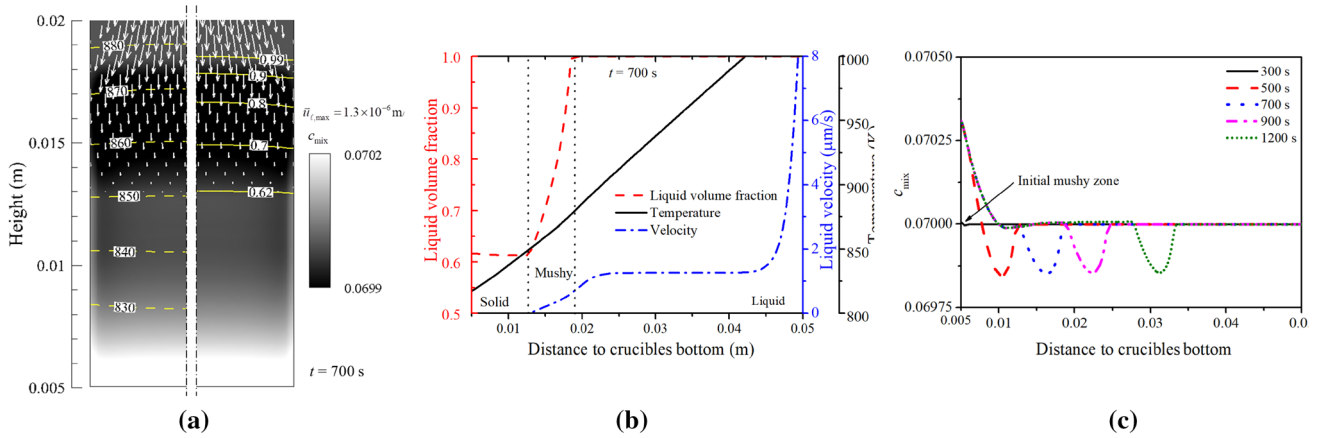
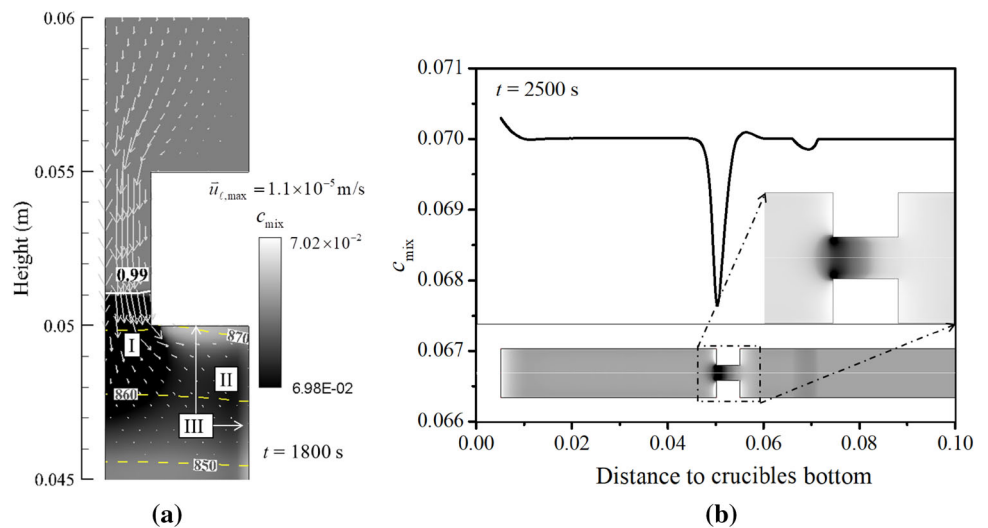


Fig. 2 Analysis of the inverse segregation in the bottom of the sample Case 1. **a** The mixture concentration (c_{mix}) in gray scale at 700 s, overlaid with the liquid velocity in vectors, isotherms (left) and isolines of volume fraction liquid (right); **b** distribution profiles of volume fraction of liquid, temperature and liquid velocity along the axis at 700 s; **c** evolution of macrosegregation (c_{mix}) along the axis

Fig. 3 Analysis of macrosegregation formation in the region of cross-sectional change for Case 1. **a** The mixture concentration (c_{mix}) in gray scale at 1800 s, overlaid with the liquid velocity in vectors and isotherms (the solidification front is indicated by a white solid line $f_l = 0.99$); **b** c_{mix} profile along the axis at $t = 2500$ s



isotherms are no longer flat, and the solidification front is bulged in the sample center. A so-called steeping convection is developed, i.e., the flow goes downward against the solidification front in the sample center and upward along the sample outer surface. Enriched solute in the mushy zone is swept to the periphery of the sample, leading to a positive segregation in the outer region of the casting surface and negative segregation in the casting center. The bulged solidification front in the sample center is the outcome of the macrosegregation: The denser solute-enriched melt concentrated in the periphery of the sample inhibits the solidification there.

Final segregation profiles along the radial and axial directions of the sample are shown in Fig. 5. The calculated segregation profile along the radial direction is found to agree almost perfectly with the experimentally measured result [4], except for one point at the casting surface. This

is the only disagreement point at the sample surface which may be due to the experimental measurement method which has exaggerated the positive segregation there, or may be due to numerical model which has underestimated positive segregation by missing some other mechanisms.

It is worth mentioning that a further simulation (Case 3) is made, i.e., the macrosegregation is caused by the thermo-solutal convection only (ignoring the shrinkage-induced feeding flow), which is compared with Case 2, as shown in Fig. 5b. The macrosegregation mechanism due to the thermo-solutal convection is dominant. The shrinkage-induced feeding flow enhances the negative segregation (or reduces the positive segregation) near the region of cross-sectional change.

Fig. 4 Analysis of macrosegregation formation for Case 2. **a** c_{mix} distribution in gray scale at $t = 366$ s, overlaid with liquid velocity in vectors and isotherms. **b** c_{mix} distribution in gray scale at $t = 1666$ s, overlaid with liquid velocity in vectors, isolines of c_{mix} (left half) and isolines of liquid volume fraction (right half)

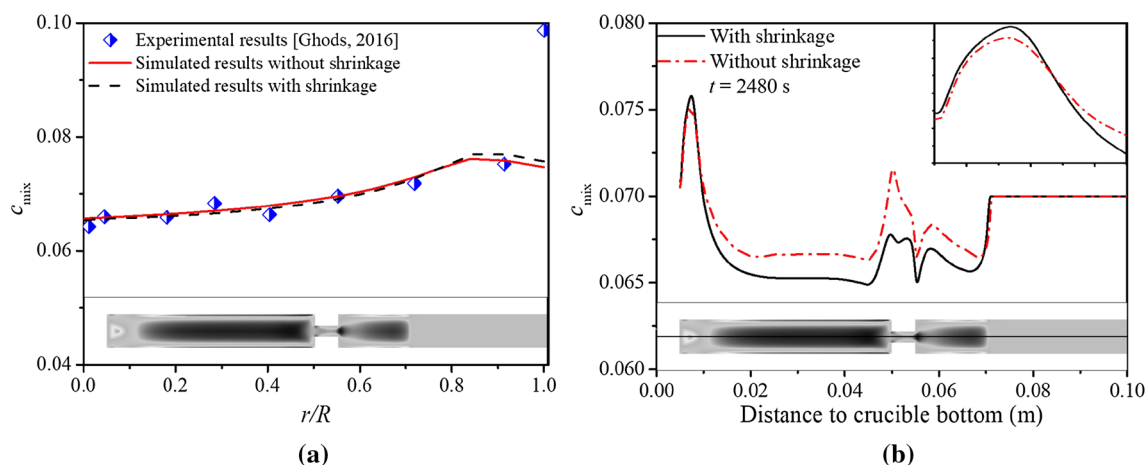
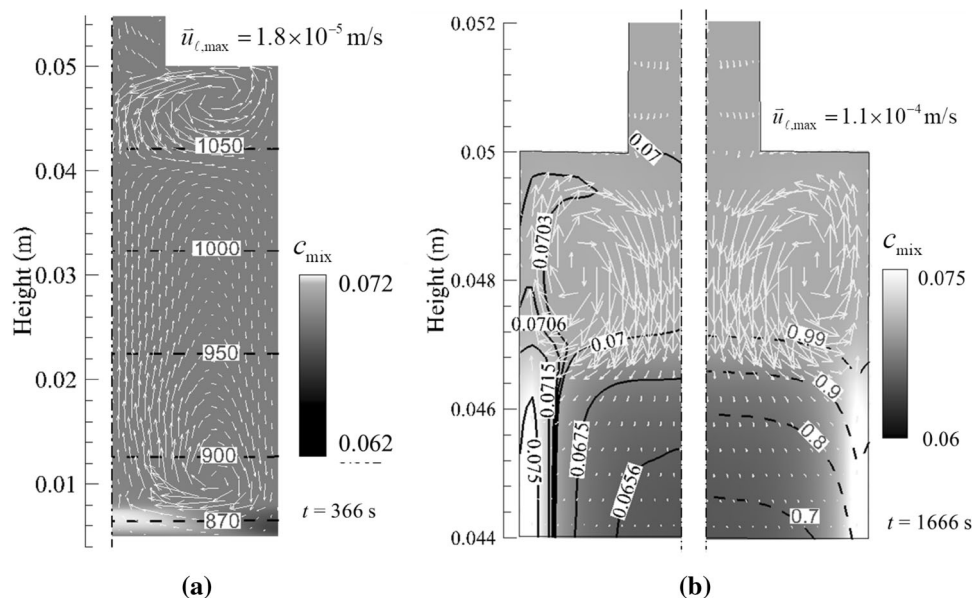


Fig. 5 Final macrosegregation (c_{mix}) profiles along the radial **(a)** and axial **(b)** directions for Case 2. Comparison of the segregation profiles along the radial direction between simulation and experiment [4] is made

4 Conclusions

A two-phase solidification model has been used to “reproduce” the unidirectional solidification experiment with the Al-7.0 wt%Si alloy and a casting sample of cross-sectional change, as carried out by Ghods [4]. Numerical parameter studies have been made by considering different flow mechanisms. When only shrinkage-induced feeding flow is considered, the typical inverse macrosegregation in the sample bottom and a relatively strong negative segregation in the region below the cross-sectional change are predicted, which agrees with the classical work of Flemings [10]. Thermo-solutal buoyancy leads to a so-called steeping convection in the main part of the sample (away from the bottom and the region of cross-sectional change), and this kind of flow leads to a negative segregation in the

sample center and positive macrosegregation in the periphery of the sample, which agrees with the experiment of Ghods [4].

5 Acknowledgements

Open access funding has been provided by Montanuniversität Leoben. The authors acknowledge the financial support from Austrian Research Promotion Agency (FFG)-Austrian Space Application Program (ASAP) through the project FLOWSICONS (No. 859777), as well as the support from European Space Agency (ESA) through the project MICAST.

Open Access This article is distributed under the terms of the Creative Commons Attribution 4.0 International License (<http://creativecommons.org/licenses/by/4.0/>), which permits unrestricted use, distribution, and reproduction in any medium, provided you give appropriate credit to the original author(s) and the source, provide a link to the Creative Commons license, and indicate if changes were made.

References

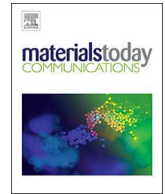
1. Flemings M C, *Trans Iron Steel Inst Jpn* **40** (2000) 838.
2. Beckermann C, *Metall Rev* **47** (2002) 243.
3. Ludwig A, Wu M, and Kharicha A, *Metall Mater Trans A* **46** (2015) 4854.
4. Ghods M, Johnson L, and Lauer M, *J Cryst Growth* **441** (2016) 107.
5. Ghods M, Johnson L, and Lauer M, *J Cryst Growth* **449** (2016) 134.
6. Ghods M, Lauer M, and Grugel R N, *J Mater Eng Perform* **26** (2017) 1.
7. Li J, Wu M, and Kharicha A, *Comput Mater Sci* **55** (2012) 419.
8. Li J, Wu M, and Kharicha A, *Comput Mater Sci* **55** (2012) 407.
9. Wu M, Zheng Y, A, and Kharicha, *Comput Mater Sci* **124** (2016) 444.
10. Flemings M C, and Nereo G E, *Trans Metall Soc AIME* **242** (1968) 41.



ELSEVIER

Contents lists available at ScienceDirect

Materials Today Communications

journal homepage: www.elsevier.com/locate/mtcomm

Numerical study of the role of mush permeability in the solidifying mushy zone under forced convection

Haijie Zhang, Menghuai Wu*, Yongjian Zheng, Andreas Ludwig, Abdellah Kharicha

Montanuniversitaet Leoben, Austria

ARTICLE INFO

Keywords:

Fluid flow
Permeability
Mushy zone
Macrosegregation
Rotating magnetic field

ABSTRACT

Permeability of the mushy zone during alloy solidification is an important modeling parameter for many phenomena which accompany solidification, such as the formation of macrosegregation, shrinkage porosity, hot tearing, etc. The current study incorporates a two-phase, volume-average based columnar solidification model to study the role of mush permeability in the solidifying mushy zone under forced convection conditions. A unidirectional solidification of Al-7.0 wt %Si alloy sample (cylindrical with a diameter of 8 mm), referring to the experiments of MICAST project [Ratke, et al., MICAST research report – Phase IV, ESA-MAP AO-99-031, 2013], is considered. The forced convection is applied with a rotating magnetic field (20 m T). The basic permeability law for the numerical model is derived from Carman-Kozeny, but it has been modified by an artificial factor for the parameter study. The modeling results show that (1) the thickness of the mushy zone decreases and (2) the global macrosegregation intensity increases monotonically with growing permeability. A special macrosegregation profile resembling a “Christmas tree”, as typically observed experimentally, could also be numerically predicted. However, the formation of the “Christmas tree” segregation profile depends strongly on the permeability of the material. The formation mechanism of “Christmas tree” segregation can be analyzed according to the flow-solidification interaction in the mushy zone. A quantitative determination of the permeability, depending on the dendritic structure of the mushy zone, is beyond the scope of the current study, nevertheless it also includes a brief discussion (literature review) on this topic.

1. Introduction

The interaction between the melt flow and developing mushy zone during solidification is still an issue that is not yet completely understood, although it plays an important role in the formation of microstructures and many other associated phenomena like macrosegregation, shrinkage porosity, hot tearing, etc. [1–4]. To investigate this flow-solidification interaction, a series of unidirectional solidification experiments on the Al-Si alloy system in the framework of the project MICAST (Microstructure Formation in Casting of Technical Alloys under Diffusive and Magnetically Convection Condition, supported by Europe Space Agency) were performed on Earth and in space [4–7]. A central Si-segregation in the shape of “Christmas tree” forms as the induction of the rotating magnetic field (RMF) becomes more intense, [6,7]. This “Christmas tree” segregation is characterized by a distinct accumulation of solute element (Si) along the axis of the sample, accompanied by many side-arms. Hereafter we also refer to the “Christmas tree” segregation as a central segregation channel with side-arms. A tentative explanation to this phenomenon would be that the

solute rejected from the mushy zone was captured by multiple traveling Taylor-Görtler (T-G) vortices and brought back to the mushy zone [6]. Noepfel et al. [8] studied the effects of both rotating and travelling magnetic fields on macrosegregation during directional solidification, and suggested that the side-arms of the “Christmas tree” might form at the junction of two meridional T-G vortices ahead of the mushy zone. Similar studies were conducted by Budenkova et al. [9], but they found that the origins of the “Christmas tree” side-arms seem to occur independently of the T-G vortices. This is because the formation frequency of T-G vortices differs from the formation frequency of the segregation side-arms.

One parameter used to characterize the fluid flow in the mushy zone is permeability, which is normally described as a function of the liquid volume fraction and dendritic morphology of crystals in the mush (λ_1 and/or λ_2) [10–12]. The role of mush permeability in the formation of meso- or macro-segregation under natural convection conditions was studied as follows: the experimentally-reported macrosegregation pattern could only be modelled when a proper mush permeability law is implemented [13]; the formation of meso-segregation seems more

* Corresponding author at: Department of Metallurgy, Montanuniversitaet Leoben, Franz-Josef Street 18, A-8700, Leoben, Austria.

E-mail address: menghuai.wu@unileoben.ac.at (M. Wu).

<https://doi.org/10.1016/j.mtcomm.2019.100842>

Received 11 October 2019; Received in revised form 11 December 2019; Accepted 11 December 2019

Available online 19 December 2019

2352-4928/ © 2019 Elsevier Ltd. All rights reserved.

sensitive to the mush permeability than the formation of macrosegregation [14]. However, the influence of mush permeability on the mushy zone itself (e.g. mushy zone thickness), especially under forced convection conditions, is not yet sufficiently understood.

This paper presents a two-phase volume-average based solidification model, developed by Wu et al. [15–18], to simulate the unidirectional solidification of the binary Al-7.0 wt.%Si alloy under the conditions of RMF and nature convection. The main goal is to investigate the role of permeability in the formation of dendritic mushy zone (thickness) and macrosegregation. The formation mechanism of the “Christmas tree” segregation is analyzed in detail.

2. Numerical model and simulation settings

The two-phase volume-average based solidification model has already been described elsewhere [15–18]. The main features of the model and some assumptions are outlined below.

- (1) The two phases refer to the liquid melt and columnar dendrite trunks as a solid phase. Both the liquid and solid phases are quantified by their volume fractions.
- (2) The morphology of the columnar trunks is approximated as stepwise cylinders, growing unidirectionally along temperature gradient. The primary dendrites' arm spacing, λ_1 , taken from the as-solidified structure, is assumed to be constant during solidification. The columnar tip front is traced according to LGK model [19].
- (3) The net mass transfer rate from liquid to solid due to solidification is calculated according to the lateral growth speed of the columnar trunks, which is governed by the solute diffusion in the interdendritic melt around the columnar trunks.
- (4) Volume-averaged concentrations of both liquid and solid phases are calculated. Macrosegregation is characterized by the mixture concentration among the liquid and solid. A thermodynamic equilibrium is assumed at the solid-liquid interface to determine the interfacial concentration. The concentration difference between the liquid thermodynamic equilibrium at the solid-liquid interface and the volume-averaged concentration in the interdendritic liquid is the driving force for the growth of columnar trunks. Back diffusion in the solid phase is not considered for the purpose of this study.
- (5) A linearized binary Al-Si phase diagram with a constant liquidus slope and solute partition coefficient is considered.
- (6) Fluid flow resistance through the mushy zone is calculated by means of a permeability law, referring to the Carman-Kozeny approach. For the purpose of conducting a numerical parameter study, it arbitrarily increases/decreases by orders of magnitude.
- (7) Solidification shrinkage is not considered, and thermo-solutal convection is modelled with the Boussinesq approach.

The configuration of the sample is shown in Fig. 1. The cylindrical geometry, the alloy (Al-7.0 wt.% Si) and the cooling conditions are taken from published work [9,20]. The alloy sample solidifies in an Al_2O_3 crucible directionally. The initial concentration (c_0) is set to be homogeneous in the sample. The initial temperature (T_0) of the liquid is set at 1190 K. On the top and bottom of the sample, a decreasing temperature is imposed T_{Top} and T_{Bottom} . As demonstrated in Fig. 1, before $t = 100$ s, T_{Top} is equal to T_{Bottom} . After $t = 100$ s, the temperature at the bottom (T_{Bottom}) begins to decrease. At $t = 150$ s the initial temperature gradient (\vec{G}) is generated. Then both T_{Top} and T_{Bottom} drop at the same cooling rate R , and the solidification subsequently occurs. The lateral wall of the sample is considered to be adiabatic. The mushy zone thickness (δ) is calculated as the distance from the solidification front to the point of eutectic temperature isotherm. An RMF inductor is installed outside the sample, which is controlled by a switch (on/off). The rotating magnetic field with a constant rotating frequency (f) and magnetic induction (B) is applied. The RMF is activated at the beginning of

the calculation ($t = 0$ s) in the cases of chapter 3.1 and chapter 3.3, while the RMF is switched on at $t = 650$ s in the case of chapter 3.2. An analytical approximation of the azimuthal component of the electromagnetic force (\vec{F}_θ) is valid (Eq. (1)) [6,21,22].

$$\vec{F}_\theta = \frac{1}{2} \sigma \omega B^2 r \left(1 - \frac{u_\theta}{\omega R} \right) \vec{e} \quad (1)$$

where σ is the electrical conductivity of the melt, $\omega = 2\pi f$ is angular frequency, B is the magnetic induction, r and $R (= d/2)$ is a radial coordinate and radius of the sample, and u_θ is the azimuthal velocity magnitude of the melt at a radial coordinate r , \vec{e} is the tangential unit vector. The material properties and other parameters used in the study are summarized in Table 1.

Two laws of the isotropic permeability (K) of the mushy zone, derived from the Carman-Kozeny law, are deployed: one as reported by Noepfel [8] referring to the secondary dendrite arm space λ_2 ; one as reported by Ramirez [24] referring to the primary dendrite arm space λ_1 .

$$K = \frac{\lambda_2^2 f_\ell^3}{4\pi^2 K_c (1 - f_\ell)^2} \quad (2)$$

$$K = \frac{\lambda_1^2 f_\ell^3}{1667(1 - f_\ell)^2} \quad (3)$$

where K_c is a constant ($K_c = 5$), f_ℓ is the liquid volume fraction.

For the purpose of a numerical parameter study, five simulation cases are defined in Table 2. We take the permeability as reported by Ramirez as a reference case (K), three further cases are considered, for which the permeability is increased/decreased arbitrarily by a factor, i.e. 10 K , 0.1 K and 0.01 K .

The model is implemented in ANSYS FLUENT version 14.5, which uses a control-volume finite difference numerical method. All phases share a single pressure field, p , which is solved via a pressure correction equation. This, in turn is obtained from the sum of the normalized mass continuity equations, using the phase-coupled SIMPLE (PC-SIMPLE) algorithm. For each time step, 30 iterations are adopted to decrease the normalized residuals of concentration, flow quantities and continuity below 10^{-4} and enthalpy quantities below 10^{-7} . The decision to select a time step that ensures a high accuracy solution must be determined empirically by test simulations. In this study all calculations are run with a time-step of 0.0005 s. Parameter studies were performed in 2D axisymmetric (swirl) calculation; but full 3D simulations were made to verify the validity of 2D axisymmetric simulations for the flow (Chapter 3.1) and to analyze the solidification sequence (Chapter 3.2). The maximum mesh sizes are 3.0×10^{-4} m (3D) and 1.0×10^{-4} m (2D), respectively. One 3D simulation takes ca. 4 weeks; while one 2D simulation takes only a week on a high performance cluster (2.6 GHz, 12 cores).

3. Simulation results

3.1. Fluid flow

Fig. 2 shows the melt flow pattern in the sample at $t = 80$ s. The RMF is activated at the beginning of the calculation ($t = 0$ s). Under the RMF (20 m T, 50 Hz), an intensive azimuthal flow up to the velocity magnitude of 0.15 m/s is generated in the region at the center of the radius. Due to the non-slip flow boundary conditions at the lateral and bottom walls, a so-called Ekman effect [25] leads to a meridional circulation. The meridional velocity is 0.04 m/s, one order of magnitude smaller than the azimuthal velocity. As clearly demonstrated by the streamline in Fig. 2(b), the fluid rotates downwards at the periphery of the sample, then it rotates and flows upwards in the sample's center. What is more interesting to see is that the fluid flow is very unstable, as depicted in Fig. 2(a) and (c). The meridional velocity is characterized

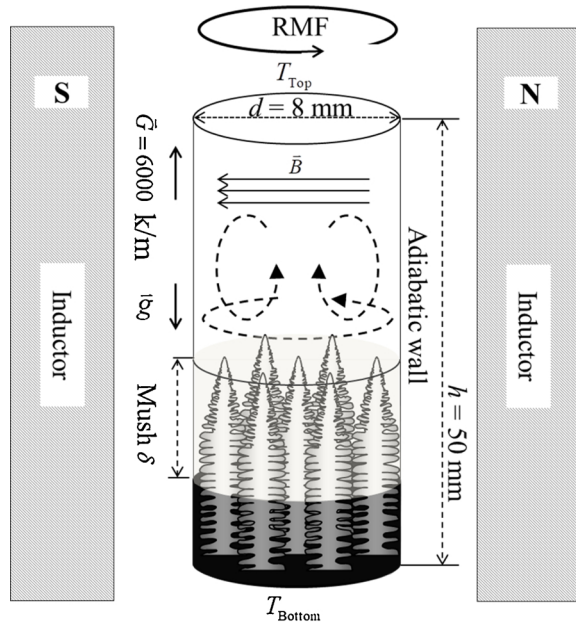


Fig. 1. Geometry configuration and boundary conditions.

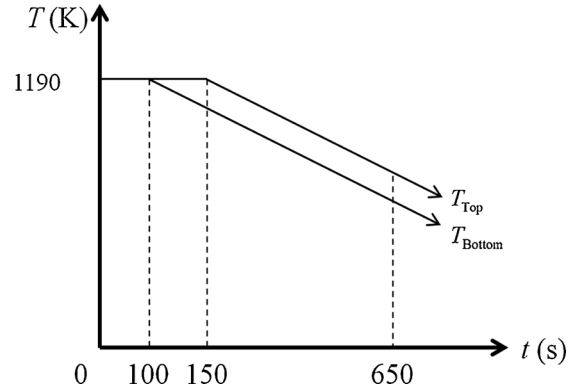


Table 1
Summary of material properties and other parameters [8,23].

Property	Symbol	Units	Values
Thermophysical properties			
Specific heat	C_p^l, C_p^s	$J \cdot Kg^{-1} \cdot K^{-1}$	1140.0
Latent heat	Δh_f	$J \cdot Kg^{-1}$	400000.0
Diffusion coefficient (solid)	D_c	$m^2 \cdot s^{-1}$	1.0×10^{-12}
Diffusion coefficient (liquid)	D_e	$m^2 \cdot s^{-1}$	6.45×10^{-9}
Thermal conductivity	k_p^l, k_p^s	$W \cdot m^{-1} \cdot K^{-1}$	100.0
Liquid thermal expansion coefficient	β_T	K^{-1}	-1.85×10^{-4}
Liquid solutal expansion coefficient	β_c	$wt.\%^{-1}$	1.3×10^{-3}
Reference density (solid)	ρ_{ref}	$Kg \cdot m^{-3}$	2535.0
Boussinesq density difference	$\Delta \rho$	$Kg \cdot m^{-3}$	165.0
Viscosity	μ_e	$Kg \cdot m^{-1} \cdot s^{-1}$	2.52×10^{-3}
Electrical conductivity	σ	$\Omega^{-1} \cdot m^{-1}$	3.65×10^6
Thermodynamic parameters			
Eutectic composition	c_{eu}	wt.%	12.6
Eutectic temperature	T_{eu}	K	850.0
Liquidus slope	m	$K (wt.\%)^{-1}$	-6.62
Equilibrium partition coefficient	k	-	0.13
Primary dendritic arm spacing	λ_1	μm	300.0
Secondary arm spacing	λ_2	μm	50.0
Gibbs Thomson coefficient	Γ	m·K	2.41×10^{-7}
Melting point of solvent	T_f	K	933.5
Other parameters			
Initial concentration	c_0	wt.%	7.0
Initial temperature	T_0	K	1190.0
Cooling rate of top and bottom	R	K/s	0.16
Temperature gradient	\vec{G}	K/m	6000.0
Magnetic induction	B	mT	20.0
Angular frequency	ω	rad/s	314.0
Rotating frequency	f	Hz	50.0

by a random occurrence of Taylor-Görtler (T-G) vortices along the lateral wall of the sample [25]. Some T-G vortices move up and down to the top/bottom surface, and then disappear; while some of the vortices aggregate with the neighboring ones to form a large vortex. The generation and aggregation of these vortices seem to appear randomly. The space between every two vortices is about 5 mm. Note that this kind of flow pattern remains during solidification, interacting with the growing mushy zone.

Table 2
Cases definition for parameter study by varying permeability.

Cases	Expression	Relationship	Referred to	Parameters
A	-	0.01 K	-	$\lambda_1 = 300 \mu m$ and
B	-	0.1 K	-	$\lambda_2 = 50 \mu m$, which are
C	$K = \frac{\lambda_1^2 f_e^3}{1667(1-f_e)^2}$	K	Ramirez [24]	taken from experi-
D	$K = \frac{\lambda_2^2 f_e^3}{4\pi^2 K_c (1-f_e)^2}$	4K	Noepfel [8]	ments [4].
E	-	10K	-	

As a comparison to the 3D model, a 2D axisymmetric (swirl) calculation is performed, as depicted in Fig. 2(d). It is clear that the 2D axisymmetric calculation can successfully reproduce the 3D calculation results, in terms of both the velocity magnitude (azimuthal ~ 0.15 m/s, meridional ~ 0.04 m/s) and the flow pattern (e.g. T-G vortices). Even the spacing of each T-G vortex is also quite similar to that of the full 3D calculation. It can be concluded that the subsequent parameter study for the solidification based on 2D axisymmetric calculations is able to reproduce the key features of solidification as performed in full 3D. Two minor differences between 2D axisymmetric and 3D calculations should be kept in mind for the purpose of interpreting the solidification results from 2D calculations. One is that the instability of the flow, especially in the center region, is understated by the 2D axisymmetric calculation: the oscillation of the flow pattern in the center (3D) is smeared (averaged) when applying the 2D calculation. Another point is that the ideal axisymmetry of the result rendered in 2D would never occur in the full 3D calculation.

3.2. Solidification under RMF

The solidification process of the sample at $t = 945$ s under the influence of RMF is shown in Fig. 3. The RMF is activated at $t = 650$ s. The top and bottom boundaries of the mushy zone are represented by iso-surfaces of the liquid phase fraction ($f_e = 0.85$) and eutectic temperature ($T = 850$ K), respectively. The distribution of the liquid phase fraction in the mushy zone, overlaid with the vectors of the liquid velocity is depicted in Fig. 3(a). The vector length is scaled by a log function. A tube-like channel, filled with solute-enriched liquid, forms in the sample center. It penetrates the entire mushy zone. In the mushy

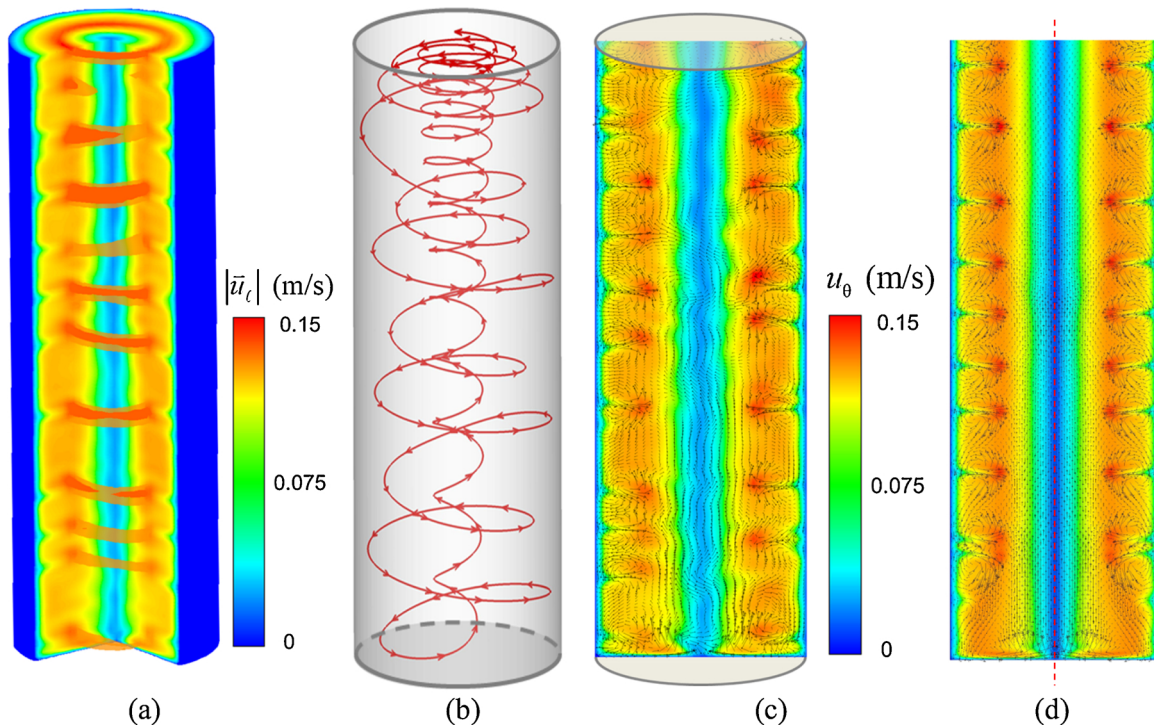


Fig. 2. Flow pattern of pure liquid melt under RMF (20 mT, 50 Hz) at the moment of 80 s before solidification starts: (a)–(c) in full 3D calculation, (d) in axisymmetric calculation. The domain is down-scaled in axis direction to allow a better view of the entire domain of the sample (φ 8 mm \times 50 mm). (a) Contours of velocity magnitude (color scaled) in two vertical sections and one horizontal section at the top boundary, combined with two tube-like iso-surfaces of the velocity magnitude, which is used to indicate the typical Taylor–Görtler vortices [25]: one iso-surface is for the velocity magnitude of 0.135 m/s, one iso-surface, which is made transparent, is for the velocity magnitude of 0.13 m/s; (b) One streamline to show the mass transfer; (c) Contour of the azimuthal velocity (color scaled) in the central section, overlaid with the vectors of the meridional velocity in the central section; (d) Same contours/vector as in (c) in a 2D axisymmetric calculation (one half section is mirrored from another).

zone, the fluid flow is suppressed by the dendrites to a magnitude of $10^{-3} \sim 10^{-6}$ m/s, and the maximum liquid velocity is observed in the tube-like channel. The flow pattern in the mushy zone is similar to that in the bulk liquid, as demonstrated in Chapter 3.1. The fluid rotates downwards at the periphery of the sample, then it rotates and flows upwards into the center tube-like channel – as demonstrated by the vectors in Fig. 3(a) and streamlines in Fig. 3(b). The central tube-like channel acts as a pump, sucking solute-enriched melt out of the mush and transporting it back into the bulk region of the sample.

As shown in Fig. 3(c)–(e), there is almost no macrosegregation in the lower part of the sample before the RMF is activated (before 650 s). The central segregation channel occurs only after the RMF stirring. The aforementioned T-G vortices still remain during solidification. With the gradual enrichment of the solute in the bulk melt region, the liquidus temperature decreases to about 873 K at 945 s. Fig. 3(d) shows the solute mixture concentration (c_{mix}). A strong positive macrosegregation channel, accompanied by side-arms, appears along the axis of the sample forms and it assumes the appearance of a “Christmas tree”. Liquid and columnar phase fractions are shown in Fig. 3(e) and (f). The distribution pattern of the liquid phase fraction (f_ℓ) is similar to that of c_{mix} . When the temperature is lower than eutectic temperature (T_{eu}), the remaining solute-enriched inter-dendritic liquid solidifies eutectically.

3.3. Role of the permeability in solidification

The calculation results of the solidification (620 s) by varying degrees of permeability are shown in Fig. 4. These five cases correspond to those in Table 2, which only lists the results in the mushy zone. In all cases, a central segregation channel with a diameter of 1 mm, strongly enriched with Si forms, where c_{mix} is close to the eutectic concentration. At the periphery of the sample, c_{mix} decreases with the rate of

permeability. The degree of macrosegregation increases with the permeability. Except for the cases (a) and (e), all simulations present a “Christmas tree” segregation pattern. A characteristic time for the periodical formation of channels is relatively long (40 ~ 110 s).

Near the solidification front, the liquid velocity is close to that in the bulk liquid. In the deep mushy zone, the liquid velocity is decelerated by the resistance of the columnar dendrites, and the component of meridional liquid velocity ($\sim 10^{-5}$ m/s) is several orders of magnitude smaller than that in the bulk liquid ($\sim 10^{-2}$ m/s). As demonstrated by the pink dash lines in Fig. 4, as soon as side-arms of the segregation channel forms, the flow takes the path of the least resistance through the side-arms of the channel, hence the flow directions are strongly influenced by the forming side-arms. It is difficult to determine the maximum or average liquid velocity in the mushy zone, but it is still evident that the meridional liquid velocity increases with the rate of permeability. The mushy zone thickness (δ) is calculated from the distance between the solidification front and the eutectic isotherm. Clearly, δ decreases with the permeability.

4. Discussion

4.1. Relationship between the T-G vortex and segregation channel formation

As shown in Figs. 2 and 3, some T-G vortices form in the bulk liquid and move up/down to the top/bottom surface, and then disappear; while some of the vortices aggregate with the neighboring ones to form a big vortex. Taking the simulation case in Chapter 3.2 as a reference point, we measure the life time (formation interval) of each T-G vortex, which is compared with the time interval of formation of each side-arm of segregation channel. It is clear that the formation frequency of the side-arm is inverse proportional to its formation interval. The results

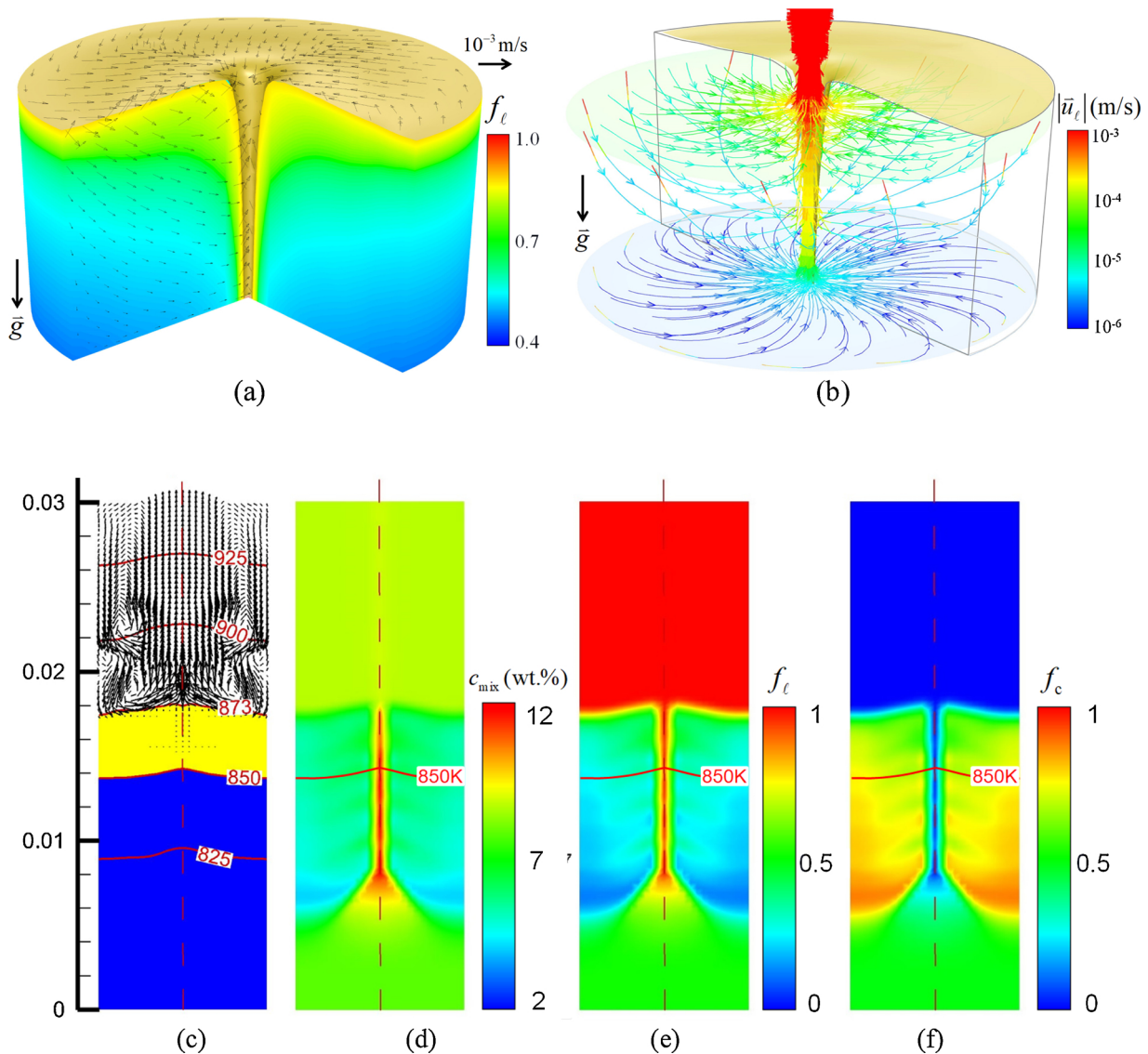


Fig. 3. The solidification process of the sample at the moment of 945 s: (a) and (b) in the mushy zone (3D), (c)–(f) in the whole domain (2D). (a) Contour of the liquid phase fraction (color scaled) in the mushy zone in two vertical sections and one iso-surface of the liquid phase fraction ($f_l = 0.85$) at the top and center of the mush, overlaid with the vectors of the liquid velocity; (b) streamlines of the flow in the mushy zone colored by liquid velocity magnitude ($|\vec{u}_l|$); (c) different phase regions: bulk liquid by white, full solid by blue and the mushy zone by yellow, overlaid by isotherms and vectors of the meridional liquid velocity; (d) – (f) contours of mixture concentration (c_{mix}), liquid phase fraction (f_l), and columnar phase fraction (f_c).

are plotted in Fig. 5. If one T-G vortex disappears at the solidification front, we record the time it takes for the melt to solidify. The interval of T-G vortex formation is calculated by the time difference between two subsequent records. Similarly, if one side segregation channel forms, we make a record of the solidification time. The formation interval of each segregation side-arm is calculated by the time difference between the two recorded time intervals.

As shown in Fig. 5 (insert), the formation interval of T-G vortex varies randomly between 0.3 and 1.2 s. On average, one T-G vortex disappears every 0.7 s at the solidification front. As the RMF is switched on at $t = 650$ s in this case, the first side channel forms at $t = 680$ s. The solute is gradually enriched in the bulk liquid due to the meridional liquid velocity. The enrichment of solute in the bulk liquid influences the solidification process. One influence is the increase of the formation interval of segregation side-arms. This interval changes from 40 to 110 s. A similar phenomenon was observed experimentally [26]. In the process of forming one side-arm, dozens of vortices form. The origin of the side-arms of the “Christmas tree” seems independent from the T-G vortices, supporting the conclusion of Bodenkova et al. [6], because the

formation frequency of T-G vortices is approximately two orders of magnitude larger than the formation frequency of the side-arms of the “Christmas tree”.

4.2. Role of permeability in mushy zone thickness and macrosegregation

The interaction between the melt flow and the formation of mushy zone is highly complex [27,28]. The fluid flow may influence the mushy zone by modifying the dendrite morphology: inducing the macrosegregation; causing segmentation and fragmentation. In turn, the mushy zone can affect the fluid flow by changing the flow intensity and pattern [28]. One parameter used to characterize the fluid flow in the mushy zone is permeability, *i.e.* a tensor to measure the ease of fluid flow through the solid network [12].

This article cannot cover all of the aforementioned aspects of the flow-solidification interaction, as it would go beyond the scope of an individual scientific paper. One of the most important objectives of this study is to demonstrate the influence of mush permeability on the solidification process by increasing or decreasing the permeability

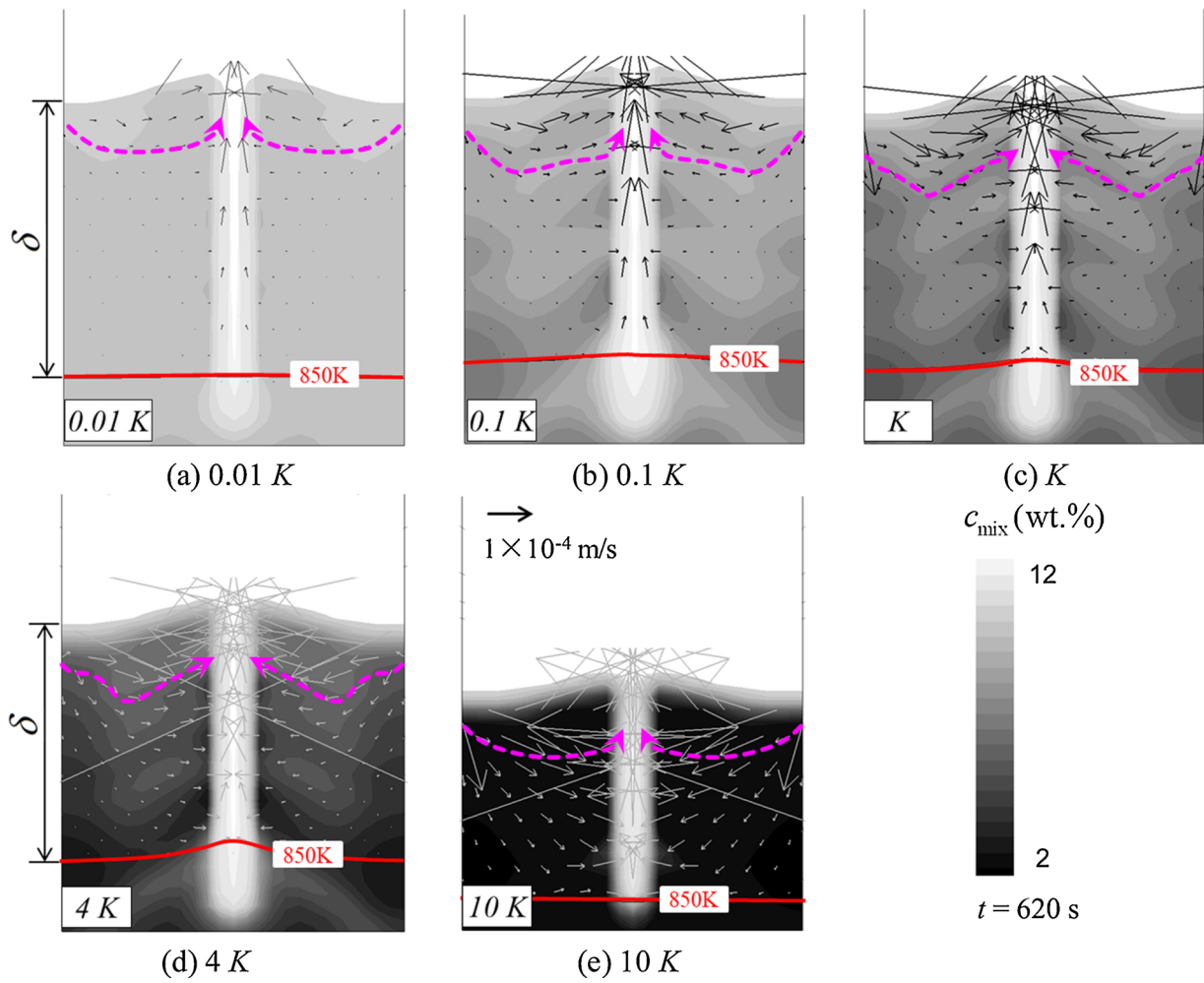


Fig. 4. Parameter study by varying rates of permeability. Cases (a)–(e), corresponding to those in Table 2, show the solidification in the mushy zone at 620 s. The gray-scale shows mixture concentration (c_{mix}) that is lighter for higher concentrations. Vector shows the meridional component of liquid velocity. The red solid lines are isotherms of the eutectic temperature, pink dash lines indicate the flow direction, and the top profile is the solidification front.

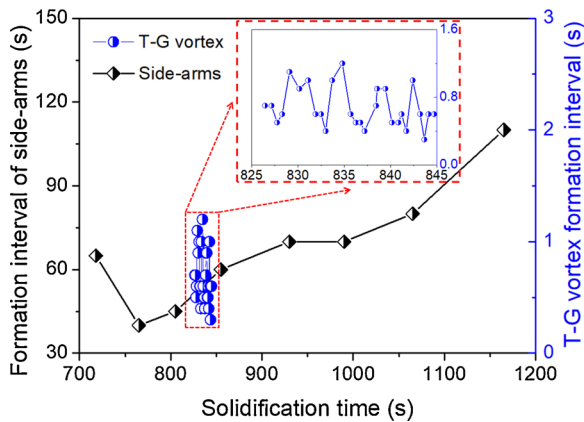


Fig. 5. Time intervals of the formation of T-G vortices and side-arms of central segregation channel.

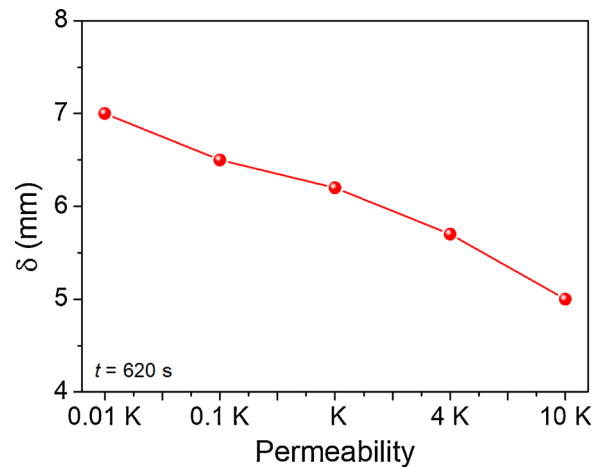


Fig. 6. Influence of permeability on mushy zone thickness (δ).

arbitrarily. This may help in understanding the effect of permeability on the flow-solidification interaction.

Based on the numerical simulation results, we have found that the thickness of mushy zone (δ) decreases with the permeability, and the macrosegregation severity increases, respectively. Quantitative analyses of the thickness of the mushy zone and mixture concentration have been performed. The mushy zone's thickness (δ) against the

permeability is plotted in Fig. 6. Mushy zone thickness decreases from 7 mm to 5 mm when increasing the permeability by three orders of magnitude. The liquid velocity in the mushy zone is relatively rapid when there is a greater degree of permeability. The intense liquid velocity in the mushy zone promotes energy (enthalpy) and mass transport. This enhances the temperature gradient in/near the mushy zone.

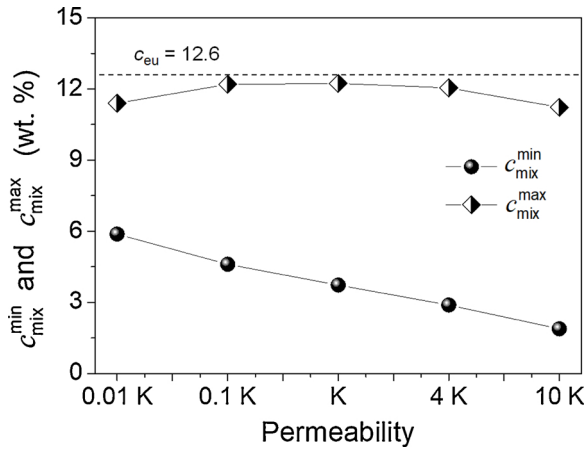


Fig. 7. Influence of permeability on macrosegregation.

The greater the temperature gradient, the thinner the mushy zone.

The minimum and maximum mixture concentrations ($c_{\text{mix}}^{\text{min}}$), ($c_{\text{mix}}^{\text{max}}$) against the permeability in the whole domain are plotted in Fig. 7. The hollow circles represent the maximum mixture concentration ($c_{\text{mix}}^{\text{max}}$), and the solid circles stand for the minimum mixture concentration ($c_{\text{mix}}^{\text{min}}$). The distance between these two lines indicates how heterogeneous the solute distribution actually is. This is consistent with the results shown in Fig. 4. The maximum mixture concentration ($c_{\text{mix}}^{\text{max}}$) of all these five cases, corresponding to the central positive segregation channel, is close to the eutectic concentration. The minimum mixture concentration, corresponding to negative segregation in the lower part of the periphery regions of the sample, decreases with the permeability. The more permeable the mush is, the stronger the flow, hence more solute will be transported from the periphery into the center and bulk regions of the sample.

Plenty of experiments and numerical simulations have been performed to determine the permeability of different alloys under varying casting conditions, and various permeability laws are therefore proposed [29–37]. The permeability was measured for different alloys [34,36,37]. Experimental methods fail to measure permeability when $f_\ell > 0.66$ in columnar structures, due to ripening and the fragile nature of dendrites. Recently, experimental 3D mapping of the sample using synchrotron X-ray micro-tomography followed by image analysis to distinguish the eutectic (interdendritic liquid) from the dendrite skeleton was used to reconstruct the dendritic morphology to generate 3D geometry [12,29–33], which makes the permeability calculations more accurate. However, the permeability values given by the different permeability formulas differ by two orders of magnitude. Extreme caution must be taken in order to be able to precisely determine the permeability.

4.3. Side-arm formation of the central segregation channel

Reproducing the experimentally observed “Christmas tree” macrosegregation pattern works well by applying the current two-phase volume-average based solidification model. Li and Wu have proposed a formula to analyze the formation mechanism of channel segregation in the case of pure columnar solidification [16,17]. This formula is used to analyze the formation of the side-arms of the central segregation channel. The concentration difference between the liquid thermodynamic equilibrium at the solid-liquid interface and the volume-averaged concentration in the interdendritic liquid ($c_\ell^* - c_\ell$) is the driving force for both solidification and remelting. The local solidification/melting rate, $M_{\ell c}$, is proportional to $\frac{\partial(c_\ell^* - c_\ell)}{\partial t}$. The remelting of the dendrites is not considered in this work. The local solidification rate ($M_{\ell c}$) is the result of three contributions, corresponding to the three right hand side (RHS) terms of Eq. (4).

$$M_{\ell c} \propto \frac{\partial(c_\ell^* - c_\ell)}{\partial t} = \frac{(c_\ell - c_s^*)}{f_\ell} \frac{\partial f_\ell}{\partial t} + \frac{1}{m} \frac{\partial T}{\partial t} + \vec{u}_\ell \cdot \nabla c_\ell \quad (4)$$

where f_ℓ is liquid volume fraction, c_ℓ is species concentration in the liquid phase, c_ℓ^* and c_s^* are thermodynamic equilibrium species concentrations at the liquid/solid interface, and m is the liquidus slope. The first RHS term is the solidification-induced solute enrichment of the interdendritic melt. This term is always negative for solidification. The second RHS term is the contribution of the cooling rate, which is always positive. The third RHS term is the flow-solidification interaction term, which can be positive or negative, depending on the interdendritic flow direction. Local solidification behavior strongly depends on the intensity of the flow-solidification interaction.

In a region where the melt flows (\vec{u}_ℓ) in the same direction as the liquid concentration gradient (∇c_ℓ), the flow-solidification interaction term is positive. The local increase in flow velocity due to a flow perturbation accelerates solidification. As a consequence, the local permeability (K) becomes relatively smaller than that of its neighboring zones, which decelerates the interdendritic fluid flow. Hence, side-arms would not form. On the contrary, in regions where the melt flows in the opposite direction of the concentration gradient, the flow-solidification interaction term is negative. The local increase in flow velocity due to flow perturbation suppresses the solidification rate. This region with a relatively lower solid fraction has a greater degree of permeability. The interdendritic fluid flow becomes stronger and side-arms form.

As shown in Fig. 8(a), the vectors of liquid velocity and solute gradient are both plotted in green and black, respectively. When the angle between these two vectors is larger than 90° , the flow-solidification interaction term should be negative. The suppressed solidification zone, corresponding to negative $\vec{u}_\ell \cdot \nabla c$, is shown in Fig. 8(b). It is evident that the solidification rate ($M_{\ell c}$) is far lower than that of the neighboring cells at the solidification front and sample center, where the flow-solidification interaction term ($\vec{u}_\ell \cdot \nabla c$) is negative. The suppressed solidification rate possibly leads to the formation of the side-arms of the channel. As depicted in Figs. 4 and 8(c), once the side-arm forms, the solute-enriched inter-dendritic liquid takes the path of least resistance through these zones. The enrichment of the solute-enriched liquid in the side-arms suppresses the solidification and even causes them to remelt [16,17]. Formation of the side-arms is a self-reinforcing process until the temperature falls below the eutectic temperature. The final segregation pattern is shown in Fig. 8(d), and the side-arm enclosed within the blue outline is newly formed at 620 s.

The “Christmas tree” macrosegregation under RMF has been experimentally observed for different alloys [38–40]. When the magnetic induction is weak, the solidified microstructure is dominated by columnar dendrites [41]. With the increase of the magnetic induction, some equiaxed crystals form in the sample center [42]. Under a strong RMF, fragmentation occurs, leading to a transition in the microstructure from columnar to equiaxed (CET) [38]. The critical magnetic induction for CET is dependent on the respective alloy-system and cooling conditions. Study of CET under RMF is beyond the scope of the current paper. Based on the published results, the solidified microstructure of the sample under current cooling conditions and RMF strength should be dominated by columnar dendrites [6,42].

5. Conclusion

A two-phase volume-average based columnar solidification model is used to calculate the unidirectional solidification process of a cylindrical sample (φ 8 mm \times 50 mm, Al-7.0 wt.%Si alloy) under RMF (Rotating magnetic field, 20 m T, 50 Hz) with a focus on evaluating the effects of mush permeability on the solidifying mush zone. Following conclusions are drawn.

- 1) It is verified that the flow calculation under RMF in 2D axisymmetry (swirl) can sufficiently reproduce the full 3D calculation, in terms of

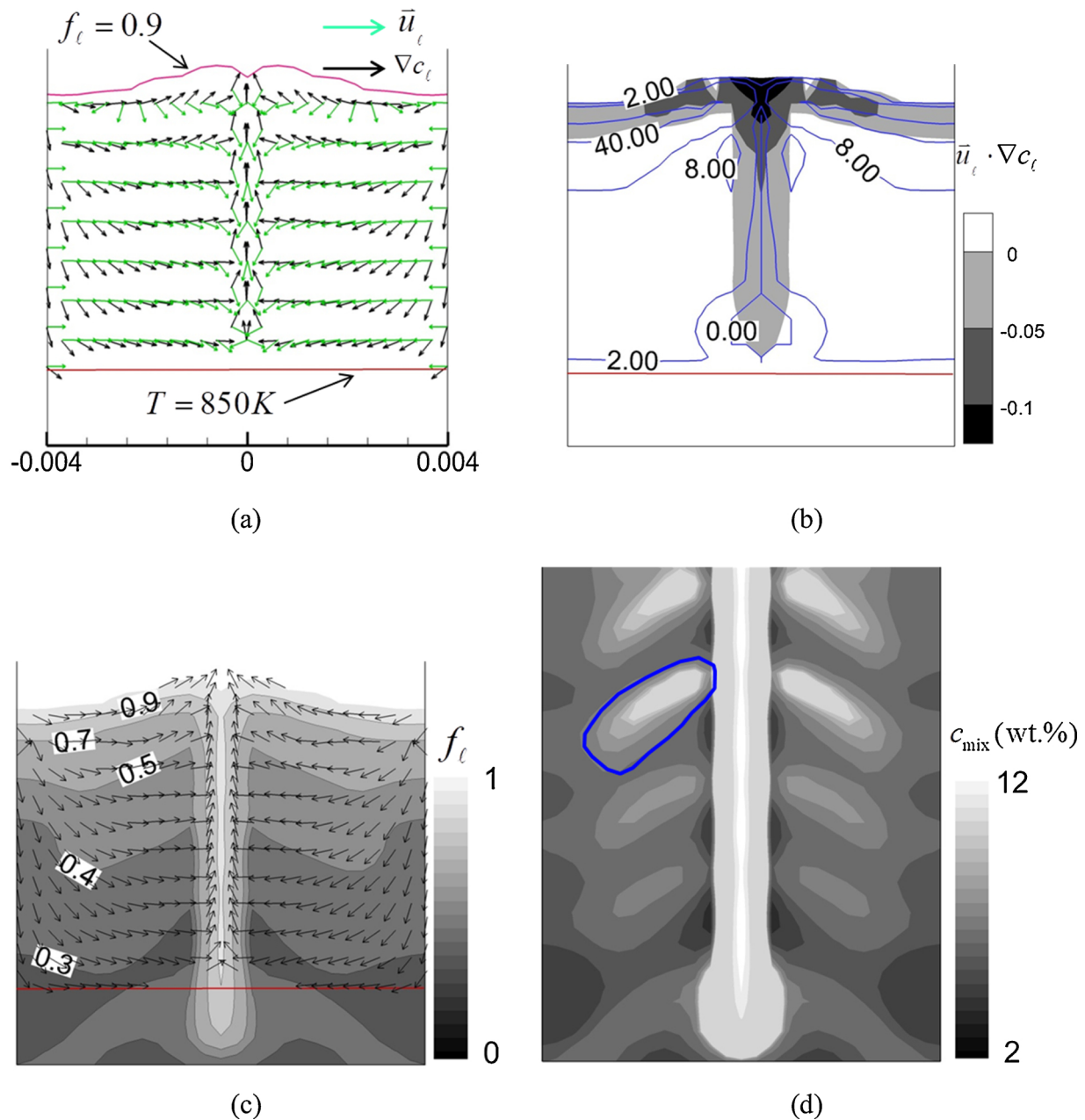


Fig. 8. Analysis of the formation of the side-arms in the central segregation channel at $t = 620$ s: (a) vector of liquid velocity (green) overlaid by vector of solute gradient; (b) contours of the flow-solidification interaction term ($\vec{u}_l \cdot \nabla c_l$) in white (positive value) and dark (negative value) overlaid by the solidification rate (M_e) isolines; (c) liquid volume fraction (f_l) contours and isolines overlaid by vectors of liquid velocity; and (d) final mixture concentration (c_{mix}).

both the velocity magnitude (azimuthal ~ 0.15 m/s, meridional ~ 0.04 m/s) and the flow pattern (e.g. T-G vortices). Mesh sizes of both 2D and 3D calculations must be rigorously controlled.

- Numerical parameter study shows that the thickness of the mushy zone decreases and the global macrosegregation intensity increases monotonically with the mush permeability.
- The “Christmas tree” macrosegregation pattern, sometimes observed experimentally, can only occur when the permeability falls in a certain range for the case of pure columnar solidification. Literature studies indicate that permeability rates, as suggested by different permeability laws, differ from by two orders of magnitude, hence extreme caution must be taken in order to correctly determine the permeability. The formation of side-arms of “Christmas tree” macrosegregation during solidification can be analyzed in accordance with the flow-solidification term ($\vec{u}_l \cdot \nabla c$).
- The origin of the “Christmas tree” channels seems independent from

the T-G vortices, supporting the conclusion of Bodenkova et al. [6], as the formation frequency of T-G vortices is approximately two orders of magnitude greater than the formation frequency of the “Christmas tree” channels.

CRediT authorship contribution statement

Haijie Zhang: Conceptualization, Methodology, Investigation, Writing - original draft, Visualization. **Menghuai Wu:** Conceptualization, Methodology, Writing - review & editing, Project administration. **Yongjian Zheng:** Conceptualization, Methodology. **Andreas Ludwig:** Conceptualization, Supervision. **Abdellah Kharicha:** Conceptualization, Software.

Declaration of Competing Interest

None.

Acknowledgements

The authors acknowledge the financial support from Austrian Research Promotion Agency (FFG) -Austrian Space Application Program (ASAP) through the project FLOWSICONS (No. 859777), as well as the support from European Space Agency (ESA) through the project MICAST.

References

- [1] A.V. Reddy, N.C. Beckermann, *Metall. Mater. Trans. B* 28 (1997) 479–489.
- [2] M. Rappaz, J.M. Drezet, M. Gremaud, *Metall. Mater. Trans. A* 30 (1999) 449–455.
- [3] D.M. Stefanescu, *Int. J. Cast Met. Res.* 18 (2005) 129–143.
- [4] Ratke, et al., MICAST Research Report – Phase IV, ESA-MAP AO-99-031 (2013).
- [5] D.R. Liu, N. Mangelinck-Noël, C.A. Gandin, G. Zimmermann, L. Sturz, H.N. Thi, B. Billia, *Acta Mater.* 64 (2014) 253–265.
- [6] O. Budenkova, A. Noeppel, J. Kovács, A. Rónaföldi, A. Roósz, A.M. Bianchi, F. Baltaretu, M. Medina, Y. Fautrelle, *Mater. Sci. Forum.* 649 (2010) 269–274.
- [7] J. Kovács, A. Rónaföldi, A. Roósz, *Mater. Sci. Forum.* 649 (2010) 263–268.
- [8] A. Noeppel, A. Ciobanas, X.D. Wang, K. Zaidat, N. Mangelinck, O. Budenkova, A. Weiss, G. Zimmermann, Y. Fautrelle, *Metall. Mater. Trans. B* 41 (2010) 193–208.
- [9] O. Budenkova, F. Baltaretu, J. Kovács, A. Roósz, A. Rónaföldi, A.M. Bianchi, Y. Fautrelle, *IOP Conf. Series: Mater. Sci. Eng.* 33 (2012) 012046.
- [10] D.R. Poirier, *Metall. Mater. Trans. B* 18 (1987) 245–255.
- [11] M.C. Schneider, C. Beckermann, *Int. J. Heat Mass Transf.* 38 (1995) 3455–3473.
- [12] C. Puncreobutr, A.B. Phillion, J.L. Fife, P.D. Lee, *Acta Mater.* 64 (2014) 316–325.
- [13] A.K. Singh, B. Basu, A. Ghosh, *Metall. Mater. Trans. B* 37 (2006) 799–809.
- [14] A. Kumar, M. Založnik, H. Combeau, *Int. J. Therm. Sci.* 54 (2012) 33–47.
- [15] M. Wu, Y. Zheng, A. Kharicha, A. Ludwig, *Comput. Mater. Sci.* 124 (2016) 444–455.
- [16] J. Li, M. Wu, J. Hao, A. Kharicha, A. Ludwig, *Comput. Mater. Sci.* 55 (2012) 419–429.
- [17] J. Li, M. Wu, J. Hao, A. Ludwig, *Comput. Mater. Sci.* 55 (2012) 407–418.
- [18] M. Wu, A. Ludwig, A. Kharicha, *Appl. Math. Model.* 41 (2017) 102–120.
- [19] J. Lipton, M.E. Glicksman, W. Kurz, *Mater. Sci. Eng.* 65 (1984) 57–63.
- [20] J. Kovács, A. Rónaföldi, A. Roósz, *Trans. Indian Inst. Met.* 62 (2009) 475–477.
- [21] J.K. Roplekar, J.A. Dantzig, *Int. J. Cast Met. Res.* 14 (2001) 79–95.
- [22] A. Noeppel, A. Ciobanas, X.D. Wang, K. Zaidat, N. Mangelinck, O. Budenkova, A. Weiss, G. Zimmermann, Y. Fautrelle, *Metall. Mater. Trans. B* 41 (2010) 193–208.
- [23] M. Ghods, L. Johnson, M. Lauer, R.N. Grugel, S.N. Tewari, D.R. Poirier, *J. Cryst. Growth* 441 (2016) 107–116.
- [24] J.C. Ramirez, C. Beckermann, *Metall. Mater. Trans. A* 34 (2003) 1525–1536.
- [25] B. Willers, S. Eckert, P.A. Nikrityuk, D. Rábiger, J. Dong, K. Eckert, G. Gerbeth, *Metall. Mater. Trans. B* 39 (2008) 304–316.
- [26] A. Roósz, J. Kovács, A. Rónaföldi, Á. Kovács, *Mater. Sci. Forum.* 752 (2013) 57–65.
- [27] H. Wang, M.S. Hamed, S. Shankar, *J. Mater. Sci.* 53 (2018) 9771–9789.
- [28] M. Wu, A. Vakhrushev, G. Nummer, C. Pfeiler, A. Kharicha, *Open Transp. Phenom. J.* 2 (2010) 16–23.
- [29] D. Bernard, Ø. Nielsen, L. Salvo, P. Cloetens, *Mater. Sci. Eng. A* 392 (2005) 112–120.
- [30] D. Fuloria, P.D. Lee, D. Bernard, *Mater. Sci. Eng. A* 494 (2008) 3–9.
- [31] E. Khajeh, D.M. Maijer, *Mater. Sci. Technol.* 26 (2010) 1469–1476.
- [32] E. Khajeh, D.M. Maijer, *Acta Mater.* 58 (2010) 6334–6344.
- [33] E. Khajeh, D.M. Maijer, *Acta Mater.* 59 (2011) 4511–4524.
- [34] N. Streat, F. Weinberg, *Metall. Trans. B* 7 (1976) 417–423.
- [35] T. Takaki, S. Sakane, M. Ohno, Y. Shibuta, T. Aoki, *Acta Mater.* 164 (2019) 237–249.
- [36] A.J. Duncan, Q. Han, S. Viswanathan, *Metall. Mater. Trans. B* 30 (1999) 745–750.
- [37] D. Apelian, M.C. Flemings, R. Mehrabian, *Metall. Trans.* 5 (1974) 2533–2537.
- [38] J. Kovács, A. Rónaföldi, Á. Kovács, A. Roósz, *Trans. Indian Inst. Met.* 62 (2009) 461–464.
- [39] M. Svéda, A. Sycheva, J. Kovács, A. Rónaföldi, A. Roósz, *Mater. Sci. Forum.* 790–791 (2014) 414–419.
- [40] J. Kovács, A. Rónaföldi, A. Roósz, *Mater. Sci. Forum.* 790–791 (2014) 408–413.
- [41] S. Steinbach, L. Ratke, *Mater. Sci. Eng. A* 413–414 (2005) 200–204.
- [42] G. Zimmermann, A. Weiss, Z. Mbaya, *Mater. Sci. Eng. A* 413 (2005) 236–242.



Geometrical effect on macrosegregation formation during unidirectional solidification of Al–Si alloy

Haijie Zhang^a, Menghuai Wu^{a,*}, Surendra N. Tewari^b, Andreas Ludwig^a, Abdellah Kharicha^a

^a Chair for Simulation and Modelling of Metallurgy Processes, Department of Metallurgy, University of Leoben, A-8700 Leoben, Austria

^b Chemical and Biomedical Engineering Department, Cleveland State University, Cleveland, OH, 44115, United States

ARTICLE INFO

Associate Editor: A Luo

Keywords:

Geometrical effect
Macrosegregation
Unidirectional solidification
Solidification shrinkage
Stray crystals

ABSTRACT

In the production of single-crystal turbine blades for use in aircraft engines with unidirectional solidification techniques, it is confirmed that the casting geometry had great influence on the formation of macrosegregation or spurious/stray crystals. In this study, a two-phase solidification model is used to investigate the geometrical effect on the unidirectional solidification of Al–7.0 wt.% Si alloy. The study is based on the experiment of Ghods et al. (2016a), in which the diameter of the sample is changed between $\phi 9.5$ and $\phi 3.2$ mm along the solidification direction to highlight the geometrical effect. The first part of the investigation is to verify the numerical model by ‘reproducing’ the experimentally obtained macrosegregation and phase distribution in an as-cast sample. The second part is to explore the macrosegregation mechanism. It is found that the main geometrical effect is the modification of the bulk and the interdendritic melt flow during solidification. Different flow patterns are found in different locations, e.g. below or above the cross-section contraction; however, details of the macrosegregation formation can be explained by a scalar product of two vectors, i.e. the flow velocity and the concentration gradient of the melt. Based on the positive/negative value of the scalar product, i.e. the flow direction in comparison with the direction of the concentration gradient, it is possible to determine where a negative/positive segregation will occur. The above scalar product is also found valid for analysing the possible formation of spurious/stray crystals, and it is numerically demonstrated that the cross-section expansion in casting geometry leads to high risk of spurious/stray crystals.

1. Introduction

The casting geometry is an important factor influencing the melt flow pattern during solidification, and an inappropriate geometry design may intensify macrosegregation or cause formation of other defects. Turbine blades, which are key components in aircraft engines, are produced as single crystals by a unidirectional solidification technique. However, several geometrical features of the turbine blade casting, e.g. abrupt change in the casting section, can lead to onset of freckles (‘channel segregates’) or formation of spurious/stray crystals, which severely deteriorate the creep-rupture life of single-crystal blades. Freckle appears as solute-enriched phases and long chain of equiaxed grains in the direction roughly parallel to the gravity. It is generally believed that the formation of freckles is caused by the thermo-solutal convection. Recent investigation by Ma and Bührig-Polaczek (2014) confirmed that the casting geometry significantly affected the onset of freckles during the unidirectional solidification.

Flemings et al. (1968) carried out a unidirectional solidification experiment with a casting sample of cross-section contraction, and they found a positive macrosegregation before the cross-section contraction, and a strong negative macrosegregation after the cross-section contraction. Ma et al. (2012) performed experiments to investigate the geometrical effect on the freckle formation in superalloy components. The sudden contraction of the cross-section revealed a promoting effect on the freckle onset. With cross section expansion, the freckles did not occur immediately after the cross-section expansion, but the freckles occurred after an incubation distance. The above experiments studies were extended by Hong et al. (2015) with numerical modelling, and improved knowledge about the freckle formation was obtained by considering the geometrical effect on the local heat transfer and flow pattern. In the Hong’s work macrosegregation was not directly modelled.

Ghods et al. (2016a) performed a unidirectional solidification experiment with both cross-section contraction and expansion between

* Corresponding author.

E-mail address: menghuai.wu@unileoben.ac.at (M. Wu).

<https://doi.org/10.1016/j.jmatprotec.2020.116913>

Received 19 May 2020; Received in revised form 10 August 2020; Accepted 21 September 2020

Available online 24 September 2020

0924-0136/© 2020 The Author(s).

Published by Elsevier B.V. This is an open access article under the CC BY-NC-ND license

(<http://creativecommons.org/licenses/by-nc-nd/4.0/>).

$\phi 9.5$ and $\phi 3.2$ mm in one cylindrical casting sample (Al-7 wt.% Si). In the meantime the authors Ghods et al. (2016b) did numerical analysis of the experiment. As a 2D planar simulation, instead of 2D axi-symmetrical or 3D simulation, was made, the modelling results could only be used to explain the experimental phenomena qualitatively. Although no notable freckle and spurious crystals were observed in the small casting sample, a few misoriented dendrite fragments near the sample surface were detected by Ghods et al. (2018). This unidirectional solidification experiment provides an excellent benchmark for further development of the numerical models.

A series of multiphase solidification models were developed. Wu et al. (2019) did a comprehensive review recently. Those models have been evaluated with some benchmark castings and also applied to predict the macrosegregation in large steel ingots. The current study uses a multiphase volume-average-based solidification model to simulate the Ghods' experiment. The main goal is to investigate the macrosegregation mechanism induced by the geometry as well as the potential impact of the casting geometry on the formation of spurious grains. A further goal is to verify the numerical model.

2. Model description and simulation settings

As-solidified casting samples are experimentally observed to be dominant in columnar structures. Therefore, a two-phase solidification model was considered here. Wu et al. (2016) have described details of this model. The main features/assumptions are outlined below.

- (1) The two phases refer to solid columnar and liquid melt.
- (2) The columnar morphology is simplified as cylinders growing unidirectionally along the temperature gradient. The columnar tip front is traced according to the LGK model reported by Lipton et al. (1984).
- (3) The arm spacing of the primary and secondary dendrites, λ_1 and λ_2 , taken from the as-solidified structure measured by Ghods et al. (2016a), are assumed to be constant during solidification.
- (4) The average liquid and solid concentrations are calculated. The solid-liquid interface is presumed to be thermodynamic equilibrium.

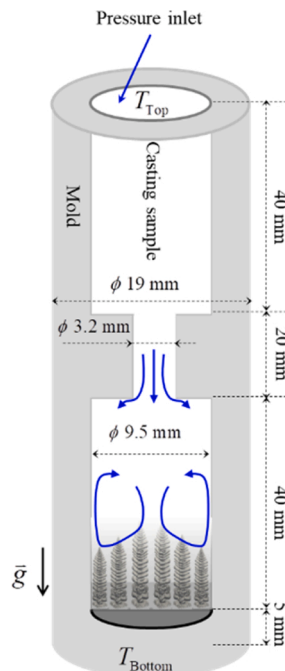


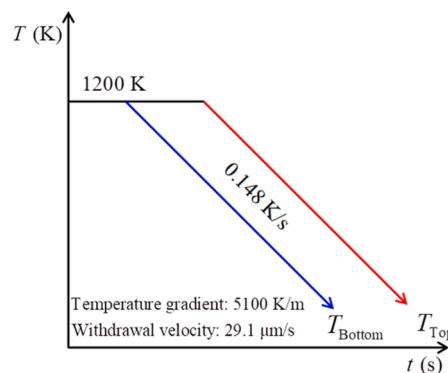
Fig. 1. Geometry configuration and boundary conditions.

Table 1

Summary of the material properties and other parameters (Ghods et al., 2016a; Zhang et al., 2020).

Properties/parameters	Symbol	Units	Values
Thermophysical			
Specific heat of the alloy	c_p^c, c_p^s	$\text{J kg}^{-1} \text{K}^{-1}$	1170.0
Specific heat of the mould	c_m	$\text{J kg}^{-1} \text{K}^{-1}$	1570.0
Latent heat	Δh_f	J kg^{-1}	4.0×10^5
Solid diffusion coefficient	D_c	$\text{m}^2 \cdot \text{s}^{-1}$	1.0×10^{-12}
Liquid diffusion coefficient	D_ℓ	$\text{m}^2 \cdot \text{s}^{-1}$	6.45×10^{-9}
Liquid thermal conductivity	k_ℓ	$\text{W m}^{-1} \text{K}^{-1}$	76.7
Solid thermal conductivity	k_s	$\text{W m}^{-1} \text{K}^{-1}$	185.0
Mould thermal conductivity	k_m	$\text{W m}^{-1} \text{K}^{-1}$	65.0
Liquid thermal expansion coefficient	β_T	K^{-1}	-1.85×10^{-4}
Liquid solutal expansion coefficient	β_c	$\text{wt.}\%^{-1}$	1.31×10^{-3}
Liquid density	ρ_ℓ	kg m^{-3}	2408.0
Solid density	ρ_s	kg m^{-3}	2545.0
Mould density	ρ_m	kg m^{-3}	2100.0
Viscosity	μ_ℓ	$\text{kg m}^{-1} \cdot \text{s}^{-1}$	1.16×10^{-3}
Thermodynamic			
Eutectic composition	c_{eu}	wt.%	12.6
Eutectic temperature	T_{eut}	K	850.15
Liquidus slope	m	$\text{K (wt.}\%)^{-1}$	-7.619
Equilibrium partition coefficient	k	-	0.131
Primary dendritic arm spacing	λ_1	μm	300.0
Secondary arm spacing	λ_2	μm	50.0
Gibbs Thomson coefficient	Γ	m K	2.41×10^{-7}
Melting point of the solvent	T_f	K	946.15
Others			
Initial concentration	c_0	wt.% Si	7.0
Initial temperature	T_0	K	1200.0
Cooling rate of the top and the bottom	R	K/s	0.148
Temperature gradient	\bar{G}	K/m	5100.0
Withdrawal velocity	v	$\mu\text{m/s}$	29.1

- (5) A shrinkage-induced flow is considered. According to Magnusson and Arnberg (2001), the density of the as-solidified eutectic phase



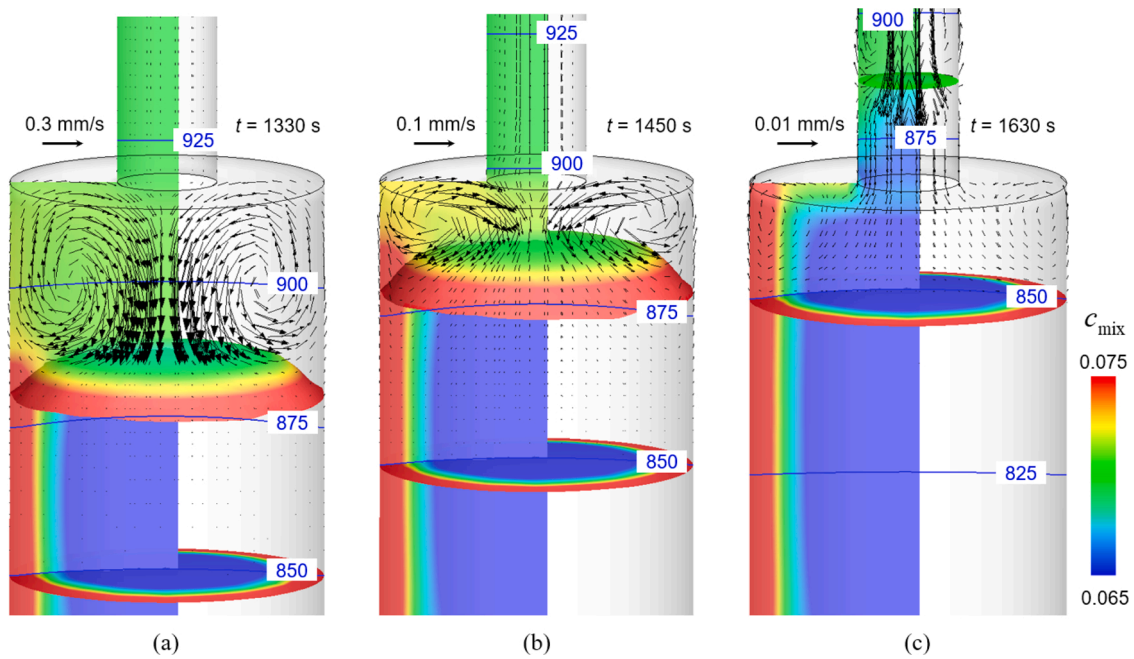


Fig. 2. Solidification sequence when the columnar tip front (iso-surface of $f_\ell = 0.95$) approaches and passes the position of the cross-section contraction: (a) $t = 1330$ s; (b) $t = 1450$ s; (c) $t = 1630$ s. Vectors on the vertical section of the sample indicate the liquid velocity, overlaid by isotherms (solid lines). Two iso-surfaces depict the mushy zone: top one for $f_\ell = 0.95$, bottom one for $T_{\text{eut}} = 850$ K. The colour in all the section/iso-surfaces denotes c_{mix} .

is similar to the density of the primary dendrites. The thermo-solutal convection is modelled using the Boussinesq approach.

- (6) As the secondary dendrite arm space changes during solidification due to the fact of coarsening, permeability of the mushy zone is treated as a function of the liquid volume fraction and primary dendrite arm space.
- (7) The mixture concentration is calculated by $c_{\text{mix}} = (f_\ell \cdot \rho_\ell \cdot c_\ell + f_c \cdot \rho_c \cdot c_c) / (f_\ell \cdot \rho_\ell + f_c \cdot \rho_c)$, and macrosegregation is characterized by the segregation index, $c^{\text{index}} = (c_{\text{mix}} - c_0) \times 100 / c_0$, in which c_ℓ and c_c are the concentrations of the liquid and columnar, respectively.

Ghods et al. (2016a) published the cooling conditions of the casting sample (Al-7.0 wt.% Si). A graphite crucible (mould) of 30 cm in length was used. The first part of the crucible cavity (casting sample) was 130 mm in length and $\phi 9.5$ mm in diameter; in the second part, the sample section was reduced to the diameter of $\phi 3.2$ mm for a length of 50 mm. In the third part, the sample section was increased to $\phi 9.5$ mm for a length of 120 mm. In the simulation, however, only 105 mm of the crucible is simulated, including the two large section zones and one small section zone, as displayed in Fig. 1. The reason why such a length is chosen will be discussed later. The calculation is initialized with a constant temperature (T_0) in the alloy and the crucible and a homogeneous solute distribution (c_0) in the alloy. On the top and bottom, a Dirichlet boundary condition (decreasing temperature: T_{Top} and T_{Bottom}), which corresponds to the experimentally imposed temperature gradient (\bar{G}) and withdrawal speed (v), is applied. The temperature boundary condition on the outer wall of the crucible is a spatial interpolation of T_{Top} and T_{Bottom} . A pressure inlet is applied on the top surface of the sample, and a hot melt is allowed to feed the solidification shrinkage. At the mould–alloy interface, a non-slip boundary condition is used for the melt flow. All the material properties of the alloy and the crucible can be found in Table 1.

The model is implemented in ANSYS FLUENT version 17.1. A control-volume based Eulerian–Eulerian multiphase solver is used. The maximum volume element (mesh) sizes are 3.5×10^{-4} m (3D) and

1.0×10^{-4} m (2D), respectively. The time step is set as 5×10^{-4} s. A maximum of 30 iterations per time step are conducted to ensure normalized residuals of the concentration and flow quantities, continuity below 10^{-4} , and enthalpy quantities below 10^{-7} . One 3D and 2D simulations requires 6 and 2 weeks, respectively, on a high-performance cluster (2.6 GHz, 28 cores).

3. Simulation results

3.1. Solidification process

The solidification sequence when the columnar tip front approaches and passes the position of the cross-section contraction is displayed in Fig. 2. The mushy zone is represented and confined by two iso-surfaces: top one for $f_\ell = 0.95$, and bottom one for T_{eut} . At $t = 1330$ s (Fig. 2(a)), the solidification front is still far from the position of the cross-section contraction. The thermal conductivity of the solid phase is higher than those of the graphite mould and liquid phase ($k_s \approx 2.5k_\ell$ or $2.8k_m$), and this causes a radial heat transfer from the graphite mould to the casting sample towards the solidification front. In the sample centre, a so-called ‘steeping convection’ is developed, and the solidification front is bulged. The bulk melt streams downwards to the sample centre against the solidification front, penetrating into the mushy zone, subsequently flows gradually along the curved profile of the mushy zone towards the periphery of the sample, and finally rises upwards at the sample surface. The solute-enriched interdendritic melt is gradually transported from the sample centre to the periphery. This type of solute transport causes a negative macrosegregation at the casting centre and a positive macrosegregation at the outer periphery. Concurrently, it causes a speed-up of the solidification in the sample centre and a slow-down of the solidification in the outer periphery. This suggests that the steeping convection accelerates itself, causing the solidification front to become more bulged. The liquid velocity reaches as high as $406 \mu\text{m/s}$, which is mainly driven by the thermo-solutal buoyancy. Zhang et al. (2018) studied the flow pattern and solute macrosegregation under pure shrinkage-induced feeding flow condition. They found that the pure shrinkage-induced feeding flow in this section was much slower ($1.3 \mu\text{m/s}$)

At 1450s, when the solidification front is approaching the position of

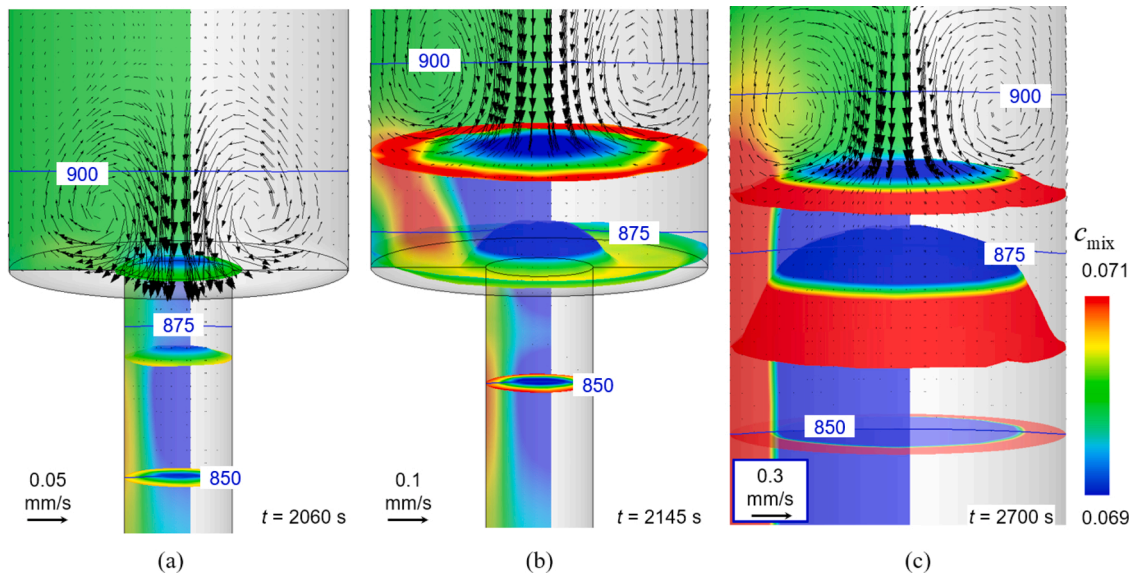


Fig. 3. Solidification sequence when columnar tip front (iso-surface of $f_\ell = 0.95$) reaches and passes the position of the cross-section expansion: (a) $t = 2060$ s; (b) $t = 2145$ s; (c) $t = 2700$ s. Vectors on the vertical section of the sample indicate the liquid velocity, overlaid by the isotherms (solid lines). The two iso-surfaces display the mushy zone: top one for $f_\ell = 0.95$, bottom one for $T_{eut} = 850$ K. An additional iso-surface ($f_\ell = 0.7$) is drawn in the mushy zone. The colour in all the section/iso-surfaces denotes c_{mix} .

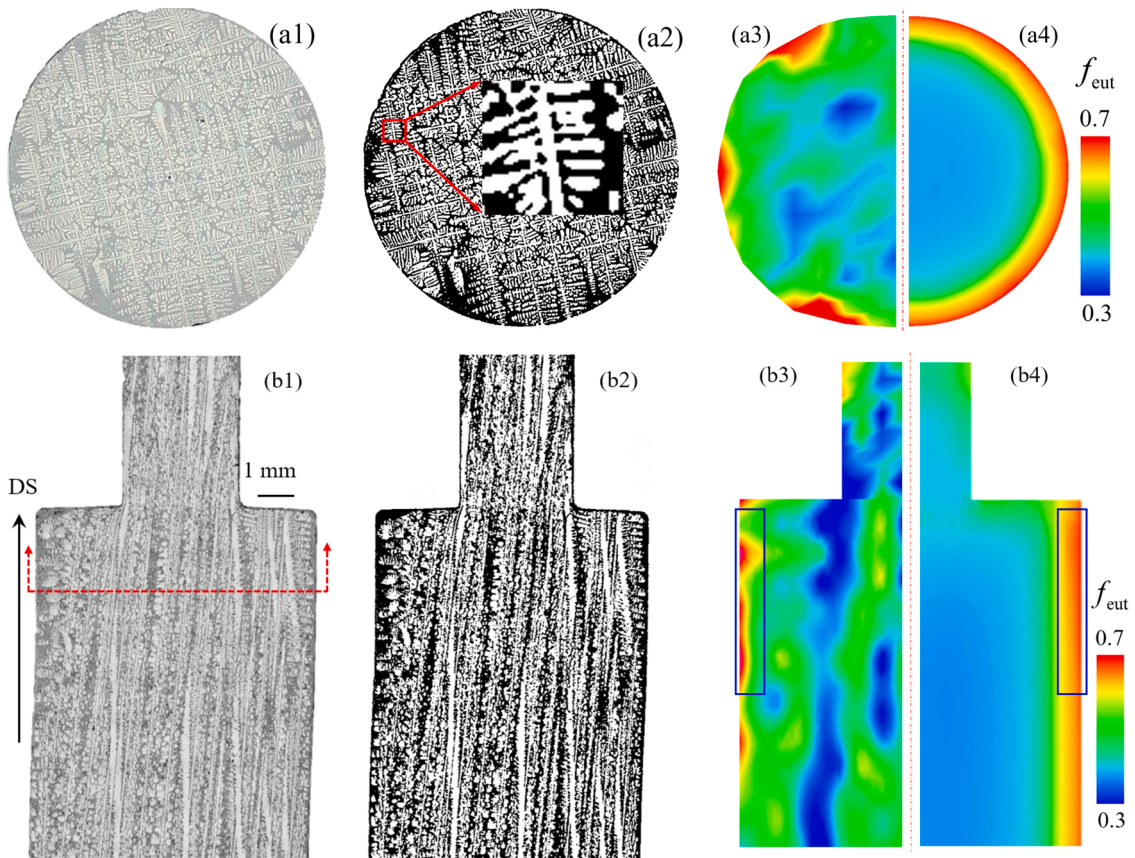


Fig. 4. Experiment–simulation comparison of the phase distribution. The first row displays the transverse section of the sample, and the second row depicts the vertical section of the sample. (a1) and (b1) Metallography with bright region denoting the primary dendrites and dark region denoting the eutectic phase. (a2) and (b2) Binary threshold images: primary dendrite is in white colour and eutectic phase is in black. (a3) and (b3) Distribution of the volume fraction of the eutectics (f_{eut}) from the experimental results. (a4) and (b4) Simulated distribution of f_{eut} . The position of the transverse section in the first row is marked by a dashed line in (b1). Figs. (a1) and (b1) are reproduced from (Ghods et al., 2016a, 2016b) with permission of Elsevier.

the cross-section contraction (Fig. 2(b)), the space for the bulk flow is largely limited to the volume between the columnar tip front and the ‘shoulder’ of the sample. Owing to this space limitation, the maximum liquid velocity reduces to $93 \mu\text{m/s}$. The solidification shrinkage-induced feeding flow in the small-section zone becomes more significant. Although the shrinkage-induced flow acts in the same direction as the thermo-solutal convection in the casting centre, it is not sufficient to compensate the effect of the space limitation. From c_{mix} , the bulk liquid between the columnar tip front and the sample shoulder enriched with solute can be seen.

Fig. 2(c) depicts the simulation result at 1630s when the solidification tip front passes the position of the cross-section contraction. Above the solidification front, the steeping convection also develops in a small section, but the bulk liquid velocity ($\sim 17 \mu\text{m/s}$) is weaker than that presented in Fig. 2(a). In the mush, the interdendritic melt flows downward to compensate the volume shrinkage. In the large cross-section zone, the steeping convection can still be observed in the mushy zone near the sample shoulder surface, but with a low intensity ($\sim 5 \mu\text{m/s}$). This interdendritic flow, despite its low intensity, strengthens the positive macrosegregation below the sample shoulders significantly. A solute-depleted region covering the whole cross-section of the sample is observed exactly above the cross-section contraction.

Fig. 3 displays the solidification sequence near the cross-section expansion. As the solidification front reaches the position of the cross-section expansion (Fig. 3(a)), the bulk flow is still quite weak ($50 \mu\text{m/s}$); only a weak negative macrosegregation forms at the sample centre. After the solidification front passes the cross-section expansion (Fig. 3(b)), a flow pattern similar to that in Fig. 2(a) develops. The iso-surface of $f_\ell = 0.7$ appears like a growing mushroom: a small cap develops from the contraction zone, which subsequently grows and extends sideways along the platform of the expansion region. At 2700s (Fig. 3(c)) the bulk flow becomes stronger ($243 \mu\text{m/s}$). The melt, as enriched with solute, accumulates near the sample surface, and suppresses the solidification locally. The solidification front becomes further bulged, and the aforementioned steeping convection continues again.

3.2. Model validation

3.2.1. Phase distribution

The numerically calculated eutectic phase distribution (f_{eut}) is compared with metallography performed on an as-cast sample, as displayed in Fig. 4. The Al-7.0 wt.% Si alloy mainly solidifies as primary aluminium dendrites with embedded eutectics. Fig. 4(a1) and (b1) present the original metallographic images. They were first converted to 8-bits, and subsequently the eutectic component was depicted in black and the primary aluminium dendrites in white (Fig. 4(a2) and (b2)) by adjusting the contrast ‘threshold’ in the ImageJ software. These black and white images were cut into small rectangular blocks of sizes $0.6 \times 0.6 \text{ mm}$ using MATLAB software. The area fraction of the black area in each block (e.g. a zoom-in view in Fig. 4(a2)) was counted, and the counting results are plotted as contours in Fig. 4(a3) and (b3). The eutectic phase distributes non-uniformly. Significant eutectic phase accumulates at the sample surface. The simulation results are displayed in Fig. 4(a4) and (b4). Consistent with the experimental results in Fig. 4(a3) and (b3), the eutectic phase accumulates near the sample surface, particularly before the cross-section contraction (the blue rectangles in Fig. 4(b3) and (b4)), whereas that in the sample centre is depleted. As reported by Ghods et al. (2016a), owing to the dendrite ‘clustering’ during the solidification, the microstructures in the different vertical sections are different. A better approach to validate the simulation results is to average the experimentally observed eutectic distribution in the different vertical sections, so that the dark blue region in Fig. 4(b3) disappears.

3.2.2. Macrosegregation

The experiment–simulation comparison of macrosegregation is presented in Fig. 5. The macrosegregation is characterized by its index ($c^{\text{index}} = (c_{\text{mix}} - c_0) \times 100/c_0$), where the c_{mix} is the mixture concentration of the primary dendrites and the eutectic phase. Ghods et al. (2016a) proposed a simple equation to evaluate the mixture concentration (c_{mix}). Experimentally, c_{mix} is derived from the experimentally

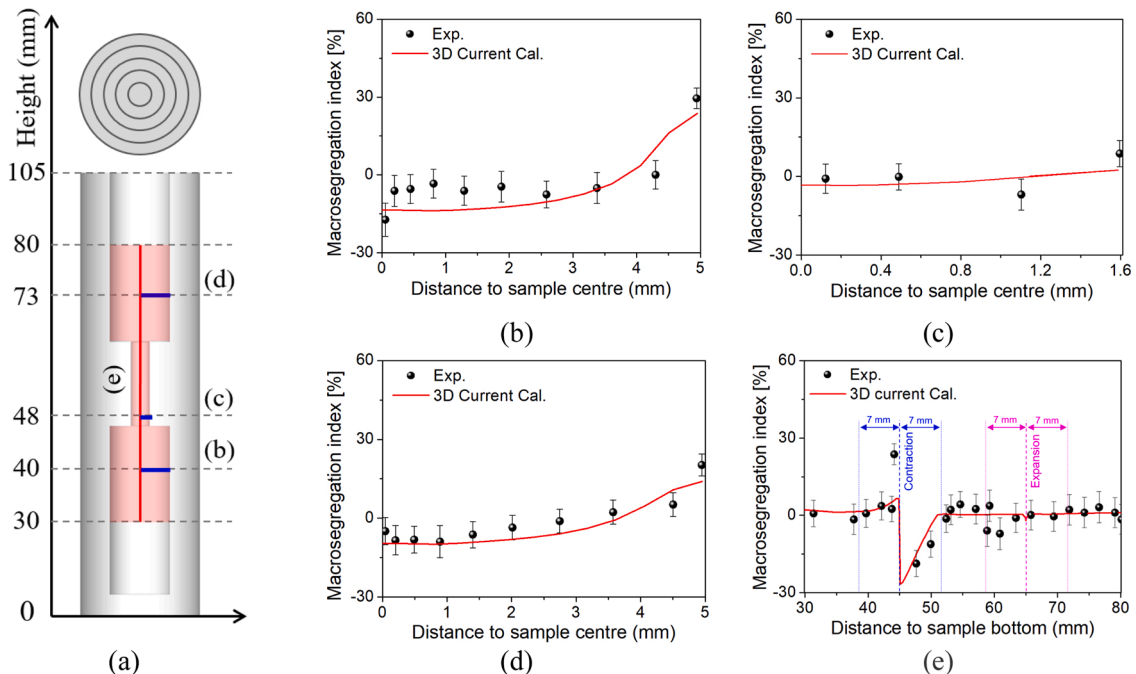


Fig. 5. Experiment–simulation comparison of the macrosegregation. (a) Schematic of the sample geometry and the evaluation method/positions for the macrosegregation measurement; (b)–(d) radial distribution of the macrosegregation (c^{index}) on different cross-sections, whose positions are marked in (a); (e) macrosegregation (section-averaged c^{index}) distribution along the axial direction. Black dots denote the experimental measurements, which are taken from Ghods et al. (2016b). The red lines denote the simulation results (For interpretation of the references to colour in this figure legend, the reader is referred to the web version of this article).

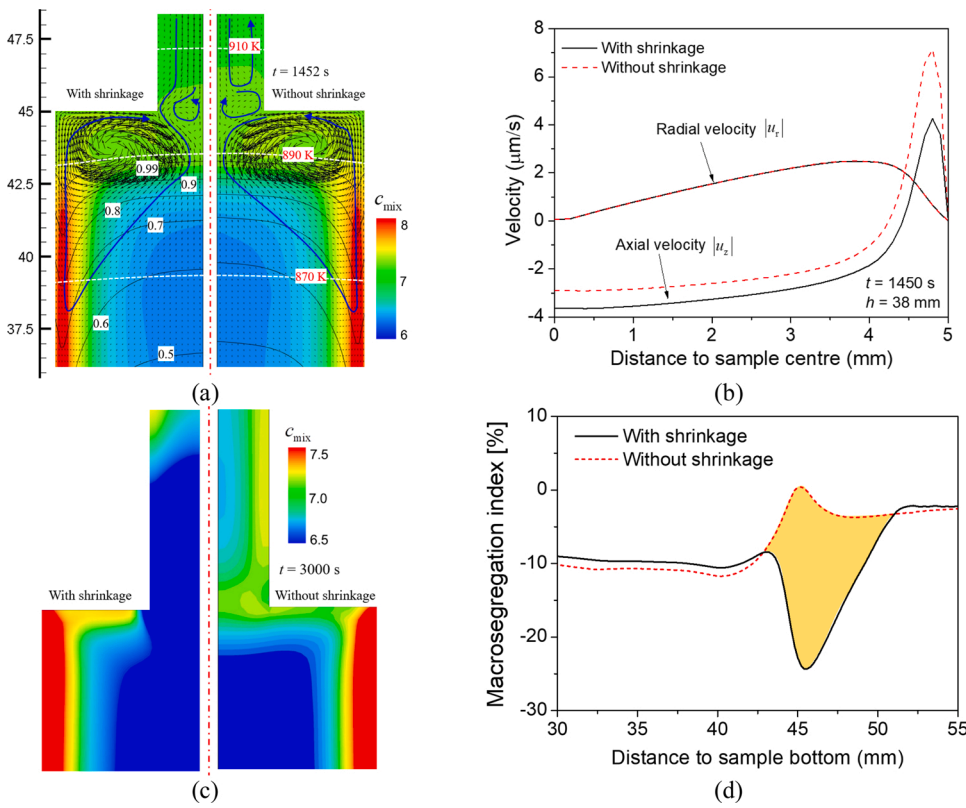


Fig. 6. Numerical analysis of the solidification shrinkage-induced feeding flow and its effect on the solidification by comparison of two simulation cases. Left-halves of (a) and (c) display the simulation case considering the solidification shrinkage in addition to the thermo-solutal convection; their right-halves display the simulation case ignoring shrinkage (pure thermo-solutal convection). (a) Contour of c_{mix} overlaid with isotherms (white dash lines), isopleths of the liquid volume fraction (dark solid lines), and vectors of the liquid velocity; the long blue vectors indicate the flow pattern; (b) comparison of the liquid velocity at the height of 38 mm; (c) c_{mix} contour at solidified state; (d) c_{mix} along the axis of the sample. These two cases were conducted with 2D axisymmetric model (For interpretation of the references to colour in this figure legend, the reader is referred to the web version of this article).

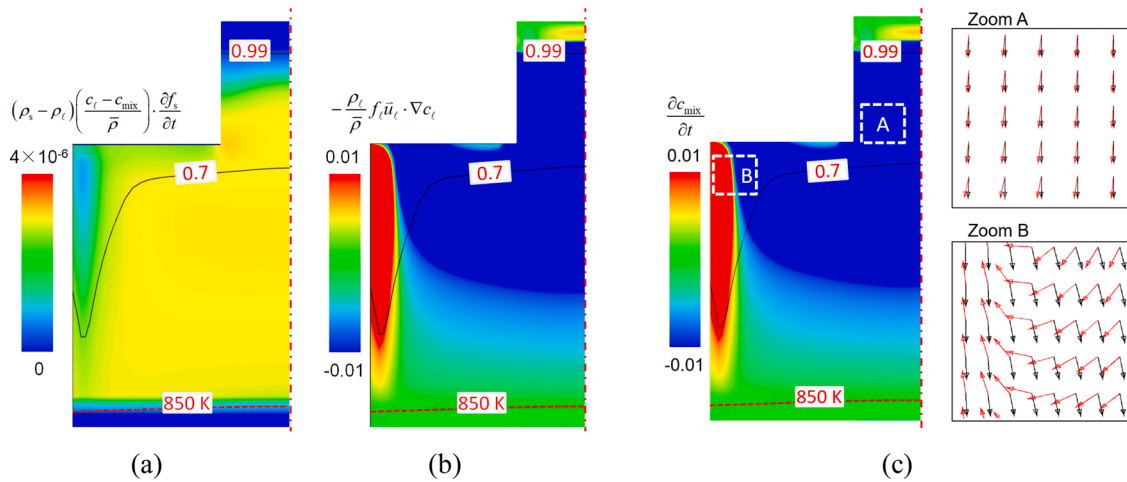


Fig. 7. Analyses of the macrosegregation mechanism for the moment at $t = 1580s$. (a) and (b) Contours of the first and second RHS terms in Eq. (1), overlaid by the isopleths of f_e (back solid lines) and T_{eut} (red dash lines); (c) zoom-views of \vec{u}_e (vectors in red) and ∇c_e (vectors in black) (For interpretation of the references to colour in this figure legend, the reader is referred to the web version of this article).

determined volume fraction of the eutectic phase (f_{eut}) based on $c_{mix} = (1.094 + 11.60f_{eut})/100$. To obtain the radial distribution of the macrosegregation, as schematically displayed in Fig. 5(a), a series of concentric neighbouring rings was drawn on the transverse section of this sample. The volume fraction of eutectic phase (f_{eut}) in each ring was determined by measuring the area fraction of the eutectic phase using ImageJ, so that the average mixture concentration in this ring was calculated. Using the same method, the average c_{mix} over each transverse section was estimated by evaluating f_{eut} on the corresponding section. Fig. 5(b)–(d) display the radial macrosegregation distributions on different transverse sections, whose positions are marked in Fig. 5(a). Excellent agreement between the experimental and the calculated

results is obtained. Fig. 5(e) illustrates the axial macrosegregation (c^{index}) distribution. Both the experimental and calculated results exhibit a significant positive macrosegregation before the cross-section contraction, and then show strong negative macrosegregation after the cross-section contraction. Finally, the negative macrosegregation gradually recovers to a neutral composition along the axial direction. A weak negative macrosegregation, with the local minimum c^{index} of 3%, is numerically predicted at the position of the cross-section expansion; this minor negative macrosegregation appears difficult to detect experimentally. Note that the experimentally detected positive macrosegregation before the section contraction is underestimated by the simulation. The main reason is as follows. At that instant, when the

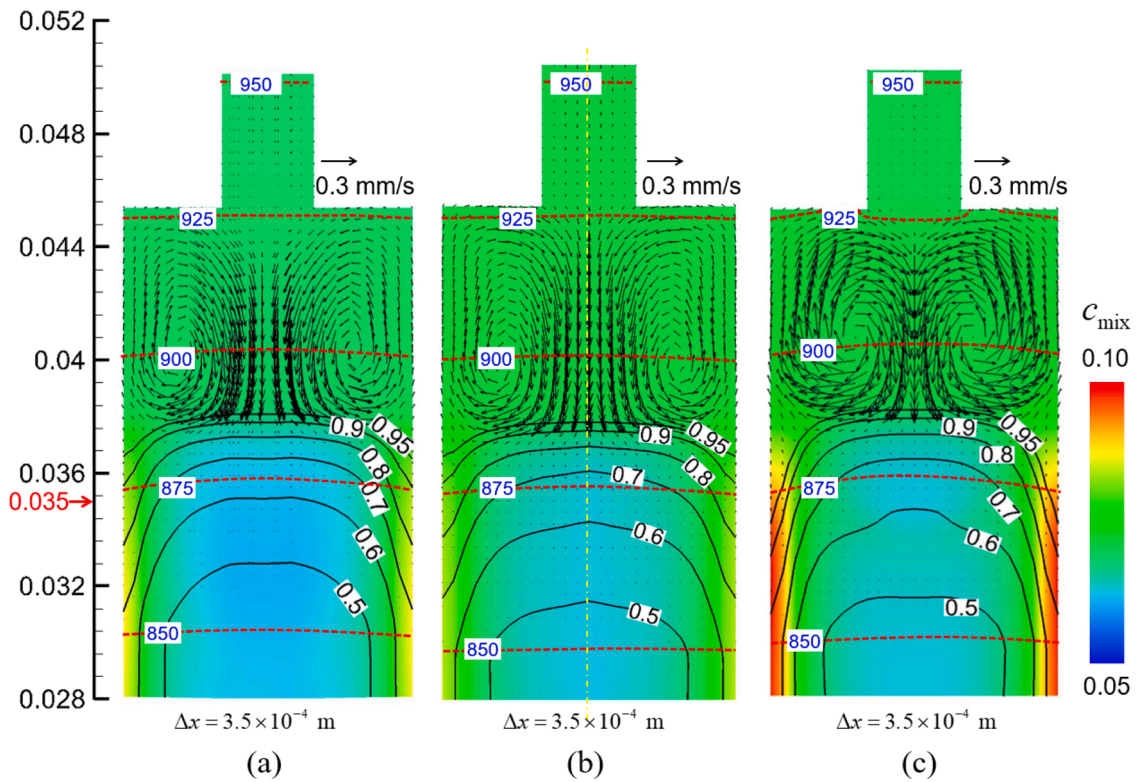


Fig. 8. Comparison of the simulations in 3D (a), 2D axis-symmetry (b) and 2D planar (c). The simulation results are evaluated at $t = 1272s$. Vectors denote the liquid velocity, colour scale represents c_{mix} , black solid lines are isopleths of f_l , and red dash lines denote isotherms (For interpretation of the references to colour in this figure legend, the reader is referred to the web version of this article).

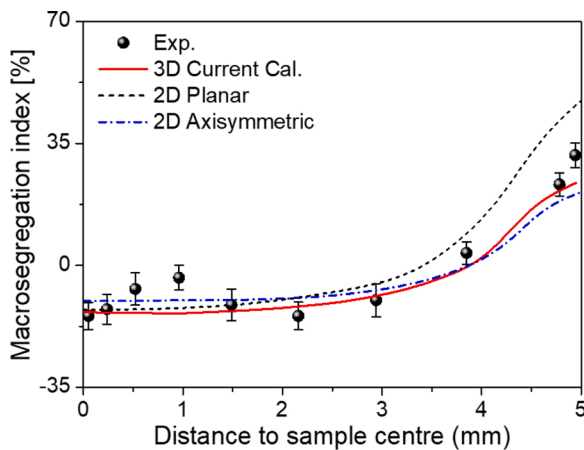


Fig. 9. Macroregregation (c^{index}) profiles in as-solidified sample along the radial direction as calculated in different dimensions, in comparison with the experimental measurements.

mushy zone is passing the position of the cross-section contraction, referring to Fig. 2(c), the as-solidified part of the sample shrinks and forms a gap between the sample and the mould, exactly below the shoulder; the interdendritic solute-enriched melt from the small section region is drained down and tends to feed the gap. This type of sample shrinkage and gap formation and the corresponding drainage and gap-feeding phenomena were ignored by the current model.

Note that the length of the sample used in the current simulation (100 mm) is shorter than the length of the sample in the experiments (300 mm). The reason is to reduce the calculation cost. The key feature of this sample is the cross-section change (contraction and expansion). In order to ensure the modelling accuracy, the length of the sample

before and after the cross-section change must be larger than the thickness of a mushy zone. The mushy zone thickness is estimated as $(T_\ell - T_{eut})/G$ i.e. ca. 7 mm. The length of the sample used in the current simulation (100 mm) is long enough to study the effect of the cross-section change on the solidification. In the first and third parts of the sample, where the diameter is $\phi 9.5$ mm, the length of the sample is 40 mm, ca. five times the thickness of the mushy zone. In the second part of the sample, where the diameter is $\phi 3.2$ mm, the length of the sample is equal to 20 mm, ca. three times of the thickness of the mushy zone. As shown in Fig. 5(e), only near the cross-section contraction region, strong macrosegregation occurs. 7 mm away from the cross-section change, no evident macrosegregation is observed, i.e. macrosegregation index is nearly zero.

3.3. Effect of shrinkage-induced feeding flow on macrosegregation

To study the effect of the solidification-shrinkage-induced feeding flow on the solidification, an additional case is simulated by ignoring the solidification shrinkage, e.g. by assuming $\rho_\ell = \rho_s$ while keeping the thermo-solutal convection (Boussinesq approach). The simulation results of this case ($t = 1450s$), in comparison to the previous case considering both solidification shrinkage and thermo-solutal convection, are presented in Fig. 6(a). Both the cases predict quite similar flow patterns and c_{mix} profiles in the large section zone. The isotherms and the isopleths of the liquid volume fraction are approximately the same. Main difference can be found in and near the small section zone. With the consideration of the shrinkage, a small vortex forms in the region of the section contraction. The melt from the small section flows downward besides the small vortex, to compensate the volume shrinkage in the mushy zone. Without the consideration of the shrinkage, a small vortex also forms there, but the melt in the small section is separated by this small vortex, so it cannot flow into the large section part.

The feeding flow is generally to compensate the solidification

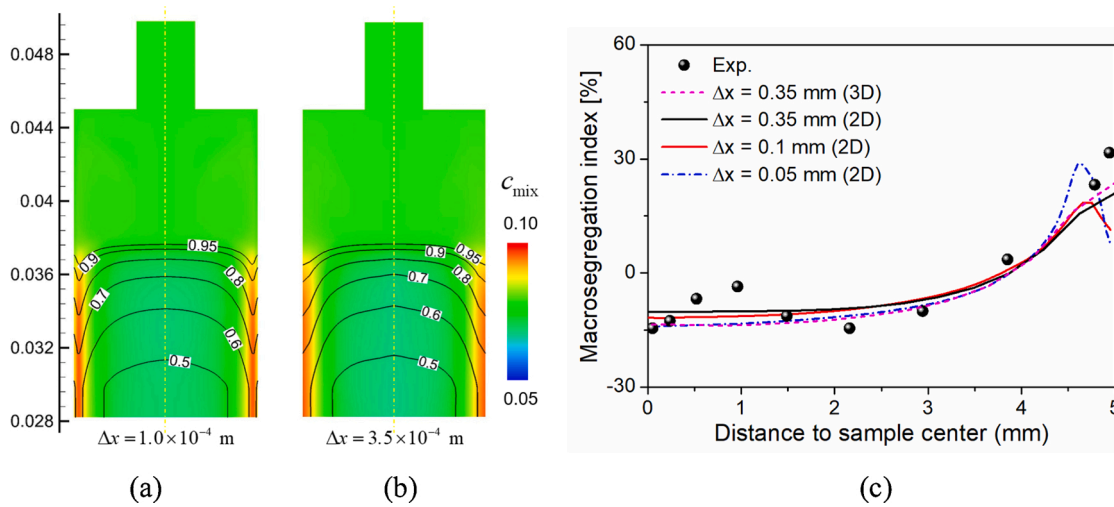


Fig. 10. Mesh sensitivity study. (a) and (b) contour of mixture concentration overlaid by the isolines of liquid phase fraction for cases with the fine mesh and the coarse mesh, respectively. (c) Macroseggregation profiles along the sample radius for different cases.

shrinkage. For this unidirectional solidification sample, the shrinkage-induced feeding flow is parallel to the melt convection in the sample centre, whereas near the sample surface, it is in the opposite direction to the melt convection. The liquid velocity components (u_r and u_z) are plotted in Fig. 6(b). The shrinkage-induced feeding flow has almost no effect on the radial flow, but it strengthens the axial flow in the central part and suppresses the axial flow near the sample surface.

Fig. 6(c) depicts the as-solidified c_{mix} distribution. Significant difference is found in the lower part of the small section zone: the negative macroseggregation there for the case considering the shrinkage is not predicted by the case ignoring the shrinkage. This difference is more clearly seen in Fig. 6(d), where the c_{mix} profiles along the sample axis are plotted. The orange area depicts the significant difference in the calculated c_{mix} of these two cases.

3.4. Mechanism of macroseggregation

Zhang et al. (2018) studied the feeding-flow-induced inverse segregation in the 1D solidification case. The simulation results were verified to be in line with the Flemings theory (Flemings et al., 1968). The following part is to analyse the feeding-flow-induced macroseggregation in multi-dimensions (2D or 3D) according to

$$\frac{\partial c_{mix}}{\partial t} = (\rho_s - \rho_\ell) \left(\frac{c_\ell - c_{mix}}{\rho} \right) \frac{\partial f_s}{\partial t} - \frac{\rho_\ell}{\rho} f_\ell \vec{u}_\ell \cdot \nabla c_\ell. \quad (1)$$

The derivation of this equation can be found in Appendix A. Corresponding to the two right hand side (RHS) terms in Eq. (1), the local variation rate of c_{mix} is the outcome of two contributions. The first term is related to the solidification shrinkage, and the second term is due to the melt flow, where the flow can be caused by the solidification shrinkage, thermo-solutal convection, or geometry. An example of the macroseggregation mechanism analysis for the moment at 1580s is presented in Fig. 7. The first RHS term is always positive; the second RHS term can be negative/positive depending on the directions of the flow (\vec{u}_ℓ) and the solute concentration gradient of the liquid phase (∇c_ℓ). The value of the second RHS term is several orders of magnitude larger than that of the first RHS term, indicating the dominant role of the second RHS term. Wu et al. (2008) found that if $f_\ell \vec{u}_\ell$ and ∇c_ℓ point in the similar direction (the angle less than 90°), the flow depletes the local c_{mix} . Specifically, the melt with a lower c_ℓ entering a region to replace the melt of a higher c_ℓ leads to depletion of c_{mix} . This mechanism operates in the small section zone (e.g. Zoom A of Fig. 7(c)). In the opposite situation (the angle larger than 90°), i.e. the melt with a higher c_ℓ entering a

region to replace the melt of a lower c_ℓ leads to an increase in c_{mix} . This mechanism operates near the sample surface of the large section zone (e.g. Zoom B of Fig. 7(c)).

4. Discussion

Excellent quantitative simulation–experiment agreement is achieved regarding the macroseggregation in the unidirectionally solidified sample with a specially-designed geometry (cross-section contraction or expansion). In principle, each detail of the macroseggregation can be explained, e.g. by Eq. (1). From Fig. 7, the melt flow (\vec{u}_ℓ) as part of the second RHS term of Eq. (1) plays the critical role in the formation macroseggregation, whereas from Figs. 2 and 3, \vec{u}_ℓ is largely dependent on the geometry. From this study, one can infer the importance of the geometry in some critical components, like turbine blades, which are cast with segregation-prone Ni-based superalloys. From computational fluid dynamics (CFD) perspective, all the flows are 3D in nature, and the numerical calculation accuracy depends on the mesh size. In this regard, some discussions are presented in the following sections.

4.1. 3D vs. 2D

Ghods et al. (2016a) have simulated the solidification process of this benchmark. Most experimentally observed phenomena were qualitatively explained. However, their simulations were based on a 2D planar model. In the current work, three simulations are conducted: full 3D, 2D axis-symmetry and 2D planar. They are compared in Figs. 8 and 9. The 2D axisymmetric calculation (Fig. 8(b)) can reproduce the 3D calculation well (Fig. 8(a)). The simulation results in 2D planar are displayed in Figs. 8(c) and 9. It can qualitatively reproduce the flow and the macroseggregation pattern, but the liquid velocity magnitude and the segregation severity are remarkably overestimated, particularly at the sample surface. Note that the above statement on the reproducibility of the full 3D calculation by the 2D axisymmetric calculation may be only applicable to the current casting sample possessing a small cross-section. For casting with large sections, the 3D nature of the flow may not be reproduced by a 2D asymmetrical model, even though the casting geometry is ideally asymmetrical.

4.2. Mesh sensitivity

Here only 2D axisymmetric calculations were conducted. The calculated macroseggregation in the as-cast sample using three mesh sizes

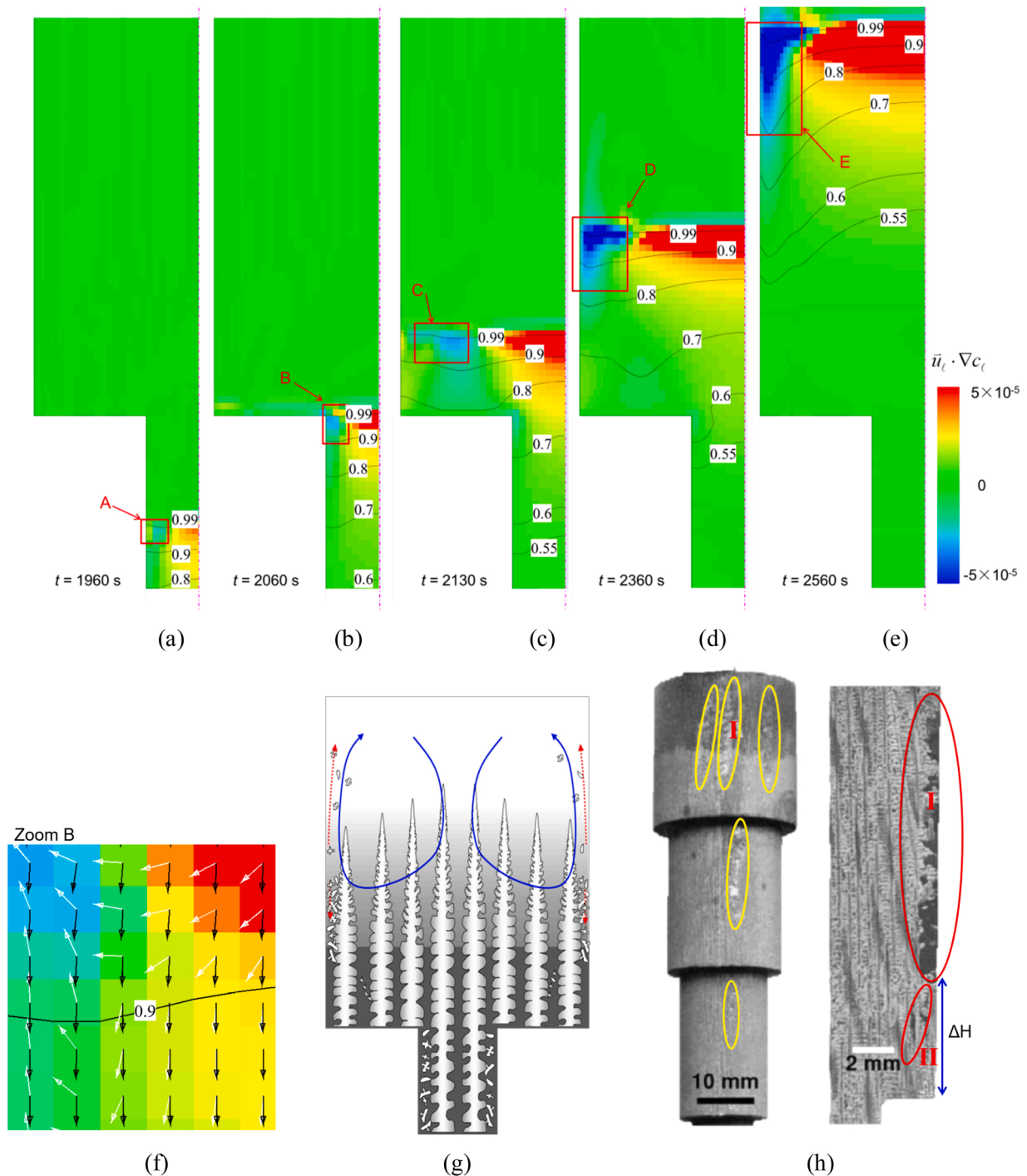


Fig. 11. Analysis of the possible formation of spurious/stray crystals. (a)–(e) Evolution sequence $\bar{u}_t \cdot \nabla c_t$ contours; (f) zoom-in view of Zoom B in (b); (g) schematics of the solidification and the melt flow; (h) Example of the stray crystals coupled with freckles in the laboratory castings. Figure (h) is cited from [Ma et al. \(2012\)](#), with permission of Springer Nature.

(0.35, 0.1, and 0.05 mm) are compared in [Fig. 10](#). The contours of the mixture concentration (c_{mix}) for cases with the fine mesh and the coarse mesh are shown in [Fig. 10\(a\)](#) and [\(b\)](#). They present similar segregation pattern. One minor difference between [Fig. 10\(a\)](#) and [\(b\)](#) is in the shape of the f_t isopleth near the sample surface. The details of the f_t distribution near the sample surface cannot be resolved appropriately by the coarse mesh (0.35 mm). Macrosegregation profiles along the sample surface for different cases with different mesh sizes are displayed in [Fig. 10\(c\)](#). All the simulations display similar segregation profiles. The abrupt change in c^{index} due to the abrupt change in the f_t distribution

near the sample surface is not resolvable when the mesh is coarse (0.35 mm). This can also be seen in [Figs. 8](#) and [9](#). When the simulation is conducted with a fine mesh smaller than 0.1 mm, the results can reproduce the experimental measurements well, except for one point at the sample surface. It can be concluded that the mesh size of 0.1 mm is sufficiently fine to predict all the details of the macrosegregation in this casting.

The experimental point on the casting surface, which is not correctly predicted by the simulation, may be owing to the ignorance of the shrinkage of the as-solidified dendrites in the mush by the model. It is

known that the dendrite networks in the mushy zone shrink and form a tiny gap between the casting and the mould; thus, the interdendritic melt feeds the gap, intensifying the positive segregation on the sample surface. As discussed in Section 3.2.2 (Fig. 5(e)), in the macrosegregation profile along the axial direction, a relatively large simulation error occurs near the position of the sample section extraction. This is also due to the ignorance of the shrinkage of the as-solidified part of the sample. In that case, a gap between the casting and the mould exactly below the shoulder is formed and the interdendritic melt from the small section region is drained down and tends to feed the gap. This type of sample shrinkage and gap formation and the corresponding drainage and gap-feeding phenomena must be considered in the future models. It is well known that material properties are important factor for the accuracy of the simulation results. They are mostly temperature dependent. Due to limited data resource, here they are treated as constant. The satisfied simulation-experiment agreement regarding to the macrosegregation distribution along the casting sample (Fig. 5) seems to verify that this simplification is acceptable for the case of the current laboratory experiment conditions. However, it is highly recommended more precise temperature-dependent properties should be used when this model is applied for simulation of engineering castings.

4.3. Possible formation of spurious crystals

As reported by Ma and Bührig-Polaczek (2014), spurious/stray crystals are serious casting defects during the production of turbine blades. They appear frequently along with the formation of freckles. Hellowell et al. (1997) believed that re-melting of the secondary or high-order dendrites, as enhanced by the interdendritic melt flow, is the main formation mechanism of the dendrite fragmentation, which serves as the origin of spurious/stray crystals. The detachment of fragments from the dendrite tip region of Al-10 wt.% Cu alloy was experimentally observed by Zimmermann et al. (2017). Zheng et al. (2018) have previously suggested a simple formulation in a three-phase solidification model for the crystal fragmentation: $M_{ce} = -\gamma \cdot \rho_\ell \cdot \vec{u}_\ell \cdot \nabla c_\ell$, where M_{ce} is the mass transfer rate from the columnar to equiaxed phases, attributed to the production of fragments (spurious crystals). This suggests that the interdendritic flow (\vec{u}_ℓ) in the direction opposite to the melt concentration gradient ($-\nabla c_\ell$) in the mush will promote fragmentation. However, this formulation cannot be used here to predict the formation of spurious crystals, because the so-called fragmentation coefficient, γ , is unknown and should be determined experimentally. Interestingly, the formation of spurious crystals appears to be strongly related to $\vec{u}_\ell \cdot \nabla c_\ell$, i. e. the same driving force for the onset of freckles (flow-induced macrosegregation). Therefore, $\vec{u}_\ell \cdot \nabla c_\ell$ is used here to analyse the possible formation of spurious crystals.

Fig. 11(a)–(e) display the evolution sequence of $\vec{u}_\ell \cdot \nabla c_\ell$. A zoom-in view of Zoom B, as marked by the red rectangle in Fig. 11(b), is presented in Fig. 11(f). In the ‘blue’ region with a negative value of $\vec{u}_\ell \cdot \nabla c_\ell$, where the angle between vectors \vec{u}_ℓ and ∇c_ℓ is larger than 90° , spurious crystals are prone to form. This blue region is mostly located close to the casting surface and near the front of mushy zone, where flow is still quite strong. With time evolution (from 1960 to 2560s), when the solidification front advances from the small cross-section to the large cross-section regions, the magnitude of $|\vec{u}_\ell \cdot \nabla c_\ell|$ increases, i. e. the probability to form spurious crystals increases. To assist in understanding the mechanism, the melt flow and the solidification are depicted in Fig. 11(g) schematically. The spurious crystals, attributed to the solute-driven re-melting of dendrites, possibly form near the sample surface. Few of them may be transported by the flow into the bulk liquid region and re-melted completely; however, most of them might be captured by the columnar dendrites and develop into freckle chains there.

Although no remarkable spurious crystals were observed on the sample of Al-7.0 wt.% Si alloy in Ghods’ experiments (Ghods et al.,

2018), several small misoriented dendrite fragments were detected. Ma et al. (2012) conducted a series of unidirectional solidification experiments with similar casting geometry (cross-section changes) on super-alloys, and more evidences were found. Specifically, the formation of spurious/stray crystals and freckle chain was correlated to the abrupt cross-section expansion, as displayed in Fig. 11(h). As reported by Ma et al. (2012), at the position of the abrupt section expansion, the freckle chain in the small cross-section zone cannot extend immediately along the bottom edge of the large cross-section zone, but it continues to appear after an incubation height of about $\Delta H = 10$. From the longitudinal section of the casting sample, it can be seen that below the position of the surface freckle chain (freckle I), a short but clear under-surface freckle (freckle II) forms. Although we did not perform the numerical simulations of the experiments as conducted by Ma et al. (2012), the current modelling results (Fig. 11(a)–(f)) provide relevant information to explain the experimental observations. Immediately after the solidification front passes the position of the cross-section expansion (Figs. 3(a) and 11(b)), the flow is so weak that spurious crystals may not form. In the next moment, Figs. 3(b) and 11(c), the flow becomes stronger but is still not sufficiently strong to form freckle and spurious crystals at the sample surface; some under-surface freckle (freckle II) may form. Only when the flow is sufficiently strong (Figs. 3(c) and 11(d) and (e)), surface freckles (freckle I) can generate.

5. Conclusions

In this study, a two-phase solidification model is employed to simulate the solidification benchmark with cross-section changes (Ghods et al., 2016a). Along the solidification direction, the diameter of the sample changes between $\phi 9.5$ and $\phi 3.2$ mm, highlighting the geometrical effect on the solidification. Excellent agreement is obtained between the experiment and the simulation regarding macrosegregation and phase distribution in the as-solidified sample. The numerical model is verified.

The main effect of the geometry on the unidirectional solidification is the modification of the bulk and the interdendritic flow during solidification, leading to the formation of macrosegregation and spurious/stray crystals in several critical locations.

- The flow originates from the solidification shrinkage and the thermo-solutal convection. Without any cross-sectional change, the thermo-solutal buoyancy dominates the flow, and a so-called ‘steeping convection’ is induced, leading to a relatively strong positive macrosegregation near the sample surface.
- With the cross-section contraction, the space for the flow is largely limited by the sample geometry, and a severe positive macrosegregation under the ‘shoulder’ of the cross-section contraction is induced.
- The solidification-shrinkage-induced feeding flow is magnified in the small cross-section part, where a negative segregation is formed.
- The cross-section expansion in the geometry leads to a high risk for the formation of spurious/stray crystals.

A mathematical equation (Eq. (1)) is derived to analyse the macrosegregation. The scalar product of the flow velocity and the concentration gradient of the melt ($\vec{u}_\ell \cdot \nabla c_\ell$) can be used to analyse the formation of macrosegregation and spurious/stray crystals.

- Positive and negative segregation occur at the locations where the negative and positive values of $\vec{u}_\ell \cdot \nabla c_\ell$ are distributed, respectively.
- Freckles and spurious crystals are formed at the locations where the negative value of $\vec{u}_\ell \cdot \nabla c_\ell$ is distributed.

The numerical simulation accuracy regarding the mesh quality is validated. Full 3D, 2D axi-symmetry, and 2D planar simulations are

compared. For the current cylindrical sample having a small diameter, the 2D axi-symmetry simulation can reproduce the result of the full 3D calculation.

CRedit authorship contribution statement

Haijie Zhang: Conceptualization, Methodology, Investigation, Writing - original draft, Visualization. **Menghuai Wu:** Conceptualization, Methodology, Writing - review & editing, Project administration. **Surendra N. Tewari:** Conceptualization, Validation, Writing - review & editing. **Andreas Ludwig:** Conceptualization, Supervision. **Abdellah**

Kharicha: Conceptualization, Software.

Declaration of Competing Interest

None.

Acknowledgements

This work was supported by FFG – ASAP (No. 859777), FWF (I 4278 - N36), and ESA - MICAST. Support from NASA grant NNX14AM18G is gratefully acknowledged.

Appendix A. Solidification-shrinkage-induced macrosegregation

The mixture density, ($\bar{\rho}$),

$$\bar{\rho} = f_\ell \rho_\ell + f_s \rho_s. \quad (\text{A.1})$$

The mass conservation equations are

$$\frac{\partial(f_s \rho_s)}{\partial t} + \nabla \cdot (f_s \rho_s \vec{u}_s) = M_{\ell s}, \quad (\text{A.2})$$

$$\frac{\partial(f_\ell \rho_\ell)}{\partial t} + \nabla \cdot (f_\ell \rho_\ell \vec{u}_\ell) = -M_{\ell s}, \quad (\text{A.3})$$

where $M_{\ell s}$ indicates the mass transfer rate from the liquid to the solid.

The sum of Eq. (A.2) and Eq. (A.3) yields

$$\frac{\partial \bar{\rho}}{\partial t} = -\nabla \cdot (f_\ell \rho_\ell \vec{u}) \quad (\text{A.4})$$

The species conservation equations are

$$\frac{\partial(f_s \rho_s c_s)}{\partial t} + \nabla \cdot (f_s \rho_s c_s \vec{u}_s) = \nabla \cdot (f_s \rho_s D_s \nabla c_s) + C_{\ell s}, \quad (\text{A.5})$$

$$\frac{\partial(f_\ell \rho_\ell c_\ell)}{\partial t} + \nabla \cdot (f_\ell \rho_\ell c_\ell \vec{u}_\ell) = \nabla \cdot (f_\ell \rho_\ell D_\ell \nabla c_\ell) - C_{\ell s}, \quad (\text{A.6})$$

where $C_{\ell s}$ is the species exchange between the solid and the liquid.

By ignoring the solute diffusion at the macroscopic scale ($D_\ell = D_s = 0$), the sum of Eq. (A.5) and (A.6) yields

$$\bar{\rho} \frac{\partial c_{\text{mix}}}{\partial t} + c_{\text{mix}} \frac{\partial \bar{\rho}}{\partial t} + c_\ell \nabla \cdot (f_\ell \rho_\ell \vec{u}_\ell) + f_\ell \rho_\ell \vec{u}_\ell \cdot \nabla c_\ell = 0. \quad (\text{A.7})$$

Substituting Eq. (A.4) into (A.7), the varying rate of the mixture concentration is obtained as follows:

$$\frac{\partial c_{\text{mix}}}{\partial t} = (\rho_s - \rho_\ell) \left(\frac{c_\ell - c_{\text{mix}}}{\bar{\rho}} \right) \frac{\partial f_s}{\partial t} - \frac{\rho_\ell}{\bar{\rho}} f_\ell \vec{u} \cdot \nabla c_\ell. \quad (\text{A.8})$$

References

- Flemings, M.C., Mehrabian, R., Nereo, G.E., 1968. Macrosegregation: part II. *Trans. Metall. Soc. AIME* 241, 41–49.
- Ghods, M., Johnson, L., Lauer, M., Grugel, R.N., Tewari, S.N., Poirier, D.R., 2016a. Radial macrosegregation and dendrite clustering in directionally solidified Al-7Si and Al-19Cu alloys. *J. Cryst. Growth* 441, 107–116. <https://doi.org/10.1016/j.jcrysgro.2016.02.014>.
- Ghods, M., Johnson, L., Lauer, M., Grugel, R.N., Tewari, S.N., Poirier, D.R., 2016b. Macrosegregation in Al-7Si alloy caused by abrupt cross-section change during directional solidification. *J. Cryst. Growth* 449, 134–147. <https://doi.org/10.1016/j.jcrysgro.2016.06.010>.
- Ghods, M., Lauer, M., Upadhyay, S.R., Grugel, R.N., Tewari, S.N., Poirier, D.R., 2018. Spurious grain formation at cross-sectional expansion during directional solidification: influence of thermosolutal convection. *J. Mater. Eng. Perform.* 27, 3122–3130. <https://doi.org/10.1007/s11665-018-3364-0>.
- Hellawell, A., Liu, S., Lu, S.Z., 1997. Dendrite fragmentation and the effects of fluid flow in castings. *JOM* 49, 18–20. <https://doi.org/10.1007/BF02914650>.
- Hong, J., Ma, D., Wang, J., Wang, F., Dong, A., Sun, B., Bührig-Polaczek, A., 2015. Geometrical effect of freckle formation on directionally solidified superalloy CM247 LC components. *J. Alloys. Compd.* 648, 1076–1082. <https://doi.org/10.1016/j.jallcom.2015.07.016>.
- Lipton, J., Glicksman, M.E., Kurz, W., 1984. Dendritic growth into undercooled alloy metals. *Mater. Sci. Eng.* 65, 57–63. [https://doi.org/10.1016/0025-5416\(84\)90199-X](https://doi.org/10.1016/0025-5416(84)90199-X).
- Ma, D., Bührig-Polaczek, A., 2014. The geometrical effect on freckle formation in the directionally solidified superalloy CMSX-4. *Metall. Mater. Trans. A Phys. Metall. Mater. Sci.* 45, 1435–1444. <https://doi.org/10.1007/s11661-013-2088-x>.
- Ma, D., Wu, Q., Bührig-Polaczek, A., 2012. Some new observations on freckle formation in directionally solidified superalloy components. *Metall. Mater. Trans. B Process Metall. Mater. Process. Sci.* 43, 344–353. <https://doi.org/10.1007/s11663-011-9608-0>.
- Magnusson, T., Arnberg, L., 2001. Density and solidification shrinkage of hypoeutectic aluminum-silicon alloys. *Metall. Mater. Trans. A Phys. Metall. Mater. Sci.* 32, 2605–2613. <https://doi.org/10.1007/s11661-001-0050-9>.
- Wu, M., Könözy, L., Ludwig, A., Schützenhöfer, W., Tanzer, R., 2008. On the formation of macrosegregations in steel ingot castings. *Steel Res. Int.* 79, 637–644. <https://doi.org/10.1002/srin.200806177>.
- Wu, M., Zheng, Y., Kharicha, A., Ludwig, A., 2016. Numerical analysis of macrosegregation in vertically solidified Pb-Sn test castings – part I: columnar

- solidification. *Comput. Mater. Sci.* 124, 444–455. <https://doi.org/10.1016/j.commatsci.2016.07.017>.
- Wu, M., Ludwig, A., Kharicha, A., 2019. Volume-averaged modeling of multiphase flow phenomena during alloy solidification. *Metals (Basel)* 9, 229. <https://doi.org/10.3390/met9020229>.
- Zhang, H., Wu, M., Zheng, Y., Ludwig, A., Kharicha, A., 2018. Macrosegregation formation in an Al–Si casting sample with cross-sectional change during directional solidification. *Trans. Indian Inst. Met.* 71, 2639–2643. <https://doi.org/10.1007/s12666-018-1422-9>.
- Zhang, H., Wu, M., Zheng, Y., Ludwig, A., Kharicha, A., 2020. Numerical study of the role of mush permeability in the solidifying mushy zone under forced convection. *Mater. Today Commun.* 22, 100842. <https://doi.org/10.1016/j.mtcomm.2019.100842>.
- Zheng, Y., Wu, M., Kharicha, A., Ludwig, A., 2018. Incorporation of fragmentation into a volume average solidification model. *Model. Simul. Mater. Sci. Eng.* 26, 015004. <https://doi.org/10.1088/1361-651X/aa86c5>.
- Zimmermann, G., Pickmann, C., Hamacher, M., Schaberger-Zimmermann, E., Neumann-Heyme, H., Eckert, K., Eckert, S., 2017. Fragmentation-driven grain refinement in directional solidification of AlCu10wt-% alloy at low pulling speeds. *Acta Mater.* 126, 236–250. <https://doi.org/10.1016/j.actamat.2016.12.063>.

Directional Solidification of AlSi7Fe1 Alloy Under Forced Flow Conditions: Effect of Intermetallic Phase Precipitation and Dendrite Coarsening



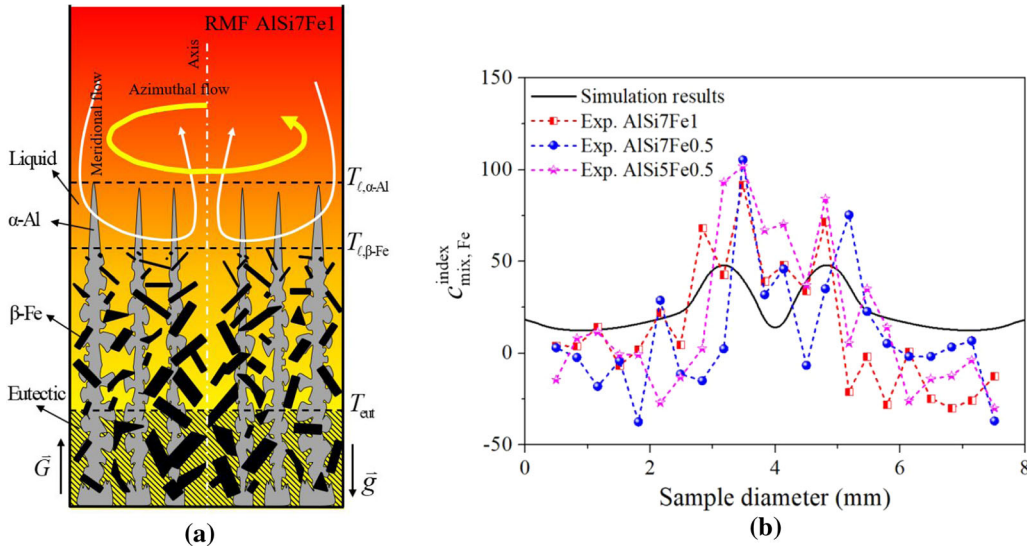
HAIJIE ZHANG, MENGHUAI WU, CHRISTIAN M.G. RODRIGUES,
ANDREAS LUDWIG, and ABDELLAH KHARICHA

A forced flow was experimentally shown to influence the solidification microstructure of metal alloys by modifying the coarsening/ripening law. In some technical alloys (AlSi7Fe1), this flow effect can also be significantly suppressed due to the formation of intermetallic precipitates (β -Al₃FeSi) that can block the flow in the mushy region. The forced flow was induced by a rotating magnetic field (RMF). Herein, a three-phase volume-average-based solidification model is introduced to reproduce the above experiment. The three phases are the melt, the primary solid phase of columnar dendrites, and the second solid phase of intermetallic precipitates. The dynamic precipitation of the intermetallic phase is modelled, and its blocking effect on the flow is considered by a modified permeability. Dendrite coarsening, which influences the permeability, is also considered. The RMF induces a strong azimuthal flow and a relatively weak meridional flow (Ekman effect) at the front of the mushy zone during unidirectional solidification. This forced flow reduces the mushy zone thickness, induces the central segregation channel, affects the distribution of the intermetallic precipitates, and influences dendrite coarsening, which in turn modifies the interdendritic flow. Both interdendritic flow and the microstructure formation are strongly coupled. The modelling results support the explanation of Steinbach and Ratke—the formed intermetallic precipitates (β -Al₃FeSi) can block the interdendritic flow, and hence influence the coarsening law. The distribution of β -Al₃FeSi is dominantly influenced by the flow-induced macrosegregation. The simulation results of the Si and Fe distribution across the sample section are compared with the experimental results, showing good simulation–experiment agreement.

HAIJIE ZHANG, MENGHUAI WU, CHRISTIAN M.G. RODRIGUES, ANDREAS LUDWIG, and ABDELLAH KHARICHA are with the Chair for Simulation and Modeling of Metallurgy Processes, Department of Metallurgy, University of Leoben, Franz-Josef-Str. 18, 8700 Leoben, Austria. Contact e-mail: menghuai.wu@unileoben.ac.at.

Manuscript submitted January 18, 2021; accepted April 14, 2021.

During alloy solidifications the flow can influence the mushy zone by inducing macrosegregation, modifying the solidification microstructure, and influencing the formation of intermetallic precipitates. The resulting microstructural features can in turn affect the melt flow by changing the flow intensity and flow pattern. A three-phase volume-average-based solidification model is introduced to study the flow-solidification interaction, and hence to improve the knowledge on the formation mechanism of intermetallics and their effect on solidification. (a) Schematic for the flow pattern and formation of different phases; (b) experiment–simulation comparison of macrosegregation (Fe) across the diameter of as-solidified sample.



<https://doi.org/10.1007/s11661-021-06295-5>
© The Author(s) 2021

I. INTRODUCTION

MELT flow is a natural phenomenon that occurs during the alloy solidification of almost all casting processes. The flow can influence the mushy zone by inducing macrosegregation,^[1] modifying the solidification microstructure,^[2] causing fragmentation,^[3] and even influencing the formation of precipitates.^[4] The resulting microstructural features in the mushy zone can in turn affect the fluid flow by changing the flow intensity and flow pattern.^[5] A recent experimental study has demonstrated the importance of the above flow-solidification interaction in the formation of the microstructure, *i.e.*, the flow can adapt the coarsening law.^[2, 6] Classically, the coarsening law is described by the correlation between the secondary dendrite arm spacing (λ_2) and the local solidification time (t_f)^[7,8]:

$$\lambda_2 = A(M \cdot t_f)^b, \quad [1]$$

where A is a geometric magnification factor, M is the alloy-dependent magnification factor, and b is the ripening exponent. Under pure diffusive conditions (or when the flow is negligible), b should be 1/3. Unidirectional solidification experiments on the alloy AlSi7 showed that the ripening exponent (b) increased to 1/2 when a forced flow was imposed by applying a rotating

magnetic field (RMF).^[2,6] Interestingly, the same experiments were repeated with another alloy (AlSi7Fe1) in which intermetallic precipitates formed (β -Al₅FeSi) during solidification, and the results showed that the applied RMF seemed to have no influence on the coarsening/ripening law, *i.e.*, b was maintained at 1/3. A tentative explanation for the undisturbed $\lambda_2 - t_f$ relationship in the solidification of AlSi7Fe1 under RMF is that the formation of the intermetallic precipitates (β -Al₅FeSi) suppresses the interdendritic flow, so that the conditions of solidification and the corresponding coarsening/ripening phenomenon approaches the pure diffusive case.^[6,9]

The motivation of the current work is to use a modelling approach to reproduce the above experiments, focusing on the blocking effect of intermetallic precipitates on the flow and its further impact on the microstructure formation. The influence of β -Al₅FeSi on the flow permeability in the interdendritic mushy region was analysed by Puncreobutr *et al.*^[10] for the alloy Al-7.52Si-3.53Cu-0.59Fe. A 4D *in situ* synchrotron X-ray tomography technique was used to reconstruct the microstructure including the primary aluminium dendrites and precipitates during solidification (Figure 1(a)), which was further used to perform computational fluid dynamics (CFD) calculations to estimate the permeability (Figure 1(b)). The results

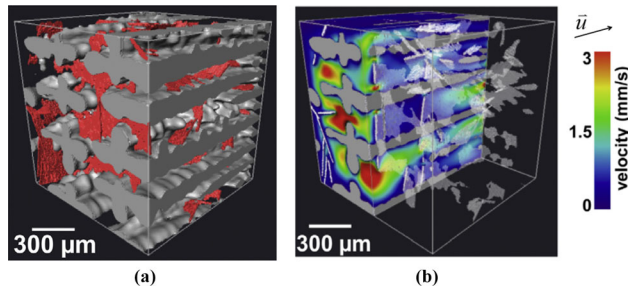


Fig. 1—CFD study of the effect of intermetallic precipitates on the interdendritic flow. (a) Reconstruction of the primary aluminium dendrites (grey) and intermetallic precipitates (red) and (b) liquid velocity at solid fraction of 0.33 (848 K (575 °C)). Reprinted from reference,^[10] under the terms of the Creative Commons CC BY license.

demonstrated the blocking effect of the intermetallic phase on the fluid flow, particularly in the direction parallel to the primary dendrites.

In most numerical models λ_2 was usually assumed to be a constant value for calculating the mushy permeability, and it was taken from the as-solidified structure.^[5,11] This assumption may reduce the credibility of the numerical model, as λ_2 is known to change with time due to coarsening/ripening. Recently, a general coarsening equation that accounts for the effects of growth, curvature-driven coarsening, and interface coalescence was proposed by Neumann-Heyme *et al.*^[12] The interfacial area density (S_v) was described as a function of the local liquid volume fraction and time. The growth and coarsening of dendrites can then be considered via a time-dependent λ_2 that is expressed by a λ_2 - S_v relation, suggested by Li and Beckermann,^[13] into the interfacial area density equation of Neumann-Heyme *et al.*^[12] This makes it possible to consider the effect of dendrite coarsening on the flow.

In the current study, a three-phase volume-average-based solidification model^[14,15] is modified to simulate the solidification of an AlSi7Fe1 alloy. The three phases are the melt, the primary solid phase of columnar dendrites, and the second solid phase of intermetallic precipitates. The growth/coarsening of the dendrites of the primary phase is considered, and the formation/growth of the intermetallic precipitates is also modelled. The block effect of the intermetallic precipitates on the flow is considered through the f_β -dependent permeability. The main goal is to quantify the effect of the intermetallic phase and dendrite coarsening on the solidification of AlSi7Fe alloy under RMF, and hence to explain the experimental results of Steinbach *et al.*,^[6] *i.e.*, the experimental observation of $b = 1/3$ (coarsening/ripening law exponent) in the presence of RMF when sufficient intermetallic precipitates are present. Although the solidification of AlSi7Fe1 alloy was also numerically studied by Budenkova *et al.*,^[16] the blocking effect of the precipitates and the dendrite coarsening were ignored.

II. MODEL DESCRIPTION

A multiphase volume-average-based solidification model was previously developed by Wu *et al.*^[15,17] Herein, this volume-average-based solidification model is modified to consider the formation of intermetallic precipitates (β -Al₅FeSi). Three phases are considered—the liquid melt, the columnar dendrites as the first solid phase, and the intermetallic precipitates as the second solid phase. The columnar dendrites are simplified as cylinders growing unidirectionally along the temperature gradient, and their tips are traced according to the Lipton–Glicksman–Kurz (LGK) model.^[18] The intermetallic phase (β -Al₅FeSi precipitates) forms during the binary eutectic solidification. A thermodynamic equilibrium is presumed at the solid–liquid interface. The concentration differences between the thermodynamic equilibrium concentration of the liquid melt at the solid–liquid interface and the volume-averaged liquid concentration serve as the driving force for the growth of columnar dendrites and intermetallic precipitates. The resistance of the mushy zone (columnar dendrites and precipitates) to the fluid flow is calculated using a modified permeability model.^[10] The primary dendrite arm spacing is taken from previous experiments,^[6,9] while the secondary dendrite arm spacing follows the ripening law.^[12] The most important model features are described below.

A. Phase Definition and Corresponding Mass Transfer Rate

The solidification of the AlSi7Fe1 alloy starts with the development of primary aluminium dendrites, followed by the formation of β -Al₅FeSi during the binary eutectic reaction, and ends with the ternary eutectic reaction at 850 K. Previous experiments^[6,9] did not provide evidence of equiaxed crystals in the sample. Therefore, we ignore the equiaxed phase in the current model. The three phases (the liquid melt, the columnar dendrites, and the intermetallic β -Al₅FeSi precipitates) are quantified by their volume fractions— f_ℓ , f_c , and f_β . The solidification of the columnar trunks and the formation of intermetallic precipitates are modelled differently. The small part of α -Al phase which forms during the binary and ternary eutectic reactions is considered a further growth of the primary columnar trunks. The columnar trunks are assumed to be rigid and stationary, and the formed β -Al₅FeSi is assumed to be immediately captured by columnar dendrites, making them also rigid/stationary.^[19,20] According to the latest work published by Puncreobutr *et al.*,^[21] nucleation of β -Al₅FeSi is presumed to occur instantaneously on/near the primary aluminium dendrites once the thermal conditions from a phase diagram are met. The solidification shrinkage is ignored in this study, and the thermo-solutal convection is modelled using the Boussinesq approach. It is known that the intermetallic phase is denser than the columnar dendrites ($\rho_\beta > \rho_c$). As the β -Al₅FeSi is captured by the columnar dendrites, the buoyancy force on the β -Al₅FeSi plays no role on the

phase sedimentation, hence ρ_β can also be treated equal to ρ_c . The mass conservation equations are

$$\frac{\partial}{\partial t}(f_\ell \rho_\ell) + \nabla \cdot (f_\ell \rho_\ell \bar{u}_\ell) = -M_{\ell c} - M_{\ell \beta}, \quad [2]$$

$$\frac{\partial}{\partial t}(f_c \rho_c) = M_{\ell c}, \quad [3]$$

$$\frac{\partial}{\partial t}(f_\beta \rho_\beta) = M_{\ell \beta}, \quad [4]$$

where $M_{\ell c}$ is the mass transfer rate from the liquid melt to the columnar dendrites due to the solidification of the primary aluminium, $M_{\ell \beta}$ is the mass transfer rate from the liquid melt to β -Al₅FeSi due to the formation of intermetallic precipitates, \bar{u}_ℓ is the velocity of the melt, and ρ_ℓ , ρ_β , ρ_c are the densities of the different phases.

The net mass transfer rates from the liquid melt to either of the solid phases ($M_{\ell c}$ and $M_{\ell \beta}$) are governed by the solute diffusion in the interdendritic melt. The concentration difference between the liquid thermodynamic equilibrium concentrations ($c_{\ell, \text{Si}}^*$, $c_{\ell, \text{Fe}}^*$) at the solid–liquid interface and the volume-averaged concentrations ($c_{\ell, \text{Si}}$, $c_{\ell, \text{Fe}}$) in the interdendritic liquid act as the driving forces for the transfer. The columnar trunks are assumed to be cylinders, and their tip fronts are traced using the LGK model.^[18] The growth of the columnar phase ($M_{\ell c}$) is assumed to be governed only by the diffusion of Si in the melt:

$$M_{\ell c} = 2v_{R_c} \cdot \frac{R_c \cdot \pi}{\lambda_1^2} \cdot \rho_c \cdot f_\ell, \quad [5]$$

$$v_{R_c} = \frac{D_{\ell, \text{Si}}}{R_c} \cdot \frac{(c_{\ell, \text{Si}}^* - c_{\ell, \text{Si}})}{c_{\ell, \text{Si}}^*(1 - k_{\text{Si}})} \cdot \ln^{-1} \left(\frac{R_{f, c}}{R_c} \right), \quad [6]$$

where R_c is the radius of the columnar trunk, v_{R_c} is the radial growth velocity, λ_1 is the primary dendrite arm spacing, $R_{f, c}$ is the limit of the radius of the columnar trunk, and k_{Si} is the solute partition coefficient of Si.

Based on the Al–Si–Fe ternary phase diagram,^[22] the solidification of AlSi7Fe1 starts with the primary aluminium while the Fe and Si elements are rejected into the liquid. It is followed by the binary eutectic, where β -Al₅FeSi forms as precipitates. The enriched Fe in the interdendritic melt during the primary aluminium solidification is consumed/absorbed by the precipitation of β -Al₅FeSi. The Al-rich corner of the Al–Si–Fe ternary phase diagram is linearised. The liquidus surface can be expressed as

$$T = T_f + m_{\ell, \text{Si}} c_{\ell, \text{Si}}^* + m_{\ell, \text{Fe}} c_{\ell, \text{Fe}}^*, \quad [7]$$

where $m_{\ell, \text{Si}}$ and $m_{\ell, \text{Fe}}$ are the partial slopes of the liquidus surface with respect to the corresponding solute elements; $c_{\ell, \text{Si}}^*$ and $c_{\ell, \text{Fe}}^*$ are the equilibrium liquid concentration of Si and Fe; and T_f is the melting point of pure Al. The solute concentrations ($c_{\text{eut, Si}}^*$ and $c_{\text{eut, Fe}}^*$)

along the binary eutectic valley are simplified as linear functions of T :

$$c_{\text{eut, Si}}^* = 131.020 - 0.139 \cdot T, \quad [8]$$

$$c_{\text{eut, Fe}}^* = -21.70691 + 0.02617 \cdot T. \quad [9]$$

The formation of the β -Al₅FeSi precipitates, represented by $M_{\ell \beta}$, is calculated by introducing a growth constant g_β ^[23]:

$$M_{\ell \beta} = g_\beta \cdot (c_{\ell, \text{Fe}} - c_{\ell, \text{Fe}}^*) \cdot \rho_\beta \cdot f_\ell. \quad [10]$$

All unknown factors contributing to $M_{\ell \beta}$ such as the diffusion of Fe and Si around the precipitates and the effect of morphology are included in g_β . It is determined through a numerical parameter study (later section).

A value of 0.1 for g_β is recommended for the current alloy and solidification conditions. The solidification path and the corresponding phase evolution under pure diffusive conditions are also analysed and evaluated against the results obtained using the commercial software Thermo-Calc and the inbuilt equilibrium solidification model.

B. Blocking Effect of Intermetallic Precipitates

The fluid flow in the mushy zone is approximated with Darcy's law in which its permeability is treated as a function of λ_1 and λ_2 by referring to the Carman–Kozeny approach. As aforementioned, the precipitated β -Al₅FeSi is assumed to be immediately captured by the columnar dendrites. An extra resistance force in addition to the drag force by the columnar dendrites will be imposed on the liquid phase. Following Puncreobutr *et al.*,^[10] the blocking effect of β -Al₅FeSi on fluid flow in the mushy zone is treated by considering an additional coefficient ($1 - \beta f_\beta$) in the permeability:

$$K_{P, \text{int}} = (1 - \beta_P f_\beta) K_P, \quad [11]$$

$$K_{N, \text{int}} = (1 - \beta_N f_\beta) K_N, \quad [12]$$

where $K_{P, \text{int}}$ and $K_{N, \text{int}}$ are the permeability components of the flow parallel (P) and normal (N) to the primary dendrites in the presence of β -Al₅FeSi; and K_P , K_N are the corresponding permeability components in the absence of β -Al₅FeSi. The values of the constants β_P and β_N are 15 and 10, respectively.^[10] K_P and K_N , valid for the whole range of the liquid volume fraction, can be calculated according to Schneider and Beckermann^[24]:

$$K_P = \begin{cases} \left[4.53 \times 10^{-4} + 4.02 \times 10^{-6} (f_\ell + 0.1)^{-5} \right] \frac{\lambda_1^2 f_\ell^3}{(1 - f_\ell)} & (f_\ell < 0.7) \\ 0.07425 \lambda_1^2 \left[-\ln(1 - f_\ell) - 1.487 + 2(1 - f_\ell) - 0.5(1 - f_\ell)^2 \right] & (f_\ell \geq 0.7) \end{cases}, \quad [13]$$

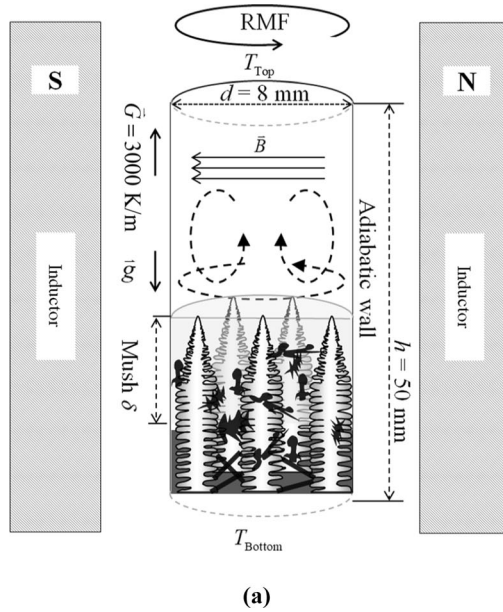
$$K_N = \begin{cases} \left[1.73 \times 10^{-3} \left(\frac{\lambda_1}{\lambda_2} \right)^{1.09} \right] \frac{\lambda_2^2 f_\ell^{\beta}}{(1-f_\ell)^{0.749}} & (f_\ell < 0.7) \\ 0.03979 \lambda_1^2 \left[-\ln(1-f_\ell) - 1.476 + 2(1-f_\ell) - 1.774(1-f_\ell)^2 \right. \\ \left. + 4.076(1-f_\ell)^3 \right] & (f_\ell \geq 0.7) \end{cases} \quad [14]$$

C. Dendrite Coarsening

The permeability depends on both λ_1 and λ_2 . During unidirectional solidification under a constant temperature gradient and cooling rate, λ_1 may not change after the solidification reaches a steady state,^[7] while λ_2 undergoes coarsening. Li and Beckermann^[13] found that λ_2 can be estimated by using the interfacial area density (S_v) through $\lambda_2 = 1.6/S_v$, where S_v is defined as the interface area divided by the sample volume that contains both the solid and liquid phases. Recently, a general formulation was suggested for S_v that accounts for the effects of growth, curvature-driven coarsening, and interface coalescence^[12]:

$$S_v = f_s(1-f_s)^{-r} (S_{s0}^{-3} + K_0 t)^{-b}, \quad [15]$$

where S_v is a function of the local solid volume fraction ($f_s = f_c + f_\beta$) and time (t). It should be stressed that this t denotes the time from the start of the solidification to the current moment (*i.e.*, the solidification has not yet finished). It is different from t_f (the local solidification time in Eq. [1]), which denotes the duration from the start to the end of solidification. The values of the coarsening parameters (r , S_{s0} , and K_0) as suggested for Eq. [15] were verified for the crystal growth under pure diffusive conditions.^[12] Under stirring conditions by RMF, they may be adapted.



D. Auxiliary Equations

The mixture concentrations are calculated according

$$\text{to: } c_{\text{mix,Si}} = \frac{(c_{\ell,\text{Si}} \cdot \rho_\ell f_\ell + c_{c,\text{Si}} \cdot \rho_c f_c + c_{\beta,\text{Si}} \cdot \rho_\beta f_\beta)}{(\rho_\ell f_\ell + \rho_c f_c + \rho_\beta f_\beta)} \cdot 100 \text{ pct} \quad \text{and}$$

$$c_{\text{mix,Fe}} = \frac{(c_{\ell,\text{Fe}} \cdot \rho_\ell f_\ell + c_{c,\text{Fe}} \cdot \rho_c f_c + c_{\beta,\text{Fe}} \cdot \rho_\beta f_\beta)}{(\rho_\ell f_\ell + \rho_c f_c + \rho_\beta f_\beta)} \cdot 100 \text{ pct}, \quad \text{where } c_{\ell,\text{Si}},$$

$c_{c,\text{Si}}$, and $c_{\beta,\text{Si}}$ are Si concentrations; $c_{\ell,\text{Fe}}$, $c_{c,\text{Fe}}$, and $c_{\beta,\text{Fe}}$ are Fe concentrations; ρ_ℓ , ρ_c , and ρ_β are the densities; and f_ℓ , f_c , and f_β are the volume fractions of the liquid melt, columnar dendrite, and intermetallic precipitate, respectively. Macro-segregation is characterised by the segregation index, $c_{\text{mix,Si}}^{\text{index}} = \frac{c_{\text{mix,Si}} - c_{0,\text{Si}}}{c_{0,\text{Si}}} \cdot 100 \text{ pct}$ and $c_{\text{mix,Fe}}^{\text{index}} = \frac{c_{\text{mix,Fe}} - c_{0,\text{Fe}}}{c_{0,\text{Fe}}} \cdot 100 \text{ pct}$.

III. SIMULATION CONFIGURATION AND CASE DEFINITION

The configuration of the simulation domain, as shown in Figure 2, is taken from the experimental setup.^[25] A cylindrical sample (ϕ 8 mm) of an AlSi7Fe1 alloy is solidified unidirectionally in an Al₂O₃ crucible. The initial temperature (T_0) of the melt is 1190 K. The Dirichlet boundary conditions are imposed at the top and bottom: T_{Bottom} starts to decrease with a cooling rate of 0.12 K/s from $t = 0$ s, while T_{Top} starts to decrease with the same cooling rate from $t = 50$ s to maintain a target temperature gradient (\bar{G}). The lateral walls of the sample are treated as adiabatic. When the RMF is applied with a constant rotational frequency (f) and magnetic induction (B), the azimuthal component of the induced electromagnetic force (\bar{F}_θ) can be calculated analytically as follows^[26]:

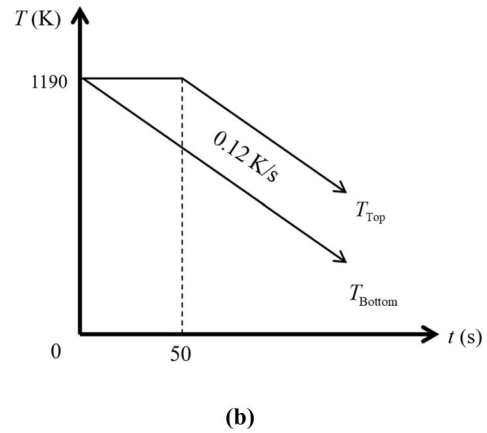


Fig. 2—Geometric and boundary conditions of the experimental setup. (a) Schematic for the flow pattern and formation of different phases and (b) cooling conditions at the top and bottom of the sample.

$$\bar{F}_\theta = \frac{1}{2} \sigma \omega B^2 r \left(1 - \frac{u_\theta}{\omega r}\right) \bar{e}, \quad [16]$$

where σ is the electrical conductivity of the melt, $\omega = 2\pi f$ is the angular frequency, B is the magnetic induction, u_θ is the azimuthal velocity component of the melt at a radial coordinate r , and \bar{e} is the tangential unit vector. The material properties and other parameters can be found in Table I.

As shown in Table II, six simulation cases are designed. Case I is solidified under pure diffusive condition. Cases II and III are designed to verify the consistency between the 2D axisymmetric and full 3D simulations under the forced flow condition, where λ_2 is assumed to be a constant. Due to the high cost of the 3D simulation, the rest of the simulations are performed only in 2D axisymmetry. Cases IV and V are designed with varying values of λ_2 , *i.e.*, considering dendrite coarsening, in which the former is for the ternary alloy

and the latter is for the binary alloy. The last case (VI) considers natural convection only, *i.e.*, thermo-solutal convection (TSC), which can be compared with previous cases of forced flow (RMF + TSC).

The model is implemented in ANSYS FLUENT version 17.1, which uses a control-volume finite difference numerical method. For each time step, 30 iterations are adopted to decrease the normalised residuals of concentration, flow quantities, and continuity below 10^{-4} and enthalpy quantities below 10^{-7} . The decision to select a time step that ensures a high accuracy solution must be determined empirically by test simulations. In this study, all calculations are run with a time step of 0.001 s. The maximum mesh sizes are 2.5×10^{-4} m (3D) and 1.5×10^{-4} m (2D). One 3D simulation takes approximately seven weeks, while one 2D simulation takes approximately one week on a high-performance cluster (2.6 GHz, 12 cores).

Table I. Summary of Material Properties and Other Parameters ^[5,10,12,16]

Properties/Parameters	Symbol	Units	Values
Thermophysical Properties			
Specific Heat	c_p^l, c_p^c, c_p^β	J Kg ⁻¹ K ⁻¹	1140.0
Latent Heat	Δh_f	J Kg ⁻¹	4.0×10^5
Diffusion Coefficient (Liquid)	D_ℓ	m ² s ⁻¹	6.45×10^{-9}
Thermal Conductivity	k_p^l, k_p^c, k_p^β	W m ⁻¹ K ⁻¹	100.0
Liquid Thermal Expansion Coefficient	β_T	K ⁻¹	-1.85×10^{-4}
Liquid Solutal Expansion Coefficient	β_c (Si)	wt pct ⁻¹	1.3×10^{-3}
Density	$\rho_\ell, \rho_c, \rho_\beta$	Kg m ⁻³	2535.0
Viscosity	μ_ℓ	Kg m ⁻¹ s ⁻¹	2.52×10^{-3}
Electrical Conductivity	σ	Ω^{-1} m ⁻¹	3.65×10^6
Thermodynamic Parameters			
Concentrations of Binary Eutectic Valley	$c_{\text{eut,Si}}, c_{\text{eut,Fe}}^*$	—	Eqs. [8] and [9]
Growth Constant for β -Al ₃ FeSi	g_β	1/s	0.1
Ternary Eutectic Temperature	T_{eu}	K	850.0
Liquidus Slope (Si)	m_{Si}	K (wt pct) ⁻¹	- 6.62
Liquidus Slope (Fe)	m_{Fe}	K (wt pct) ⁻¹	- 3.93
Equilibrium Partition Coefficient	$k_{\text{Si}}, k_{\text{Fe}}$	—	0.13, 0.01
Primary Dendrite Arm Spacing	λ_1	μm	300.0
Secondary Dendrite Arm Spacing	λ_2	μm	coarsening law
Gibbs Thomson Coefficient	Γ	m K	2.41×10^{-7}
Melting Point of Solvent	T_f	K	935.5
Coarsening Parameters			
Coarsening Exponent	b	—	1/3
Coarsening Constant	r	—	0.25
	S_{S0}	μm	2.46
	K_0	$\mu\text{m}^3/\text{s}$	23.5
Other Parameters			
Initial Concentrations	$c_{0,\text{Si}}, c_{0,\text{Fe}}$	wt pct	7.0, 1.0
Initial Temperature	T_0	K	1190.0
Cooling Rate at Top and Bottom of the Sample	R	K/s	0.12
Temperature Gradient	\bar{G}	K/m	3000.0
Magnetic Induction	B	mT	6.0
Angular Frequency of Magnetic Field	ω	rad/s	314.0
Rotating Frequency of Magnetic Field	f	Hz	50.0
Blocking Effect Constants in Eqs. [11] through [12]	β_P, β_N	—	15, 10

Table II. Simulations of the AlSi7Fe1 Alloy

Case	Diffusive vs. RMF	Ternary (β -Al ₅ FeSi) vs. Binary	Coarsening Law vs. Constant λ_2
I	diffusive	2D axis. ternary (β -Al ₅ FeSi)	coarsening law
II	flow (RMF + TSC)	3D ternary (β -Al ₅ FeSi)	$\lambda_2 = 120 \mu\text{m}$
III		2D axis. ternary (β -Al ₅ FeSi)	
IV	flow (RMF + TSC)	2D axis. ternary (β -Al ₅ FeSi)	coarsening law
V	flow (RMF + TSC)	2D axis. binary	coarsening law
VI	flow (only TSC)	2D axis. ternary (β -Al ₅ FeSi)	coarsening law

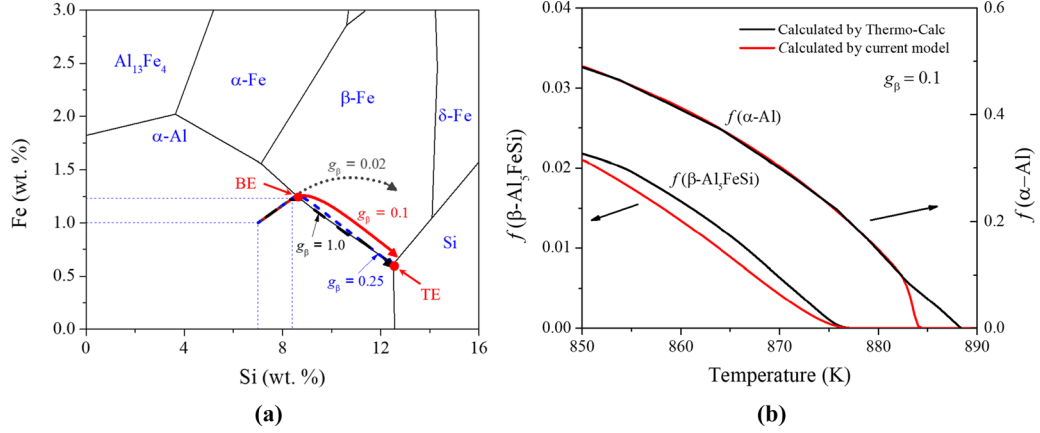


Fig. 3—Thermodynamics (phase diagram) of AlSi7Fe1 and calculated solidification path for Case I. (a) Evolution of solute concentrations ($c_{\ell, \text{Fe}}$, $c_{\ell, \text{Si}}$) when g_{β} takes different values. (b) Comparison of the evolution of the phases calculated with the current solidification model and with the commercial software Thermo-Calc.

IV. SIMULATION RESULTS

A. Dendrite Coarsening and Formation of β -Al₅FeSi

The calculated solidification path of the ternary alloy AlSi7Fe1 considering the formation of β -Al₅FeSi, based on Case I, is compared with the thermodynamic analysis by the commercial software Thermo-Calc, as shown in Figure 3. The Al-rich corner of the Al–Si–Fe phase diagram is shown in Figure 3(a), where the red solid line indicates the calculated solidification path by the current model (assuming the growth constant for β -Al₅FeSi, $g_{\beta} = 0.1$). The calculated concentrations of Si and Fe are exported along the axis of the sample. The solidification starts with the development of the primary aluminium phase (α -Al), and the Si and Fe elements are rejected into the rest of the melt which enriches their concentrations. As their concentrations reach the binary eutectic point BE, binary eutectic reaction starts, $L \rightarrow \alpha - \text{Al} + \beta - \text{Al}_5\text{FeSi}$.^[19–21] The formed α -Al is considered to be the further growth of the primary aluminium phase, and the intermetallic phase (β -Al₅FeSi) precipitates as a secondary phase. A large amount of Fe in the rest of the melt is consumed, and the solidification path turns towards the direction of the ternary eutectic point TE at 850 K, then ternary reaction occurs, $L \rightarrow \alpha - \text{Al} + \beta - \text{Al}_5\text{FeSi}$.^[19–21] The solidification path during the formation of binary eutectic is almost parallel (not identical) to the binary eutectic valley of the phase diagram (thermodynamic

equilibrium). The deviation between the simulation and the equilibrium data can be attributed to the growth kinetics of β -Al₅FeSi, *i.e.*, the value of g_{β} . Thus, calculated solidification paths with different values of g_{β} (from 0.02 to 1.0) are compared in Figure 3(a). The larger the value of g_{β} , *i.e.*, the faster (or easier) the growth of β -Al₅FeSi, the closer the calculated solidification path is to the thermodynamic equilibrium one. This is further discussed in Section V.

The calculated phase fractions obtained by using the current numerical model and the thermodynamic equilibrium data (Thermo-Calc) are compared, as shown in Figure 3(b). The initial temperature of the primary aluminium phase (α -Al) is approximately 4.3 K lower than the equilibrium liquidus temperature (888.4 K). This is due to the growth kinetics of the columnar primary dendrite tip.^[18] In the later stage of solidification, the calculated phase fractions of α -Al are almost identical between the two models. The numerically calculated phase fraction of β -Al₅FeSi is smaller than that predicted by Thermo-Calc.

Under the pure diffusive crystal growth condition (Case I), the evolution of the microstructure considering coarsening is also evaluated. The specific interfacial area (S_v) and the corresponding λ_2 as a function of the local solid volume fraction ($f_s = f_c + f_{\beta}$) are shown in Figure 4(a). At the columnar dendrite tips, according to both the experimental observation and numerical model,^[12] there should be no side branches. Thus, λ_2

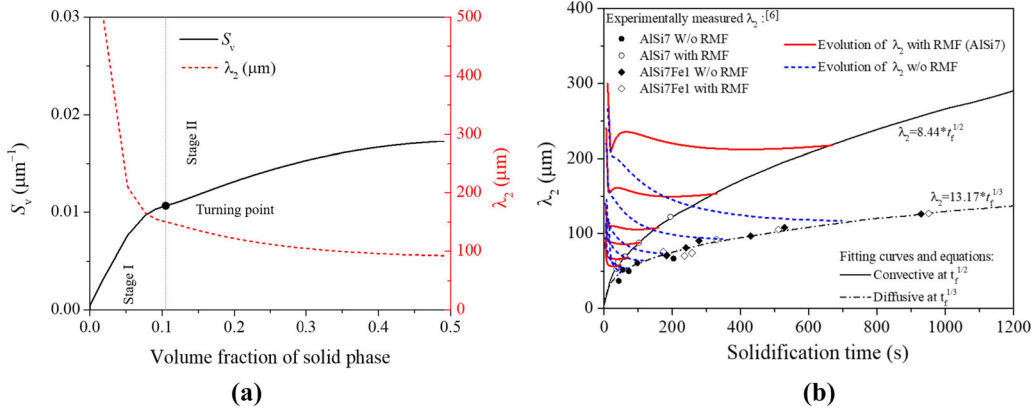


Fig. 4—Microstructure evolution of Case I. (a) The specific interfacial area (S_v) and λ_2 as a function of the local solid volume fraction. (b) The evolution of λ_2 with time. In (b), further simulation cases are included to study the effect of forced flow and intermetallic precipitates (β -Al₅FeSi) on the evolution of λ_2 . The black circles and squares are the experimentally measured λ_2 of the as-solidified state with/without RMF; the black lines are the fitting curves. The red and blue lines are the calculated λ_2 evolutions with RMF (Case V) and without RMF (Case I), respectively.

starts from a large value and is followed by a drastic decrease. By contrast, S_v starts from a small value and is followed by a steep increase. The reason for this rapid decrease in λ_2 and corresponding increase in S_v is due to high undercooling. This period is called stage I according to Neumann-Heyme,^[12] corresponding to the initial free dendritic growth and side-branch extension. After the turning point as marked in Figure 4(a), the solidification is characterised by concurrent growth and coarsening without significant interface coalescence (stage II), during which the increase rate of S_v and decrease rate of λ_2 decelerate. Since the eutectic reaction occurs after $f_s = 0.5$ (Figure 3(b)), stage III, during which coalescence of the interfaces leads to a decrease in S_v , is not observed in the current case.

The transient evolution of λ_2 during solidification (red solid and blue dash lines) and the experimentally measured λ_2 of the as-solidified state (black circles and squares) are plotted in Figure 4(b). The experiments were conducted by Steinbach *et al.*^[6] on the AISi7 and AISi7Fe1 alloys with and without RMF. Two equations were obtained by fitting their experimental results: $t_f = 8.44 * t_f^{1/2}$ for the AISi7 alloy under RMF, and $t_f = 13.17 * t_f^{1/3}$ for both the AISi7 alloy without RMF and the AISi7Fe1 alloy with RMF. The simulation results of the coarsening process are shown as blue dash lines in Figure 4(b). The simulation results of Case V (red solid lines), which is conducted under RMF on the binary alloy AISi7, are also included here for further discussion in Section V. It is still unclear how the secondary dendrites initiate and what the initial value for λ_2 is. In the current study, a simple assumption is made that λ_2 starts to develop at the position 300 μm ($\sim \lambda_1$) from the tips of the primary dendrites. As depicted in Figure 4(b), different blue dash lines denote the evolution of λ_2 at different cooling rates. For all cases, λ_2 has a large value at the beginning of the solidification, and then decreases gradually. As expected, the final values of λ_2 (ends of blue lines) fall on the curve of $\lambda_2 = 13.17 * t_f^{1/3}$, following the classical coarsening law with $b = 1/3$.

B. Directional Solidification Under Forced Convective Conditions

1. Flow pattern and solidification

The calculated solidification sequences of Case II (full 3D calculation) and Case III (axisymmetric calculation) are shown in Figure 5 for comparison. In both cases, RMF is applied. An azimuthal flow (~ 24.1 mm/s) and a meridional flow (~ 9.0 mm/s) as induced by the Ekman effect are generated. As shown in Figures 5(a) and (c), the fluid rotates and moves downwards near the sample surface, and then rotates and moves upwards along the centreline of the sample. The flow pattern in the mushy zone is similar to that in the bulk liquid, although the fluid flow is suppressed by the dendrites to a low magnitude.^[5] As demonstrated by the iso-surface in Figure 5(a), the solute-enriched interdendritic liquid is swept to the centre of the sample, leading to the formation of a central macrosegregation channel with some sidearms. The shape of the central segregation is sometimes referred to as ‘‘Christmas tree’’. This kind of segregation distribution has been repeatedly observed in experiments.^[27] The accumulation of the solute in the central part decreases the liquidus temperature of the melt, and hence delays (slows down) the local solidification. As shown in Figure 5(b), there is a hollow tube in the centre, which is filled with the solute-enriched melt. The 2D axisymmetric calculation (Figure 5(d)) can successfully reproduce the full 3D calculation (Figures 5(b) through (c)). Therefore, the subsequent parameter studies presented in the following sections are conducted with the 2D axisymmetric calculations.

2. Model validation

The experiment–simulation comparison of macrosegregation based on Case IV is presented in Figures 6(a) and (b). Mikolajczak and Ratke carried out a series of unidirectional solidification experiments to study the effect of RMF on the formation and distribution of β -Al₅FeSi in Al–Si–Fe alloys.^[4,25] The configuration of their experiments (including the temperature gradient, withdrawal velocity, RMF intensity and frequency) is

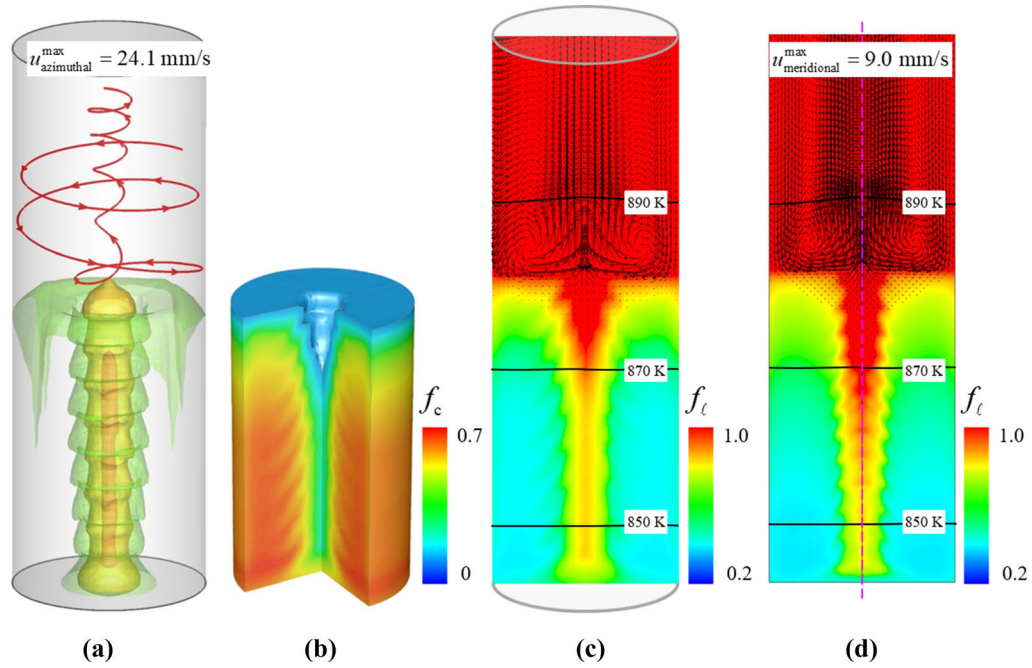


Fig. 5—Solidification sequence of the sample under RMF at 550 s: (a) through (c) Case II with full 3D calculation and (d) Case III with 2D axisymmetric calculation. (a) Iso-surfaces of Si macrosegregation index ($c_{\text{mix,Si}}^{\text{index}}$): the innermost iso-surface (orange) is for $c_{\text{mix,Si}}^{\text{index}} = 43$ pct, the middle one (yellow) for $c_{\text{mix,Si}}^{\text{index}} = 14$ pct, the outermost (green) for $c_{\text{mix,Si}}^{\text{index}} = -3$ pct; one streamline is drawn to show the flow. (b) Contour of the columnar phase fraction (f_c) in two vertical sections and one iso-surface of $f_c = 0.01$ on the top indicating the position of the columnar tip front. (c) Contour of f_l (colour scaled) along the centre of the longitudinal section, overlaid with isotherms and vectors of the meridional flow. (d) Same result as (c) but in a 2D axisymmetric calculation (one half section is mirrored from the other) (Color figure online).

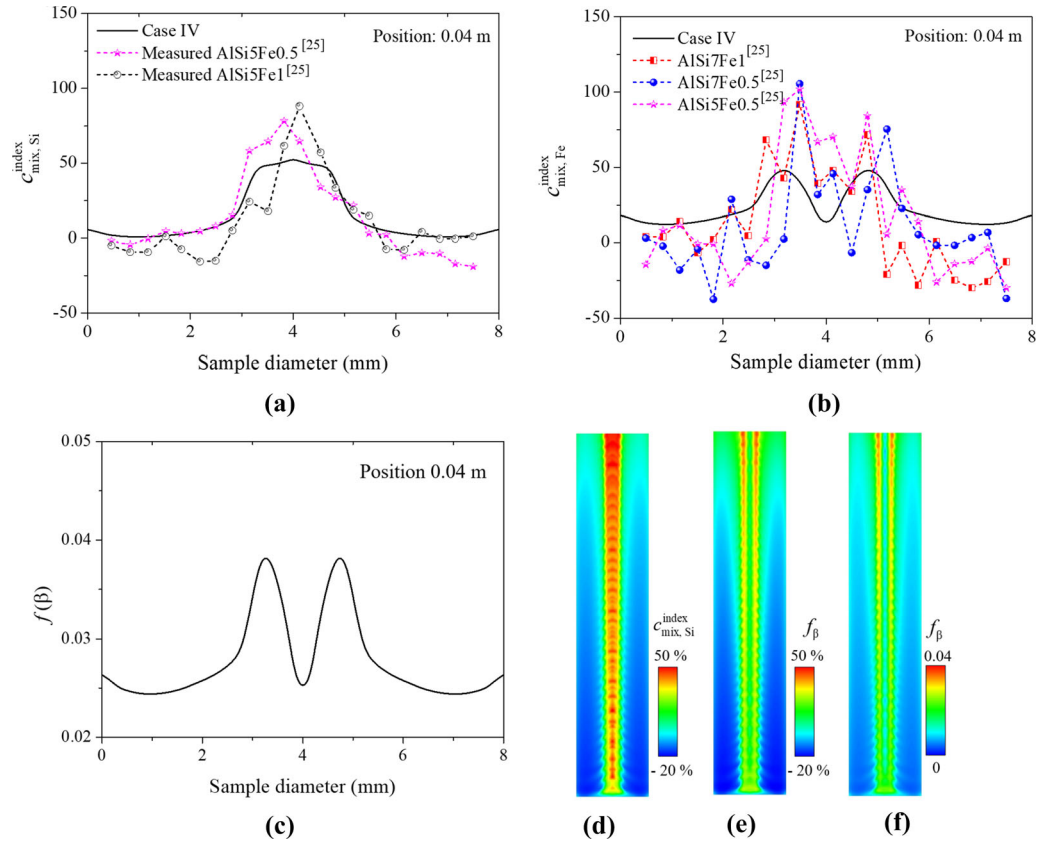


Fig. 6—Experiment-simulation comparison. Radial distribution of the segregation indexes of (a) Si ($c_{\text{mix,Si}}^{\text{index}}$) and (b) Fe ($c_{\text{mix,Fe}}^{\text{index}}$) along the sample diameter. (c) Distribution of β -Al₅FeSi along the sample diameter. Contours of (d) $c_{\text{mix,Si}}^{\text{index}}$, (e) $c_{\text{mix,Fe}}^{\text{index}}$, and (f) $f(\beta)$.

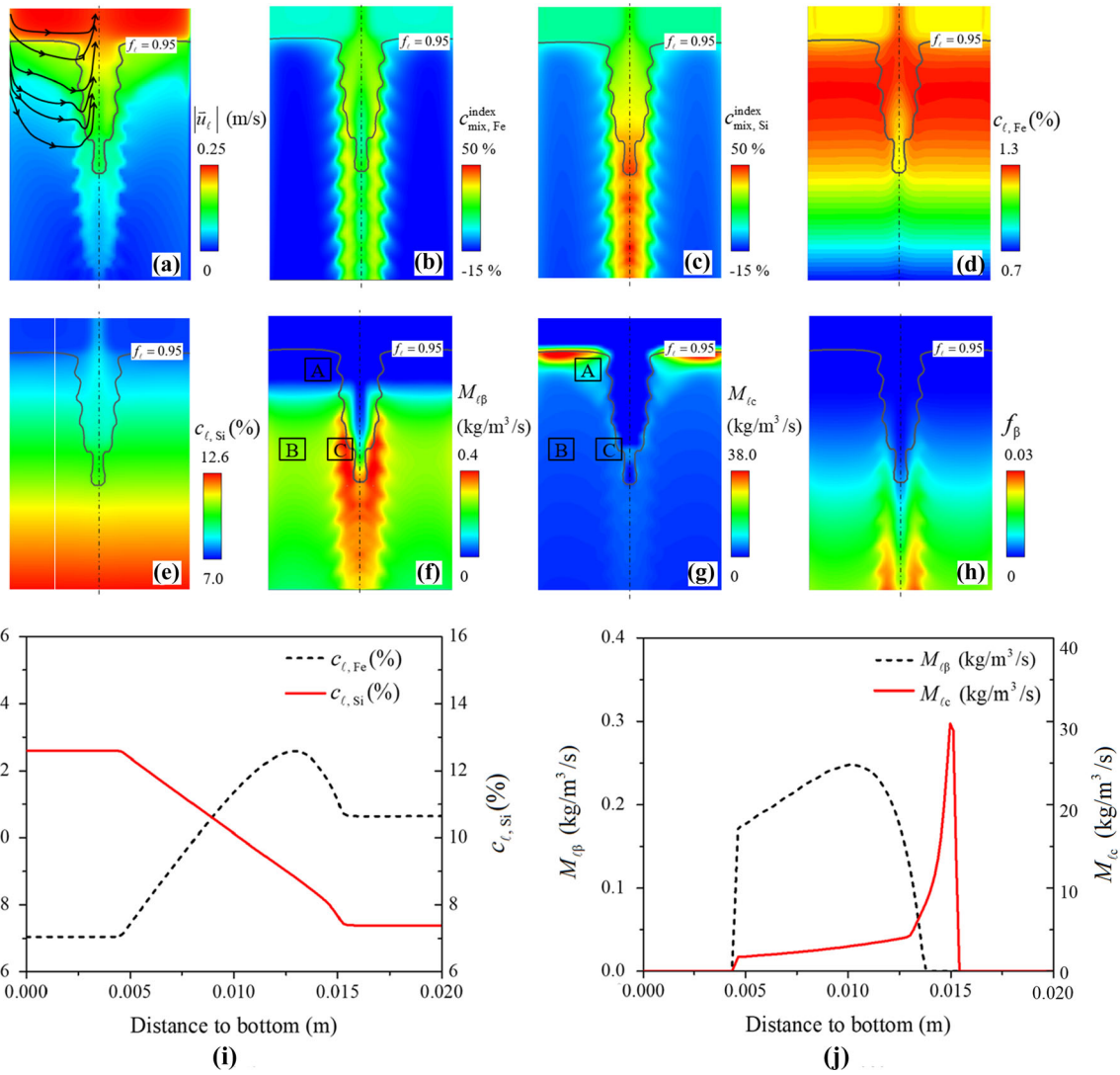


Fig. 7—Analysis of the solidification sequence and the formation/distribution of β -Al₅FeSi at $t = 600$ s for Case IV. The black solid isopleth in (a) through (h) denotes the solidification front ($f_l = 0.95$), and the bottom of these figures coincides with the position of the ternary eutectic isotherm (850 K). (a) Liquid velocity magnitude ($|\bar{u}_l|$) overlaid by streamlines of the meridional flow; macrosegregation indices for (b) Fe ($c_{\text{mix,Fe}}^{\text{index}}$) and (c) Si ($c_{\text{mix,Si}}^{\text{index}}$); liquid concentrations of (d) Fe ($c_{l,\text{Fe}}$) and (e) Si ($c_{l,\text{Si}}$); mass transfer rates (f) from liquid to intermetallic precipitates ($M_{f\beta}$) and (g) from liquid to columnar phase (M_{lc}); (h) volume fraction of intermetallic precipitates (f_β); (i) liquid concentration profiles and (j) mass transfer rate profiles along the middle radius of the sample (as marked by the white solid line in (e)).

identical to what was used in this study. EDX analysis was made to determine the solute concentration distribution across the as-solidified sample section. The macrosegregation distributions along the diameter of the sample are displayed in Figures 6(a) and (b). Very good agreement between the experimental and the calculated results is obtained. As shown in Figure 6(a), both simulation and experimental results show that the centre of the sample is positively segregated and the periphery is negatively segregated. The maximum value of $c_{\text{mix,Si}}^{\text{index}}$ (~ 52.7 pct) is observed at the centreline of the sample. The segregation index profile of Fe, $c_{\text{mix,Fe}}^{\text{index}}$, is presented in Figure 6(b). In contrast to the distribution of $c_{\text{mix,Si}}^{\text{index}}$, the maximum of $c_{\text{mix,Fe}}^{\text{index}}$ (~ 48.3 pct) is not observed at the centreline of the sample, but at

approximately 1 mm from the centreline. The current simulation results are different from those of previous studies,^[16,28] in which Fe exhibited the same segregation pattern as Si. The final distribution of the volume fraction of β -Al₅FeSi (f_β) is shown in Figure 6(c). The distribution pattern of β -Al₅FeSi is similar to that of $c_{\text{mix,Fe}}^{\text{index}}$, indicating that Fe is mainly solidified in the form of intermetallic precipitates. The corresponding contours of $c_{\text{mix,Si}}^{\text{index}}$, $c_{\text{mix,Fe}}^{\text{index}}$, and f_β are displayed in Figures 6(e) through (g). Si is accumulated in the central segregation channel, Fe is concentrated in the sidearms beside the central channel, and the distribution of β -Al₅FeSi is similar to that of Fe. Due to the forced flow under the RMF, the solute-enriched liquid is continuously transported to the bulk liquid.

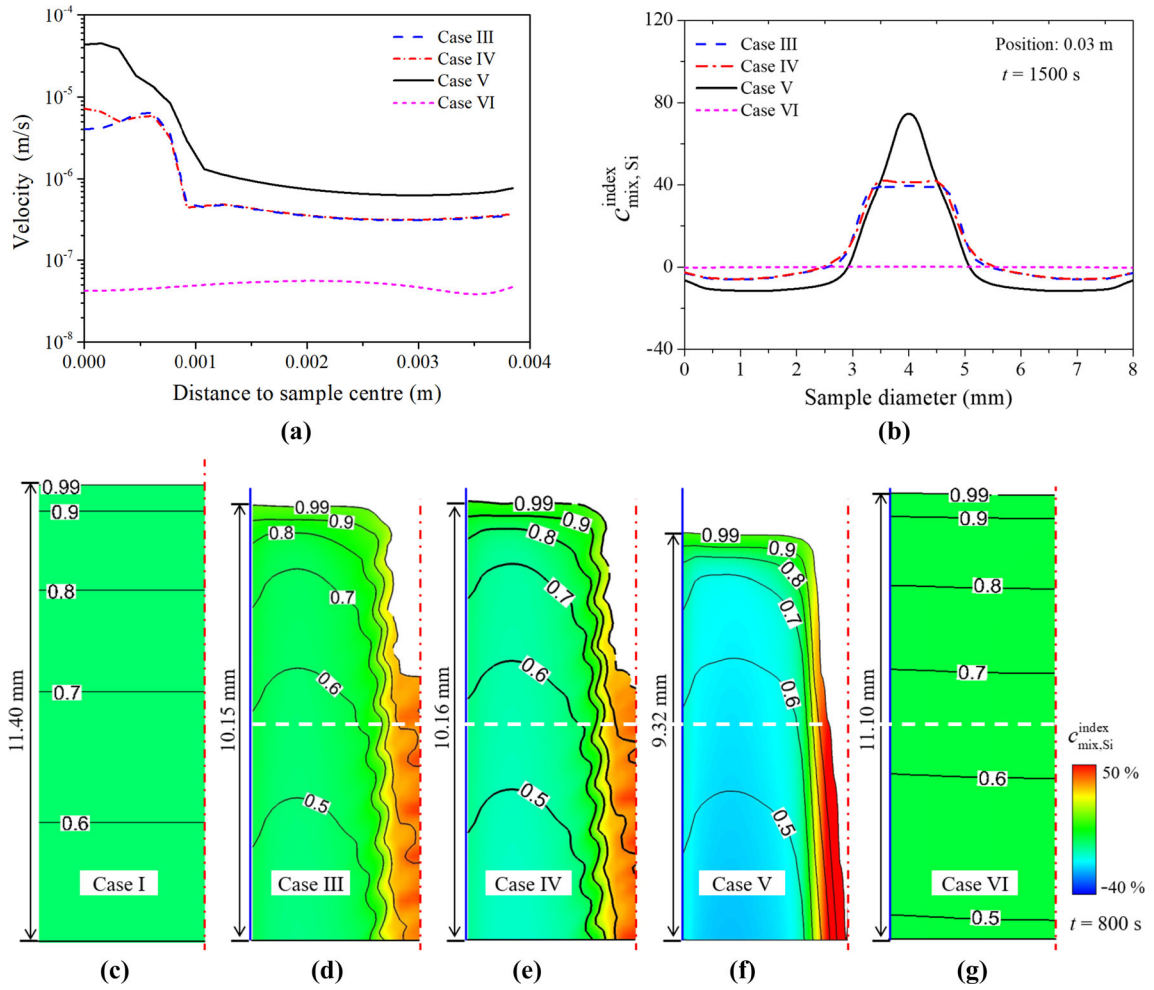


Fig. 8—Calculation results of the mushy zone for all simulation cases (except for Case II) at $t = 800$ s. (a) Comparison of the liquid velocity magnitude at the middle height of the mush (marked by white dash lines). (b) Macrosegregation index of Si along the diameter of the sample after the sample is fully solidified. (c) through (g) Contours of $c_{mix,Si}^{index}$ overlaid with isopleths of f_{ℓ} , with the mushy zone thickness marked on the left of each figure.

3. Formation of intermetallic precipitates during solidification under RMF

The simulation results of Case IV at $t = 600$ s are shown in Figure 7. Since the interdendritic liquid prefers to take the path with a higher liquid volume fraction, streamlines near the sidearms of the central channel are twisted/distorted, as evident in Figure 7(a). This kind of flow transports solute-enriched liquid from the periphery of the sample to the central part, forming the central segregation channel, as shown by $c_{mix,Fe}^{index}$ and $c_{mix,Si}^{index}$ in Figures 7(b) and (c). Some solute-enriched liquid is further transferred into the bulk liquid, enriching the solute in the bulk liquid. In contrast to Si, Fe is less segregated along the centreline of the sample. As shown in Figure 7(d), $c_{\ell,Fe}$ starts with an increase near the solidification front due to solute rejection during the formation of the primary aluminium dendrites, until it reaches a maximum value ($c_{\ell,Fe} = 1.29$ pct). Since the formation of $\beta\text{-Al}_5\text{FeSi}$ by the binary eutectic reaction consumes a large amount of Fe, $c_{\ell,Fe}$ gradually decreases until the ternary eutectic reaction occurs. This can also

be clearly observed in Figure 7(i). The liquid concentration of Si ($c_{\ell,Si}$) is displayed in Figures 7(e) and (i). Although the formation of $\beta\text{-Al}_5\text{FeSi}$ also consumes a considerable amount of Si, due to the massive rejection of Si during the solidification of $\alpha\text{-Al}$, $c_{\ell,Si}$ increases consistently until the ternary eutectic point. The mass transfer rates from the liquid to $\beta\text{-Al}_5\text{FeSi}$ ($M_{\ell\beta}$) and to the columnar phase ($M_{\ell c}$) are presented in Figures 7(f), (g), and (j). In the upper part of the mushy zone (A in Figures 7(f) and (g)), only $\alpha\text{-Al}$ develops. As the solidification path reaches the binary eutectic valley, $\beta\text{-Al}_5\text{FeSi}$ starts to precipitate. In the periphery region (B in Figure 7(f)), due to the low liquid volume fraction and small $c_{\ell,Fe}$ (Figures 5(c) and (d)), $M_{\ell\beta}$ is small (~ 0.15 Kg/m³/s). Near the central channel (C in Figure 7(f)), where $c_{\ell,Fe}$ is large and the liquid volume fraction is high, $M_{\ell\beta}$ is quite large (~ 0.4 Kg/m³/s). In contrast to $M_{\ell\beta}$, the value of $M_{\ell c}$ reaches a maximum near the solidification front at a value of 38.6 Kg/m³/s, and then sharply drops to a value of 5.0 Kg/m³/s. As shown in Figure 7(h), the volume fraction of $\beta\text{-Al}_5\text{FeSi}$

gradually increases as the solidification progresses. The intermetallic phase increases faster in the centre part than in the periphery of the sample. Most of β -Al₅FeSi forms near the sidearms of the central channel. The maximum value of f_β is 0.034.

4. Effect of intermetallic phases on solidification

The simulation results of the mushy zone for all the cases (except for Case II) are compared, as shown in Figure 8. The dendrite coarsening parameters as used in Eq. [15] and listed in Table I are only valid for Case I (crystal growth by diffusion). They are assumed to be valid for the cases where β -Al₅FeSi exist and the flow is significantly blocked. As reported by Steinbach *et al.*,^[2,6] the ripening exponent (b) changed from 1/3 to 1/2 under the influence of an RMF for the AlSi7 binary alloy (without β -Al₅FeSi). Neumann-Heyme *et al.*^[12] indicated that K_0 in Eq. [15] is dependent on the flow condition, cooling rate, and alloy composition. In the current study, a numerical parameter study is carried out to determine the value of K_0 under the RMF condition. In Case V, b changes from 1/3 to 1/2, and a value of $4.6 \mu\text{m}^3$ is used for K_0 . The evaluation of K_0 for Case V is further discussed in Section V. In the other cases, b and K_0 use the original values that are listed in Table I.

A quantitative analysis of the interdendritic flow along the radial direction at the mid-height of the mush thickness is presented in Figure 8(a). There is no velocity for Case I. For all the cases under RMF, the forced flow transports the solute-enriched liquid to the centre, and hence lowers the melting point there. Since f_ℓ is higher in this region, the flow permeability is higher. In Cases III–V, the liquid velocity at the centre is much larger than that at the periphery region. The flow of Case III is almost the same as that of Case IV. The flow in the central part of Case V is larger by one order of magnitude than those of Cases III and IV. A consideration of the formation of the intermetallic precipitates is

the critical factor for the flow calculation, as the permeability is directly influenced by the intermetallic precipitates,^[10] according to Eqs. [11] and [12]. If the sample is solidified under TSC without RMF (Case VI), the flow is very weak ($\sim 10^{-8}$ m/s). After the sample is fully solidified, $c_{\text{mix,Si}}^{\text{index}}$ along the diameter of the sample for all cases is analysed, as shown in Figure 8(b). The value of $c_{\text{mix,Si}}^{\text{index}}$ in Case V with the binary alloy (AlSi7) is evidently higher than those in Cases III and IV with the ternary alloy (AlSi7Fe1), although the same RMF is applied. This result can be explained by the block effect on the flow due to the formed intermetallic precipitates in Cases III and IV. The value of $c_{\text{mix,Si}}^{\text{index}}$ in Case III is slightly smaller than that in Case IV. Under the TSC condition, the segregation is negligible ($c_{\text{mix,Si}}^{\text{index}} \approx \pm 2$ pct).

The thicknesses of the mushy zone and the corresponding contours of $c_{\text{mix,Si}}^{\text{index}}$ are shown in Figures 8(c) through (g). The simulation results of Case I (pure diffusive condition) is shown in Figure 8(c). There is no flow and no macrosegregation. This case has the largest mushy zone thickness (11.4 mm), which is calculated as the height from the eutectic isotherm to the solidification front ($f_\ell = 0.99$). Figure 8(f) shows the simulation results of another extreme case of the binary alloy, *e.g.*, Case V, where there is no β -Al₅FeSi to block the flow. In this case, the flow is relatively strong in the mushy zone (Figure 8(a)). The strongest segregation index ($c_{\text{mix,Si}}^{\text{index}}$) is observed and the minimum mushy zone thickness (9.32 mm) is obtained. Figure 8(d) presents the simulation results of Case III, which emphasises the necessity of considering the dependence of f_β on the locally varying composition of Fe and Si. Although the mushy zone thickness ($\delta = 10.15$ mm) of Case III is still not as thick as that of Case I, it is much thicker than the mushy zone of Case V. A central segregation channel/tube is still observed, but the severity of the segregation is significantly lower than that of Case V. Figure 8(e) presents

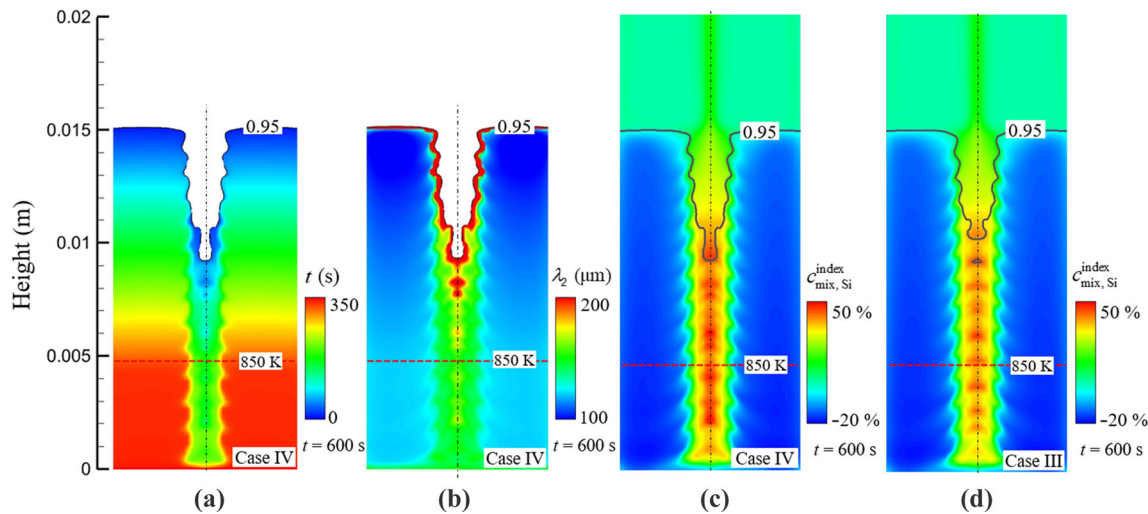


Fig. 9—Effect of dendrite coarsening on macrosegregation. Simulation results of (a) through (c) Case IV and (d) Case III. One iso-line of $f_\ell = 0.95$ indicates the solidification front, and the red dash lines are isotherms of the eutectic temperature. Contours of (a) t , *i.e.*, the duration of the solidification from the formation of the first local solid, (b) calculated λ_2 , and (c) through (d) $c_{\text{mix,Si}}^{\text{index}}$.

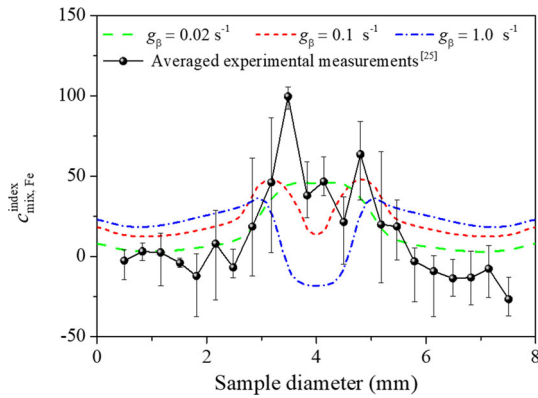


Fig. 10—Effect of g_β on the distribution profile of $c_{\text{mix,Fe}}^{\text{index}}$ (Case IV) and comparison with experimental results.

the simulation results of Case IV, which is conducted to reveal the effect of dendrite coarsening. There is almost no difference in the mushy zone thickness and macrosegregation between Cases III and IV. The mushy zone thickness of Case VI is shown in Figure 8(g). In terms of the mushy zone thickness and macrosegregation, the simulation results of Case VI are very similar to that of Case I due to the weak fluid flow.

5. Effect of dendrite coarsening on solidification

The simulation results of Case IV are presented in Figure 9. Figure 9(a) shows the duration of the local solidification. At the periphery of the sample, it takes approximately 345 s from the beginning of solidification to reach the eutectic reaction. In the centre, the solute accumulation delays the solidification, and the solidification process requires approximately 155 s. The calculated value of λ_2 is shown in Figure 9(b). The value of λ_2 is relatively large ($> 200 \mu\text{m}$) at the sample centre, while at the periphery, the value of λ_2 is relatively small ($\sim 120 \mu\text{m}$). A comparison of $c_{\text{mix,Si}}^{\text{index}}$ between Case III and Case IV is made, as shown in Figures 9(c) and (d). A consideration of dendrite coarsening enhances the central positive segregation ($c_{\text{mix,Si}}^{\text{index}}$) by approximately 4 pct.

V. DISCUSSION

The morphology of the intermetallic precipitates ($\beta\text{-Al}_5\text{FeSi}$) is very complex. It can be curved, bent, branched, hole-shaped, and with imprints.^[4,10,20] The growth kinetics of the precipitates with such complex morphologies is unclear. As a first attempt, a simple formulation for the growth of $\beta\text{-Al}_5\text{FeSi}$ is introduced in this work (Eq. [10]). All unknown factors contributing to its growth are treated as a growth constant g_β . As shown in Figure 3(a), the value of g_β significantly influences the solidification path. A very large g_β (1.0) leads to a solidification path that is almost identical to the thermodynamic equilibrium binary eutectic reaction valley (BE–TE line), while a very small g_β (0.02) leads to a solidification path that lies far from the binary eutectic reaction valley. To determine the appropriate value for g_β , a series of simulations with varying g_β are performed,

and the calculated macrosegregation profiles are validated against experimental results, as shown in Figure 10. When g_β is very small (0.02), positive macrosegregation of Fe ($c_{\text{mix,Fe}}^{\text{index}}$) is mostly concentrated at the sample centre. This is different from the experimental results, which shows two positive segregation peaks at approximately 1 mm from the sample centre. This simulation–experiment disagreement is attributable to an underestimation of the growth rate of $\beta\text{-Al}_5\text{FeSi}$ (or g_β is too small). Thus, the Fe-enriched melt is transported to the central part before the formation of $\beta\text{-Al}_5\text{FeSi}$. When g_β is too large (1.0), the growth rate of $\beta\text{-Al}_5\text{FeSi}$ is overestimated. The formation of $\beta\text{-Al}_5\text{FeSi}$ occurs as soon as the thermodynamic condition for $\beta\text{-Al}_5\text{FeSi}$ is favourable. The formed $\beta\text{-Al}_5\text{FeSi}$ is immediately captured by the columnar phase. The transport of the solute-enriched liquid is effectively blocked by the formed $\beta\text{-Al}_5\text{FeSi}$, and there is only a limited amount of Fe that can reach the sample centre, leading to a relatively lower concentration of Fe (even negative segregation) there. The best simulation–experiment agreement is obtained when $g_\beta = 0.1$. Therefore, this value is recommended in this study. It should be mentioned that g_β may depend on alloys and other factors. Further investigations are required to better understand the growth kinetics of $\beta\text{-Al}_5\text{FeSi}$ which is outside the scope of the current study.

The melt flow accelerates both the heat and solute transfer near the solidification tip front, and thereby affects the growth kinetics of the dendrite tip. Lee *et al.*^[29] presented a comprehensive literature review on this topic, while most studies were done in the presence of the thermal convection. A stagnant film model of thermosolutal convection during free dendritic growth of alloys was developed by Li and Beckermann.^[30] The convection effect was considered by introducing the thermal and solutal boundary layer in the transport solutions for the dendrite tip. The boundary layer thicknesses were evaluated through appropriate Nusselt and Sherwood number correlations. However, this model is not valid for the AlSi7Fe1 alloy where the buoyancy ratio is negative. Note that, in the current study, as the sample is solidified unidirectionally in a Bridgman furnace where the withdrawal velocity of the sample and the temperature gradient are superimposed. The growth velocity of the primary dendrite tips is consistent with the sample withdrawal velocity, and the convection has only effect on the position of the dendrite tips. Based on the current simulation results, the columnar tip front is $\sim 0.9 \text{ mm}$ behind the liquidus isotherm. This distance is about one order of magnitude smaller than the mushy zone thickness ($> 10 \text{ mm}$ shown in Figure 8). It indicates that the flow effect on the dendrite growth kinetics, *i.e.* on the position of the primary dendrite tips, is very limited in the current unidirectional solidification condition.

A wide variety of experiments have been done to investigate the nucleation mechanisms of $\beta\text{-Al}_5\text{FeSi}$. Previous investigations suggested that $\beta\text{-Al}_5\text{FeSi}$ prefer to nucleate on small entrained oxide films,^[31,32] double oxide films,^[33] and aluminium phosphide particles.^[34]

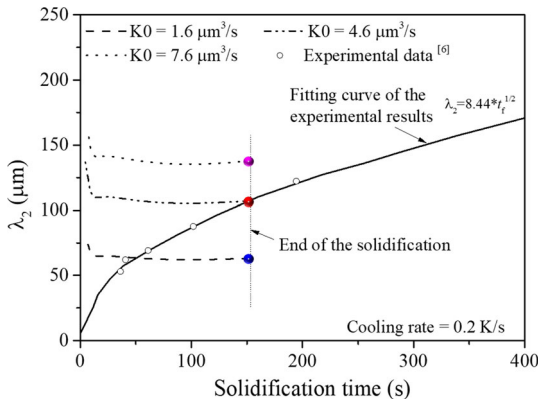


Fig. 11—Numerical parameter study of the effect of K_0 on λ_2 based on Case V.

Recent experimental studies have focused on the use of *in situ* methodologies to reveal and quantify nucleation mechanisms of β -Al₅FeSi. Terzi *et al.*^[35] found that four β -Al₅FeSi plates nucleated heterogeneously near the surface of the samples, but no nucleation was observed in the interior of the samples. Different from the work done by Terzi *et al.*,^[35] Puncreobutr *et al.*^[21] found that the main mechanism of nucleation was on/near aluminum dendrites, occurring in 617 of 959 events, or ~64 pct of the time, while the surface oxide only played a small role on the nucleation. To be best knowledge of the authors, although different nucleation mechanisms have been proposed, it is still very difficult to quantify their individual effect during the precipitation of intermetallics, especially for the alloy solidified under convection conditions. In the current paper, the nucleation of β -Al₅FeSi was presumed to occur instantaneously when the thermal conditions (phase diagram) are fulfilled.

Based on the in-situ observation, β -Al₅FeSi appeared on or near the well-developed primary aluminium dendrites.^[20,21,35] Once nucleated, β -Al₅FeSi plates formed via fast lateral growth (0.03 ~ 0.1 mm/s), wrapping around and in between the primary dendrite arms.^[20] Nearly 90 pct of the total volume of the β -Al₅FeSi forms via a eutectic reaction ($L \rightarrow \alpha$ -Al + β -Al₅FeSi).^[19,21] For AlSi7Fe1, λ_2 varies from 50 to 100 μm .^[9] The formed β -Al₅FeSi is generally close to or even larger than the secondary dendrite spacing.^[4,20,21,25] All those works imply that the migration of β -Al₅FeSi in the mush is unlikely to occur, and β -Al₅FeSi was usually considered to be fixed with the primary dendrites.^[10] Therefore, the migration of β -Al₅FeSi, which may be another mechanism for macrosegregation (transporting element Fe with the β -Al₅FeSi), can be ignored. Furthermore, ignoring the migration of the precipitates, the current simulation results can reproduce the experimentally obtained segregation profile of Fe, *e.g.*, the two positive segregation peaks of $c_{\text{mix,Fe}}^{\text{index}}$ approximately 1 mm from the centre (Figure 6(b)). This simulation–experiment agreement reveals that the formation and distribution of β -Al₅FeSi are due to the interdendritic flow which transports the

Fe-enriched melt, rather than the migration of β -Al₅FeSi.

Although studies on the precipitation/formation of β -Al₅FeSi are plentiful, studies on the blocking effect of β -Al₅FeSi on the interdendritic flow are scarce. To the best of our knowledge, Eqs. [11] and [12]^[10] are the only equations available to quantify the blocking effect on the fluid flow. These equations were directly implemented in the current model and indirectly validated by the model through a comparison of the calculated and experimentally determined macrosegregation. The good simulation–experiment agreement indicates that Eqs. [11] and [12] are valid. Note that in Eqs. [11] and [12], two blocking effect constants (β_P , β_N) were used, which were experimentally obtained based on the Al–7.52Si–3.53Cu–0.59Fe alloy. This alloy is similar, but not identical to the alloy of the current study. The valid scope of Eqs. [11] and [12], including β_P , β_N , is not clear. Therefore, the study of Puncreobutr *et al.*^[10] is necessarily extended to a broader range of alloys and solidification conditions.

Dendrite coarsening is considered by Eq. [15]. As shown by the blue lines in Figure 4(b), under diffusive crystal growth conditions, good agreement between the experimental results^[6] and the simulation results is obtained. To investigate the mechanism of solidification under the influence of an RMF, a series of simulations with various cooling rates were carried out for Case V. However, the dendrite coarsening parameters developed for the diffusive crystal growth condition are not valid in Case V, in which the AlSi7 binary alloy is solidified under the RMF. According to the work of Steinbach *et al.*,^[2,6] the ripening exponent (b) should increase from 1/3 to 1/2. Neumann-Heyme *et al.*^[12] indicated that K_0 in Eq. [15] is dependent on the flow condition, cooling rate, and alloy composition. A numerical parameter study was performed by varying K_0 between 1.0 $\mu\text{m}^3/\text{s}$ and 30.0 $\mu\text{m}^3/\text{s}$ and the results are shown in Figure 11. If a small value (*e.g.*, 1.6 $\mu\text{m}^3/\text{s}$) is used for K_0 , the calculated as-solidified λ_2 falls below the experimental curve. Similarly, if the value of K_0 is too large (*e.g.*, 7.6 $\mu\text{m}^3/\text{s}$), the calculated as-solidified λ_2 also deviates from the experiment curve. The best simulation–experiment agreement is obtained when the value of K_0 is 4.6 $\mu\text{m}^3/\text{s}$. It is noteworthy that when the value of K_0 is 4.6 $\mu\text{m}^3/\text{s}$, all calculated values of λ_2 under different cooling conditions fall on the experiment curve (Figure 4(b)). Therefore, a value of 4.6 $\mu\text{m}^3/\text{s}$ for K_0 is recommended for the current RMF condition. From Figure 4(b), with an extremely low cooling rate (< 0.1 K/s), a local minimum of λ_2 is observed at a very early stage of the solidification. This might not be expected. The evolution of the secondary dendrites in the undercooled melt near the solidification front is an ongoing topic. A perturbation of the local temperature or solute concentration can initialise the secondary arms.^[7] It seems that this local minimum of λ_2 is not fully valid at this very early stage of the solidification. For the subsequent stages of the solidification, Eq. [15] has been verified by experimental results.^[6,12]

VI. CONCLUSIONS

A novel three-phase volume-average-based solidification model is introduced to simulate the unidirectional solidification of an AlSi7Fe1 alloy under RMF (6 mT, 50 Hz). The modelling results of the Si and Fe distribution across the sample section were validated against reported laboratory experiments, and good simulation–experiment agreement is obtained. Knowledge on the dynamic precipitation of β -Al₅FeSi and its effect on solidification and the flow are improved.

- (1) The solidification of the AlSi7Fe1 alloy starts with the development of primary aluminium dendrites (α -Al), followed by the precipitation of β -Al₅FeSi during the binary eutectic reaction. The primary aluminium dendrites of α -Al and β -Al₅FeSi precipitates are considered as two different solid phases, and their formations follow different growth kinetics. Herein, a simple formulation for the growth of β -Al₅FeSi is proposed. Despite its simplicity, the solidification path (microsegregation) of this ternary alloy and formed macrosegregation under the influence of an RMF have been demonstrated to be successfully ‘reproduced’ by the proposed model.
- (2) During directional solidification of AlSi7Fe1 under the stirring of RMF, an azimuthal flow and superimposed meridional flow (Ekman effect) are generated at the solidification front. The forced flow decreases the thickness of the mushy zone, modifies the morphology of the mushy zone, and causes the formation of the central segregation channel with sidearms. In the mushy zone, $c_{\ell, \text{Si}}$ and $c_{\ell, \text{Fe}}$ start with an increase near the solidification front due to solute rejection during the formation of primary aluminium dendrites until the binary eutectic reaction occurs. Since the subsequent formation of β -Al₅FeSi during the binary eutectic reaction consumes a large amount of Fe, $c_{\ell, \text{Fe}}$ gradually decreases. The consumption of Si in the formation of β -Al₅FeSi is very limited, and hence $c_{\ell, \text{Si}}$ increases consistently.
- (3) The macrosegregation profiles of Si and Fe across the RMF-stirred sample section are very different: Si is mostly concentrated at the sample centre, while Fe shows two segregation peaks at approximately 1 mm from the centre. This is due to the maximal amount of β -Al₅FeSi formed at approximately 1 mm from the centre. The formed β -Al₅FeSi is captured by the columnar dendrites where Fe is ‘frozen’. Migration of β -Al₅FeSi in the mushy zone is likely negligible.
- (4) In a technical alloy like AlSi7Fe1, the formed β -Al₅FeSi significantly blocks the interdendritic flow under the influence of an RMF. Hence, dendrites appear to follow the coarsening law ($\lambda_2 \propto t_f^{1/3}$) of solidification under pure diffusive conditions. This conclusion supports the work of Steinbach *et al.*^[6,9]
- (5) The dendrite coarsening law of Neumann-Heyme *et al.*^[12] is incorporated in the model to consider

the dynamic evolution of λ_2 and its effect on the interdendritic flow (varying permeability^[10]). Compared with previous models where a constant λ_2 (as-solidified value) is used for the permeability, the current model can improve the simulation accuracy by 8 pct, demonstrated by the results for the Si macrosegregation index.

ACKNOWLEDGMENTS

The authors acknowledge the financial support from Austrian Research Promotion Agency (FFG) -Austrian Space Application Program (ASAP) through the project FLOWSICONS (No. 859777), Austria Science Fund (FWF, I4278-N36), as well as the support from European Space Agency (ESA) through the project MICAST.

FUNDING

Open access funding provided by Montanuniversität Leoben.

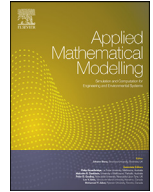
Open Access This article is licensed under a Creative Commons Attribution 4.0 International License, which permits use, sharing, adaptation, distribution and reproduction in any medium or format, as long as you give appropriate credit to the original author(s) and the source, provide a link to the Creative Commons licence, and indicate if changes were made. The images or other third party material in this article are included in the article’s Creative Commons licence, unless indicated otherwise in a credit line to the material. If material is not included in the article’s Creative Commons licence and your intended use is not permitted by statutory regulation or exceeds the permitted use, you will need to obtain permission directly from the copyright holder. To view a copy of this licence, visit <http://creativecommons.org/licenses/by/4.0/>.

REFERENCES

1. M.C. Flemings: *ISIJ Int.*, 2000, vol. 40, pp. 833–41.
2. S. Steinbach and L. Ratke: *Mater. Sci. Eng. A*, 2005, vols. 413–414, pp. 200–04.
3. T. Campanella, C. Charbon, and M. Rappaz: *Metall. Mater. Trans. A Phys. Metall. Mater. Sci.*, 2004, vol. 35A, pp. 3201–10.
4. P. Mikolajczak and L. Ratke: *Metall. Mater. Trans. A Phys. Metall. Mater. Sci.*, 2015, vol. 46, pp. 1312–27.
5. H. Zhang, M. Wu, Y. Zheng, A. Ludwig, and A. Kharicha: *Mater. Today Commun.*, 2020, vol. 22, p. 100842.
6. S. Steinbach, L. Ratke, G. Zimmermann, L. Sturz, A. Roósz, J. Kovács, Y. Fautrelle, O. Budenkova, L. J., S. Dost, G. G.-U, N. Warnken, M. Wu, and W.H. Sillekens: *Proceedings of the 5th Decennial International Conference on Solidification Processing*, Old Windsor, 2017, pp. 267–71.
7. W. Kurz and D.J. Fisher: in *Metallography and Microstructures*, second., Trans Tech Publications Ltd, Zuerich, 2018, pp. 71–92.
8. D.H. Kirkwood: *Mater. Sci. Eng.*, 1985, vol. 73, pp. L1–L4.
9. S. Steinbach and L. Ratke: *Int. J. Cast Met. Res.*, 2009, vol. 22, pp. 290–93.

10. C. Puncreobutr, A.B. Phillion, J.L. Fife, and P.D. Lee: *Acta Mater.*, 2014, vol. 64, pp. 316–25.
11. J.C. Ramirez and C. Beckermann: *Metall. Mater. Trans. A Phys. Metall. Mater. Sci.*, 2003, vol. 34A, pp. 1525–36.
12. H. Neumann-Heyme, K. Eckert, and C. Beckermann: *Acta Mater.*, 2017, vol. 140, pp. 87–96.
13. Q. Li and C. Beckermann: *Phys. Rev. E Stat. Phys. Plasmas Fluids Relat. Interdiscip. Top.*, 1998, vol. 57, pp. 3176–88.
14. Y. Zheng, M. Wu, E. Karimi-Sibaki, A. Kharicha, and A. Ludwig: *Int. J. Heat Mass Transf.*, 2018, vol. 122, pp. 939–53.
15. M. Wu, A. Ludwig, and A. Kharicha: *Metals*, 2019, vol. 9, p. 229.
16. O. Budenkova, F. Baltaretu, S. Steinbach, L. Ratke, A. Roósz, A. Rónaföldi, J. Kovács, A.M. Bianchi, and Y. Fautrelle: *Mater. Sci. Forum*, 2014, vols. 790–791, pp. 46–51.
17. M. Wu and A. Ludwig: *Metall. Mater. Trans. A Phys. Metall. Mater. Sci.*, 2007, vol. 38A, pp. 1465–75.
18. J. Lipton, M.E. Glicksman, and W. Kurz: *Mater. Sci. Eng.*, 1984, vol. 65, pp. 57–63.
19. G. Sha, K.A.Q. O'Reilly, B. Cantor, J.M. Titchmarsh, and R.G. Hamerton: *Acta Mater.*, 2003, vol. 51, pp. 1883–97.
20. J. Wang, P.D. Lee, R.W. Hamilton, M. Li, and J. Allison: *Scr. Mater.*, 2009, vol. 60, pp. 516–19.
21. C. Puncreobutr, A.B. Phillion, J.L. Fife, P. Rockett, A.P. Horsfield, and P.D. Lee: *Acta Mater.*, 2014, vol. 79, pp. 292–303.
22. D. Ferdian, B. Suharno, B. Duployer, C. Tenaillieu, L. Salvo, and J. Lacaze: *Trans. Indian Inst. Met.*, 2012, vol. 65, pp. 821–25.
23. A. Ludwig and M. Wu: *Metall. Mater. Trans. A Phys. Metall. Mater. Sci.*, 2002, vol. 33, pp. 3673–83.
24. M.C. Schneider and C. Beckermann: *Int. J. Heat Mass Transf.*, 1995, vol. 38, pp. 3455–73.
25. P. Mikolajczak and L. Ratke: *Int. J. Cast Met. Res.*, 2013, vol. 26, pp. 339–53.
26. J.K. Roplekar and J.A. Dantzig: *Int. J. Cast Met. Res.*, 2001, vol. 14, pp. 79–95.
27. A. Rónaföldi, J. Kovács, and A. Roósz: *Trans. Indian Inst. Met.*, 2009, vol. 62, pp. 475–77.
28. O. Budenkova, F. Baltaretu, J. Kovács, A. Roósz, A. Rónaföldi, A.M. Bianchi, and Y. Fautrelle: *IOP Conference Series: Materials Science and Engineering*, 2012, pp. 012046.
29. Y.W. Lee, R.N. Smith, M.E. Glicksman, and M.B. Koss: *Annu. Rev. Heat Transf.*, 1996, vol. 7, pp. 59–139.
30. Q. Li and C. Beckermann: *J. Cryst. Growth*, 2002, vol. 236, pp. 482–98.
31. D.N. Miller, L. Lu, and A.K. Dahle: *Metall. Mater. Trans. B Process Metall. Mater. Process. Sci.*, 2006, vol. 37, pp. 873–78.
32. G. Sigworth, J. Campbell, and J. Jorstad: *Int. J. Met.*, 2009, vol. 3, pp. 65–78.
33. X. Cao and J. Campbell: *Metall. Mater. Trans. A Phys. Metall. Mater. Sci.*, 2003, vol. 34, pp. 1409–20.
34. Y.H. Cho, H.C. Lee, K.H. Oh, and A.K. Dahle: *Metall. Mater. Trans. A Phys. Metall. Mater. Sci.*, 2008, vol. 39, pp. 2435–48.
35. S. Terzi, J.A. Taylor, Y.H. Cho, L. Salvo, M. Suéry, E. Boller, and A.K. Dahle: *Acta Mater.*, 2010, vol. 58, pp. 5370–80.

Publisher's Note Springer Nature remains neutral with regard to jurisdictional claims in published maps and institutional affiliations.



Modelling melting and grain destruction phenomena during globular equiaxed solidification

Haijie Zhang^a, Menghuai Wu^{a,*}, Peter Schumacher^b, Christian M.G. Rodrigues^a,
Andreas Ludwig^a, Abdellah Kharicha^a

^aChair for Simulation and Modeling of Metallurgy Processes, Department of Metallurgy, University of Leoben, Franz-Josef-Str. 18, Leoben A-8700, Austria

^bChair of Casting Research, Department of Metallurgy, University of Leoben, Leoben A-8700, Austria

ARTICLE INFO

Article history:

Received 18 February 2021

Revised 14 April 2021

Accepted 28 April 2021

Available online 11 May 2021

Keywords:

Melting

Solidification

Nucleation

Macrosegregation

Modelling

ABSTRACT

Melting or re-melting accompanies solidification in many technical castings. For example, during ingot casting, some crystal fragments or equiaxed grains can enter the superheated region and re-melt, while solidification continues in other regions. Solidification and remelting occurring simultaneously at different locations present an important species/energy transport mechanism, which impacts the structural/compositional homogeneity of the castings. The re-melting is typically understood as a reduction in the equiaxed grain size, but it can also lead to the destruction (disappearance) of equiaxed grains. Existing process-based models cannot treat the solidification/melting by considering both grain nucleation and destruction properly. Therefore, a new model is proposed based on a two-phase volume-average approach. In this model, nucleation of equiaxed grains occurs when inoculants (free growth sites) are activated by undercooling, while destruction of equiaxed grains occurs only when the equiaxed grains are completely re-melted by superheating. The mass, momentum, species, and enthalpy conservation equations are solved for the solidification/melting. The transport equations for the number densities of equiaxed grains and inoculants are calculated separately. A test casting (Al–7 wt.% Si) is calculated to illustrate the modelling features. This study improves understanding of grain melting and grain destruction as well as their impact on the as-solidified structure.

© 2021 The Author(s). Published by Elsevier Inc.
This is an open access article under the CC BY license
(<http://creativecommons.org/licenses/by/4.0/>)

1. Introduction

The melting or re-melting of equiaxed grains is an important phenomenon, which accompanies the solidification process in many technical castings. Melting and solidification can occur simultaneously or alternately at different locations of the casting domain. For example, during ingot casting, some crystal fragments or equiaxed grains can move and enter the superheated region and re-melt, while solidification continues in other regions. In practice, two conditions can lead to re-melting: an increase in the local temperature and a change in the local solute concentration [1–3]. Thermo-solutal

* Corresponding author.

E-mail address: menghuai.wu@unileoben.ac.at (M. Wu).

and/or forced convections are mainly responsible for these processes [4,5]. It was experimentally confirmed that grain nucleation, solidification, transport, re-melting, and destruction can occur simultaneously [5,6]. These simultaneous solidification/melting processes together with grain migration provide an important species/energy transport mechanism, impact the final as-formed structure, and influence the heterogeneity (macrosegregation) of castings.

While knowledge about nucleation and solidification appears to be well established [7,8], research on melting and grain destruction lags greatly behind the rest of the field. Based on published work [1,2,9–11], melting is not simply ‘inverse solidification’. Complex kinetics that breaks the solidification/melting symmetry involve solute partitioning and solute redistribution, which can consistently update the grain morphology in the mushy zone. A temperature gradient zone melting experiment was performed to investigate the melting and re-solidification of an Al–Cu alloy under a stationary temperature gradient [2,12]. Melt convection and grain transport were not a/the focus of that experiment.

Melting experiments under natural convection condition were also performed [13–15]. By melting organic materials or metals in a rectangular enclosure vertically from one side, the motion and shape of the solid–liquid interface was tracked and analysed. These studies focused on the melt convection and its impact on the profile of the melting front, while grain transport was not explicitly discussed. However, the experimentally measured temperature information does imply that transport of crystal fragments and re-solidification could accompany the melting process as well. The transport, re-melting, and annihilation (destruction) of equiaxed grains by melt convection appears to be evidenced by Rerko et al. [16] in a grain-refinement Al–10 wt.% Cu solidification experiment. The grain size in the top-cooled ingots was approximately 3 times larger than that in the bottom-cooled ones. This difference was interpreted to be due to advection of nucleated grains and re-melting. For the top-cooled ingots, the cold solute-segregated melt descended and brought the equiaxed grains to warmer areas where some of them melted, leaving fewer equiaxed grains in the upper region to grow into a large size.

In the past decades, some efforts have been made in modelling the melting process [17]. Most simulations [18,19] focused on the melting of pure substance under natural/forced convection. The effect of thermo-solutal convection and the influence of solute transport on alloy solidification were investigated by Voller et al. [20] based on the enthalpy–porosity model. This model can be easily extended for the melting of alloys, but it is limited to rigid solid structures, such as eutectics and columnar dendrites. Similar work was done by Kumar et al. [11]. The cellular automaton (CA) method has also been used to simulate the melting and solidification of equiaxed grains, where solute redistribution during the phase transformation was calculated [21]. Once again, solid transport was not considered. The most promising model is the multiphase volume-average model [4,22–24] because it provides the flexibility to treat grain nucleation, liquid convection, grain transport and sedimentation, solute redistribution, and different growth kinetics during solidification/melting of equiaxed grains and columnar dendrites. The importance of grain destruction was addressed [24–27], but the proposed models for melting were greatly simplified, i.e. the grain number density was set to zero as soon as grains were advected into the superheated region.

In the current paper, a new model for treating melting and grain destruction during alloy solidification is proposed based on a two-phase volume-average approach. Both nucleation and destruction of equiaxed grains are considered. The mass, momentum, species, and enthalpy conservation equations are solved for globular equiaxed solidification/melting. The transports of the number densities of equiaxed grains and inoculants (free growth sites) are calculated individually. The modelling features are verified based on simulations of an Al-casting (Al–7 wt.% Si).

2. Model description (a two-phase model)

The fundamentals of volume-average-based solidification models can be found elsewhere [25,28,29]. In the current paper, the model is extended to cover the re-melting and destruction of equiaxed grains. It is well known that most alloys solidify into a mixed columnar–equiaxed structure. To focus on grain re-melting and destruction, here a two-phase globular equiaxed solidification model is used. The two phases are the liquid phase and solid phase (equiaxed grains). The volume fractions of the two phases always sum to 1.0, i.e. $f_\ell + f_e = 1$. The morphology of equiaxed grains is assumed to be spherical. Heterogeneous nucleation of equiaxed grains occurs by activating inoculants, i.e. free growth sites, when a necessary undercooling is achieved. Growth of the grains is governed by diffusion. A thermodynamic equilibrium applies at the solid–liquid interface, and the concentration difference between the thermodynamic equilibrium concentration of the liquid melt at the solid–liquid interface and the volume-averaged liquid concentration is the driving force for grain growth. The re-melting process includes two steps: reduction in the grain size (melting) and the destruction of the grain (disappearance). Re-melting occurs only when the equiaxed grains are exposed to the superheated melt. The reduction in the grain size is also governed by diffusion. Destruction of the grain occurs only when the grain is completely re-melted. It is assumed that the inoculant, on which the original equiaxed grain nucleated, is released after re-melting. This means that one re-melted/disappeared equiaxed grain will turn into one inoculant, which is reserved as a future potential nucleation (free growth) site. Therefore, the total number of grains and inoculants in the casting domain is conserved.

2.1. Transport of equiaxed grains and inoculants

The velocities of the melt and solid phase (equiaxed grains) are known by solving the Navier–Stokes equations (\vec{u}_ℓ and \vec{u}_{eq} , respectively). The motion of inoculants follows the velocity of the melt [28]. The transport equations for the number

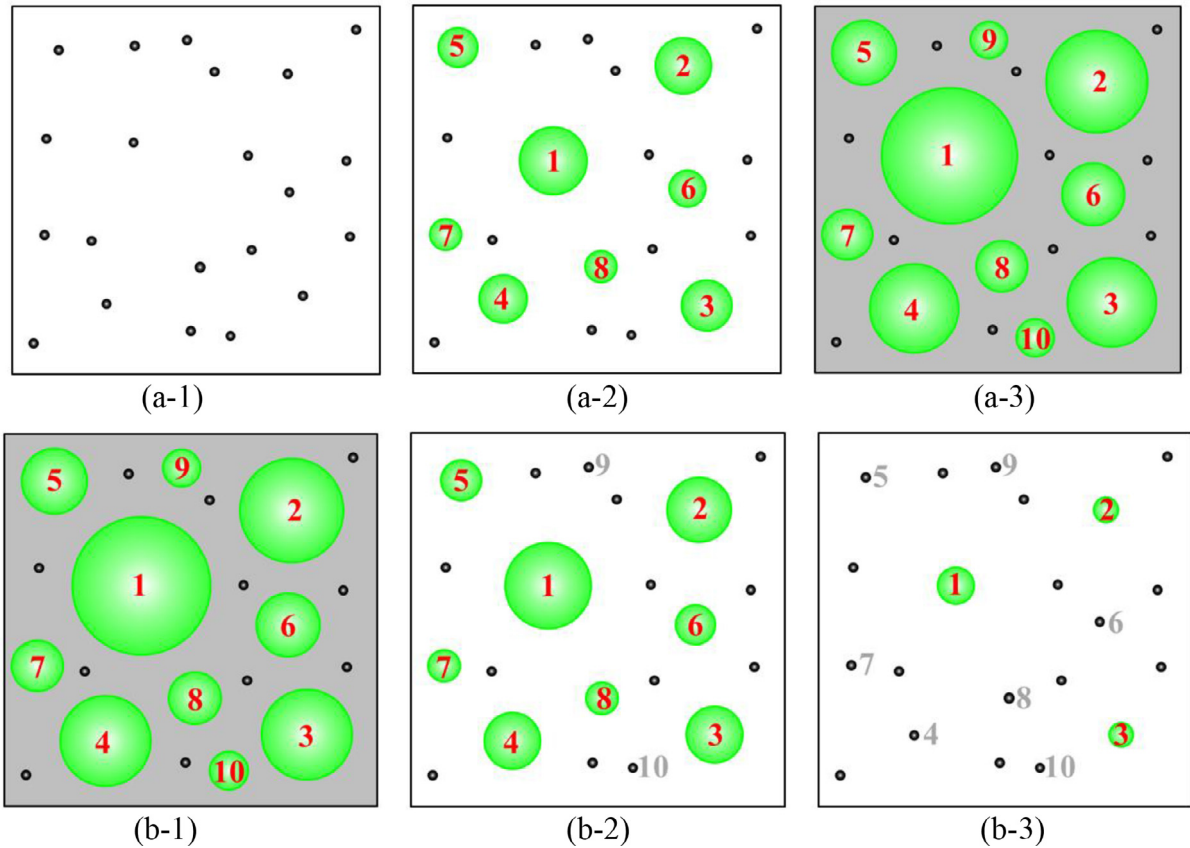


Fig. 1. Schematic of (a) the nucleation and grain growth and (b) the re-melting and grain destruction processes. The black dots denote the inoculants, the green spheres indicate the equiaxed grains, and the grey background indicates the eutectic phase. All grains are numbered from 1 to 10.

densities of equiaxed grains and inoculants are

$$\frac{\partial}{\partial t} n_{eq} + \nabla \cdot (\vec{u}_{eq} n_{eq}) = \dot{n}, \tag{1}$$

$$\frac{\partial}{\partial t} n_{in} + \nabla \cdot (\vec{u}_\ell n_{in}) = -\dot{n}, \tag{2}$$

where n_{in} and n_{eq} are the number densities of the inoculants and equiaxed grains, respectively; \dot{n} is the nucleation/destruction rate. The drag force between the liquid melt and the solid equiaxed grains is approximated by the Kozeny–Carman equation for $f_e < 0.7$ and the Blake–Kozeny equation for $f_e \geq 0.7$ [30]. The interactions between neighbouring equiaxed grains are modelled by the effective viscosity. A mixing rule was employed to estimate the viscosity of the equiaxed phase, which can be calculated via $\mu_e = \frac{\mu_\ell}{f_e} ((1 - f_e/f_e^c)^{-2.5} f_e^c - (1 - f_e))$ [26]. To deal with the hydrodynamic interaction between phases, the equiaxed grains are assumed to have envelopes and their volume fractions are indicated by f_e^{Env} . The volume fraction of grain envelope (f_e^{Env}) is related to the volume fraction of solid (f_e) through $f_{si} = f_e/f_e^{Env}$, where f_{si} is the volume ratio of the solid grain to the equiaxed grain envelope. In this study, f_{si} is set as a constant value (0.235). When f_e^{Env} is beyond the packing limit ($f_e^c = 0.637$), the equiaxed phase becomes a rigid porous medium, through which the liquid is still able to penetrate via the voids between the closely packed grains. Further discussion on “envelope concept” is made in Section 5.4.

2.2. Heterogeneous nucleation and solidification

The nucleation sequence during the solidification process is schematically shown in Fig. 1(a). Inoculants exist in the parent melt (Fig. 1 (a-1)). With sufficient undercooling, they are activated to become equiaxed grains (Fig. 1 (a-2)). The undercooling for activating an inoculant depends on its size [31]. Consequently, the number of inoculants in the melt gradually decreases. The final solidification structure of the sample may consist of a eutectic phase, primary equiaxed grains with various sizes, and inactivated inoculants embedded in the eutectic phase (Fig. 1 (a-3)). It is well known that certain alloying

and impurity elements can poison the inoculants (grain refiners) and therefore adversely affect grain refinement [32]. The poisoning effect is ignored in the current study.

A continuous nucleation formulation (Gaussian distribution), as proposed by Rappaz and Gandin [33,34], has been widely used to model heterogenous grain nucleation during solidification [35,36]. A Gaussian distribution can be used as an approximation of a log normal distribution if the inoculant diameter is relatively large [31,37]. The originally proposed Gaussian distribution assumed that there were a certain amount of free nucleation sites (inoculants) in the melt (n_{max}), and the free nucleation sites were uniformly distributed in the casting. This assumption is inconsistent with practical solidification conditions. An uneven distribution of inoculants will be achieved owing to nucleation and/or advection. The number density of the inoculant gradually decreases as nucleation occurs. In the current paper, the inoculants and equiaxed grains are distinguished and quantified by their number densities (n_{in} and n_{eq} , respectively). The number density of the inoculants can be transported, and it changes depending on local nucleation or grain destruction. The original continuous nucleation formulation of Rappaz and Gandin [33,34] is slightly updated by replacing n_{max} with the number density of the available inoculants n_{in} [28,38]:

$$\frac{dn_{eq}}{d(\Delta T)} = \frac{n_{in}}{\sqrt{2\pi} \cdot \Delta T_{\sigma}} \cdot e^{-\frac{1}{2} \cdot \left(\frac{\Delta T - \Delta T_N}{\Delta T_{\sigma}}\right)^2}, \tag{3}$$

where ΔT is the undercooling, and ΔT_{σ} and ΔT_N are the standard deviation and mean of the Gaussian distribution of nucleation undercooling. The local undercooling can be calculated by

$$\frac{D(\Delta T)}{Dt} = \frac{\partial \Delta T}{\partial t} + m \cdot \vec{u}_{\ell} \cdot \nabla c_{\ell} - \vec{u}_{\ell} \cdot \nabla T_{\ell}, \tag{4}$$

where t is time, m is the liquidus slope from the phase diagram, T_{ℓ} and ∇T_{ℓ} are the temperature and its gradient of the liquid phase, c_{ℓ} and ∇c_{ℓ} are the volume-averaged concentration and its gradient of the melt. ΔT can be calculated via $\Delta T = T_f + m \cdot c_{\ell} - T$, in which T_f is the melting point of solvent. The nucleation rate, $\dot{n} = D(n_{eq})/Dt$, is calculated by

$$\dot{n} = \frac{D(\Delta T)}{Dt} \cdot \frac{dn_{eq}}{d(\Delta T)}. \tag{5}$$

Note that groups of inoculants with different sizes could be followed individually [39]. However, it would require massive computational resources. Therefore, all inoculants are assumed to have the same size, but they are activated as nuclei at different undercoolings, statistically following the Gaussian distribution. The solidification rate, i.e. the rate of mass transfer from the liquid to the equiaxed solid ($M_{\ell e}$), is calculated by

$$M_{\ell e} = v_{Re} \cdot (n_{eq} \cdot \pi d_e^2) \cdot \rho_e \cdot f_{\ell}, \tag{6}$$

with

$$v_{Re} = \frac{D_{\ell}}{l_{\ell}} \cdot \frac{(c_{\ell}^* - c_{\ell})}{(1 - k)c_{\ell}^*} + \frac{D_e}{l_e} \cdot \frac{(c_e^* - c_e)}{(1 - k)c_{\ell}^*}, \tag{7}$$

where v_{Re} is the grain growth speed, d_e is the average grain diameter, ρ_e is the density of the equiaxed phase, k is the solute partition coefficient, c_{ℓ}^* is the thermodynamic equilibrium concentration of the liquid, D_{ℓ} and D_e are the solute diffusion coefficients, l_{ℓ} ($= d_e$) and l_e ($= d_e/6$) are the corresponding diffusion lengths in the liquid melt and solid grains, respectively.

2.3. Melting and grain destruction

The melting/grain-destruction process is schematically shown in Fig. 1(b). The primary material includes the as-cast structure, i.e. eutectic phase, equiaxed grains and some inactivated inoculants (Fig. 1 (b-1)). As the temperature increases, the eutectic phase begins melting first. This process releases the embedded equiaxed grains and inactivated inoculants, and they are free to move again. With further re-melting of the equiaxed grains, their sizes decrease, which is followed by grain destruction (Fig. 1 (b-2)). The two smallest equiaxed grains (numbered 9–10) are completely melted/destroyed; thus, they are turned into inoculants. At a later stage, Fig. 1 (b-3), most grains are melted/destroyed, and there are only three equiaxed grains (1–3) that remain.

Although the volume-average model computes only one average grain size (d_e), the equiaxed grains are assumed to follow a lognormal size distribution (Appendix A).

$$\frac{d(n_{eq})}{d(x)} = \frac{n_{eq}}{\sqrt{2\pi}\sigma x} e^{-\frac{1}{2} \left(\frac{\ln(x) - \ln(\bar{d}_e)}{\sigma}\right)^2}, \tag{8}$$

where

$$1 = \int_0^{\infty} \frac{1}{\sqrt{2\pi}\sigma x} e^{-\frac{1}{2} \left(\frac{\ln(x) - \ln(\bar{d}_e)}{\sigma}\right)^2} d(x), \tag{9}$$

where σ is the geometric standard deviation of the lognormal distribution, the dummy variable (x) corresponds the grain diameter of different size classes, and \bar{d}_e is the geometrical mean. Note that the geometrical mean of the grain size (\bar{d}_e) is

different from the volume-averaged grain size (d_e). However, it is assumed that their variation during melting follows a similar trend, i.e. $d(\hat{d}_e)/dt \approx d(d_e)/dt$, which can be estimated by v_{Re} . A critical value of the grain size ($d_{e,critical}$) is introduced. When a size class of equiaxed grains is melted to smaller than $d_{e,critical}$, it will be eliminated from n_{eq} . Therefore, the grain destruction rate, $\dot{n} = dn_{eq}/dt$, is calculated by

$$\dot{n} = v_{Re} \cdot \left. \frac{d(n_{eq})}{d(x)} \right|_{x=d_{e,critical}} \quad (10)$$

Because melting is assumed to be governed by diffusion, Eq. (7) is valid for calculating v_{Re} . During melting, the equilibrium concentrations (c_ℓ^* and c_e^*) are lower than the volume-averaged concentrations (c_ℓ and c_e); therefore, a negative value of v_{Re} is obtained. Because dn_{eq}/dx is always positive, if v_{Re} is negative, the \dot{n} calculated by Eq. (10) is also negative. The melting rate, i.e. the rate of mass transfer from the equiaxed to the liquid ($M_{\ell e}$), is calculated by

$$M_{\ell e} = v_{Re} \cdot (n_{eq} \cdot \pi d_e^2) \cdot \rho_\ell \quad (11)$$

Because no geometrical impingement factor is necessary for melting, Eq. (11) differs from Eq. (6). The energy, momentum, and species transfer between the liquid and the equiaxed solid during the solidification/melting process can be found in our previous papers [23,28]. Eutectic reaction/melting occurs when the temperature decreases/increases to the eutectic isotherm. In the current model, the release/absorption of latent heat during the eutectic reaction/melting is approximated with the temperature compensation method. The remaining liquid after the eutectic reaction is considered as eutectic phase. To analyse the macrosegregation, a mixture concentration is defined: $c_{mix} = (c_\ell \cdot \rho_\ell \cdot f_\ell + c_e \cdot \rho_e \cdot f_e) / (\rho_\ell \cdot f_\ell + \rho_e \cdot f_e)$. The macrosegregation intensity is characterised by its index: $c_{mix}^{index} = (c_{mix} - c_0) / c_0 \cdot 100\%$.

2.4. Solution procedures/strategy

The current model was implemented in the commercial Ansys Fluent software (version 17.1), which uses a control-volume method. The solver in Ansys Fluent provides a platform to solve the global transport equations. In addition, it provides flexibility (open program interface) in defining the exchange/source terms for the transport equations, and even allows modification of the solution procedure [29]. One numerical constraint is applied, i.e. the minimum value of n_{in} and n_{eq} was enforced to be 10^7 m^{-3} . It is difficult for Eqs. (1) and (2) to converge when the transport quantity becomes too small in comparison to its source term. All transport equations were solved in an iterative manner. For each time step, up to 20 iterations were used to decrease the normalised residuals of the phase fraction, velocity components, pressure, and species below 10^{-4} and enthalpy quantities below 10^{-7} . The time step that ensures a high accuracy solution must be determined empirically by test simulations. In this study, all calculations were conducted with a time step of 0.001 s. Conservation of the species and number densities of the grains and inoculants is guaranteed in the system.

3. Configuration of test simulation cases

A 2D geometry (60width \times 80height mm^2) was meshed to a size of $1.0 \times 1.0 \text{ mm}^2$, and an Al–7 wt.% Si alloy was calculated. The Al–Si binary phase diagram was linearised, and the liquidus slope (m) and the solute partition coefficient (k) were assumed to be constant. A no-slip boundary condition was assumed to be valid on the domain surface. Before the start of the simulation, the domain was set to be uniform in concentration ($c_0 = 0.07$) and temperature ($T_0 = 900 \text{ K}$). As the initial condition, the minimum value was assigned for n_{eq} (10^7 m^{-3}), while a very large value was assigned for n_{in} ($2.0 \times 10^{10} \text{ m}^{-3}$). The material properties and other parameters are summarised in Table 1.

Two simulation cases were designed. Case I was used to check the model implementation. The sample was solidified and re-melted under purely diffusive condition. No flow and grain sedimentation were considered. A Dirichlet boundary condition was applied on four walls. The corresponding temperature profiles can be found in Fig. 2(a). The sample was cooled to below eutectic temperature in stage A, heated to over the melting point in stage B, and then cooled again in stage C. To simplify case I, the latent heat was not considered, and an extreme large conductivity ($10^7 \text{ W} \cdot \text{m}^{-1} \cdot \text{K}^{-1}$) was used for both the liquid and equiaxed phases. Therefore, the entire sample had a nearly uniform temperature during the cooling/heating processes.

Case II was similar to a practical solidification/melting process, where thermo-solutal convection and grain sedimentation were considered. In case II (stage A), only the right wall was cooled, following the temperature profile shown in Fig. 2(b). The other three walls were adiabatic. The as-solidified phase distribution of case II (stage A) was used as the initial condition for case II (stage B). The left wall was heated again, following the temperature profile of Fig. 2(c), while other walls were adiabatic. In case II, the true physical values of latent heat and heat conductivities of the alloy were used.

4. Simulation results

4.1. Case I: solidification and melting under purely diffusive conditions

The solidification/melting sequence of the sample is shown in Fig. 3. All solidification quantities were taken from the domain centre. The calculated T followed the pre-defined temperature profiles exactly (Fig. 3(a)). The calculated undercooling (ΔT) is plotted in Fig. 3(b). At the beginning of stage A, the melt was superheated. With the decrease in T , the melt

Table 1
Material properties of Al–7 wt.% Si and other parameters [40–42].

Properties/parameters	Symbol	Units	Values
Thermophysical			
Specific heat	c_p^ℓ, c_p^e	$J \cdot kg^{-1} \cdot K^{-1}$	1140.0
Latent heat	Δh_f	$J \cdot kg^{-1}$	4.0×10^5
Diffusion coefficient (liquid)	D_ℓ	$m^2 \cdot s^{-1}$	6.5×10^{-9}
Diffusion coefficient (solid)	D_e	$m^2 \cdot s^{-1}$	1.0×10^{-12}
Thermal conductivity (liquid)	k_p^ℓ	$W \cdot m^{-1} \cdot K^{-1}$	76.7
Thermal conductivity (solid)	k_p^e	$W \cdot m^{-1} \cdot K^{-1}$	185.0
Liquid thermal expansion coefficient	β_T	K^{-1}	-1.85×10^{-4}
Liquid solutal expansion coefficient	β_c	$wt.\%^{-1}$	1.3×10^{-3}
Density	ρ_ℓ, ρ_e	$kg \cdot m^{-3}$	2535.0
Density difference (Boussinesq)	$\Delta \rho (= \rho_e - \rho_\ell)$	$kg \cdot m^{-3}$	137.0
Viscosity	μ_ℓ	$kg \cdot m^{-1} \cdot s^{-1}$	2.52×10^{-3}
Thermodynamic			
Eutectic temperature	T_{eu}	K	850.0
Liquidus slope	m	$K \cdot wt.\%^{-1}$	-6.62
Equilibrium partition coefficient	k	-	0.13
Primary dendrite arm spacing	λ_1	m	3.0×10^{-4}
Secondary dendrite arm spacing	λ_2	m	5.0×10^{-5}
Gibbs–Thomson coefficient	Γ	m·K	2.4×10^{-7}
Melting point of solvent	T_f	K	933.4
Nucleation/Destruction			
Standard deviation for nucleation	ΔT_σ	K	0.5
Mean nucleation undercooling	ΔT_N	K	4.0
Standard deviation for destruction	σ	-	0.873
Critical diameter for grain destruction	$d_{e,critical}$	m	3.0×10^{-5}
Other			
Initial concentration	c_0	wt.%	7.0
Initial temperature	T_0	K	900.0
Initial number density of equiaxed grains	$n_{eq,0}$	m^{-3}	1.0×10^7
Initial number density of inoculants	$n_{in,0}$	m^{-3}	2.0×10^{10}
Cooling/heating rate	R	$K \cdot s^{-1}$	± 0.25

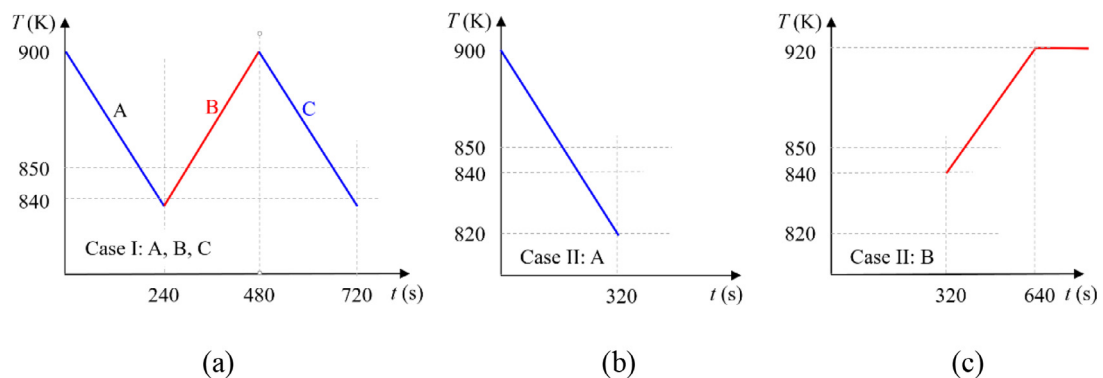


Fig. 2. Dirichlet thermal boundary conditions for different test simulation cases. (a) Case I: cooling and heating in different stages (A–C) equally from all walls; (b) case II (stage A): cooling from the right wall only; and (c) case II (stage B): heating from the left wall only. The heating/cooling rate had the same magnitude: $0.25 K \cdot s^{-1}$.

became undercooled at 30 s. Because of the undercooling, inoculants started to be activated as nuclei. As shown in Fig. 3(c), a number of inoculants were consumed, and the same number of equiaxed grains were generated. The formed grains grew in the undercooled melt. This can be seen through the positive $M_{\ell e}$ in Fig. 3(d). The direct outcomes of nucleation and solidification are an increase in f_e and a decrease in f_ℓ (Fig. 3(e)). The calculated volume-averaged diameter of the equiaxed grains, $d_e = \sqrt[3]{6f_e/\pi n_{eq}}$, is plotted in Fig. 3(f). d_e exhibited an increasing trend in stage A, except for a singular point at around 60 s. This singular point was caused by an instantaneous nucleation event. A sudden increase in n_{eq} will reduce the volume-averaged grain diameter (d_e). From Fig. 3(c), it can be seen the nuclei mainly formed during the early stage of solidification (30–85 s). After 85 s, there was almost no new nucleation. Only the formed equiaxed grains continued to grow. The mass transfer between the liquid and the equiaxed phases ($M_{\ell e}$) terminated when the temperature was below T_{eu} . At the end of stage A, the sample solidified with $n_{eq} = 1.4 \times 10^{10} m^{-3}$, $n_{in} = 5.6 \times 10^9 m^{-3}$, $f_e = 0.48$, $f_{eut} = 0.52$, and $d_e = 4.0 \times 10^{-4} m$.

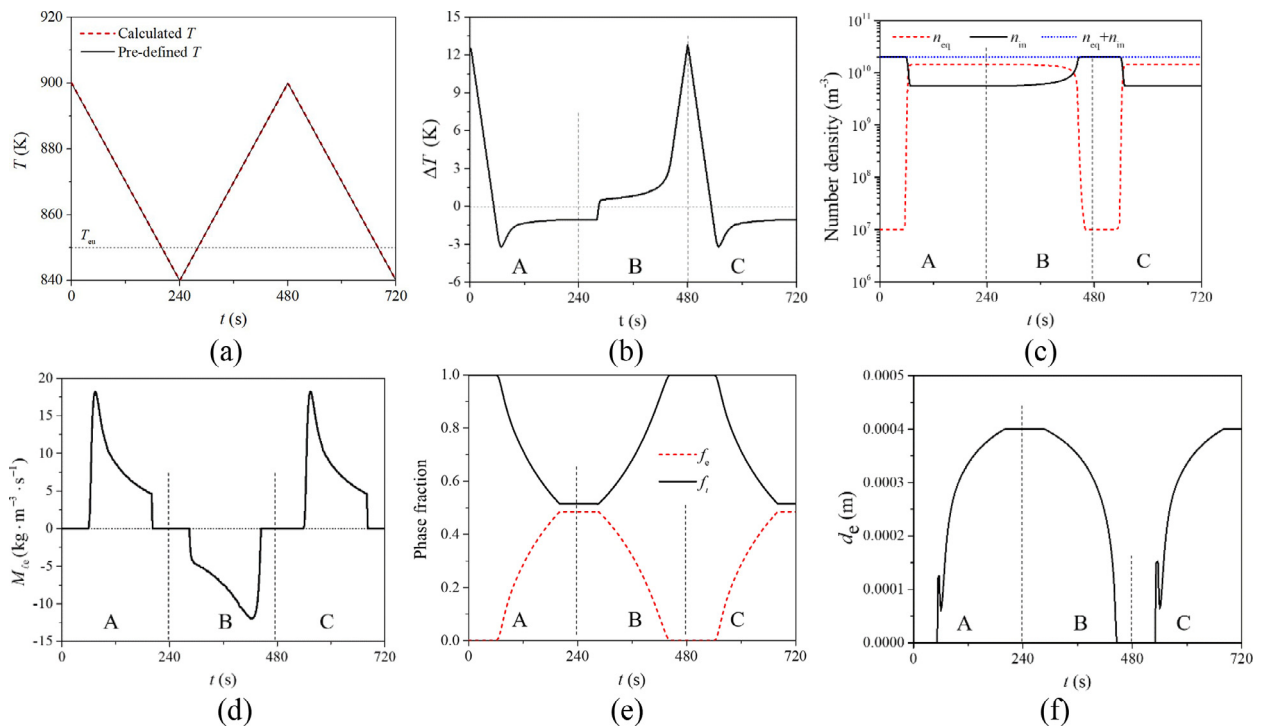


Fig. 3. Solidification/melting sequences of case I under purely diffusive conditions: (a) T ; (b) ΔT ; (c) n_{eq} , n_{in} , and the sum of n_{eq} and n_{in} ; (d) $M_{\ell e}$; (e) f_e and f_i ; and (f) d_e .

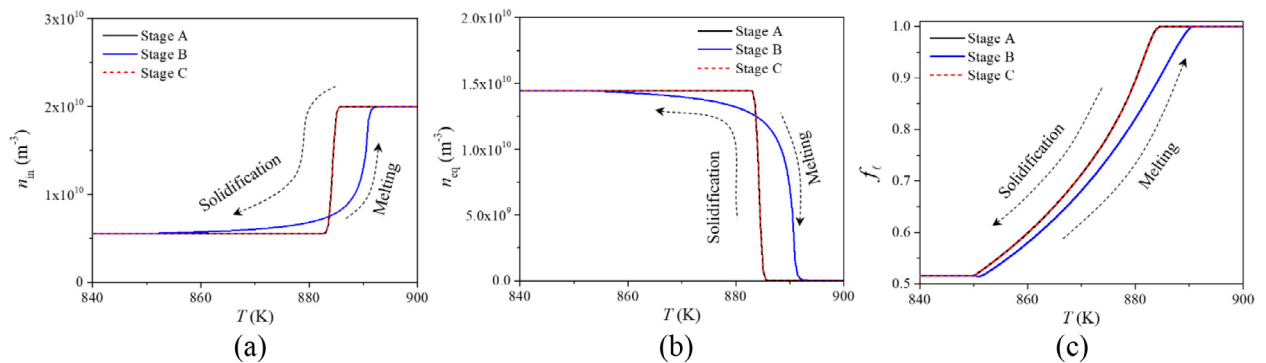


Fig. 4. Variations in (a) n_{in} , (b) n_{eq} , and (c) f_{ℓ} with T .

The melting sequence is shown in stage B in Fig. 3. T rose gradually, and ΔT changed from negative (undercooled) to positive (superheated). With the increase in T , the eutectic phase melted first, which was followed by melting of the equiaxed grains (as indicated by the negative $M_{\ell e}$). The equiaxed grains decreased in size (d_e) and phase fraction (f_e). At 420 s, when T rose to 884 K, n_{eq} decreased by 14.3% (from 1.4×10^{10} to $1.2 \times 10^{10} \text{ m}^{-3}$), but d_e reduced by 40.0% (from 4.0×10^{-4} to $2.4 \times 10^{-4} \text{ m}$) relative to the beginning of stage B. This is reasonable because a reduction in grain size (melting) always occurs before grain destruction. At 480 s, the minimum number density of grains was reached ($n_{eq} = 1.0 \times 10^7 \text{ m}^{-3}$), and f_s and d_e vanished, indicating that all equiaxed grains had been melted and destroyed. In stage C (re-solidification), the sample was cooled again. The solidification in stage C repeated the results of stage A. As displayed in Fig. 3(c), the sum of n_{eq} and n_{in} was always conserved during the solidification and melting processes.

The variations in f_{ℓ} , n_{eq} , and n_{in} with T from stage A to C are plotted in Fig. 4. With decreasing T , the inoculants were activated as nuclei. With further solidification, f_{ℓ} decreased. In the opposite condition, when T rose, f_{ℓ} increased, and the equiaxed grains melted and finally turned into inoculants. The overlap of these lines is indicative of the excellent self-consistency of the current model and method.

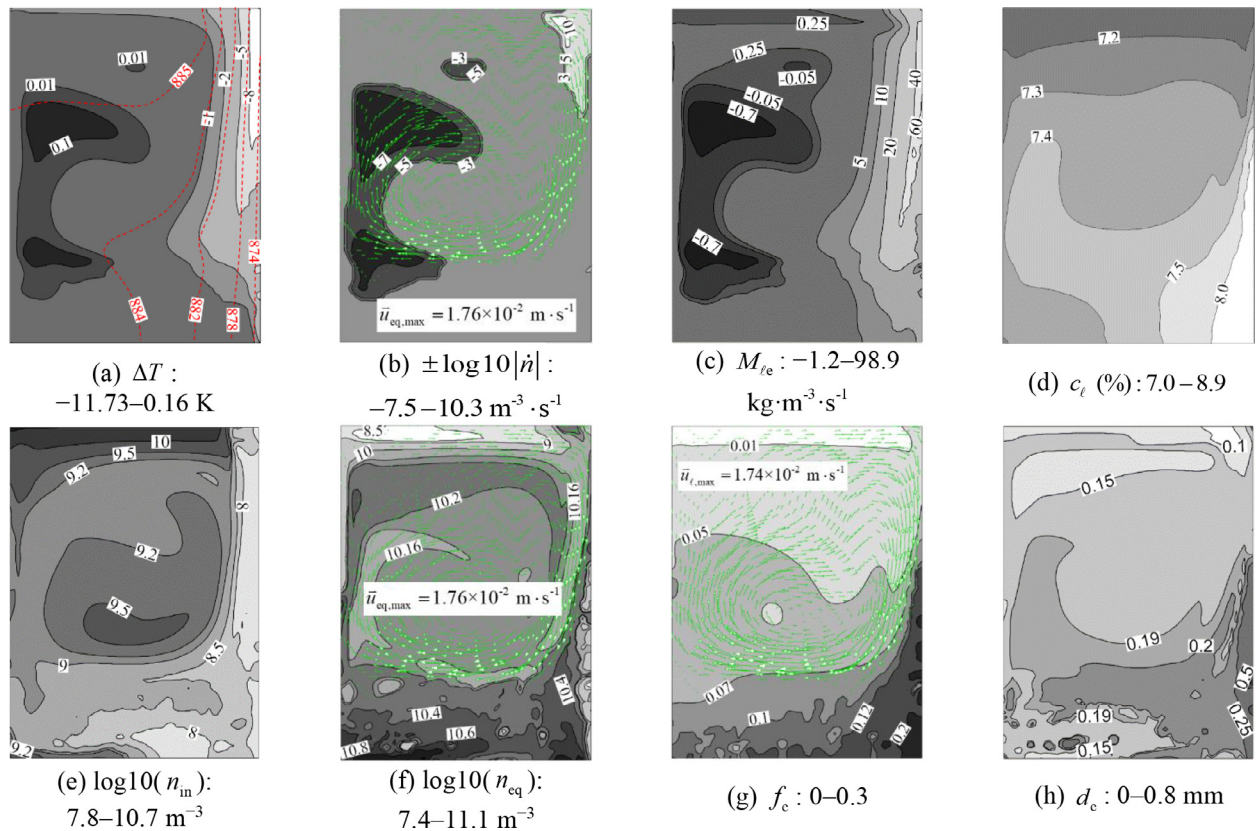


Fig. 5. Solidification sequence of case II (stage A) at 110 s. Contours and corresponding isolines of (a) ΔT overlaid by isotherms (red dashed lines); (b) $\pm \log_{10}|\dot{n}|$ overlaid by the vectors of \vec{u}_{eq} ; (c) $M_{\ell e}$; (d) c_{ℓ} ; (e) $\log_{10}(n_{in})$; (f) $\log_{10}(n_{eq})$ overlaid by the vectors of \vec{u}_{eq} ; (g) f_c overlaid by the vectors of \vec{u}_{eq} ; and (h) d_c (For interpretation of the references to color in this figure legend, the reader is referred to the web version of this article).

4.2. Case II: solidification and melting under thermo-solutal convection

4.2.1. Case ii (stage A): cooling from the right side

Solidification was triggered by cooling from the right wall. The solidification sequence at 110 s is shown in Fig. 5. A clockwise thermo-solutal convection formed (Fig. 5(g)). The flow transported both the liquid and solid phases and modified the temperature field. T and ΔT are shown in Fig. 5(a), which shows that the melt was strongly undercooled near the right surface and slightly superheated in the left part. As shown in Fig. 5(b), in the upper-right corner where the melt was most undercooled ($\Delta T \approx -11$ K), the fastest nucleation rate was observed ($\dot{n} \approx 2.0 \times 10^{10} \text{ m}^{-3} \cdot \text{s}^{-1}$). Because the grains were denser than the liquid, the formed grains sedimented and dragged the liquid melt to flow with them. Some of these newly formed equiaxed grains (with small size) were transported to the superheated region. As displayed in Fig. 5(c), the grains further solidified in the undercooled melt (as indicated by the positive $M_{\ell e}$), and those grains that were transported to the hot region melted ($M_{\ell e} < 0$). Re-melting accompanying solidification during casting process was numerically verified by the current model. As shown in Fig. 5(b), melting in the superheated region caused the grains to be destroyed, which reduced n_{eq} locally (as shown in Fig. 5(f)). Owing to solute partitioning ($m = 0.13$), solute-enriched liquid was rejected during the solidification process. High c_{ℓ} can be seen in Fig. 5(d) near the right surface. The rejected c_{ℓ} modified ΔT ($\Delta T = T_f + m \cdot c_{\ell} - T$) and thereby affected $M_{\ell e}$. n_{in} and n_{eq} are shown in Fig. 5(e)–(f), respectively. Nucleation consumed a large number of inoculants near the right surface (Fig. 5(b)), leading to a lower value of n_{in} in this region. After nucleation, the grains were transported along the vertical wall and piled up in the bottom ($n_{eq} \approx 10^{11} \text{ m}^{-3} \cdot \text{s}^{-1}$). The calculated f_c and d_c are shown in Fig. 5(g)–(h), respectively. The grains that nucleated on the surface adhered to the wall owing to the applied no-slip boundary condition. These grains grew quickly under strong undercooling, leading to a high f_c and large d_c on the right surface. In the lower-left corner, numerous small grains piled up. These small grains grew slowly because of the relatively high local temperature. From Fig. 5(g), it can be seen f_c was below f_c^c in the lower-left corner, which means that these small grains could be advected by liquid flow.

Analysis of the entire solidification sequence is shown in Fig. 6. During the early stage (0–120 s), the nucleation rate had a high magnitude of $\sim 10^{14} \text{ m}^{-3} \cdot \text{s}^{-1}$ near the right wall (Fig. 6(a-1)–(a-2)). Afterwards, the formed grains sank and were transported by the flow (Fig. 6(b-1)–(b-2)). Most grains piled up in the bottom. The grains could grow further or be re-

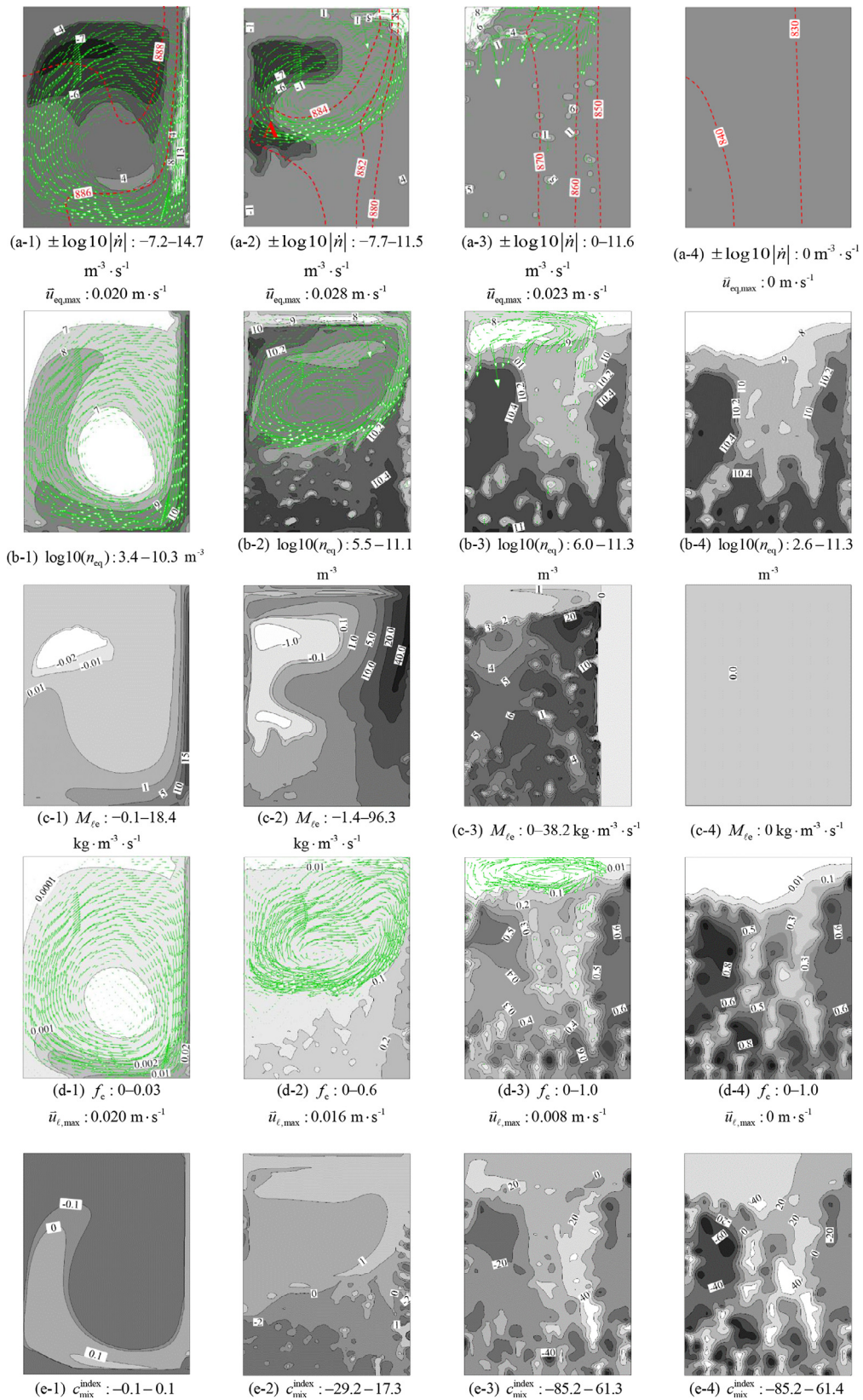


Fig. 6. Solidification sequence of case II (stage A). Contours and corresponding isolines of (a) $\pm \log_{10}|\dot{\gamma}|$ overlaid by the isolines of T (red dashed lines) and vectors of \vec{u}_{eq} ; (b) $\log_{10}(n_{\text{eq}})$ overlaid by the vectors of \vec{u}_{e} ; (c) $M_{\ell e}$; (d) f_{ℓ} overlaid by the vectors of \vec{u}_{ℓ} ; and (e) $c_{\text{mix}}^{\text{index}}$. Figures in the columns from left to right show the solidification sequence at 60, 120, 240, and 320 s, respectively. (For interpretation of the references to color in this figure legend, the reader is referred to the web version of this article.)

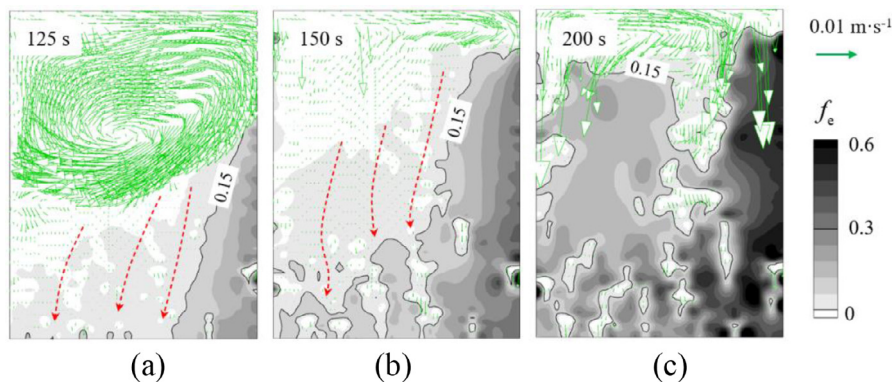


Fig. 7. Formation of a heterogeneous structure during solidification (case II, stage A). Contour of f_e overlaid by the vectors of \vec{u}_{eq} (in green). The solid isoline denotes the grain packing front ($f_e = f_{si} \cdot f_e^c = 0.15$), and the red vectors indicate the grain sedimentation trajectory. (For interpretation of the references to color in this figure legend, the reader is referred to the web version of this article.)

melted/destroyed, depending on the local ΔT . As shown in Fig. 6(a-2) and (c-2), the grains continued to solidify ($M_{le} > 0$) on the right side. On the left side, where the melt was relatively hot, the negative M_{le} indicates re-melting. The segregation index (c_{mix}^{index}) is shown in Fig. 6(e-1)–(e-2). The grains with a low solute concentration sank to the bottom, causing negative macrosegregation there. During the later stage (120–320 s), re-melting and grain destruction was almost impossible. As displayed in Fig. 6(d-3), only some liquid pockets survived in the lower part. Because of the small liquid regions, the liquid velocity was considerably smaller than the equiaxed velocity. As shown in Fig. 6(a-3), nucleation mainly occurred in the upper-left corner, where sufficient inoculants remained. In these liquid pockets, new grains were generated, but the nucleation rate was very low ($\dot{n} < 10^6 \text{ m}^{-3} \cdot \text{s}^{-1}$). Fig. 6(b-3) depicts the distribution of n_{eq} . The grains were transported from the right to the left, and then sedimented there. Some small grains were advected to the liquid region, but most of the domain was almost completely solidified (Fig. 6(c-3)). When the temperature decreased to the eutectic temperature, the remaining liquid solidified as the eutectic phase. Fig. 6(d-3) and (e-3) present the distribution of f_e and c_{mix}^{index} , respectively. Negative macrosegregation can be observed in the region where f_e was large. The final solidification results are shown in Fig. 6(a-4)–(e-4). The volume average of n_{in} was equal to $3.7 \times 10^8 \text{ m}^{-3}$, which indicates that most of the inoculants were activated as nuclei in the current case.

A value of 0.637 was used for the grain packing limit f_e^c . When $f_e > f_{si} \cdot f_e^c$, a rigid solid structure is generated. In Fig. 7, one solid isoline ($f_e = 0.15$) is drawn for the packing front. As shown in Fig. 7(a), in addition to the highly packed area in the lower-right corner, some lower-packed islands formed in the bottom. The equiaxed grains settled in the liquid–solid slurry. As presented in Fig. 7(b), the sedimentation and solidification of grains broadened the packed region, resulting in a heterogeneous solid structure. At a later moment (Fig. 7(c)), packed grains occupied most of the domain. Between the packed grains, there were some isolated liquid pockets, in which grains could still sink. Because the solid grains had a lower concentration than the surrounding eutectic phase, c_{mix}^{index} (Fig. 6(e)) exhibited a heterogeneous distribution similar to that of f_e (Fig. 6(d)).

4.2.2. Case ii (stage B): re-heating from the left side

The melting sequence at 380 s is presented in Fig. 8. The eutectic phase melted first at the eutectic isotherm, followed by gradual melting of the equiaxed grains. The left part of the domain was heated above the eutectic isotherm (Fig. 8(a)). After the eutectic phase melted, some liquid pockets were created, and a clockwise flow develops. The embedded grains (or grain clusters) were released and began to move again (Fig. 8(e)). c_ℓ (Fig. 8(b)) is large in region A, but it is relatively small in regions B and C. Because $\Delta T = T_f + m \cdot c_\ell - T$, ΔT is as a function of c_ℓ and T . As shown in Fig. 8(c), the alloy was overheated in region A and undercooled in regions B and C, which led to melting in region A and re-solidification in regions B and C (Fig. 8(d)). As shown in Fig. 8(e), from 320 to 380 s, d_e increased from 3.1 to 3.8 mm in region C and decreased from 0.48 to 0.37 mm in region A. The large grains sedimented quickly, but the small grains could easily be advected by the liquid flow. As shown in Fig. 8(f), nucleation occurred in regions B and C, but the nucleation rate was very small ($\sim 10^5 \text{ m}^{-3} \cdot \text{s}^{-1}$). In region A, the destruction rate was $-7.1 \times 10^7 \text{ m}^{-3} \cdot \text{s}^{-1}$. n_{eq} and n_{in} are presented in Fig. 8(g)–(h), respectively. Because only few grains were destroyed before this moment, there is no significant difference between Fig. 6 (b-4) and Fig. 8(g).

Analysis of the entire melting process is shown in Fig. 9. T and M_{le} are shown Fig. 9(a). In a majority of the domain, M_{le} was negative. In some regions (Fig. 9 (a-2)–(a-3)), M_{le} was positive, indicating local solidification. This can be better understood with the help of Fig. 8. The flow affects c_ℓ and T , and ΔT is calculated by $\Delta T = T_f + m \cdot c_\ell - T$. If c_ℓ is sufficiently high, the alloy can be undercooled even at an elevated T . Although local solidification was possible, the solidification rate was very small. Comparing Fig. 9(a)–(b), there was no new nucleation in the undercooled region. According to Fig. 9 (b-3), the maximum destruction rate during the late stage of the melting process (615 s) was $-3.2 \times 10^{10} \text{ m}^{-3} \cdot \text{s}^{-1}$, which is

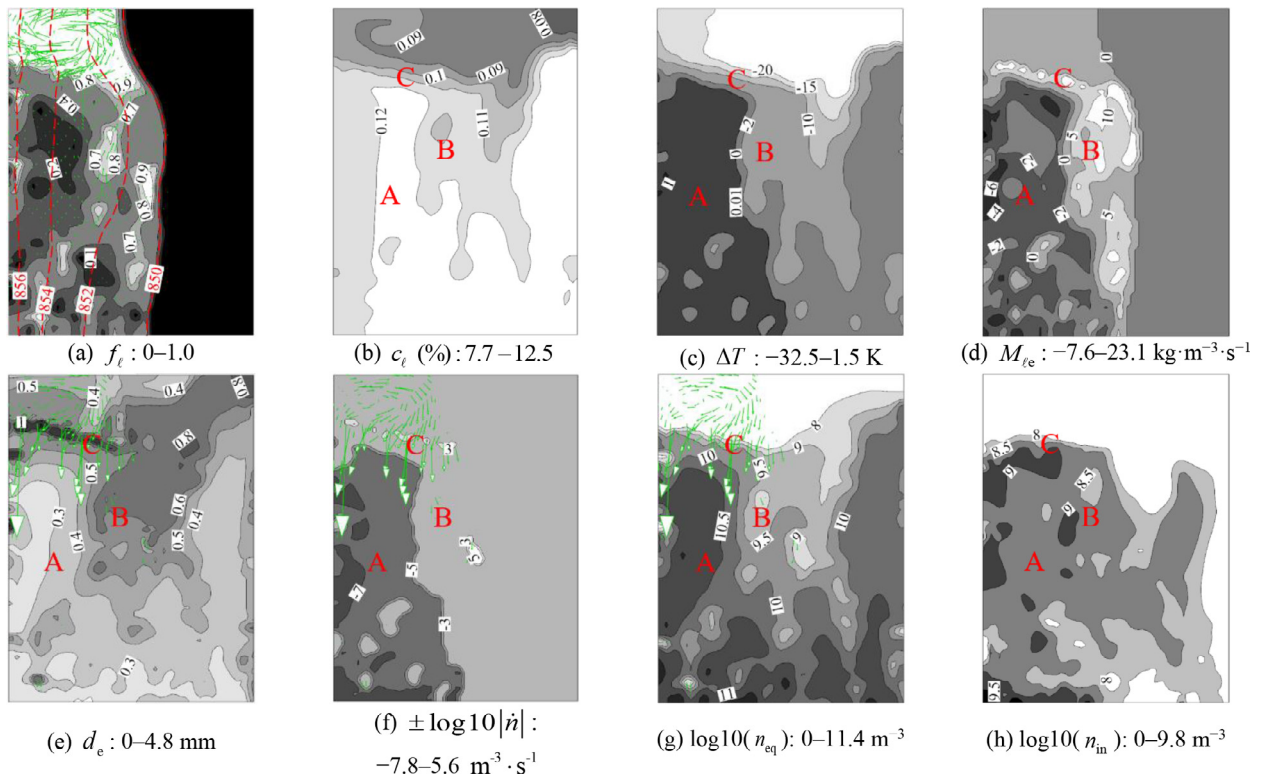


Fig. 8. Melting sequence of case II (stage B) at 380 s. Contours and corresponding isolines of (a) f_l overlaid by the isotherms (red dashed lines) and vectors of \vec{u}_l ; (b) c_s ; (c) ΔT ; (d) $M_{l,e}$; (e) d_e overlaid by the vectors of \vec{u}_{eq} ; (f) $\pm \log_{10}|\dot{n}|$ overlaid by the vectors of \vec{u}_e ; (g) $\log_{10}(n_{eq})$ overlaid by the vectors of \vec{u}_{eq} ; and (h) $\log_{10}(n_{in})$. (For interpretation of the references to color in this figure legend, the reader is referred to the web version of this article.)

three orders of magnitude larger than that at 380 s (Fig. 8(f)). f_e and n_{eq} are shown in Fig. 9(c)–(d), respectively. As melting progressed, f_e decreased, and when $f_e < f_{si} \cdot f_e^c$, the grains were movable. As the liquid regions expanded, the liquid velocity became increasingly stronger. Equiaxed grains were transported to the superheated regions and be melted/destroyed. The evolution of c_{mix}^{index} is shown in Fig. 9(e). As melting progressed, fresh liquid with a low solute concentration was released, which diluted the positive segregation. From 500 to 640 s, c_{mix}^{index} at point A was reduced from 32.6 to 3.2.

An interesting phenomenon was observed: transport of a bulk grain network during melting, as shown in Fig. 10. Two isolines are drawn: $f_e = 0.01$ (indicating the melt front), and $f_e = 0.15$ (indicating the packing front). At 600 s (Fig. 10(a)), more than half of the domain had melted. The packed region is marked as A, B, and C. Region A is connected to the main solid part (region C) through a thin bridge (region B). Two flow vortices developed, which were separated by the rigid solid structure. Only the liquid could flow through this rigid porous medium. At 610 s (Fig. 10(b)), region B had re-melted. Region A detached from region C, but it was still partially connected to the left wall. At 615 s (Fig. 10(c)), region A detached from the left wall and turned into the bulk melt region. The red vectors in Fig. 10 indicate the direction of rotation. In the subsequent melting process, this bulk grain network became increasingly smaller until it was completely melted.

5. Discussion

This work is an extension of the previous volume-average solidification model [4,22,24,26], which considers melting and grain destruction. Because this extension is implemented based on an ideal scenario of two-phase globular equiaxed solidification, for which no direct experiments are available to compare, numerical parameter studies were performed (1) to demonstrate the importance of melting and grain destruction during alloy solidification and (2) to investigate the effect of uncertainty in the parameters.

5.1. Importance of melting/grain destruction

To illustrate the importance of melting during solidification, an extra simulation case was conducted. All the settings were the same as those in case II (stage A) except that melting was ignored. A comparison between the simulation results of the two cases at 120 s is shown in Fig. 11. As shown in Fig. 11(a), melting occurred near the left wall region.

Re-melting consumed some latent heat, leading to a decrease in the local temperature. In comparison with the case without melting (Fig. 11(b)), the case with melting (Fig. 11(a)) predicted a slightly lower local temperature near the left wall. In Fig. 11(c), the contour of the sum of the re-melted mass, $\int_0^t M_{le} dt$, during the entire cooling (solidification) process is shown. Equiaxed grains, which were transported from other regions to the left wall region, re-melted. The volume average of $\iiint_{vol} (\int_0^t M_{le} dt) dV$ inside the solid isoline in Fig. 11(c) was $-8.3 \text{ kg}\cdot\text{m}^{-3}$. Re-melting $8.3 \text{ kg}\cdot\text{m}^{-3}$ of equiaxed grains will dilute the local melt concentration there. Correspondingly, $3.3 \times 10^6 \text{ J}\cdot\text{m}^{-3}$ of energy will be consumed as the latent heat of melting. The re-melting of the as-formed solid phase is an important mechanism of species and energy transport.

In the solidification model, if the accompanying melting and grain destruction were ignored, the volume integral of n_{eq} in the entire sample domain of the as-solidified sample would be overestimated by $\sim 2.0\%$, the volume integral of f_e would be overestimated by $\sim 1.7\%$, the volume integral of d_e would be underestimated by $\sim 3.0 \mu\text{m}$, and the integral of $|c_{mix}^{index}|$ would be underestimated by ~ 0.9 . Note that the casting sample used in the current study was very small, and

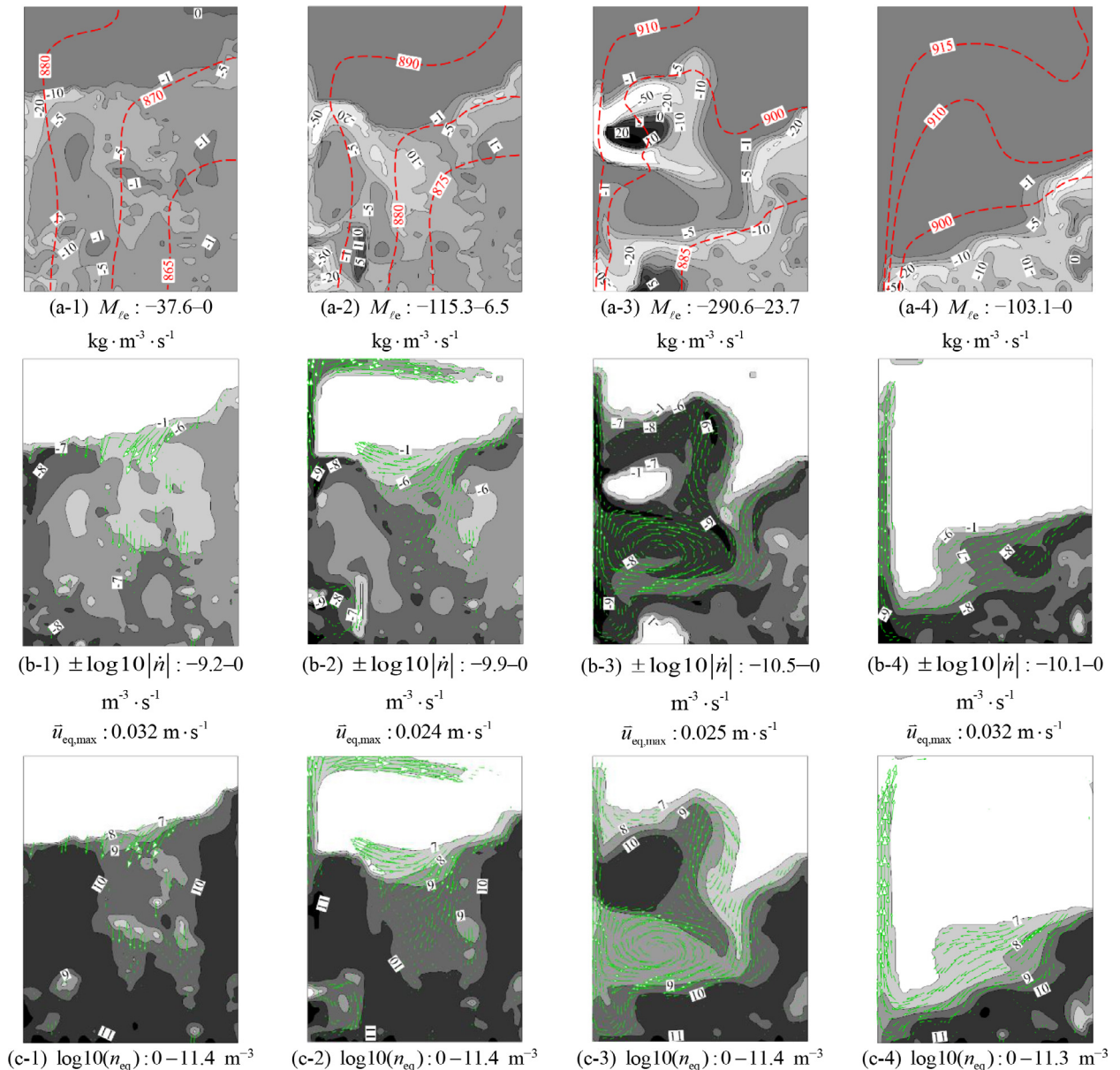


Fig. 9. Melting sequence of case II (stage B). Contours and corresponding isolines of (a) M_{le} overlaid by T (red dashed lines); (b) $\pm \log_{10}|\dot{n}|$ overlaid by the vectors of \bar{u}_{eq} ; (c) $\log_{10}(n_{eq})$ overlaid by the vectors of \bar{u}_{eq} ; (d) f_e overlaid by the vectors of \bar{u}_t ; and (e) c_{mix}^{index} . Figures in the columns from left to right show the melting sequences at 500, 560, 615, and 640 s, respectively. (For interpretation of the references to color in this figure legend, the reader is referred to the web version of this article.)

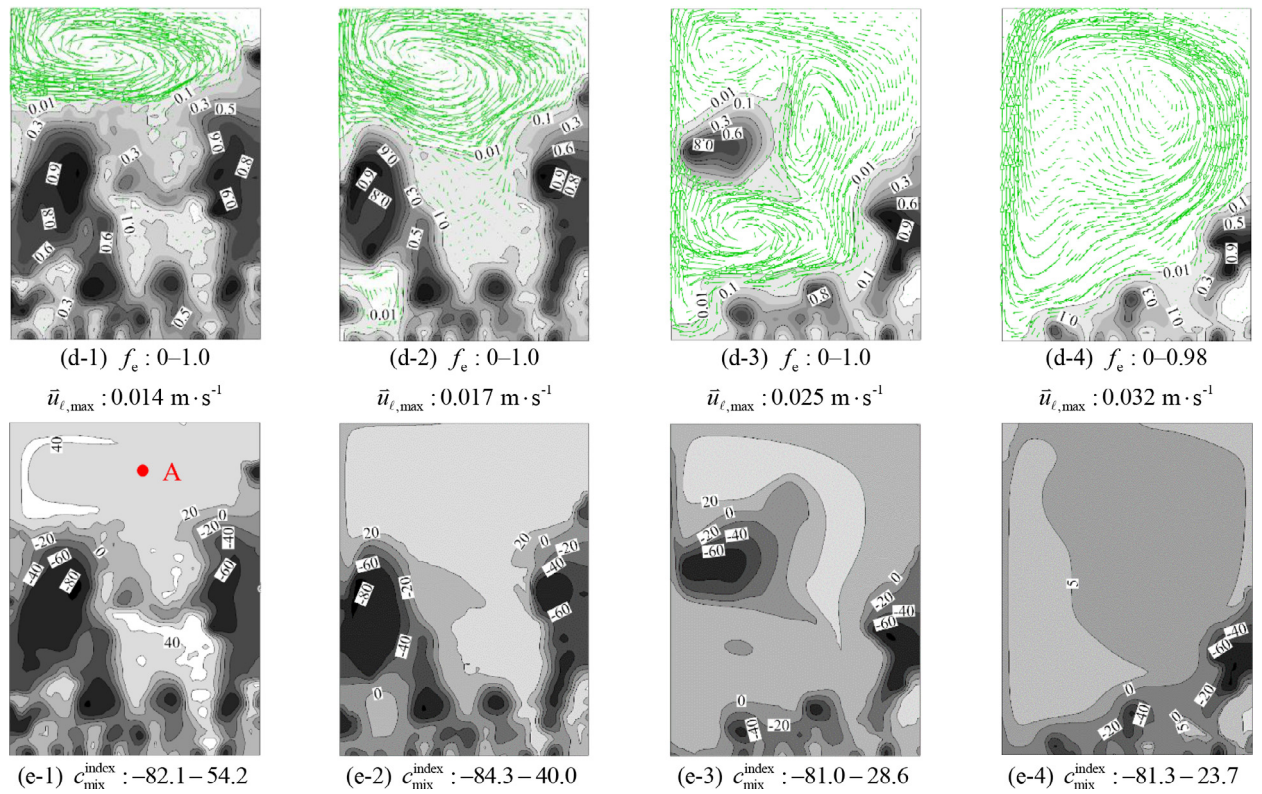


Fig. 9. Continued

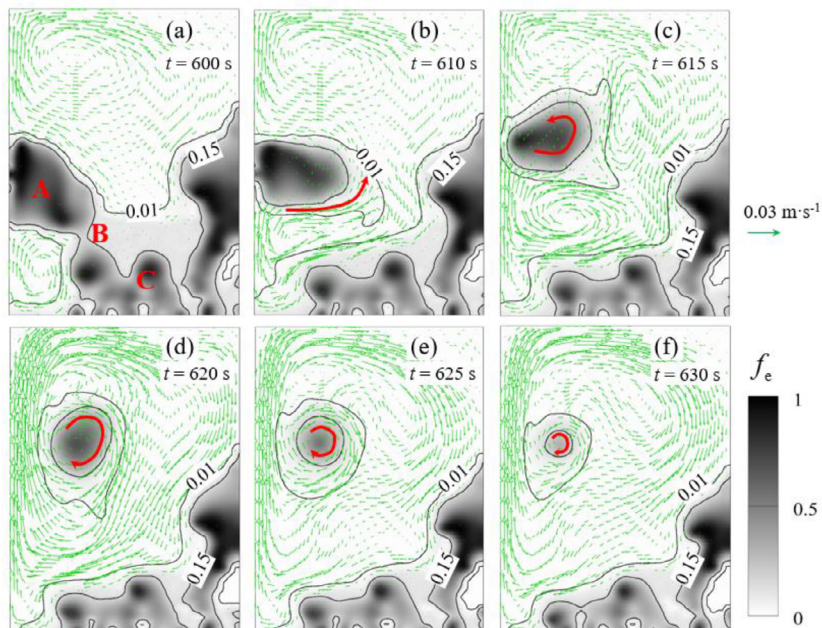


Fig. 10. Transport of a bulk grain network during the melting process shown by the contours of f_e overlaid by the vectors of \bar{u}_t . The red vectors indicate the rotation direction of the bulk grain network. (For interpretation of the references to color in this figure legend, the reader is referred to the web version of this article.)

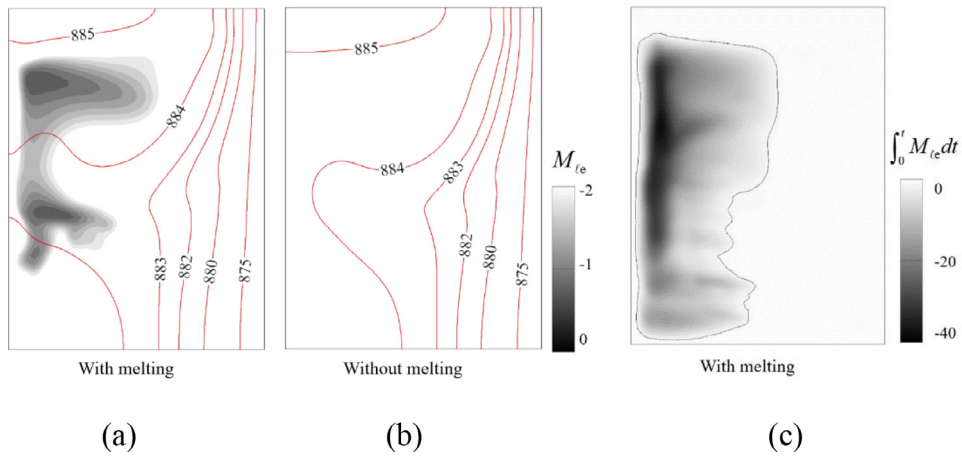


Fig. 11. Comparison of two simulations for case II (stage A): (a) with melting and (b) without melting at 120 s. In (a), the contour of M_{le} (only $M_{le} < 0$ is shown) is overlaid by isotherms. (c) Contour of the sum of the re-melted mass $\int_0^t M_{le} dt$ during the entire cooling (solidification) process.

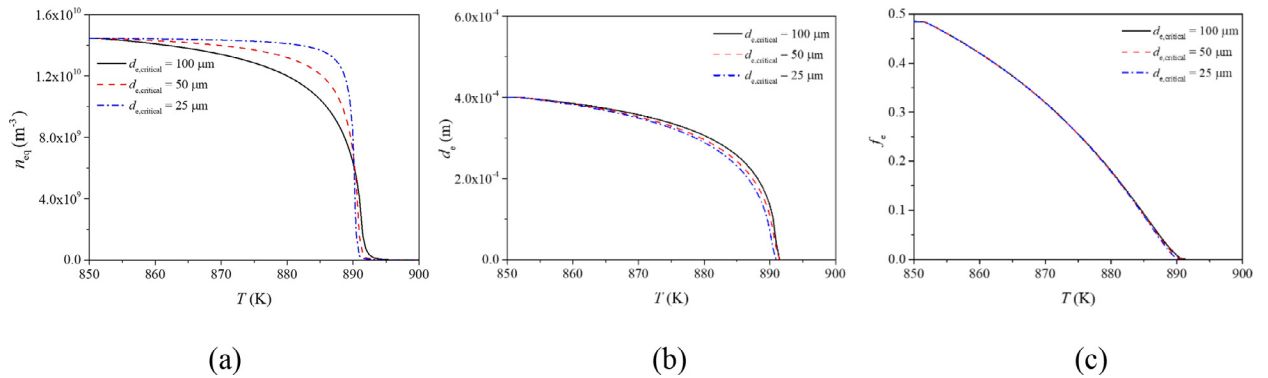


Fig. 12. Effect of $d_{e,critical}$ on the calculated (a) n_{eq} , (b) d_e , and (c) f_e as a function of T . These simulations were performed based on case I (stage B), and all quantities were taken from the domain centre.

the aforementioned differences were not very significant. However, the role of re-melting and grain destruction, which accompany alloy solidification, would become more obvious for casting with larger dimensions. For example, in engineering ingot or continuous castings, the melt flow and grain transport are approximately 1–2 orders of magnitude more intensive. Therefore, the re-melting effect should be more significant.

5.2. Effect of $d_{e,critical}$

$d_{e,critical}$ was introduced as the critical grain size for grain destruction. Determining the exact value of $d_{e,critical}$ is beyond the scope of this study. However, a numerical parameter study can be performed to analyse the sensitivity of the melting process to its value. The calculated n_{eq} , d_e , and f_e are shown in Fig. 12(a)–(c), respectively. As expected, when $d_{e,critical}$ was larger, n_{eq} decreased faster, and d_e became larger. However, $d_{e,critical}$ has a minimal effect on f_e . This is understandable because n_{eq} and f_e are calculated from their conservation equations, out of which the volume-averaged grain size is derived: $d_e = \sqrt[3]{6f_e/\pi n_{eq}}$. The combination of decreased n_{eq} and increased d_e results in almost no change in the solidification; hence, f_e appears to be independent from $d_{e,critical}$. It should be stressed that $d_{e,critical}$ cannot be too small or too large. Physically, $d_{e,critical}$ should be larger than the size of inoculants (~2 μm). An excessive $d_{e,critical}$ results in equiaxed grains that cannot be realistically melted in one time step ($\Delta t = 0.001s$). From the parameter study shown in Fig. 12, the calculated d_e and f_e appear to not be sensitive to the chosen $d_{e,critical}$ when its value falls in the range 25–100 μm, but the exact value of $d_{e,critical}$ requires further investigation.

5.3. Mesh sensitivity study

Simulations with three different mesh sizes ($\Delta x = 2.0, 1.0,$ and 0.5 mm) were performed to examine the mesh sensitivity. The distribution of f_e in the as-solidified sample is shown in Fig. 13. Although the distributions of f_e were not identical,

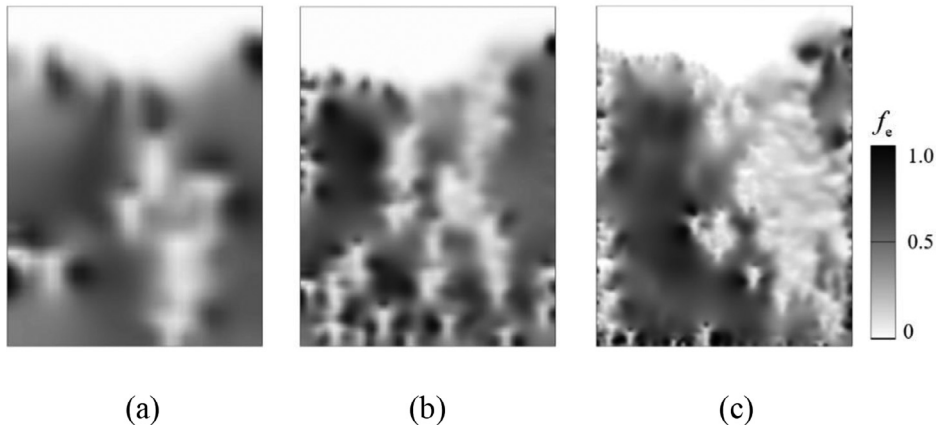


Fig. 13. Simulation results with different mesh size: (a) $\Delta x = 2.0\text{mm}$, (b) $\Delta x = 1.0\text{mm}$, and (c) $\Delta x = 0.5\text{mm}$. The contour denotes f_e at the end of solidification. These simulations were performed based on case II (stage A).

an equiaxed-free region was observed in the upper-left corner of all simulations. For all three simulations, the volume-averaged f_e over the entire casting domain was 41.6, 39.7, and 38.3%, and the volume-averaged $|c_{\text{mix}}^{\text{index}}|$ was 21.9, 25.1, and 25.0, respectively. With the current mesh size, it is not possible to get a quantitatively converged result. However, it can be safely concluded that calculations with a mesh size smaller than 1.0 mm can reproduce the phase distribution pattern.

5.4. Grain packing

f_e^c plays important role in the formation of the as-solidified microstructure and macrosegregation. Some previous models used a value of 0.637 for f_e^c by assuming ideal face-centred close packing of equal-diameter spheres [4,22,29,43,44], while most industry alloys with dendritic solidification would pack at a much lower f_e^c , e.g. 0.27 was used for an Al-22 wt.% Cu alloy [39] and 0.4 for a steel ingot [45]. Most recent works have shown that as the morphology of the particles changes from spherical towards a more nonconvex geometry, the packing fraction decreases [46,47]. Plotkowski and Krane [48,49] investigated the effect of the local velocity field on the likelihood of packing. They proposed that particles were more likely to pack if their velocity was directed towards a packed interface, and less likely to attach when they were advected away from the interface. Experimental data for different alloys revealed that the packing limit could be reached when the solid fraction was approximately 0.1–0.3 in large-grained casting [24,50,51].

Similar to previous studies [4,22,29,43,44], f_e^c was assumed to equal to 0.637 in this study. As aforementioned, a simplified dendritic morphology of equiaxed grain was considered to calculate the hydrodynamic interactions. When the solid grain is considered as an equiaxed grain envelope, the corresponding packing solid fraction can be evaluated by $f_e = f_e^c \cdot f_{\text{si}}$. In this study, because $f_e^c = 0.637$ and $f_{\text{si}} = 0.235$, the corresponding packing solid fraction is equal to 0.15. f_{si} is a parameter related to the morphology of the equiaxed grain. A numerical study was performed to study the effect of f_{si} on the solidification results. The simulation results at 100 s for three different f_{si} are compared in Fig. 14(a). When a small f_{si} was used (dendritic grain), the grains packed shortly after nucleation. When a large f_{si} was used (globular grain), more grains could be transported, causing grains to pile up at the bottom. The as-solidified structure is shown in Fig. 14(b). A large f_{si} was beneficial for phase separation and therefore the extension of the equiaxed-free (pure eutectic) region at the top.

In the current paper, two cases were designed to study the melting and grain destruction phenomena during equiaxed solidification. The first simple case (Case I) is a 0-dimensional case, i.e. the simulation results represent the solidification/melting in one isolated volume element. No flow and grain transport are considered. With this simple case, one can verify all modelling concepts/assumptions in mathematical way. The second case (Case II) is closer to reality, but not consistent with a real casting. Flow and grain transport in 2-dimensional situation are considered, but still some assumptions were made and some modelling parameters might not be realistic. For example, a real casting mostly solidifies in a mixed columnar-equiaxed solidification. Here, the columnar structure has to be ignored in this step. Nevertheless, this modelling step (Case II) is very necessary. It helps to verify the modelling capacity (functionalities) for the remelting/grain destruction with melt flow and grain transport. Although the modelling result is difficult to compare with that of a real casting benchmark quantitatively, the modelling result can qualitatively explore important phenomena which would occur in real castings. The next step of the modelling part would be to compare quantitatively with real casting benchmark. For that purpose, some unrealistic assumptions (e.g. ignorance of columnar structure) must be released, and reliable modelling parameters must be determined through parameter studies and necessary experimental measurements. This work will continue, especially regarding to validation of the model by comparison with more realistic benchmark and laboratory casting experiments.

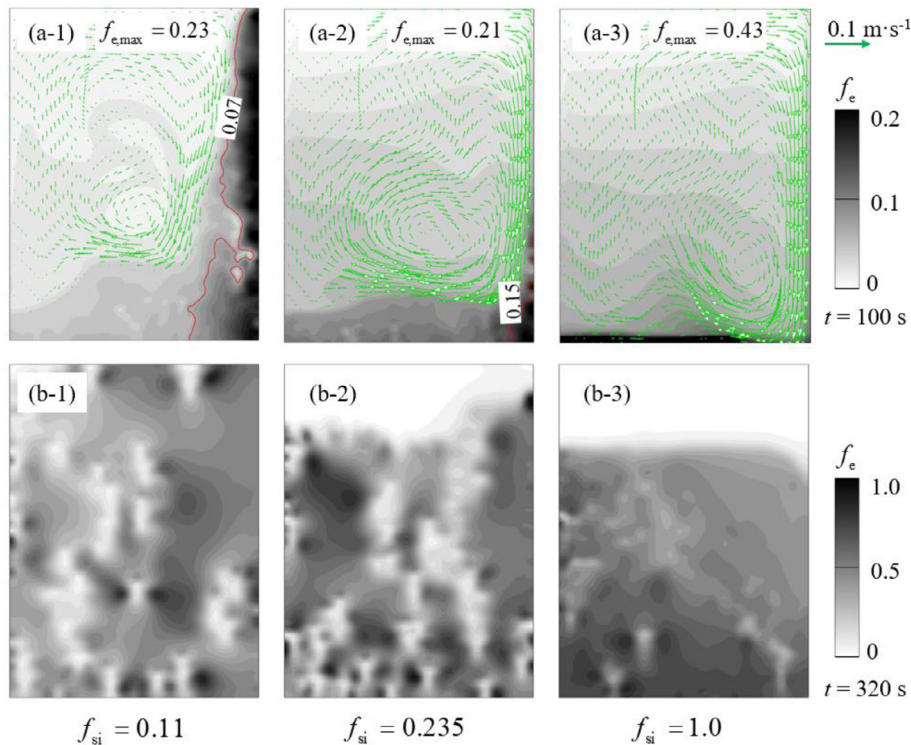


Fig. 14. Effect of f_{si} (0.11, 0.235, and 1.0) on the simulation results. (a-1)–(a-3) Simulation results at 100 s with the contours of f_e overlaid by the vectors of \vec{u}_{eq} . The red isolines of $f_e = f_e^c \cdot f_{si}$ in (a-1) and (a-2) indicate the packing fronts. (b-1)–(b-3) Simulation results with the contours of f_e at the end of solidification. These simulations were performed based on case II (stage A). (For interpretation of the references to color in this figure legend, the reader is referred to the web version of this article.)

6. Conclusions

A volume-average-based two-phase globular equiaxed solidification model was extended to include the melting and grain destruction. To verify the model, simulations of solidification/melting of a 2D rectangular Al–7 wt.% Si casting were performed.

Under the purely diffusive solidification/melting condition, the sum of the number densities of the inoculants (free growth sites) and activated equiaxed grains ($n_{in} + n_{eq}$) was always locally conserved. Although the same diffusion-governed kinetics applied for growth and size-reduction of the equiaxed grains, the obtained $f_e - T$ curves during cooling (solidification) and heating (melting) were not identical. Therefore, melting cannot be simply considered to be inverse solidification.

With the addition of thermo-solutal convection and grain transport, it is only the volume integral of the number densities of the inoculants and activated equiaxed grains over the entire casting domain ($\Sigma(n_{in} + n_{eq})$) that is conserved. During cooling (solidification), some as-nucleated equiaxed grains were transported to superheated regions where re-melting and grain destruction occurred. In the opposite condition, during heating (melting), there were some locally undercooled regions where nucleation and solidification could occur. This simultaneous solidification/melting phenomenon presents an important species/energy transport mechanism, influencing the structural and compositional heterogeneity of the final as-cast product.

Acknowledgments

The authors acknowledge the financial support from Austrian Research Promotion Agency (FFG) –Austrian Space Application Program (ASAP) through the project FLOWSCONS (No. 859777), [Austria Science Fund](#) (FWF, I4278-N36), as well as the support from European Space Agency (ESA) through the project MICAST.

Appendix A. Lognormal grain size distribution

The lognormal distribution is widely used in the probabilistic description of engineering quantities that only have positive values [52–55]. It is introduced here to characterise the grain size distribution. The probability distribution function (PDF)

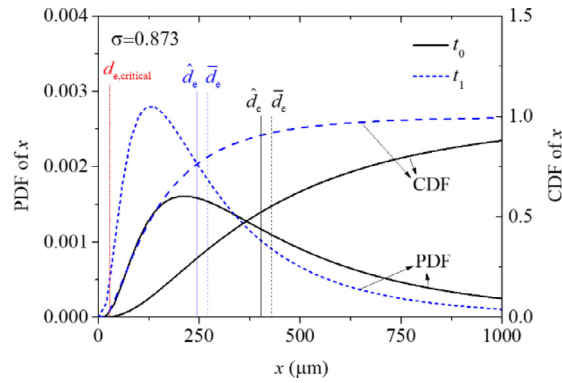


Fig. A1. Description of the melting process (from t_0 to t_1) with a lognormal grain size distribution. PDF: probability distribution function; CDF: cumulative distribution function.

of grain size is written as

$$f(x) = \frac{1}{\sqrt{2\pi}\sigma x} e^{-\frac{1}{2}\left(\frac{\ln(x)-\ln(\hat{d}_e)}{\sigma}\right)^2}, \tag{A.1}$$

where x is the dummy variable corresponding to the grain diameter of different size classes, σ is the geometric standard deviation, and \hat{d}_e is the geometric mean of the grains:

$$\hat{d}_e = \sqrt[n]{\prod_{i=1}^n d_{e,i}}. \tag{A.2}$$

The PDF and the corresponding cumulative distribution function (CDF) of the grain size at two different moments (t_0 and t_1) are shown in Fig. A1. As melting occurs between t_0 and t_1 , \hat{d}_e decreases, and the PDF curve changes correspondingly. Note that the volume-averaged grain diameter d_e is calculated by

$$d_e = \sqrt[3]{\frac{6f_e}{\pi n_{eq}}}, \tag{A.3}$$

which is not equal to \hat{d}_e . For the current volume-average model, only a volume-averaged grain diameter can be obtained. In this paper, \hat{d}_e is approximated by d_e . A further assumption is made: the variation in d_e and \hat{d}_e due to melting follows the same trend, i.e. $d(\hat{d}_e)/dt \approx d(d_e)/dt$, which can be estimated by v_{Re} .

References

- [1] D.J. Allen, J.D. Hunt, Melting during solidification, *Metall. Trans. A.* 7 (1976) 767–770, doi:10.1007/BF03186812.
- [2] M. Rettenmayr, Melting and remelting phenomena, *Int. Mater. Rev.* 54 (2009) 1–17, doi:10.1179/174328009X392930.
- [3] M.E. Glicksman, Melting kinetics in microgravity, *J. Phys. Conf. Ser.* 327 (2011) 012001, doi:10.1088/1742-6596/327/1/012001.
- [4] J. Ni, C. Beckermann, Modeling of globulitic alloy solidification with convection, *J. Mater. Process. Manuf. Sci.* 2 (1993) 217–231.
- [5] J.W. Gao, C.Y. Wang, An experimental investigation into the effects of grain transport on columnar to equiaxed transition during dendritic alloy solidification, *J. Heat Transf.* 121 (1999) 430–437, doi:10.1115/1.2825996.
- [6] J.W. Gao, C.Y. Wang, Effects of grain transport on columnar to equiaxed transition in dendritic alloy solidification, *Model. Cast. Weld. Adv. Solidif. Process.* VIII (1998) 425–432.
- [7] W. Kurz, D.J. Fisher, R. Trivedi, Progress in modelling solidification microstructures in metals and alloys: dendrites and cells from 1700 to 2000, *Int. Mater. Rev.* 64 (2019) 311–354, doi:10.1080/09506608.2018.1537090.
- [8] W.J. Boettinger, S.R. Coriell, A.L. Greer, A. Karma, W. Kurz, M. Rappaz, R. Trivedi, Solidification microstructures: recent developments, future directions, *Acta Mater.* 48 (2000) 43–70, doi:10.1016/S1359-6454(99)00287-6.
- [9] C. Beckermann, R. Viskanta, M. Buchmann, M. Rettenmayr, Microstructure evolution during melting and resolidification in a temperature gradient, *J. Cryst. Growth* 284 (2005) 544–553, doi:10.1016/j.jcrysgro.2005.06.044.
- [10] L.S. Yao, J. Prusa, Melting and Freezing, *Adv. Heat Transf.* 19 (1989) 1–95, doi:10.1016/S0065-2717(08)70211-9.
- [11] A. Kumar, P. Dutta, S. Sundarraj, M.J. Walker, Remelting of solid and its effect on macrosegregation during solidification, *Numer. Heat Transf. Part A Appl.* 51 (2007) 59–83, doi:10.1080/10407780600710391.
- [12] U. Bösenberg, M. Buchmann, M. Rettenmayr, Initial transients during solid/liquid phase transformations in a temperature gradient, *J. Cryst. Growth* 304 (2007) 281–286, doi:10.1016/j.jcrysgro.2007.03.001.
- [13] C. Gau, R. Viskanta, Melting and solidification of a pure metal on a vertical wall, *J. Heat Transfer.* 108 (1986) 174–181, doi:10.1115/1.3246884.
- [14] Y. Wang, A. Amiri, K. Vafai, An experimental investigation of the melting process in a rectangular enclosure, *Int. J. Heat Mass Transf.* 42 (1999) 3659–3672, doi:10.1016/S0017-9310(99)00024-1.
- [15] H. Yin, J.N. Koster, Double-diffusive convective flow and interface morphology during transient Ga-5% In alloy melting, *J. Cryst. Growth* 217 (2000) 170–182, doi:10.1016/S0022-0248(00)00411-5.
- [16] R.S. Renko, H.C. de Groh, C. Beckermann, Effect of melt convection and solid transport on macrosegregation and grain structure in equiaxed Al-Cu alloys, *Mater. Sci. Eng. A* 347 (2003) 186–197, doi:10.1016/S0921-5093(02)00592-0.
- [17] H. Hu, S.A. Argyropoulos, Mathematical modelling of solidification and melting: a review, *Model. Simul. Mater. Sci. Eng.* 4 (1996) 371–396, doi:10.1088/0965-0393/4/4/004.

- [18] S. Jana, S. Ray, F. Durst, A numerical method to compute solidification and melting processes, *Appl. Math. Model.* 31 (2007) 93–119, doi:[10.1016/j.apm.2005.08.012](https://doi.org/10.1016/j.apm.2005.08.012).
- [19] H. Zhang, M. Charmchi, D. Veilleux, M. Faghri, Numerical and experimental investigation of melting in the presence of a magnetic field: simulation of low-gravity environment, *J. Heat Transfer.* 129 (2007) 568–576, doi:[10.1115/1.2709961](https://doi.org/10.1115/1.2709961).
- [20] V.R. Voller, A. Mouchmov, M. Cross, An explicit scheme for coupling temperature and concentration fields in solidification models, *Appl. Math. Model.* 28 (2004) 79–94, doi:[10.1016/S0307-904X\(03\)00115-X](https://doi.org/10.1016/S0307-904X(03)00115-X).
- [21] Q. Zhang, H. Fang, H. Xue, Q. Tang, S. Pan, M. Rettenmayr, M. Zhu, Modeling of melting and resolidification of equiaxed microstructures in a temperature gradient, *Scr. Mater.* 151 (2018) 28–32, doi:[10.1016/j.scriptamat.2018.03.031](https://doi.org/10.1016/j.scriptamat.2018.03.031).
- [22] M. Wu, A. Ludwig, A. Bührig-Polaczek, M. Fehlbier, P.R. Sahn, Influence of convection and grain movement on globular equiaxed solidification, *Int. J. Heat Mass Transf.* 46 (2003) 2819–2832, doi:[10.1016/S0017-9310\(03\)00054-1](https://doi.org/10.1016/S0017-9310(03)00054-1).
- [23] M. Wu, A. Ludwig, Modeling equiaxed solidification with melt convection and grain sedimentation-I: model description, *Acta Mater.* 57 (2009) 5621–5631, doi:[10.1016/j.actamat.2009.07.056](https://doi.org/10.1016/j.actamat.2009.07.056).
- [24] C.Y. Wang, C. Beckermann, Equiaxed dendritic solidification with convection: part I. Multiscale/multiphase modeling, *Metall. Mater. Trans. A Phys. Metall. Mater. Sci.* 27 (1996) 2754–2764, doi:[10.1007/BF02652369](https://doi.org/10.1007/BF02652369).
- [25] J. Ni, C. Beckermann, A volume-averaged two-phase model for transport phenomena during solidification, *Metall. Trans. B.* 22 (1991) 349–361, doi:[10.1007/BF02651234](https://doi.org/10.1007/BF02651234).
- [26] A. Ludwig, M. Wu, Modeling of globular equiaxed solidification with a two-phase approach, *Metall. Mater. Trans. A Phys. Metall. Mater. Sci.* 33 (2002) 3673–3683, doi:[10.1007/s11661-002-0241-z](https://doi.org/10.1007/s11661-002-0241-z).
- [27] J.P. Gu, C. Beckermann, A.F. Giamei, Motion and remelting of dendrite fragments during directional solidification of a nickel-base superalloy, *Metall. Mater. Trans. A Phys. Metall. Mater. Sci.* 28 (1997) 1533–1542, doi:[10.1007/s11661-997-0215-2](https://doi.org/10.1007/s11661-997-0215-2).
- [28] Y. Zheng, M. Wu, A. Kharicha, A. Ludwig, Numerical analysis of macrosegregation in vertically solidified Pb-Sn test castings-part II: equiaxed solidification, *Comput. Mater. Sci.* 124 (2016) 456–470, doi:[10.1016/j.commatsci.2016.07.018](https://doi.org/10.1016/j.commatsci.2016.07.018).
- [29] M. Wu, A. Ludwig, A. Kharicha, Volume-averaged modeling of multiphase flow phenomena during alloy solidification, *Metals* 9 (2019) 229 Basel, doi:[10.3390/met9020229](https://doi.org/10.3390/met9020229).
- [30] R.B. Bird, W.E. Stewart, E.N. Lightfoot, *Transport Phenomena, Revised 2n*, 2006. 10.1002/aic.690070245.
- [31] A.L. Greer, P.S. Cooper, M.W. Meredith, W. Schneider, P. Schumacher, J.A. Spittle, A. Tronche, Grain refinement of aluminium alloys by inoculation, *Adv. Eng. Mater.* 5 (2003) 81–91, doi:[10.1002/adem.200390013](https://doi.org/10.1002/adem.200390013).
- [32] A.M. Bunn, P. Schumacher, M.A. Kearns, C.B. Boothroyd, A.L. Greer, Grain refinement by Al-Ti-B alloys in aluminium melts: a study of the mechanisms of poisoning by zirconium, *Mater. Sci. Technol.* 15 (1999) 1115–1123, doi:[10.1179/026708399101505158](https://doi.org/10.1179/026708399101505158).
- [33] M. Rappaz, Modelling of microstructure formation in solidification processes, *Int. Mater. Rev.* 34 (1989) 93–124, doi:[10.1179/imr.1989.34.1.93](https://doi.org/10.1179/imr.1989.34.1.93).
- [34] M. Rappaz, C.A. Gandin, Probabilistic modelling of microstructure formation in solidification processes, *Acta Metall. Mater.* 41 (1993) 345–360, doi:[10.1016/0956-7151\(93\)90065-Z](https://doi.org/10.1016/0956-7151(93)90065-Z).
- [35] M. Wu, A. Ludwig, Using a three-phase deterministic model for the columnar-to-equiaxed transition, *Metall. Mater. Trans. A Phys. Metall. Mater. Sci.* 38 A (2007) 1465–1475, doi:[10.1007/s11661-007-9175-9](https://doi.org/10.1007/s11661-007-9175-9).
- [36] C.A. Gandin, M. Rappaz, A coupled finite element-cellular automaton model for the prediction of dendritic grain structures in solidification processes, *Acta Metall. Mater.* 42 (1994) 2233–2246, doi:[10.1016/0956-7151\(94\)90302-6](https://doi.org/10.1016/0956-7151(94)90302-6).
- [37] T.E. Quested, A.L. Greer, Grain refinement of Al alloys: mechanisms determining as-cast grain size in directional solidification, *Acta Mater.* 53 (2005) 4643–4653, doi:[10.1016/j.actamat.2005.06.018](https://doi.org/10.1016/j.actamat.2005.06.018).
- [38] Y. Zheng, M. Wu, E. Karimi-Sibaki, A. Kharicha, A. Ludwig, Use of a mixed columnar-equiaxed solidification model to analyse the formation of as-cast structure and macrosegregation in a Sn-10 wt% Pb benchmark experiment, *Int. J. Heat Mass Transf.* 122 (2018) 939–953, doi:[10.1016/j.ijheatmasstransfer.2018.02.012](https://doi.org/10.1016/j.ijheatmasstransfer.2018.02.012).
- [39] M. Bedel, K.O. Tveito, M. Založnik, H. Combeau, M. M'Hamdi, A model study of the impact of the transport of inoculant particles on microstructure formation during solidification, *Comput. Mater. Sci.* 102 (2015) 95–109, doi:[10.1016/j.commatsci.2015.01.028](https://doi.org/10.1016/j.commatsci.2015.01.028).
- [40] H. Zhang, M. Wu, S.N. Tewari, A. Ludwig, A. Kharicha, Geometrical effect on macrosegregation formation during unidirectional solidification of Al-Si alloy, *J. Mater. Process. Technol.* 288 (2020) 116913, doi:[10.1016/j.jmatprotec.2020.116913](https://doi.org/10.1016/j.jmatprotec.2020.116913).
- [41] H. Zhang, M. Wu, Y. Zheng, A. Ludwig, A. Kharicha, Numerical study of the role of mush permeability in the solidifying mushy zone under forced convection, *Mater. Today Commun.* 22 (2020) 100842, doi:[10.1016/j.mtcomm.2019.100842](https://doi.org/10.1016/j.mtcomm.2019.100842).
- [42] M. Ghods, L. Johnson, M. Lauer, R.N. Grugel, S.N. Tewari, D.R. Poirier, Radial macrosegregation and dendrite clustering in directionally solidified Al-7Si and Al-19Cu alloys, *J. Cryst. Growth* 441 (2016) 107–116, doi:[10.1016/j.jcrysgro.2016.02.014](https://doi.org/10.1016/j.jcrysgro.2016.02.014).
- [43] T. Wang, L. Hachani, Y. Fautrelle, Y. Delannoy, E. Wang, X. Wang, O. Budenkova, Numerical modeling of a benchmark experiment on equiaxed solidification of a Sn-Pb alloy with electromagnetic stirring and natural convection, *Int. J. Heat Mass Transf.* 151 (2020) 119414, doi:[10.1016/j.ijheatmasstransfer.2020.119414](https://doi.org/10.1016/j.ijheatmasstransfer.2020.119414).
- [44] C.Y. Wang, C. Beckermann, Equiaxed dendritic solidification with convection: part II. Numerical simulations for an Al-4 Wt pct Cu alloy, *Metall. Mater. Trans. A Phys. Metall. Mater. Sci.* 27 (1996) 2765–2783, doi:[10.1007/BF02652370](https://doi.org/10.1007/BF02652370).
- [45] H. Combeau, M. Založnik, S. Hans, P.E. Richey, Prediction of macrosegregation in steel ingots: influence of the motion and the morphology of equiaxed grains, *Metall. Mater. Trans. B Process Metall. Mater. Process. Sci.* 40 (2009) 289–304, doi:[10.1007/s11663-008-9178-y](https://doi.org/10.1007/s11663-008-9178-y).
- [46] A. Olmedilla, M. Založnik, B. Rouat, H. Combeau, Packing of sedimenting equiaxed dendrites, *Phys. Rev. E.* 97 (2018) 1–10, doi:[10.1103/PhysRevE.97.012910](https://doi.org/10.1103/PhysRevE.97.012910).
- [47] A. Olmedilla, M. Založnik, T. Messmer, B. Rouat, H. Combeau, Packing dynamics of spherical and nonconvex grains sedimenting at low Stokes number, *Phys. Rev. E.* 99 (2019) 1–11, doi:[10.1103/PhysRevE.99.012907](https://doi.org/10.1103/PhysRevE.99.012907).
- [48] A. Plotkowski, M.J.M. Krane, The effect of velocity based packing schemes on macrosegregation development in simulations of equiaxed solidification, *Appl. Math. Model.* 40 (2016) 9212–9227, doi:[10.1016/j.apm.2016.05.031](https://doi.org/10.1016/j.apm.2016.05.031).
- [49] A. Plotkowski, M.J.M. Krane, The discrete nature of grain attachment models in simulations of equiaxed solidification, *Appl. Math. Model.* 47 (2017) 31–44, doi:[10.1016/j.apm.2017.03.009](https://doi.org/10.1016/j.apm.2017.03.009).
- [50] M.C. Flemings, Behavior of metal alloys in the semisolid state, *Metall. Trans. A.* 22 (1991) 957–981, doi:[10.1007/BF02661090](https://doi.org/10.1007/BF02661090).
- [51] L. Arnberg, G. Chai, L. Backerud, Determination of dendritic coherency in solidifying melts by rheological measurements, *Mater. Sci. Eng. A* 173 (1993) 101–103, doi:[10.1016/0921-5093\(93\)90195-K](https://doi.org/10.1016/0921-5093(93)90195-K).
- [52] G. Maymon, Some important statistical distributions, 2018. doi:[10.1016/b978-0-12-814191-5.00002-4](https://doi.org/10.1016/b978-0-12-814191-5.00002-4).
- [53] D. Wang, L.S. Fan, Particle characterization and behavior relevant to fluidized bed combustion and gasification systems, 2013. 10.1533/9780857098801.142.
- [54] E. Limpert, W.A. Stahel, M. Abbt, Log-normal distributions across the sciences: keys and clues, *Bioscience* 51 (2001) 341–352. doi:[10.1641/0006-3568\(2001\)051\[0341:LNDATS\]2.0.CO;2](https://doi.org/10.1641/0006-3568(2001)051[0341:LNDATS]2.0.CO;2).
- [55] T.E. Quested, A.L. Greer, P.S. Cooper, The variable potency of TiB₂ nucleant particles in the grain refinement of aluminium by Al-Ti-B additions, *Mater. Sci. Forum.* 396–402 (2002) 53–58, doi:[10.4028/www.scientific.net/msf.396-402.53](https://doi.org/10.4028/www.scientific.net/msf.396-402.53).